Under pressure: exploring the mechanobiology of *Phytophthora* invasion

Jochem Bronkhorst

Propositions

1. In-vitro studies of penetration biology are misleading if the host mechanics is not closely mimicked. (This thesis)

2. Use of the word appressorium for the invasive hyphal tip facilitating host entry of oomycete plant pathogens is erroneous. (This thesis)

3. The adoption of physical tools by biologists is only possible if physicists apply the KISS principle.

4. Preaching about stimulating multidisciplinary research without dedicating funding to develop common language is an empty intent.

5. Mandatory courses in mental hygiene are crucial for maximizing the scientific potential of PhD trajectories.

6. Governed continuation of price drops in sustainable energy technology is vital to saving the planet.

7. The Downs-Thomson paradox shows that the perception of an individual's autonomy on the road is an illusion.

Propositions belonging to the thesis, entitled

Under pressure
exploring the mechanobiology of *Phytophthora* invasion

Jochem Bronkhorst

Wageningen, 20 September 2022

Under pressure

exploring the mechanobiology of *Phytophthora* invasion

Jochem Bronkhorst

Thesis committee

Promotors

Prof. Dr J. Sprakel
Professor of Biochemistry
Wageningen University & Research

Prof. Dr F. Govers
Personal chair, Laboratory of Phytopathology
Wageningen University & Research

Other members

Prof. Dr J.L.van Leeuwen, Wageningen University & Research
Prof. Dr G. Koenderink, Delft University of Technology
Prof. Dr G. van den Ackerveken, Utrecht University
Dr E. Evangelisti, Wageningen University & Research

This research was conducted under the auspices of Graduate School VLAG
(Advanced studies in Food Technology, Agrobiotechnology, Nutrition and Health Sciences).

Under pressure

exploring the mechanobiology of *Phytophthora* invasion

Jochem Bronkhorst

Thesis
Submitted in fulfillment of the requirements for the degree of doctor
at Wageningen University
by the authority of the Rector Magnificus,
Prof. Dr A.P. J. Mol,
in the presence of the
Thesis Committee appointed by the Academic Board,
to be defended in public
on Tuesday 20 September 2022
at 4 p.m. in the Omnia Auditorium.

Jochem Bronkhorst
Under pressure: exploring the mechanobiology of *Phytophthora* invasion
211 pages

PhD thesis, Wageningen University, Wageningen, The Netherlands (2022)
With references, with summary in English

ISBN: 978-94-6447-258-5
DOI: https://doi.org/10.18174/570971

Contents

Introduction

1.1 Filamentous plant pathogens

Filamentous plant pathogens are microbial pests with other living organisms as their host(s), macroscopically looking like "fluffy" mycelium which is microscopically build of many small hair-like filaments called hyphae. Although morphologically similar, we find filamentous plant pathogens in two different major branches in the tree of life, within the fungal and oomycete lineages. Filamentous plant pathogens are a major microbial threat to global food security[1], able to destroy a significant percentage of crops if left unchecked[2] and causing billions of dollars in damage yearly[3]. Food security becomes an increasingly large challenge with a growing world population[4], climate change[4] and recent global logistics challenges. Global logistics have spread filamentous plant pathogens around the world[5], e.g. the arrival of the oomycete species *Phytophthora infestans* in Europe has seen a reduction in potato crop yields[6]. Potatoes are an important crop, resulting in national instability and a time of turmoil[7] after the introduction of *Phytophthora*, showcasing pathogens large societal impact. A key feature of filamentous plant pathogens is their ability to rapidly adapt to new environments[8], making them still highly relevant today[9].

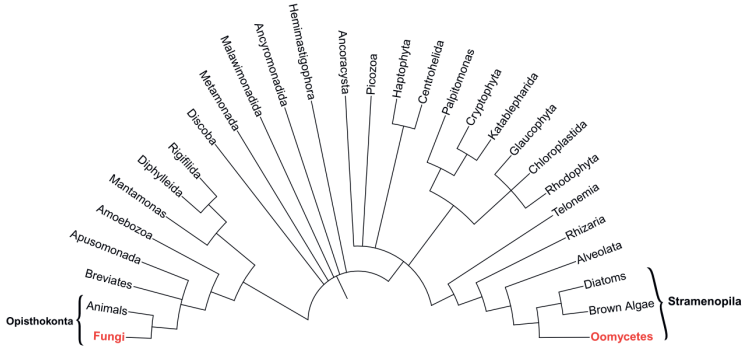

Figure 1.1. Phylogenetic tree of life, reproduced from McGowan et al.[10]. Both fungi and oomycetes have been labelled in red, with their supergroups labelled in bold.

Fungi and oomycetes are two main groups of filamentous plant pathogens. The phylogenetic lineages of fungi (Ophistokonta) and oomycetes (Straminopilia) have diverged 1.2-1.7 billion years ago in the phylogenetic tree of life[11] (Fig 1.1), and it is believed that both classes of filamentous plant pathogens show hallmarks of convergent evolution[12]. We will in the next sections focus on the fungus *Magnaporthe oryzae* and oomycete *P. infestans*, to shed light on their similarities and differences for future reference. Examining just two species is not a full

reflection of the vast diversity of fungal and oomycete plant pathogens[13], but the two mentioned species are well-studied[14,15].

1.2 Fungi and oomycetes; similarities and differences

Magnaporthe oryzae is the causal agent of rice blast disease[16]. *Phytophthtora infestans*, being an literal plant (phyto) destroyer (phthora) is the causal agent of potato and tomato late blight[17]. We will first explore the similarities between both species, showing why detailed study is needed to distinguish them. The ability to distinguish plant pathogens using genetics is vital[18], i.e. some crop protection agents highly effective for fungi don't work at all on oomycetes, requiring a tailored approach.

Magnaporthe oryzae and *Phytophthtora infestans* share many lifestyle, life cycle and morphological features. Both species infect living plant hosts (biotrophy), switching to the killing of its host in later life stages (necrotrophy)[13]. After infection, both *M. oryzae* and *P. infestans* use specialized feeding structures to enable absorption of nutrients from host plants. *M. oryzae* and *P. infestans* apply mechanical pressure on their hosts to enable invasion, mediated via an hypha that grows into the host. During entry into the host, cell-wall degrading enzymes help as well by weakening the host cell walls, making host entry easier[13,19]. *M. oryzae* uses a specialized infection organ called the appressorium, a swollen melaninized spherical septated cell that builds up turgor pressure to launch a penetration peg into its host. Here *P. infestans* acts differently; although some non-spherical hyphal swelling is observed at the point of invasion into the host, no strong septation and melanization are observed[20].

Although similar in lifestyle and morphology, *M. oryzae*, as a prototypical true fungus, and *P. infestans*, as a prototype for oomycete plant pathogens, use very different weaponry to invade their hosts, placing distinct limits on the notion that convergent evolution of oomycetes and fungi provided them with similar machinery to establish infection. Whereas the mycelium of *M. oryzae* is built up of individual cells (septated) with nuclei, *P. infestans* is a coenocyte (being aseptate and having multinucleic hyphae). *P. infestans* cell walls contain mostly cellulose and β-1,3 and β-1,6 linked glucans, but (mostly) lacks chitin, the main cell wall component of *M. oryzae*. *M. oryzae* forms an melanized appressorium with turgor pressures up to 8 MPa, while turgor pressures in *P. infestans* hyphae and other oomycetes are approximately a factor 10 lower[12] and appresorium-like swelling generally unpigmented, unseptated and non-spherical[20]. The F-actin cytoskeletal organisation during invasion is organised as an aster[21] or peripheral[22] in *P. infestans* and *M. oryzae* respectively.

The formation of a spherical, septated and highly pressurised appressorium by *M. oryzae* provides a distinct invasive lifestage that can be studied in high detail. Appressorium formation in *M. oryzae* is a clearly defined process; first a switch from polarised to unpolarised growth generates a sphere on the tip end of a hyphae, followed by melanization and turgor pressure buildup[23]. A reoganisation of the actin cytoskeleton via a septin ring is necessary to enable penetration peg formation, a reversal back to polarised hyphal growth directly into the plant[24]. As opposed to *M. oryzae*[15], *P. infestans*'s[14] mechanism and genetic regulation of host invasion is much less studied. *P. infestans* does not have a well defined appressorium-based life stage, whilst only small, non-uniform and unpigmented widening of the germ tube is observed[20,25]. The difference in appressorium-like hyphal swelling of *M. oryzae* and *P. infestans* was the starting point of this thesis, in which we aim to unravel invasion mechanisms of filamentous plant pathogens with the main focus on *Phytophthora* spp.

1.3 Oomycetes

The oomycetes class, colloquially known as water moulds, are devided over four orders; the *Peronosporales*, *Pythiales*, *Albuginales*, and *Saprolegniales*[10]. They have different habitats ranging from marine/freshwater to land with hosts stretching from plants, animals, crustaceans, amphibeans and fish[26,27] (Table 1.1). *Saprolegnia* spp. and *Aphanamyces* spp. in the order *Saprologeniales* (Table 1.1) have an aquatic lifestyle, both in marine and freshwater environment[26]. *Pythium* spp. in the order *Pythiales* have a wide range of hosts from humans and animals to fungi, but are mainly necrotrophic plant pathogens[26]. An interesting case is *Pythium oligandrum*, classed as a biological control agent of fungi and oomycetes itself, commonly found to invade other *Pythium* species but does not hurt its host plants, protecting them from pathogens[28]. *Albugo* species in the order *Albuginales* are obligate biotrophic plant pathogens causing white blister rust, perhaps best known of whom is *Albugo candida*, pathogenic on cruciferous (i.e. cabbage) plants. Of the *Saprolegniales*, two species are known as important plant pathogens, both causing root rot: *Aphanomyces euteiches*, specialized on pea and other members of the *Fabaceae* family and *Aphanomyces cochlioides* that parasitizes roots of sugar beet and spinach. We will focus on the *Phytophthora* genus, in the order of *Peronosporales*, containing over 150 species[29].

Table 1.1. Examples of different oomycete species, with their hosts and habitats. Species with an asterisk (*) have a very broad and diverse host range affecting up to 100 plant species or even more.

Species	Host	Habitat
Saprolegnia parasitica[30]	Salmonids	Marine
Aphanomyces astaci[31]	Freshwater crayfish	Freshwater
Albugo candida[32]	Brassicaceae	Foliage
Bremia lactucae[33]	Lettuce	Foliage
Plasmopara viticola[14]	Grape	Foliage
Pythium insidiosum[34]	Humans/animals	Freshwater
Pythium oligandrum[28]	fungi/oomycetes	Soil
Pythium ultimum[10]	Corn*	Soil
Phytophthora sojae[35]	Soybean	Soil
Phytophthora capsici[36]	Bell pepper*	Soil, foliage
Phytophthora palmivora[37]	Cacao*	Soil, foliage
Phytophthora infestans[5]	Potato/tomato	Soil, foliage

Phytophthora infestans is notorious for the ability to rapidly adapt to resistance genes and crop protective compounds[8] making it a highly relevant pathogen 150 year after discovery whilst still causing billions of dollars of crop losses annually[38]. Considering the life-cycle of *Phytophthora* spp, most include a soil-borne phase, either dominant and used to infect their hosts through roots (e.g. *P. sojae*) or a seasonal long-term survival strategy (e.g. *P. infestans*). Species like *P. infestans* are widely known for their notorious spreading between foliage during the growing season[14], a process driven by the very quick cycle of host invasion, colonization and sporangium formation (Fig 1.2A).

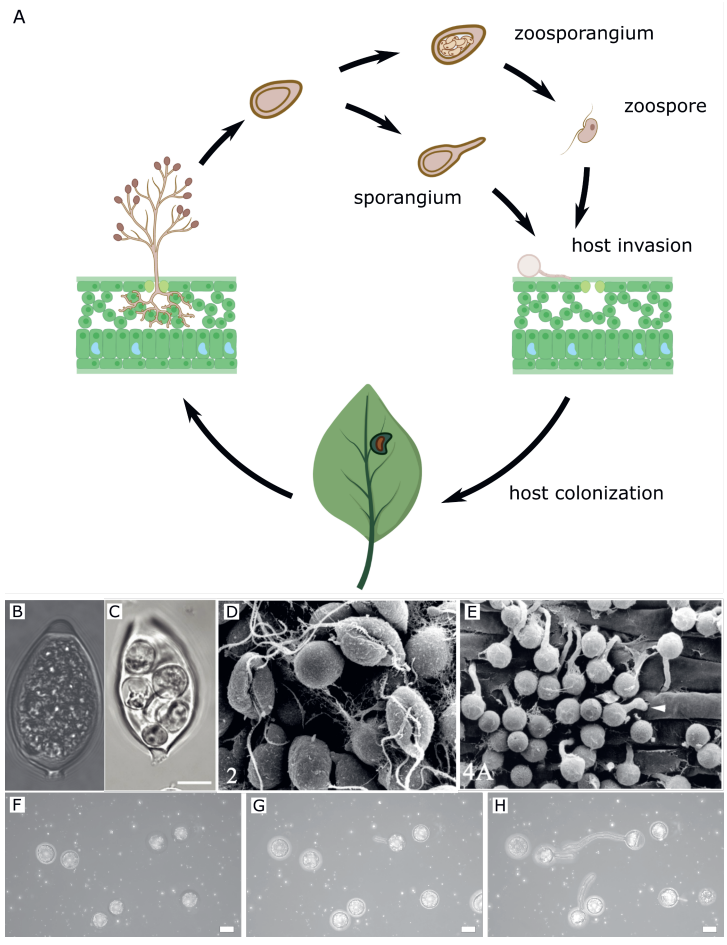

Figure 1.2. (A)Illustration of *Phytophthora infestans* summer spreading cycle. Created with BioRender.com. (B) Microscopic image of an undifferentiated sporangium (data provided by Kiki Kots, WUR.) (C) Microscopic image of *P. infestans* zoosporangium (reproduced from Boevink et al[20], light microscopy, 10 micron scale bar), (D) *Phytophthora cinnamomi* zoospores on a root (reproduced from Hardham[39], electron micrograph, 2000x) and (E) *Phytophthora cinnamomi* germinated cysts on a onion root (reproduced from Hardham[39], electron micrograph, 750x). (F-H) Confocal microscopic timeseries of brightfield images of *P. infestans-88069 (wt)* cysts germinating and growing on a PDMS substrate over approximately an hour, maximum projection. Scale bar is 10 μm.

After host colonization, *P. infestans* forms sporangia on the abaxial side of leaves. Such sporangia (Fig 1.2B) are lemon shaped sacks that are released from sporangiophores by wind and rain enabling spread over long distances to other plants. Sporangia have another important trick; in wet and cold conditions they quickly differentiate into zoosporangia from which zoospores are released (Fig 1.2C). Zoospore release is a common feature in *Phytophthora* species (Fig 1.2A-E), swimming quickly in aqueous environments and water-logged soils[40].

Upon reaching the host, topological and hydrophobicity cues[41] induce encystment, softly adhering cysts to the to be invaded host[42](Fig 1.2DE). A cell wall is formed during zoospore encystment[43], allowing the cell to build up turgor pressure[44], which in turn is required to subsequently grow a hypha and invade the host (Fig 1.2E). After encystment, the now spherical cell breaks symmetry and begins to grow a hypha, a tubular protuberance from the cell whose elongation is driven by tip growth[20] (Fig 1.2F-G). Ultimately, this hypha will begin to penetrate the host to gain entry; which signals are perceived to trigger this switch from non-invasive to invasive hyphal growth are currently unknown. The regulation of the pathogen invasion process, coupled with the complexities of plant defense measures and the lack of nutrients available to the organism during invasion, makes host invasion a key step in the pathogen's lifecycle[45]. Despite its importance in the life cycle of these pathogens, much remains unclear about the mechanisms of host entry by *Phytophthora* spp., which forms the main focus of this thesis.

1.4 Host entry

The mechanics of *Phytophthora* spp. host entry is poorly studied[20]. It is known that many genes in the pathogen are upregulated during host entry[17], that turgor pressure is a key driving force for invasion[46] and that mechanical weakening of the host cell wall plays a role in the invasion process[47]. However, what the mechanical mechanism is by which *Phytophthora* spp. pierce their host's surface, and how these invasive mechanics are regulated inside the cell, remains largely unclear. To unravel this complex physical process we distinguish a two-track invasion strategy, one being mechanical and the other biochemical.

1.4.1 Mechanical interactions

Host entry is mediated by penetration of the germ tube into the plant, requiring the buildup of considerable forces to deform and penetrate the cuticle, a waxy layer that coats leaves, and the epidermis, the outer cell layer, as a gateway to gain access to the plant tissue.

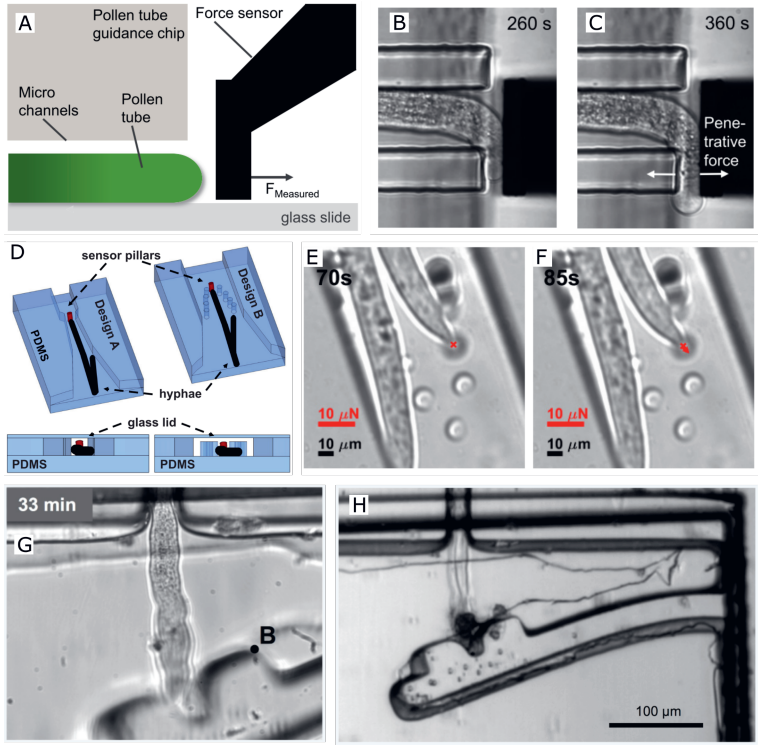

Figure 1.3. (A) Illustration of experimental setup; force-sensing plate and pollen tube growth channel, (B, C) Lilly pollen tube growth against and past force-sensing plate (reproduced from Burri et al.[48]). (D) Illustration of experimental setup; elastomeric micropillar platform, (E, F) Hyphae of the oomycete *Achlya bisexualis* encountering elastomer pillars (reproduced from Tayagui et al.[49]), (G) Cantilever displacement by pollen tube, (H) leading to bursting tip at large displacements (reproduced from Ghanbari et al.[50])

The main generator of penetration force is turgor pressure, which "inflates" the intracellular space held together by the cell wall[51]. During both non-invasive and invasion growth, the cell wall weakens and yields at the hyphal tip[52,53], resulting in growth or the generation of invasive forces during host penetration. Since invasive force generation is a critical first step in the disease cycle, several efforts have been made to quantify these forces. One approach uses a calibrated strain gauge, a solid object whose deformation can be measured and by calibration converted to the applied invasive force. A well-known example using a strain gauge is the work of Burri et al. who measured the μN forces of growing pollen tubes[48] (Fig 1.3A-C). Main drawbacks of using strain gauges are the materials required and the difference in mechanical geometry of the force-applying hyphae. The mechanical geometry probes the forces during non-invasive growth, rather than ensuring

that the cell has undergone a switch to invasive growth into a flat and compliant substrate. Strain gauges are generally build from metal, orders of magnitude stiffer than plant leaves[54], making invasive growth into this material impossible. Tip growing cells eventually tend to bend away when applying their forces to this stiff material (Fig 1.3BC), and adhesion plays (virtually) no role[48].

Another approach to measure the forces generated by tip growing hypha uses materials with a stiffness similar to that of plants[54]. These approaches use a constriction in a microchannel where the hypha encounters an obstacle, e.g. the micropillar array used by Tayagui et al[49] (Fig 1.3D-F), or the cantilever chips of Ghanbari et al[50] (Fig 1.3F-G). Forces applied by the growing hypha on these obstacles can be measured by imaging the obstacle displacement after suitable calibration. Although informative and interesting, the ability to bypass the pillar at a set indentive force[49] or tips stopping growth/bursting[50], is a distinctly different mechnical geometry compared to a hyphal tip invading a stiff plant surface where adhesion plays a major role.

Although many very interesting approaches have been pursued[48–50,53,55], new tools are needed to understand invasion mechanics. Tools that mimic both the natural geometry, surface chemistry and mechanics, such that invasion can be studied in its full complexity, including surface adhesion which is known to be critical for pathogen host entry[39]. Although it is understood that germ tubes have lower turgor pressures than melanized appressoria, they are still able to apply considerable forces in the μN range[56]. Germ tubes have however another ace up their sleeve; their ability to enzymatically weaken their host by biochemical interactions.

1.4.2 Biochemical interactions

Biochemical interactions between host and pathogen, even before invasion, play a major role in the invasion process[57,58]. We will focus here on three processes that rely on biochemical interactions between pathogen and host; host sensing by the pathogen, cell wall degradation and effector secretion.

Phytophthora zoospores swim at 100+ μm/s[59] using flagella to propel themselves to new hosts, while being guided by chemotactic[43] or electrotactic[60] cues. Host recognition leads to encystment; flagella are released and spores encyst[42,61] on their plant hosts. Host sensing plays a role in the invasion switch of germ tubes, relying on hydrophobic/topological cues[41]. *P. infestans* does not enter its host via stomata, the natural openings in leaves, although this entry route seems to be the simplest[62] when released on foliage. Another point of study is the host specialization of different *Phytophthora* spp.[10], where it is not yet fully understood if lack of physical host recognition completely impairs invasion, or if this process is solely determined by genetic (i.e. effector) incompatibility.

After encystment, a germ tube emerges which secretes enzymes. Enzymes like cutinases help in breaking down the highly crosslinked cutin network (leaves) and parts of the suberin network (roots)[63], the first mechanical barrier encountered by the germ tube when entering the plant. One can imagine that degradation of the cuticle would aid in host penetration by lowering the stiffness of the plant exterior locally; however, whether this contributes to host entry remains unproven. *Phytophthora* also secretes cell-wall degrading enzymes that target the cell wall, which forms the second layer of mechanical defence on the plant exterior. Examples include a suite of pectinases weakening the pectin contained in primary plant cell walls[64]. Pectin plays a vital role in cell wall biomechanics; 30 % of primary cell walls consists of pectin[65] networks, with mechanically adaptable properties via e.g. methylation/demethylation. The pectin network must be breached by *Phytophthora* to enter cells through the cell wall, and pectin degrading enzymes are widespread in *Phytophthora* species[63,64]. Other cell wall components like hemicellulose, cellulose and glycosides[63], which also play a major mechanical role[54] are targeted by *Phytophthora*, the degradation of which is vital for pathogenicity[66].

Phytophthora secretes many effectors[57] to hijack the plant's immune system and supress defenses, which could serve a structural purpose as well. Effectors are generally transported from pathogen to host, aiding in host invasion. Many *Phytophthora* effectors have a conserved RxLR motif that functions as a translocation signal, making an exocytotic sequence a tell-tale genetic sign of a possible mechanical effector that is transported to the host. An example mechanical disruptor is the RxLR effector IPI-O, secreted by *P. infestans*[67], disrupting the cell wall-plasma

membrane continuum via its RGD tripeptide motif, thereby pre-invasively decreasing host cell wall integrity[19]. *Phytophthora* spp. contain numerous effectors with many still having an unknown function[19], making effectors and their targets an important field of study.

1.5 Scope of this thesis

Host entry by *Phytopthora* spp. is a complex interplay of mechanics to generate indentive forces and biochemistry to weaken/disrupt hosts and enable entry of the pathogen into host plants. Although the cell biology of host invasion, coupled to dynamic processes like gene expression and actin organisation, are relatively well studied, many questions remain on host entry of *Phytophthora* spp. We know that *Phytophthora* spp. have lower turgor pressures than their fungal counterparts[56] and are unable to generate melanised and septated appressoria[68]. These observations have led to the formulation of our main research question: how do *Phytophthora* pathogens generate, perceive and respond to mechanical stresses to accomplish host entry?

In this thesis we tackle this question by considering different aspects in the coming chapters. In Chapter 2, we first develop new mechanobiological tools to aid us in answering these questions. Chapter 3 focuses on the mechanism of mechanical force generation and host penetration by *Phytophthora* pathogens. We shift to understanding pathogenic mechanoperception in Chapter 4 to study how the cytoskeleton acts as a rapid mechanosensor that controls hyphal tip shape during invasion. Finally, in chapter 5 we explore a new approach to visualise mechanical patterns as a first step to understand how mechanical signals are transduced from the pathogen-host contact interface to the cell interior.

References

[1] George Agrios. *Plant Pathology*, volume 6. Elsevier, 2005.

[2] Ramani Wijesinha-Bettoni and Béatrice Mouillé. The Contribution of Potatoes to Global Food Security, Nutrition and Healthy Diets. *American Journal of Potato Research*, 96(2):139–149, 2019.

[3] Stephan Wawra, Rodrigo Belmonte, Lars Löbach, Marcia Saraiva, Ariane Willems, and Pieter van West. Secretion, delivery and function of oomycete effector proteins. *Current Opinion in Microbiology*, 15(6):685–691, 2012.

[4] John R. Porter, Liyong Xie, Andrew J. Challinor, Kevern Cochrane, S. Mark Howden, Muhammad Mohsin Iqbal, David B. Lobell, Maria Isabel Travasso, Pramod Aggarwal, Kaija Hakala, and Joanne Jordan. Food Security and Food Production Systems. In Christopher B. Field, Vicente R. Barros, David Jon Dokken, Katharine J. Mach, and Michael D. Mastrandrea, editors, *Climate Change 2014 Impacts, Adaptation, and Vulnerability*, pages 485–534. Cambridge University Press, Cambridge, 2015.

[5] William E. Fry. *Phytophthora infestans*: the itinerant invader; "late blight": the persistent disease. *Phytoparasitica*, 48(1):87–94, feb 2020.

[6] Jean Beagle Ristaino. Tracking historic migrations of the Irish potato famine pathogen, *Phytophthora infestans*, *Microbes and Infection*, 13(4):1369–1377 2002.

[7] Brian J. Haas, Sophien Kamoun, Michael C. Zody, Rays H.Y. Jiang, Robert E. Handsaker, Liliana M. Cano, Manfred Grabherr, Chinnappa D. Kodira, Sylvain Raffaele, Trudy Torto-Alalibo, Tolga O. Bozkurt, Audrey M.V. Ah-Fong, Lucia Alvarado, Vicky L. Anderson, Miles R. Armstrong, Anna Avrova, Laura Baxter, Jim Beynon, Petra C. Boevink, Stephanie R. Bollmann, Jorunn I.B. Bos, Vincent Bulone, Guohong Cai, Cahid Cakir, James C. Carrington, Megan Chawner, Lucio Conti, Stefano Costanzo, Richard Ewan, Noah Fahlgren, Michael A. Fischbach, Johanna Fugelstad, Eleanor M. Gilroy, Sante Gnerre, Pamela J. Green, Laura J. Grenville-Briggs, John Griffith, Niklaus J. Grünwald, Karolyn Horn, Neil R. Horner, Chia Hui Hu, Edgar Huitema, Dong Hoon Jeong, Alexandra M.E. Jones, Jonathan D.G. Jones, Richard W. Jones, Elinor K. Karlsson, Sridhara G. Kunjeti, Kurt Lamour, Zhenyu Liu, Lijun Ma, Daniel MacLean, Marcus C. Chibucos, Hayes McDonald, Jessica McWalters, Harold J.G. Meijer, William Morgan, Paul F. Morris, Carol A. Munro, Keith O'Neill, Manuel Ospina-Giraldo, Andrés Pinzón, Leighton Pritchard, Bernard Ramsahoye, Qinghu Ren, Silvia Restrepo, Sourav Roy, Ari Sadanandom, Alon Savidor, Sebastian Schornack, David C. Schwartz, Ulrike D. Schumann, Ben Schwessinger, Lauren Seyer, Ted Sharpe, Cristina Silvar, Jing Song, David J. Studholme, Sean Sykes, Marco Thines, Peter J.I. Van De Vondervoort, Vipaporn Phuntumart, Stephan Wawra, Rob Weide, Joe Win, Carolyn Young, Shiguo Zhou, William Fry, Blake C. Meyers, Pieter Van West, Jean Ristaino, Francine Govers, Paul R.J. Birch, Stephen C. Whisson, Howard S. Judelson, and Chad Nusbaum. Genome sequence and analysis of the Irish potato famine pathogen *Phytophthora infestans*. *Nature*, 461(7262):393–398, sep 2009.

[8] Wiphawee Leesutthiphonchai, Andrea L. Vu, Audrey M.V. Ah-Fong, and Howard S. Judelson. How does *Phytophthora infestans* evade control efforts? Modern insight into the late blight disease. *Phytopathology*, 108(8):916–924, aug 2018.

[9] William Fry. *Phytophthora infestans*: The plant (and R gene) destroyer. *Molecular Plant Pathology*, 9(3):385–402, may 2008.

[10] Jamie McGowan and David A. Fitzpatrick. Recent advances in oomycete genomics. *Advances in Genetics*, 105:175–228, jan 2020.

[11] Susannah M. Porter. The fossil record of early eukaryotic diversification. *The Paleontological Society Papers*, 10:35–50, nov 2004.

[12] Nicholas P. Money, Christopher M. Davis, and J. P. Ravishankar. Biomechanical evidence for convergent evolution of the invasive growth process among fungi and oomycete water molds. *Fungal Genetics and Biology*, 41(9):872–876, 2004.

[13] Mihwa Yi and Barbara Valent. Communication between filamentous pathogens and plants at the biotrophic interface. *Annual Review of Phytopathology*, 51:587–611, aug 2013.

[14] Sophien Kamoun, Oliver Furzer, Jonathan D. G. Jones, Howard S. Judelson, Gul Shad Ali, Ronaldo J. D. Dalio, Sanjoy Guha Roy, Leonardo Schena, Antonios Zambounis, Franck Panabières, David Cahill, Michelina Ruocco, Andreia Figueiredo, Xiao-Ren Chen, Jon Hulvey, Remco Stam, Kurt Lamour, Mark Gijzen, Brett M. Tyler, Niklaus J. Grünwald, M. Shahid Mukhtar, Daniel F. A. Tomé, Mahmut Tör, Guido Van Den Ackerveken, John McDowell, Fouad Daayf, William E. Fry, Hannele Lindqvist-Kreuze, Harold J. G. Meijer, Benjamin Petre, Jean Ristaino, Kentaro Yoshida, Paul R. J. Birch, and Francine Govers. The Top 10 oomycete pathogens in molecular plant pathology. *Molecular Plant Pathology*, 16(4):413–434, may 2015.

[15] Ralph Dean, Jan A.L. Van Kan, Zacharias A. Pretorius, Kim E. Hammond-Kosack, Antonio Di Pietro, Pietro D. Spanu, Jason J. Rudd, Marty Dickman, Regine Kahmann, Jeff Ellis, and Gary D. Foster. The Top 10 fungal pathogens in molecular plant pathology. *Molecular Plant Pathology*, 13(4):414–430, may 2012.

[16] Andrew J Foster, Lauren S Ryder, Michael J Kershaw, and Nicholas J Talbot. The role of glycerol in the pathogenic lifestyle of the rice blast fungus *Magnaporthe oryzae*. *Environmental Microbiology*, 19(3):1008–1016, mar 2017.

[17] Howard S. Judelson, Audrey M. V. Ah-Fong, George Aux, Anna O. Avrova, Catherine Bruce, Cahid Cakir, Luis da Cunha, Laura Grenville-Briggs, Maita Latijnhouwers, Wilco Ligterink, Harold J. G. Meijer, Samuel Roberts, Carrie S. Thurber, Stephen C. Whisson, Paul R. J. Birch, Francine Govers, Sophien Kamoun, Pieter van West, and John Windass. Gene Expression Profiling During Asexual Development of the Late Blight Pathogen *Phytophthora infestans* Reveals a Highly Dynamic Transcriptome. *Molecular Plant-Microbe Interactions*, 21(4):433–447, apr 2008.

[18] E. C. Oerke. Crop losses to pests, *Journal of Agricultural Science*, 144(1):31–43 feb 2006.

[19] Jane Chepsergon, Thabiso E Motaung, Daniel Bellieny-Rabelo, and Lucy Novungayo Moleleki. Organize, Don't Agonize: Strategic Success of *Phytophthora* Species. *Microorganisms*, 8(6):917, jun 2020.

[20] Petra C. Boevink, Paul R. J. Birch, Dionne Turnbull, and Stephen C. Whisson. Devastating intimacy: the cell biology of plant– *Phytophthora* interactions. *New Phytologist*, 228(2):445–458, oct 2020.

[21] Kiki Kots, Harold J.G. Meijer, Klaas Bouwmeester, Francine Govers, and Tijs Ketelaar. Filamentous actin accumulates during plant cell penetration and cell wall plug formation in *Phytophthora infestans*. *Cellular and Molecular Life Sciences*, 74(5):909–920, 2017.

[22] Yuan Bao Li, Rui Xu, Chengyu Liu, Ningning Shen, Li Bo Han, and Dingzhong Tang. *Magnaporthe oryzae* fimbrin organizes actin networks in the hyphal tip during polar growth and pathogenesis. *PLoS Pathogens*, 16(3), 2020.

[23] Nicholas J Talbot. Appressoria, *Current Biology*, 29(5):144-146 mar 2019.

[24] Yasin F. Dagdas, Kae Yoshino, Gulay Dagdas, Lauren S. Ryder, Ewa Bielska, Gero Steinberg, and Nicholas J. Talbot. Septin-mediated plant cell invasion by the rice blast fungus, *Magnaporthe oryzae*. *Science*, 336(6088):1590–1595, jun 2012.

[25] K. W. Thilini Chethana, Ruvishika S. Jayawardena, Yi-Jyun Chen, Sirinapa Konta, Saowaluck Tibpromma, Pranami D. Abeywickrama, Deecksha Gomdola, Abhaya Balasuriya, Jianping Xu, Saisamorn Lumyong, and Kevin D. Hyde. Diversity and Function of Appressoria. *Pathogens*, 10(6):746, jun 2021.

[26] Rays H.Y. Jiang and Brett M. Tyler. Mechanisms and evolution of virulence in oomycetes. *Annual Review of Phytopathology*, 50:295–318, 2012.

[27] Marco Thines. Oomycetes. *Current Biology*, 28(15):R812–R813, aug 2018.

[28] J. Gerbore, N. Benhamou, J. Vallance, G. Le Floch, D. Grizard, C. Regnault-Roger, and P. Rey. Biological control of plant pathogens: Advantages and limitations seen through the case study of *Pythium oligandrum*. *Environmental Science and Pollution Research*, 21(7):4847–4860, 2014.

[29] Laurens P.N.M. Kroon, Henk Brouwer, Arthur W.A.M. De Cock, and Francine Govers. The genus *Phytophthora* anno 2012. *Phytopathology*, 102(4):348–364, 2012.

[30] Albert Hendrik van den Berg, Debbie McLaggan, Javier Diéguez-Uribeondo, and Pieter van West. The impact of the water moulds *Saprolegnia diclina* and *Saprolegnia parasitica* on natural ecosystems and the aquaculture industry. *Fungal Biology Reviews*, 27(2):33–42, aug 2013.

[31] Laura Martín-Torrijos, María Martínez-Ríos, Gloria Casabella-Herrero, Susan B Adams, Colin R Jackson, and Javier Diéguez-Uribeondo. Tracing the origin of the crayfish plague pathogen, *Aphanomyces astaci*, to the Southeastern United States. *Scientific Reports*, 11(1):9332, dec 2021.

[32] Volkan Cevik, Freddy Boutrot, Wiebke Apel, Alexandre Robert-Seilaniantz, Oliver J. Furzer, Amey Redkar, Baptiste Castel, Paula X. Kover, David C. Prince, Eric B. Holub, and Jonathan D. G. Jones. Transgressive segregation reveals mechanisms of *Arabidopsis* immunity to *Brassica* -infecting races of white rust (*Albugo candida*). *Proceedings of the National Academy of Sciences*, 116(7):2767–2773, feb 2019.

[33] Joost H.M. Stassen, Michael F. Seidl, Pim W.J. Vergeer, Isaäc J. Nijman, Berend Snel, Edwin Cuppen, and Guido Van Den Ackerveken. Effector identification in the lettuce downy mildew *Bremia lactucae* by massively parallel transcriptome sequencing. *Molecular Plant Pathology*, 13(7):719–731, sep 2012.

[34] Wim Gaastra, Len J.A. Lipman, Arthur W.A.M. De Cock, Tim K Exel, Raymond B.G. Pegge, Josje Scheurwater, Raquel Vilela, and Leonel Mendoza. *Pythium insidiosum*: An overview. *Veterinary Microbiology*, 146(1-2):1–16, nov 2010.

[35] Anne E. Dorrance. Management of *Phytophthora sojae* of soybean: a review and future perspectives. *Canadian Journal of Plant Pathology*, 40(2):210–219, apr 2018.

[36] Godwin R.A. Mchau and Michael D. Coffey. Evidence for the existence of two subpopulations in *Phytophthora capsici* and a redescription of the species. *Mycological Research*, 99(1):89–102, 1995.

[37] G. A. Torres, G. A. Sarria, G. Martinez, F. Varon, A. Drenth, and D. I. Guest. Bud Rot Caused by *Phytophthora palmivora* : A Destructive Emerging Disease of Oil Palm. *Phytopathology*, 106(4):320–329, apr 2016.

[38] A. J. Haverkort, P. M. Boonekamp, R. Hutten, E. Jacobsen, L. A.P. Lotz, G. J.T. Kessel, R. G.F. Visser, and E. A.G. Van Der Vossen. Societal costs of late blight in potato and prospects of durable resistance through cisgenic modification, *Potato Research*, 51(1):47–57 mar 2008.

[39] Adrienne R. Hardham. The cell biology behind *Phytophthora* pathogenicity. *Australasian Plant Pathology*, 30(2):91–98, 2001.

[40] Howard S. Judelson and Flavio A. Blanco. The spores of *Phytophthora*: weapons of the plant destroyer. *Nature Reviews Microbiology*, 3(1):47–58, jan 2005.

[41] Urs Bircher and Hans R. Hohl. Environmental signalling during induction of appressorium formation in *Phytophthora*. *Mycological Research*, 101(4):395–402, 1997.

[42] Andrea V. Robold and Adrienne R. Hardham. During attachment *Phytophthora* spores secrete proteins containing thrombospondin type 1 repeats. *Current Genetics*, 47(5):307–315, may 2005.

[43] Andrew I.M. Savory, Laura J. Grenville-Briggs, Stephan Wawra, Pieter Van West, and Fordyce A. Davidson. Auto-aggregation in zoospores of *Phytophthora infestans*: The cooperative roles of bioconvection and chemotaxis. *Journal of the Royal Society Interface*, 11(94):20140017, may 2014.

[44] Adrienne R. Hardham. Cell biology of plant-oomycete interactions. *Cellular Microbiology*, 9(1):31–39, 2007.

[45] Adrienne R. Hardham. Cell biology of plant-oomycete interactions. *Cellular Microbiology*, 9(1):31–39, jan 2007.

[46] Laura J Grenville-Briggs, Victoria L Anderson, Johanna Fugelstad, Anna O Avrova, Jamel Bouzenzana, Alison Williams, Stephan Wawra, Stephen C Whisson, Paul R.J. Birch, Vincent Bulone, and Pieter Van West. Cellulose synthesis in *Phytophthora infestans* is required for normal appressorium formation and successful infection of potato. *Plant Cell*, 20(3):720–738, 2008.

[47] Manuel D Ospina-Giraldo, Jessica Mcwalters, and Lauren Seyer. Structural and functional proWle of the carbohydrate esterase gene complement in *Phytophthora infestans*. *Curr Genet*, 56:495–506, 2010.

[48] Jan T. Burri, Hannes Vogler, Nino F. Läubli, Chengzhi Hu, Ueli Grossniklaus, and Bradley J. Nelson. Feeling the force: how pollen tubes deal with obstacles. *New Phytologist*, 220(1):187–195, oct 2018.

[49] Ayelen Tayagui, Yiling Sun, David A. Collings, Ashley Garrill, and Volker Nock. An elastomeric micropillar platform for the study of protrusive forces in hyphal invasion. *Lab on a Chip*, 17(21):3643–3653, 2017.

[50] Mahmood Ghanbari, Muthukumaran Packirisamy, and Anja Geitmann. Measuring the growth force of invasive plant cells using Flexure integrated Lab-on-a-Chip (FiLoC). *TECHNOLOGY*, 06(03n04):101–109, sep 2018.

[51] Nicholas P. Money. Insights on the mechanics of hyphal growth. *Fungal Biology Reviews*, 22(2):71–76, 2008.

[52] Roger R. Lew. How does a hypha grow? The biophysics of pressurized growth in fungi. *Nature Reviews Microbiology*, 9(7):509–518, jul 2011.

[53] Amir Sanati Nezhad and Anja Geitmann. The cellular mechanics of an invasive lifestyle. *Journal of Experimental Botany*, 64(15):4709–4728, 2013.

[54] Lorna J. Gibson. The hierarchical structure and mechanics of plant materials. *Journal of The Royal Society Interface*, 9(76):2749–2766, nov 2012.

[55] Clemens Bechinger, Karl Friedrich Giebel, Martin Schnell, Paul Leiderer, Holger B Deising, and Martin Bastmeyer. Optical measurements of invasive forces exerted by appressoria of a plant pathogenic fungus. *Science*, 285(5435):1896–1899, 1999.

[56] Nicholas P. Money, Christopher M. Davis, and J. P. Ravishankar. Biomechanical evidence for convergent evolution of the invasive growth process among fungi and oomycete water molds. *Fungal Genetics and Biology*, 41(9):872–876, sep 2004.

[57] Howard S Judelson and Audrey M V Ah-Fong. Exchanges at the Plant-Oomycete Interface That Influence Disease. *Plant Physiology*, 179(4):1198–1211, apr 2019.

[58] Klaas Bouwmeester, Mara de Sain, Rob Weide, Anne Gouget, Sofieke Klamer, Herve Canut, and Francine Govers. The lectin receptor kinase LecRK-I.9 is a novel *Phytophthora* resistance component and a potential host target for a RXLR effector. *PLoS Pathogens*, 7(3):e1001327, mar 2011.

[59] Ilaria Bassani, Marie Larousse, Quang D. Tran, Agnès Attard, and Eric Galiana. *Phytophthora* zoospores: From perception of environmental signals to inoculum formation on the host-root surface. *Computational and Structural Biotechnology Journal*, 18:3766–3773, jan 2020.

[60] B. M. Morris, B. Reid, and N. A. R. Gow. Electrotaxis of zoospores of *Phytophthora palmivora* at physiologically relevant field strengths. *Plant, Cell and Environment*, 15(6):645–653, aug 1992.

[61] Frank Gubler and Aadrienne R. Hardham. Secretion of adhesive material during encystment of *Phytophthora cinnamomi* zoospores, characterized by immunogold labelling with monoclonal antibodies to components of peripheral vesicles. *Journal of Cell Science*, 90(2):225–235, 1988.

[62] E. O'Gara, K. Howard, J. McComb, I. J. Colquhoun, and G. E. St. J. Hardy. Penetration of suberized periderm of a woody host by *Phytophthora cinnamomi*. *Plant Pathology*, 64(1):207–215, feb 2015.

[63] Henk Brouwer, Pedro M. Coutinho, Bernard Henrissat, and Ronald P. de Vries. Carbohydrate-related enzymes of important *Phytophthora* plant pathogens. *Fungal Genetics and Biology*, 72:192–200, nov 2014.

[64] Peiqian Li, Baozhen Feng, Hemei Wang, Paul W. Tooley, and Xiuguo Zhang. Isolation of nine Phytophthora capsici pectin methylesterase genes which are differentially expressed in various plant species. *Journal of Basic Microbiology*, 51(1):61–70, feb 2011.

[65] Gabriel Levesque-Tremblay, Jerome Pelloux, Siobhan A. Braybrook, and Kerstin Müller. Tuning of pectin methylesterification: consequences for cell wall biomechanics and development. *Planta*, 242(4):791–811, oct 2015.

[66] Svante Resjö, Maja Brus, Ashfaq Ali, Harold J.G. Meijer, Marianne Sandin, Francine Govers, Fredrik Levander, Laura Grenville-Briggs, and Erik Andreasson. Proteomic analysis of *Phytophthora infestans* reveals the importance of cell wall proteins in pathogenicity. *Molecular and Cellular Proteomics*, 16(11):1958–1971, 2017.

[67] V. Senchou, R. Weide, A. Carrasco, H. Bouyssou, R. Pont-Lezica, F. Govers, and H. Canut. High affinity recognition of a *Phytophthora* protein by *Arabidopsis* via an RGD motif. *Cellular and Molecular Life Sciences*, 61(4):502–509, 2004.

[68] Maita Latijnhouwers, Pierre J.G.M. de Wit, and Francine Govers. Oomycetes and fungi: similar weaponry to attack plants. *Trends in Microbiology*, 11(10):462–469, oct 2003.

Force reporting elastomer surfaces to quantify the mechanics of Pathogen/Host interactions

Introduction

Phytophthora species, in the phylum oomycetes, are filamentous plant pathogens that penetrate their hosts by applying invasive forces with a growing hyphal tip[1,2]. Since host penetration is a mechanical interaction between invasive hypha and host, studies of the mechanical interplay requires tools to quantify mechanics at the host-pathogen interface[3]. In this chapter, we developed two methods that enables the measurement of fracture forces and invasive forces, with high spatial and temporal resolution, and that is compatible with live-cell imaging, to correlate forces with sub-cellular responses, and whose geometry mimics the natural host-pathogen geometry.

We developed a method that enables the measurement of invasive forces, with high spatial and temporal resolution, and that is compatible with live-cell imaging, to correlate forces with sub-cellular responses, and whose geometry mimics the natural host-pathogen geometry. Several methods to measure mechanical interactions between hypha and host have previously been reported in literature[4–6]. For example, Bechinger et al.[4] used an optical waveguide substrate to probe indentation forces by fungal pathogens. While accurate, this approach only resolves downward (indentation) forces, while the upward and counterbalanced adhesion forces could not be detected, thereby leaving half of the mechanical scenario beyond reach. The group of Garrill[5] pioneered the use of microfluidic pillar arrays as mechanical obstacle courses to probe forces of growing hypha. However, this approach, while capable of measuring force generation by non-adhered hypha, does not closely mimic the substrate invasion by these pathogens due to a lack of adhesion site. Most likely, these assays measure forces during non-invasive growth but do not accurately capture the biological switch to invasive growth, which involves adhesion, cytoskeletal remodelling and increased turgor generation.

Traction force microscopy (TFM)[8], in which surface forces are detected by analysis of the displacement of tracer beads embedded in a soft substrate, has been extensively used to study forces generated by mammalian cells, but has yet to be applied to study host entry by (plant) pathogens. While TFM offers a detailed view on surface mechanics, its spatial resolution is limited by the spacing between the tracer beads, often several microns[9]. Since our aim is to resolve mechanics at the scale of pixels of the size of the diffraction limit (200-300 nm), we have chosen to develop a novel approach that enables us to do so.

Studying the very small (2-3 μm) invasive hypha[1] on the plant hosts is challenging; plants are highly auto-fluorescent and their multicellular tissues scatter light, making confocal imaging for quantitative measurements challenging. Moreover, to

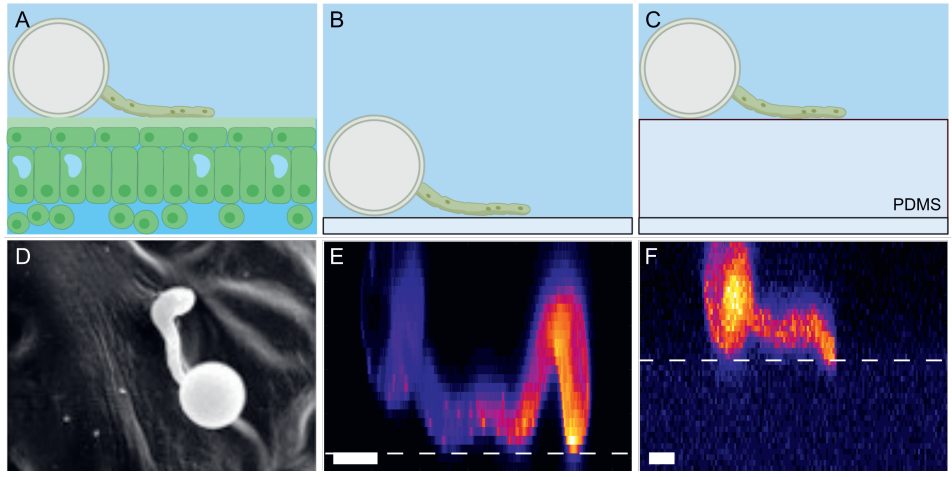

Figure 2.1. Simplified schematic of host entry geometry on (A) a leaf, (B) a glass slide and (C) a elastomer slab. Created with BioRender.com. Visualization of a germinated cysts of *P. infestans* on (D) a leaf (reproduced from Grenville-Briggs et al[7], scanning electron microscopy), (E) glass (scanning confocal microscopy) and (F) an elastomer slab (scanning confocal microscopy). Scale bar is 5 μm, dashed line indicates the interface between substrate and germinated cyst.

date no quantitative tension probes for in-situ mechanical imaging of mechanical forces are available. *Phytophthora* shows a similar growth pattern on glass to that observed on plants leaves (Figure 2.1), with glass commonly used for microscopic studies of invasive behaviour. Glass slides work twofold as a host replacement; i.e. they induce invasive growth in hypha and are highly compatible with high resolution imaging, but are a factor 100-1000 times stiffer than plants[10,11]. However, making force measurements on glass is impossible: the induced deformations of the glass slide, from which deformations could be inferred, are extremely small due to the large mismatch between glass modulus (GPa) and pressures applied by the pathogen (MPa) so they cannot be optically resolved. Optical detection of displacement is central to quantitative force microscopy techniques; displacement data is the input data of quantitative force determination. Quantitative force measurement therefore requires tuning of the sensor to the pathogens abilities and size[12].

To enable the measurement of local surface forces during invasive growth in a biomimetic geometry, a surface force measuring approach must obey the following design constraints: i) a flat substrate that features a stiffness comparable to the plant epidermis, and with a surface chemistry that triggers the pathogen to adhere and invade, ii) adequate optical transparency to enable high-resolution

confocal imaging, iii) a method to measure forces or force-induced damage and iv) non-toxic conditions to ensure cell viability.

To estimate the required surface stiffness, we first established that the typical stiffnesses for plant leaf/root surfaces range from 0.1-100 MPa[13]. Since our approach, detailed below, relies on detecting surface dispacements the stiffness should not be so high that the applied forces result in displacements below the optical resolution. We therefore can make an estimate of the suitable stiffness range of these substrates.

Estimating the optimal surface stiffness starts with the turgor pressure (P), measured in the $P = 0.1 - 10$ MPa range for filamentous plant pathogens[5,14], a portion of which is transferred to the underlying substrate. Forces generated by the hypha act over a small contact area (A) at the tip-substrate contact of several microns squared, deducting the applied force (F) using $F = P * A$. Estimates for the forces generated by filamentous plant pathogens are in the range of μN's[4,5].

Surface deformations we can probe optically must exceed several hundreds of nm in size; this is the Abbe limit. The relationship between material stiffness (E), applied stress (σ) and strain (η) is described as $E = {}^{\sigma}/_{\eta}$. If we make a sensor of $\approx$ 10 micron in size, a strain of 0.1 (10 % strain) results in a microscopically detectable 1 μm displacement. Filling in $\sigma = 0.1$ MPa for the applied stress by the pathogen , $E = 1$ MPa is found for the material stiffness. We aim for a suitable substrate stiffness in the $0.1 - 10$ MPa range, at the lower end of reported leaf stiffnesses[13,15].

PDMS bulk mechanics

A material fitting all of the required design constraints described above is Poly-DiMethyl-Siloxane (PDMS), a large molecule that can form the basis of elastomers when it is crosslinked. PDMS is spincoatable to very thin and uniform layers, has a highly apolar surface chemistry, is biocompatible, and optically transparent hence compatible with high-resolution imaging. Modifications of PDMS elastomer slabs to report forces or force-induced damage have been developed in the biophysics field; applied in a waveguide[4], in elastic resonator interference stress microscopy[16] and traction force microscopy[17]. To start, we first verified that the PDMS recipes used in our studies have the correct bulk mechanical stiffness of ≈ 1 MPa.

To tune the elastomer stiffness to match the lower end of the reported moduli for leaves[10,18], and remain within the range where we can resolve surface deformations using optical sectioning, as detailed above, we tune the crosslinker density in the PDMS. We use a commercial PDMS elastomer kit called Sylgard 184 (Dow Corp.), a commercial 2-component PDMS elastomer kit which has been extensively used in biophysical studies for its biocompatibility and optical transparency. Crosslinker density tuning is achieved by altering the crosslinker/base ratio of Sylgard 184 beyond the standard 1/10 ratio. Mixing Sylgard 184 at lower ratios and curing results in altering the crosslinker concentration in the formed elastomer, creating elastomers a factor 5-10 decrease in stiffnesses[19]. To measure the stiffness, expressed here by the Young's modulus, we perform indentation experiments visualised in Figure 2.2 A, in which a hard spherical indentor is pushed into a solid slab of the PDMS material.

The PDMS elastomer surfaces are indented using a 0.5 mm diameter spherical steel indenter probe at a fixed indentation rate of 0.5 mm/s until 5-10 mN of force was measured in the load cell. In later sections, we introduce dyes into these materials to perform mechanical measurements optically. For each sample type, N = 9 independent measurements were performed on dye-loaded PDMS slabs to determine the average value and standard deviation of Young's modulus E. These dyes are either dissolved in the matrix (PM650) or covalently bound (divinyl spiropyran). The obtained force-distance curves (Figure 2.2B-E, green spheres) were fitted using a Hertzian contact mechanics model[21] (Figure 2.2B-E, red line) to extract the Young's modulus of the PDMS slab, assuming incompressibility of both indentor and substrate Poisson ratio $\nu = \frac{1}{2}$. The Hertz model was found to describe the experimental data well and enabled determination of the Young's modulus E; one example of a force-indentation curve and Hertzian fits for each substrate are shown in Figure 2.2B-D. Young's modulus E results are summarised in Table 2.1.

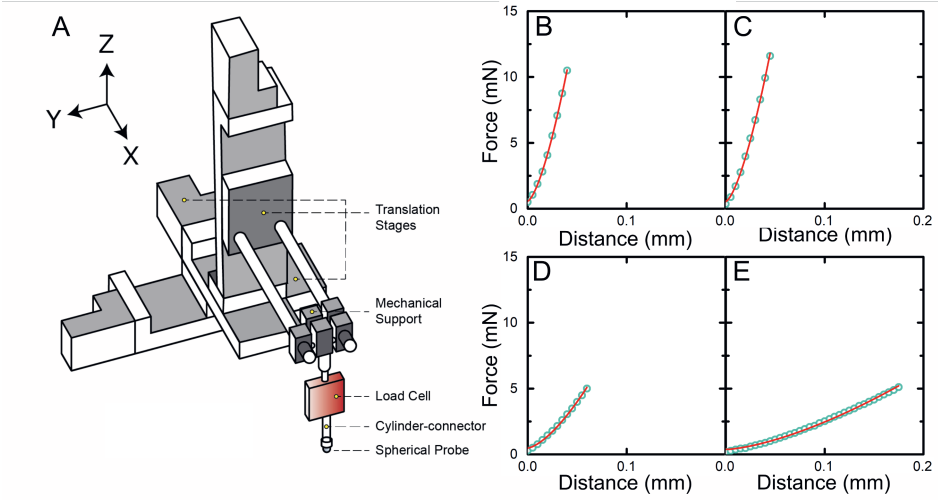

Figure 2.2. (A) Indentor setup, adapted from Boots et al.[20]. Force-Distance curves for different compositions; (B) 1/5 crosslinker/base, (C) 1/10 crosslinker/base, (D) 1/30 crosslinker/base and (E) fracture sensing.

Table 2.1. Results of indentation measurements; PM650 = Pyrromethene 650.

Crosslinker/Base	**Additives**	E_{mean} **(MPa)**	± **(MPa)**
1/30	PM650	0.58	0.11
1/10	PM650	1.49	0.29
1/5	PM650	1.84	0.22
1/20	divinyl spiropyran	0.10	0.0003

These data shows we can tune PDMS stiffness between 0.1 MPa and 1.84 MPa, which is in the range of plant material stiffnesses. We confirm that PDMS surfaces, just like glass substrates that have been used as a standard to date, can induce a transition from non-invasive hyphal growth to adherence and invasive growth (Fig 2.1F). In the two subsequent sections we use these PDMS elastomers as a platform to introduce fluorescent probes to enable the measurement of fracture processes to signal host penetration and to enable quantitative measurements of surface deformations in the stages prior to penetration.

Fracture Reporting

Host entry by *Phytophthora* spp. hyphae involves fracture nucleation[22] in the plant surface, or that of an artificial host entry substrate. How, where and when this fracture occurs is an important aspect for unravelling host penetration mechanics. Recent advances in mechanochemistry have provided several fracture-reporting fluorescent probes that can provide this information with high spatio-temporal resolution. Most fracture reporting probes, including the one we have chosen for our studies, spiropyran[23], work by the force-induced cleavage of a covalent chemical bond that switches on a pi-conjugated structure in the molecule thereby leading to force-gated turn-on fluorescence at a site of mechanical damage. We incorporated the mechanophore spiropyran in the PDMS network to detect when and where invasive stresses imposed by the invading hyphae exceed the fracture threshold of the PDMS, leading to a change from a non-fluorescent molecule (spiropyran) to a red-emitting fluorescent molecule (merocyanin).

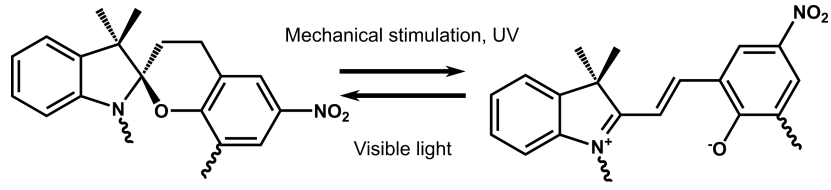

Figure 2.3. Structure formula of spiropyran (left, non-fluorescent), convertible into merocyanin (right, fluorescent) by mechanical stimulation or UV light. The conversion is reversible by visible light. The wavy lines are anchor points to the PDMS backbone via a vinyl linker.

Synthesis of spiropyran

The mechano-sensitive spiropyran is designed to carry two vinyl functional groups, placed on opposite sides of the scissile spiro bond, that incorporate into the PDMS network covalently, thereby allowing the molecule to act as a crosslink ensuring force transfer from the polymer matrix onto the mechanophore (Fig. 2.4A-C). The threshold force to convert spiropyran to merocyanin has been determined to be 240 pN, substantially weaker than the force required to break a Si-O bond in the polymeric network[24]. Spiropyran conversion to merocyanin therefore reports high stress just before the elastomer substrate begins to fail.

The mechano-sensitive spiropyran crosslinker was synthesized following established procedures[23]. First a trimethylindolenine compound was quaternised with an hydroxy (OH) containing group for future vinylization using the OH group (Fig 2.12). Separately, a benzaldehyde compound was demethylated to enable future vinylization using the OH group (Fig 2.13). Both hydroxylated compounds were

mixed and coupled using a base catalyst to create spiropyran (Fig 2.14). The formed spiropyran was then derived using Steglich esterification to add vinyl groups to both rings, resulting in a compound that can be crosslinked into the used PDMS network (Fig 2.15). The complete synthetic procedure can be found in Addendum 1. As a negative control we also synthesized a spiropyran with a single vinyl group that anchors into the PDMS network. The negative control molecule will be incorporated covalently into the PDMS network, but stress applied to the elastomer will not be transferred to the molecule. Thus the negative control molecule should not be activated when mechanical tension is applied to the elastomer network.

Fracture sensing PDMS

The mechano-sensitive spiropyran was dissolved in toluene at 75 mg/ml to add to the PDMS base at a final concentration of 10 mg spiropyran / 1 gram PDMS. The stock solution in toluene was added to the Sylgard 184 base+crosslinker mixture and homogenized thoroughly. The resulting mixture was spin-coated onto cleaned glass slides (#1, 18x18mm, 30s 500 rpm pre-spin period) for 2 minutes at 2000 rpm to obtain layers of approximately 35 μm. Spincoated glass slides were first placed inside a vacuum chamber for 30 min to remove air bubbles and toluene after which they were cured at 50°C overnight. Slides are storable for long timescales.

Optical setup

Hyphal invasion into the PDMS takes place in a 10-30 minute window; imaging conditions must be chosen in such a way that multiple observations of mechano-sensitive PDMS are obtained within the limited timespan. Merocyanin is only weakly fluorescent, requiring imaging conditions that optimise low emission sources from background at high magnification at the fracture interface. Achieving both temporal and intensity constraints, we record one z-stack in cycles of four minutes, in which the first two minutes are spend imaging the z-stack and the next two without laser excitation, ensuring a 50% dark time to reduce cellular stress. The 488 nm laser used to excite the cytoplasmic GFP within *P. infestans* hyphae was used at a very low intensity to decrease the back-photoconversion rate of the activated merocyanin as much as possible during measurement.

Method verification

We verified the functioning of fracture sensing PDMS by studying both mechanosensitive and non-mechanosensitive spiropyran, incorporated into the same network, as seen in Figure 2.4D-F. To confirm that our divinyl spiropyran is mechanosensitive, we embed it into a PDMS elastomer substrate which we indent with a W-shaped stamp (Figure 2.4F). We indeed observe local activation at the indentation sites, confirming its mechano-sensitivity in this matrix. As a negative control, we studied elastomers carrying a mono-vinyl spiropyran, which should not become under tension as the network is stressed. Indeed, this sample does not show activation and turn-on fluorescence upon cutting with a scalpel (Figure 2.4D). To confirm that the lack of spiropyran-to-merocyanine inter-conversion of this mono-vinyl spiropyran is not due to the molecule itself, we then use UV light to convert the probe to its fluorescent state (Figure 2.4E). Our control confirms that the fluorescent signal observed for the mechano-sensitive divinyl spiropyran is due to mechanical stress transfer from the matrix onto the central spiro bond.

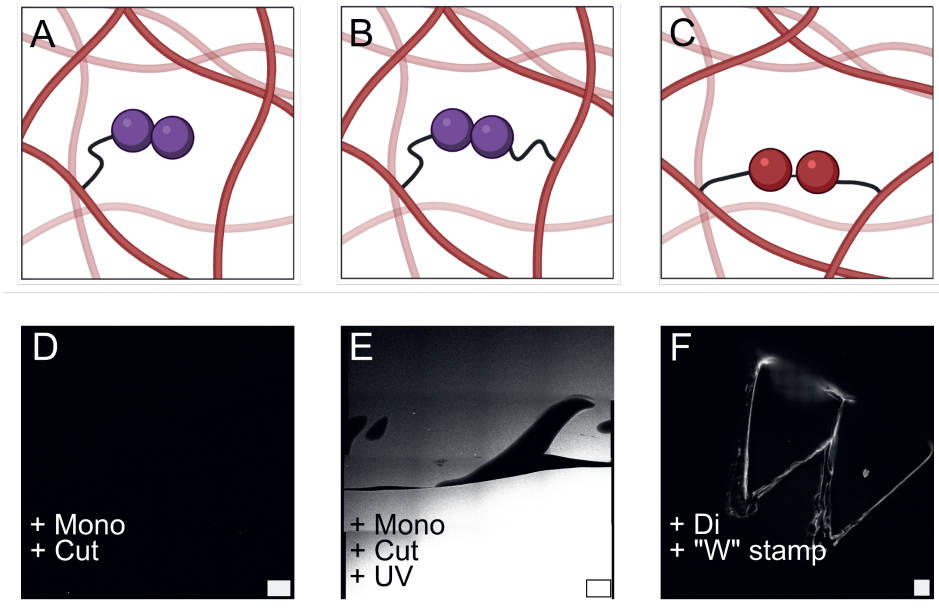

Figure 2.4. Illustrations of (A) non-mechanosensitive "Mono", (B) mechanosensitive "Di" and (C) stretched mechanosensitive spiropyran in a PDMS network. (D) Non-mechanosensitive spiropyran crosslinked into a PDMS slab, cut using a scalpel. (E) UV-pulsed slab to show photoactivation of spiropyran. (F) Mechanosensitive spiropyran after indentation with "W" metal stamp. (D-F) was visualised with confocal miscroscopy. Scale bars are 200 μm.

Output

Some examples of xy projections of the obtained z-stacks are given in Figure 2.5. We can clearly see spiropyran activation in the intimate contact of hypha and elastomer, where fracture is expected as the result of large invasive forces aimed at penetrating the substrate. Mechanosensitive spiropyran is therefore a valuable tool to resolve the location and time of fracture as the passageway for invasion of the pathogen into the substrate. Substrate invasion requires the buildup of penetration forces, a process which we cannot observe using fracture sensing spiropyran. In the following section, we develop a quantitative method to resolve the invasion mechanics in the stages that lead up to substrate fracture.

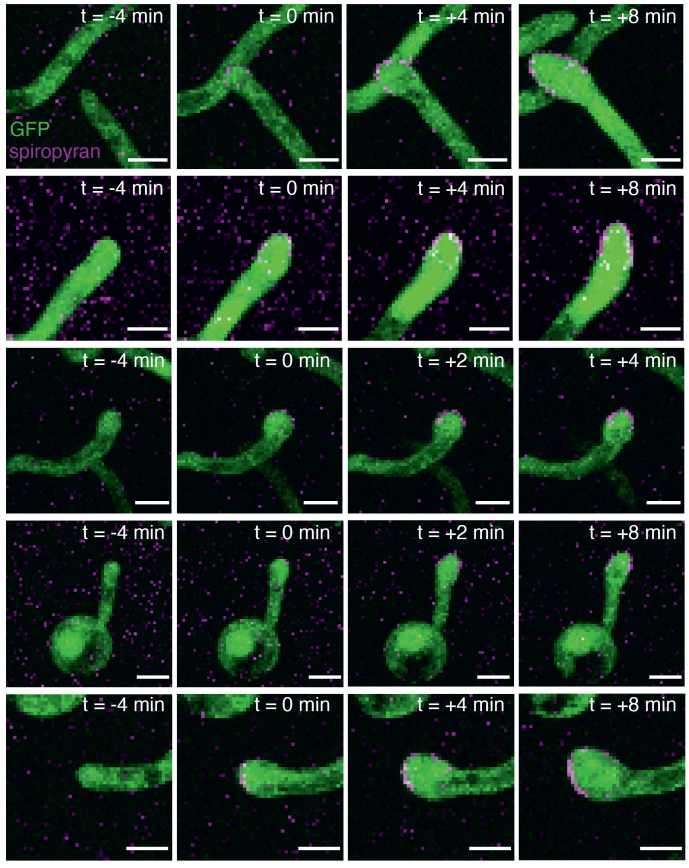

Figure 2.5. Live cell imaging showing the growth of cytoplasmic GFp labelled *Phytophtora* hypae (green) on fracture sensing PDMS (magenta). Scale bar is 3 μm

Discussion

The fracture sensing elastomers contain a high density of spiropyran to ensure a measurable signal for confocal microscopy is generated at the hyphal tip that is applying invasive forces. Although our spiropyran design is able to act as a crosslinker in the network, it binds to the crosslinker compound in the two component mixture. Such crosslinkers tend to bond to the same backbone polymer molecule instead of multiple, resulting in a non-mechanoactive spiropyran. In addition to being non-mechanoactive, the spiropyran attachment to one backbone lowers the material stiffness; these crosslinkers have become unavailable to strengthen the elastomer network. Although we have compensated partially for this effect by raising the crosslink/base ratio from 1/30 to 1/20, the obtained bulk elastic modulus has decreased from 0.58 MPa to 0.1 MPa between normal and fracture sensing PDMS. Better optimization of the fracture sensing PDMS is possible by increasing its modulus to be closer to that of stiff plant materials.

Quantitative surface Mechanics

Quantitative micromechanical methods involving PDMS as a sensor to resolve surface mechanics at cell-substrate interfaces have been developed and used previously for wave-guide mediated deformation profiling[4], elastic resonator interference stress microscopy[16] and traction force microscopy[25]. Often techniques require highly complicated optical setups and sensor preparation, or are tuned to forces in the range of pN-nN instead of μN, which is the force applied by filamentous plant pathogens during host entry.

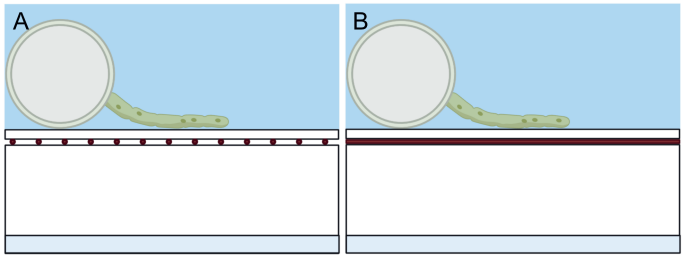

Figure 2.6. Sideview of (A) TFM sensor (B) and displacement sensor .

Traction Force Microscopy (TFM)[17] is one of the most commonly used methods to study cell-substrate contact mechanics. In TFM, one quantifies the displacement of tracer particles embedded in a (soft) matrix to deduct the forces acting on the substrate. Embedded tracer particles are coated on top of an elastomer slab, enveloped by a thin layer of elastomer cast on top, resulting in a thin layer of tracer particles close to the elastomer/water interface (Fig 2.6A). Any forces acting on the substrate, e.g. by adherent cells, result in displacements of these tracer beads from their original position. Using fluorescence super-resolution imaging techniques[9], tracer displacements can be determined with high accuracy, typically, 10-20 nm in xy-plane and 50-100 nm in z-plane. From these displacements, the force fields in the substrate can then be inferred using computational analysis. While this method has provided a wealth of insight into cellular surface forces, its main limitation is that the spatial resolution of the displacement imaging is set by the distances between tracer particles, which is often several microns to ensure particle tracking with high fidelity. While this spatial resolution is sufficient to study adherent mammalian cells, which are often tens to hundreds of microns in dimension, filamentous plant pathogens invade with a hyphal tip that is only a few microns in diameter. As a result, studying the surface mechanics of filamentous plant pathogens requires a different approach, with a spatial resolution that is ideally well below 1 micron and approaches the diffraction limit of 200-300 nm.

Design "sandwich" setup

Our initial design for a PDMS-based sensor to map surface displacements in the axial direction (i.e. normal forces rather than traction forces), was to replace the layer of tracer particles in TFM with a homogeneous fluorescent tracer layer (Figure 2.6B). By switching to a dye layer we lose information about traction forces (in the xy plane), but increase density of displacement sampling (in the z plane) to every pixel to deduct normal forces. To do so, we first spincoated a 20-30 micron thick PDMS layer on glass slides and fully cured the material. Subsequently we applied a layer of the fluorescent dye Rhodamine B, to serve as the tracer layer, which is then topped with a thin layer of PDMS to interface cysts and hyphae (Fig 2.7A and B).

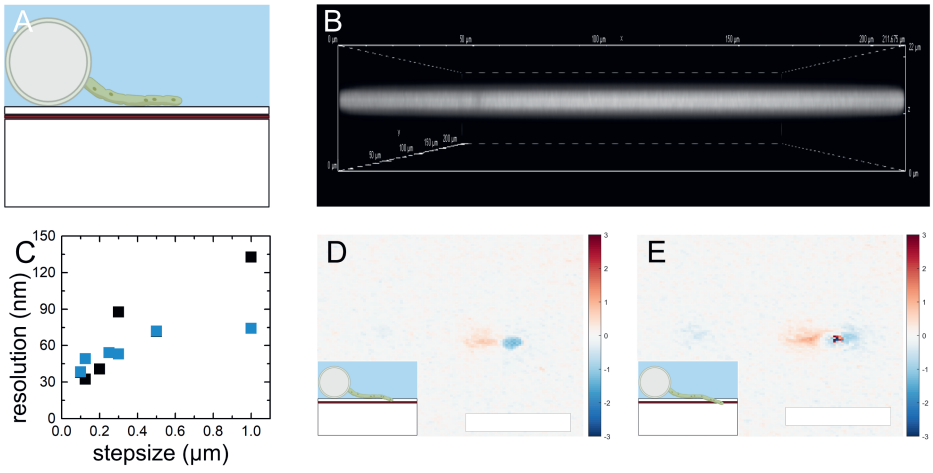

Figure 2.7. "Sandwich" sensor setup, resolution and data. (A) Schematic overview of "jelly" sensor; *Phytophthora* spp. in water phase with germinated hyphae on top of PDMS sensor with incorporated dye layer. (B) 3D rendering of emissive layer embedded in PDMS matrix, acquired by confocal microscopy. (C) Displacement resolution (δ_{z0}) of surface fluctuations as function of the step size taken to acquire a z-stack. Blue squares: pinhole 0.7 Airy units (A.U.) Black squares:pinhole 1.4 A.U. (D) displacement pattern of invasive cell pre-fracture. Cartoon of situation in bottom left. (E) Displacement pattern of invasive cell, 20 minutes after D. Cartoon of situation in bottom left. D/E scalebar is 10 microns.

By recording a three-dimensional image stack of the fluorescent tracer layer, using a confocal microscope, a gaussian intensity profile is observed of the dye layer for each xy pixel. For each pixel, the fluorescent gaussian profile was fitted and z-position deducted from the fit centroid, which is altered when the substrate is deformed, determined with sub-pixel accuracy (Figure 2.7C).

Method verification

We have analysed an unpertured, flat sample to assess the z-axis resolution of our approach (Fig 2.7C). In this reference sample, the variability in the determined z-position of the dye layer is a measure for the resolution by which displacements can be determined. We define the resolution as the FWHM of a histogram of the determined z-position data for each pixel in the sample. This results in a maximum resolution of approximately 30 nm, using small z-step sizes and long integration times. For experiments with living cells, when time resolution is crucial, increasing the z-step size to 1 micron results in a corresponding decrease in the acquisition time of a factor 8, whilst a z-resolution of approximately 100 nm is obtained. Upon loading with *P. infestans* cysts, hyphal growth and invasive force application start on the PDMS sensor. Force application results in highly localised displacement of the tracer dye layer, which is mapped as described above. Examples of obtained displacement maps by invasive hyphae are given in Fig 2.7D and E, where the formation of both an adhesion (red, upwards) and indentation (blue, downwards) site can be seen.

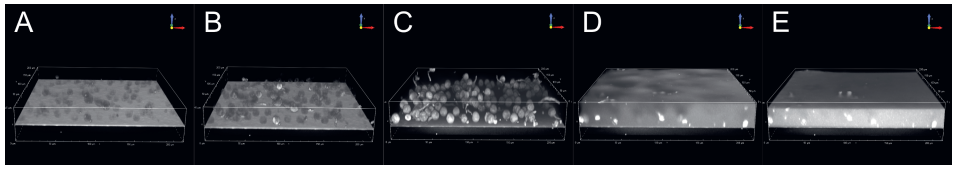

Figure 2.8. From left to right: 3D rendering of confocal microscopic z-stacks, showing release of Rhodamine B (layer) into the cells and water phase over time. Timepoints; A: 0min, B: 45min, C: 60min, D: 66min, E: 68min.

The first fluorescent probe we tried was Rhodamine B, which forms a very thin layer of fluorescent material without migrating into the PDMS, perfect for long term "jelly sandwich" storage. During invasion experiments the growing and invasive hyphal tip is always located inside of the indentation site, the blue ellipsoid in Fig 2.7E. In this diagram, we see that very high/low displacement values are found in the indentation centre, coupled to a massive decrease in fluorescence from the dye layer. The decrease in fluorescence is caused by the release of Rhodamine B into the water phase containing the cells on top once the top PDMS layer is ruptured (Fig 2.8). Between 60 and 68 minutes (Fig 2.8C and D), a large release of Rhodamine B takes place in less than eight minutes, caused by direct contact between the thin dye layer and the water phase on top.

We screened many fluorescent probes in order to find a more suitable dye not released into the aqueous phase after penetration. We encountered the problem

that hydrophilic dyes (Water soluble Quantum Dots, sulfo-Rhodamine B) are released into the aqueous phase upon penetration, whilst hydrophobic dyes (polyfluorene-benzothiadiazole, DiIC18, polyfluorene oligomers) remain trapped in the substrate and tend to aggregate over time in the thin layer, leading to inhomogeneous fluorescence. A redesign was needed.

Displacement sensor design

Based on the attempts described above, we decided to try a fundamentally different, and simpler approach (Fig 2.9A). We tracked the displacement of a PDMS slab with uniform colouration instead of a thin emission layer. Uniform colouration negates the problem of dye release into solution; we trialled highly apolar molecules that are well solvable in PDMS matrice sand with no solubility in water as summarised in table 2.2, finding Pyrromethene 650 to be the best performing compound. Pyrromethene 650 is a highly apolar and small dye making it rather mobile in the PDMS matrix but non-migrating to the water phase, whilst being quite photostable and red-emitting. Red emission is preferred from a cell compatibility perspective, whilst red light is the least photoxic for *Phytophthora*[26] and compatible with simultaneous live cell imaging of GFP labeled *Phytophthora* strains, as exploited in Chapter 2 and 3 of this thesis.

Table 2.2. Dyes trialled for displacement imaging.

Dye	**Result**	**Problem/Notes**
PDMS-Oligo-Fluor	Failure	Aggregation/low fluorescence
Oxazine	Failure	Bleaching
Pyrene	Failure	Bleaching
Perylene	Failure	Bleaching
DiI-C18	Failure	Cell affinity
Pyrromethene 597	Failure	Overlap with GFP emission
Pyrromethene 650	Success	

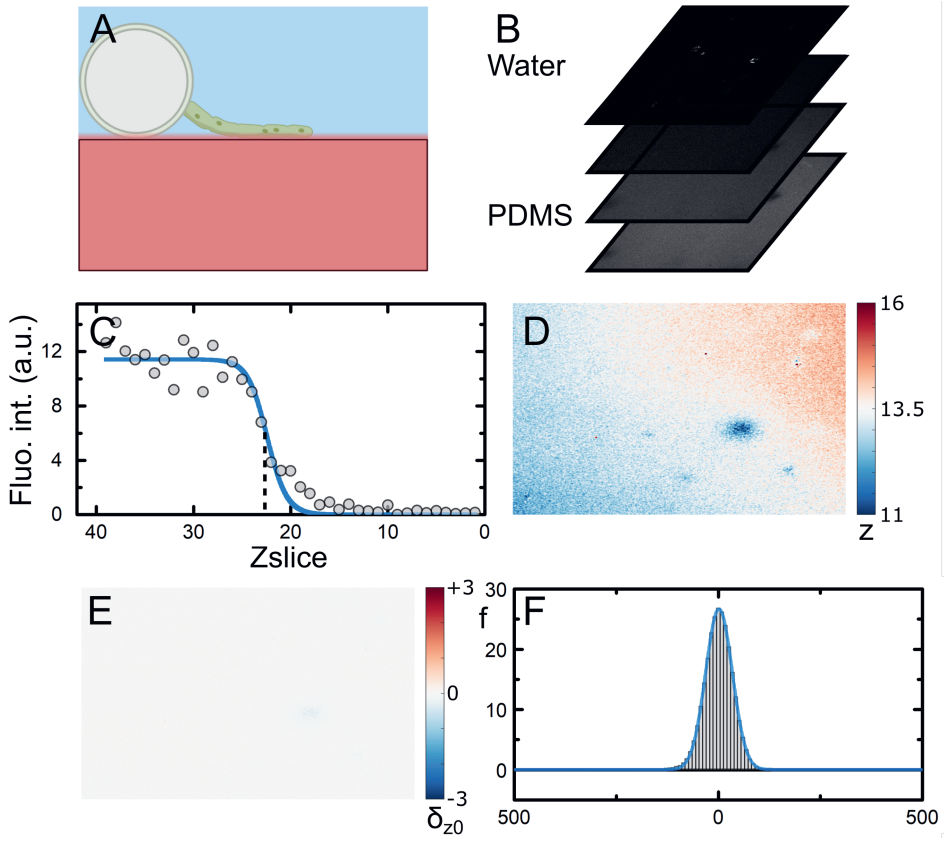

Figure 2.9. (A) Schematic overview of Surface Displacement centre with germinated *Phytophthora* cyst. (B)Example slices of a z-stack of the PDMS layer fluorescence. (C) Example of an intensity decay curve at the PDMS-medium interface from three-dimensional confocal microscopy (circles) and corresponding sigmoidal fit to extract the surface position (z, dashed line) for a single voxel in the xy plane . (D) Tilted raw height map after fitting, colorbar in μm. (E) De-tilted final relative displacement (δ_{z0}) map, colorbar in μm. (F) Histogram of detected z-displacement deviations (in nm) on a flat unperturbed substrate (gray bars), and fit to a Gaussian function to determine the detection resolution, defined as the FWHM of the fit (blue line).

Surface deformation sensor fabrication

Elastomer surface mixtures are prepared from a commercial 2-component polydimethyl siloxane rubber (Sylgard 184, Dow Corning) in the following ratios of crosslinker/base: 1/30, 1/10 and 1/5, to obtain different stiffnesses. The two components are accurately weighed on an analytical balance to deviate < 2% in mass, in 4 ml glass vials to aid in mixing. Before mixing, additives (e.g. Pyrromethene 650 dye for surface deformation profiling, or spiropyran for fracture sensing) are added as stock solutions in toluene. This mixture is thoroughly mixed by vortexing for 3 to 4 minutes. Bubbles and dust are removed from the liquid, but viscous, mixture by centrifugation at 1000g for 10 minutes.

Glass slides are cleaned prior to spincoating of elastomer precursor mixture. Slides are cleaned by sequential rinsing with isopropyl-alcohol (IPA), Milli-Q deionized water and IPA while being dried using in a nitrogen stream between rinsing steps. The slides are dried further by heating to 60-70 °C for 5 minutes to ensure complete solvent removal after the rinsing steps.

To ensure good adherence of the PDMS rubber to the glass subsurface, slides are pre-treated using an O_2/N_2 plasma for 1 minute just prior to spincoating. After mounting the slide on the spincoater chuck, 150 μl of liquid precursor is placed on the slide. Layers are then prepared by a two-step spincoating procedure: 30 s at 500 rpm to wet the substrate, followed by 2 minutes at 2000 rpm to make a uniform layer of $\approx$ 33 μm thickness, as determined by confocal microscopy.

Coated slides are transferred back to a bespoke 3D printed holder (Addendum 2), to minimize dust accumulation, and placed inside a vacuum chamber for at least 30 minutes to remove air bubbles. Samples are then placed in a 50 °C oven overnight to cure the elastomer. Sensors containing the dye Pyrromethene 650, used in surface deformation profiling, show gradual degradation over several weeks due to dye aggregation. These substrates are prepared fresh before each experiment.

Optical setup

Confocal microscopy data was acquired on a Nikon Eclipse Ti2 Confocal Laser Scanning Microscope (CLSM) with a 60x oil immersion objective. The scan area was 512×512 pixels with a pixel size of 0.41 μm/pixel, translating into a scan area of 211×211 μm, and a frame acquisition rate of 1/second. For three-dimensional image stacks, a 21 μm deep stack was recorded with a 0.5 micron step size in the axial (z) direction. The acquisition time for a single z-stack is approximately 60 seconds, and these were acquired at 1 stack per 2 minutes for an effective dark time of 50%. Multiple laser lines were used to image various fluorescent

components. GFP expressing transgenic *Phytophthora* strains were excited at 488 nm, spiropyran at 640 nm and Pyrromethene-650 at 561 nm. Substrates were placed in a bespoke 3D printed sample chamber (design available as .stl file on request from the authors) to avoid evaporation of water droplets during imaging experiments. Glass slides containing elastomer substrates were then inoculated with 0.1 ml of $\approx 3 \times 10^5$ cysts/ml. Another 0.1 ml of the cyst suspension was deposited in each of the four corners in the upper area of the sample chamber to prevent evaporation; the chamber was then sealed with a cell culture dish cover to ensure high humidity conditions over at least an 8-12 hour period.

For static data collection (e.g. for determining invasion angles), inoculated surfaces were left for 1.5h in a thermostated environment at 20 °C prior to imaging. Dynamic data was collected almost immediately after inoculation with a stack-rate of 0.5 stacks/minute. Laser powers were minimized as much as possible to prevent dye degradation and light-induced stress to the organisms. After data collection, a 3x3 tiling centered around the observed field of view was often applied to visually check if germination or invasion was effected by light exposure. At the used light conditions and dye concentrations no visible detrimental effects were observed.

Surface deformation profiling

To quantify the mechanics of surface invasion we develop an approach to map the surface deformation profile with high resolution. We record three-dimensional time series of fluorescent PDMS elastomer surfaces (see sections 'Optical setup' and 'Surface deformation sensor fabrication' for details, and figure 2.9A and B) during invasion of *Phytophthora* spp. For each xy-pixel we then extract the intensity profile of the PDMS layer as a function of the position in z; to suppress spurious noise we average the intensity using nearest-neighbour cross averaging. Figure 2.9C shows the sigmoidal fluorescent intensity decay across the PDMS-water interface. For each pixel in the xy-plane these intensity profiles are fitted to the sigmoidal function:

$$I(z) = \frac{I_{bulk}}{1 + \exp(-(z - z_0))} \tag{2.1}$$

in which I_{bulk} sets the plateau intensity in the bulk of the elastomer slab and z_0 is the centroid position of the decay, which defines the local surface height, the quantity of interest.

After reconstruction of the surface height map for the entire three-dimensional image, we perform a tilt correction as shown in figure 2.9D and E to correct for small deviations in sample placement from the horizontal axis. We find that most

samples are tilted by at most 1-2°. Tilt corrections are done from the outer 10 micron of the field of view, by fitting the tilt to a linear function in both the x and y directions. Finally, the median value of the height map is subtracted from each pixel to bring the substrate normal to $z = 0$, resulting in relative surface height maps. We use a linear approximation to ensure that no splay of the surface is induced by the de-tilting algorithm.

To determine the δz_0-resolution of our method, we record image stacks of a substrate in the absence of any microbes. This results in flat surface height maps with fluctuations of amplitude δz_0 due to the diffraction-limited images and statistical errors in the fitting procedure. Histograms of δz_0 in the absence of any microbes show a Gaussian distribution. We define the resolution as the FWHM of the δz_0 distribution. Due to the use of the entire z-intensity profile to determine the surface height, we obtain a resolution in z_0, with sub-pixel accuracy, of 46 nm for the highest resolution imaging settings used (z-step = 0.125μm).

Method Verification

Confocal studies of *Phytophthora* cysts and hyphae require laser light focused through high magnification optics, resulting in exposure of the organisms to substantial light doses. High light doses, especially of short wavelength high-energy light can be damaging to living cells and induce stress[26]. Cellular stress results in slower growth or cell death at low or high doses, respectively. Stress or cell death leads to strong autofluorescence, enabling phototoxicity monitoring by observing the amount of cells displaying high autofluorescence intensities. We first expose *Phytophthora* spp. to a high light dose of the excitation laser needed for the Pyrromethene 650 dye in the displacement sensors. We illuminate a small field of view for several minutes (square in Fig2.10A) and then quickly capture an image of a larger 3x3 tiling field-of-view to visualise photo-induced cell death in the region exposed to prolonged strong illumination. We see that cells in the illuminated sample display strong signs of phototoxicity (marked in red) as a result of the laser illumination. We have optimized the imaging settings to reduce the light doses, while maintaining sufficient signal for the displacement sensor imaging. Here we observe very limited photo-toxicity (Fig2.10B), and these settings (lower laser power, higher gain and 50% dark periods) were used in further experiments.

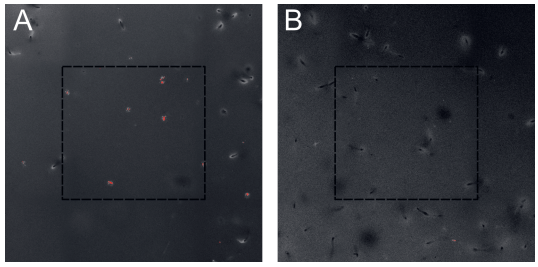

Figure 2.10. Confocal microscopic image of *P. infestans* germinated cysts to long-exposure laser light, (A) image taken after 1h of measurement in central square of 3x3 tiling. (B) Optimised settings to minimise light stress at the same duration.
Pixels $> 70\%$ intensity are coloured red, dashed outline is 212μm by 212μm.

We benchmarked our displacement imaging approach by indenting the PDMS surfaces with a spherical steel indentor of radius 0.5 mm: a classical geometry which has also been used in TFM microscopy, enabling a direct comparison[25]. The resulting displacement map is plotted in Fig2.11A, while the radially averaged displacement from the indentation centre is shown in Fig2.11B. The surface deformations show the characteristic pattern for indentation with an adhesive sphere, where the surface displacements are negative (downwards) under the sphere due to gravitational forces, and positive (upwards) at the sphere perimeter due to strong adhesion between indentor and PDMS surface. A similar experiment was conducted using TFM by Dufrense et al[25], which we have replotted in Fig2.11C. Our approach only resolves normal forces, whilst TFM provides acces to both normal and traction forces. However, our approach offers a much larger spatial resolution in xy and a higher accuracy in measuring small z-displacements, as evidenced from the much lower noise levels in Fig2.11B versus Figure 2.11c.

Discussion

Developed sensors have an approximately five-fold increase in displacement resolution (Figure 2.11B and C, 100 nm and 500 nm FWHM accuracy respectively) as compared to TFM. The developed displacement sensor is highly accurate in displacement and at a high spatial density, the central goals of the design. Optically speaking, further improvements are possible to enhance data quality and quantity, using a more complex optical setup. We use a simple point scanner which takes considerable time to build up a single frame of imaging. There are considerably faster alternative scanning methods like resonant/spinning disk scanners. Systems like the Visitech microscope are also available that build up frames much faster in z, resulting in a order of magnitude decrease in acquisition time. Faster imaging

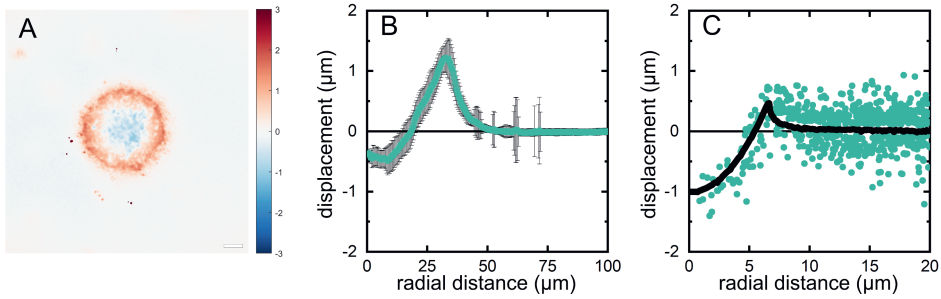

Figure 2.11. Displacement pattern of spherial indenter on elastomer sensor. (A) Displacement map of spherical indentor. Colourbar is +3μm (red) to -3μm (blue) displacement, scalebar is 10 μm. (B) Radially average displacement (green open circles) and standard deviation (error bars) plotted from the indentor centre outwards. (C) Johnson, Kendall, Rodgers model fit (red spheres) to the radially averaged displacement data.

with similar signal/noise ratio has a cell viability advantage as well, lowering light exposure time, reducing phototoxic stress of the imaged cells. Phototoxic stress was a concern in our studies; exposing cells to both a stiff surface and regular light exposure had a negative effect on invasion efficiency. We therefore were limited to studying invasion mechanics at lower stiffness PDMS at high temporal resolution. Improved optical systems could unlock higher moduli substrates for temporal analysis of invasion mechanics. We do note that observed invasion patterns are the same between high and low stiffness PDMS, but it could be interesting to study this in conjunction with cell wall mechanosensors[27].

The second factor limiting the ease-of-application is the slow aggregation of Pyrromethene 650 dye in the PDMS matrix, forming crystals over a timespan of approximately 7 days. Pyrromethene 650 crystals lower the amount of fluorescence, impacting the signal/noise ratio and therefore displacement resolution of the sensor. Diminishing resolution over time makes large batch production and storage unfeasible, requiring slides to be produced within a few days before usage to ensure highly homogenous fluorescence. We have found that sonicating dye stock solutions before mixing with the uncured elastomer helps in keeping the dye more stable, but this merely delays aggregation. A tested alternative approach was to apply the dye solution at a corner of an undyed PDMS slab at lower concentrations (10 microgram/ml PM650/toluene), give the solvent 30 minutes to evaporate slowly to stop crystal formation on top of the PDMS, and putting the post-coloured slab into a 70 ^{o}C oven overnight. We can use the slabs like normal; the overnight heat treatment induces strong diffusion of the pyrromethene 650 molecules through the slab resulting in a homogenous fluorescence. Another

alternative is switching to a more PDMS-solvable dye that has the same fluorescence characteristics by attaching $SiO(CH_3)_2$ (polymer) groups. This could be a strategy to combat aggregation, but requires new synthesis and engineering not possible within this project time-frame.

Addendum 1: Spiropyran Synthesis

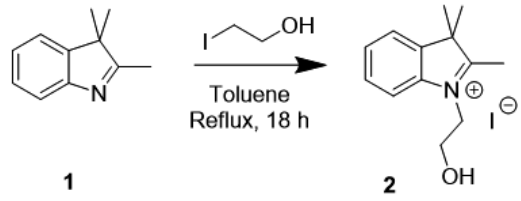

Figure 2.12. Spiropyran synthesis step 1.

Step 1: To a roundbottom flask, 5 mL of trimethylindolenine (31.4 mmol) was added. Then 3.67 mL of 2-iodoethanol (47.1 mmol) was introduced together with 56 mL of anhydrous toluene. The reaction was left under reflux for 20 hours before cooling. The product was collected by vacuum filtration. The resulting light pink solid which was washed with 210 mL of 2% (v/v) EtOH in Et_2O to remove residual 2-iodoethanol and dried under vacuum. Yield = 1.18 gram (11.3%).
1H NMR (400 MHz, DMSO-d6) δ 7.97 ppm (m, 1H), 7.85 (m, 1H) , 7.64 (m, 2H), 4.61 (m, 2H), 3.88 (m, 2H), 2.83 (s, 3H), 2.50 (s, 3H), 1.56 (s, 6H).

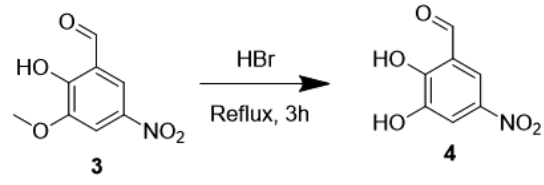

Figure 2.13. Spiropyran synthesis step 2.

Step 2: To obtain the intermediate product **4**, 5.020 g of 2-hydroxy,3-methoxy,5-nitrobenzaldehyde was dissolved in 94 ml of 48% HBr and left to reflux for 4.5 hours, diluted with 300 mL water and cooled. The reaction mixture was subsequently filtered and the solid product washed with 200 ml water and dried in-vacuo. Yield = 4.02 gram (86.1%).
1H NMR (400 MHz, CDCl3) δ 11.78 ppm (s, 1H), 10.01 (s, 1H), 8.21 (d, 1H), 8.07 (d,

1H), 5.96 (s, 1H).

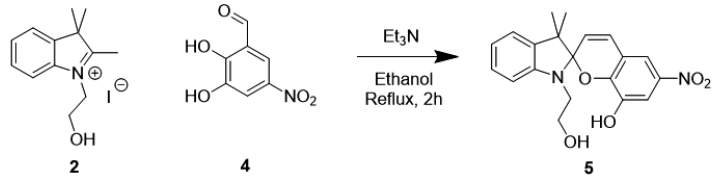

Figure 2.14. Spiropyran synthesis step 3.

Step 3: In a roundbottom flask, 1.035g of **2** (3.12 mmol) and 0.5727g of **4** (3.12 mmol) were dissolved in 25 ml ethanol. To this, 0.874 ml triethylamine (6.24 mmol) was added and the solution was brought to reflux and stirred for 2 hours. After cooling, the solution was filtered and the resulting precipitate washed with cold ethanol. The filtrate was concentrated and filtered to maximize yield; this was repeated three times. Yield = 0.83 gram (76.7%). No proton NMR was recorded for this intermediate product.

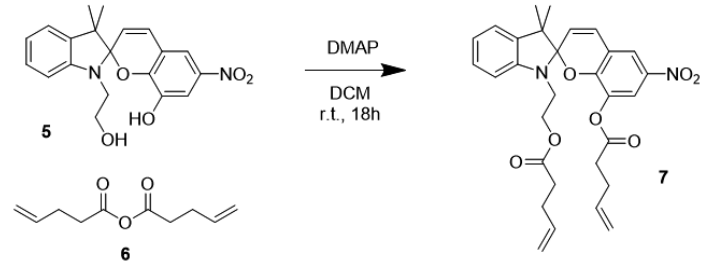

Figure 2.15. Spiropyran synthesis step 4.

Step 4: In the last step, 0.6022g of **5** (1.628 mmol) was added to a roundbottom flask along with 0.0215g 4-dimethylaminopyridine (0.1628 mmol). This was dissolved in 8 mL DCM. Under nitrogen flow, 0.64 mL of 4-pentenoic anhydride (3.502 mmol) was added dropwise at a rate of 1 drop per 15 minutes using a syringe. The reaction was left to stir under nitrogen overnight, resulting in a purple solution. This mixture was extracted against 75 ml each of: concentrated $Na(HCO_3)_2$, 1M HCl, water (2x) and brine. The organic phase was dried over magnesium sulphate and filtered, after which the filtrate was evaporated to yield product **7**. Yield = 0.62 gram (73%).
1H NMR (400MHz, DMSO-d6) δ 7.96 ppm (d, 1H), 7.85 (d, 1H), 7.18 (td, 1H), 7.08

(d, 1H), 6.97 (d, 1H), 6.88 (m, 1H), 6.67 (d, 1H), 5.97 (d, 1H), 5.78 (m, 1H), 5.58 (ddt, 1H), 4.93 (m, 4H), 4.25 (m, 1H), 4.18 (m, 1H), 3.35 (t, 2H), 2.37 (m, 4H), 2.21 (m, 2H), 1.88 (m, 2H), 1.29 (s, 3H), 1.20 (s, 3H).

Addendum 2: 3D designs holders

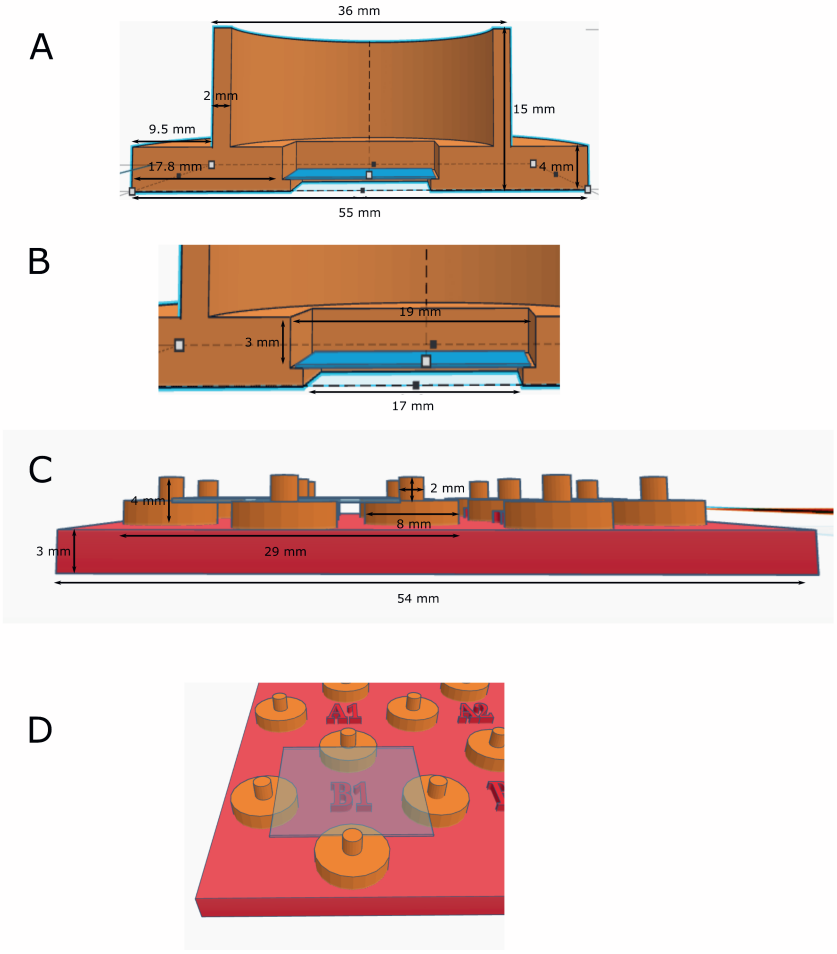

Figure 2.16. (A,B) Overview of dimensions of holder used for 18x18 mm sample for imaging and (C,D) spincoating/fabrication.

References

[1] Howard S. Judelson and Flavio A. Blanco. The spores of *Phytophthora*: weapons of the plant destroyer. *Nature Reviews Microbiology*, 3(1):47–58, jan 2005.

[2] Adrienne R. Hardham. Cell biology of plant-oomycete interactions. *Cellular Microbiology*, 9(1):31–39, 2007.

[3] Amir Sanati Nezhad and Anja Geitmann. The cellular mechanics of an invasive lifestyle. *Journal of Experimental Botany*, 64(15):4709–4728, 2013.

[4] Clemens Bechinger, Karl Friedrich Giebel, Martin Schnell, Paul Leiderer, Holger B Deising, and Martin Bastmeyer. Optical measurements of invasive forces exerted by appressoria of a plant pathogenic fungus. *Science*, 285(5435):1896–1899, 1999.

[5] Ayelen Tayagui, Yiling Sun, David A. Collings, Ashley Garrill, and Volker Nock. An elastomeric micropillar platform for the study of protrusive forces in hyphal invasion. *Lab on a Chip*, 17(21):3643–3653, 2017.

[6] Mahmood Ghanbari, Muthukumaran Packirisamy, and Anja Geitmann. Measuring the growth force of invasive plant cells using Flexure integrated Lab-on-a-Chip (FiLoC). *TECHNOLOGY*, 06(03n04):101–109, sep 2018.

[7] Laura J Grenville-Briggs, Victoria L Anderson, Johanna Fugelstad, Anna O Avrova, Jamel Bouzenzana, Alison Williams, Stephan Wawra, Stephen C Whisson, Paul R.J. Birch, Vincent Bulone, and Pieter van West. Cellulose Synthesis in *Phytophthora infestans* Is Required for Normal Appressorium Formation and Successful Infection of Potato. *The Plant Cell*, 20(3):720–738, apr 2008.

[8] Huw Colin-York and Marco Fritzsche. The future of traction force microscopy. *Current Opinion in Biomedical Engineering*, 5:1–5, mar 2018.

[9] Huw Colin-York, Dilip Shrestha, James H. Felce, Dominic Waithe, Emad Moeendarbary, Simon J. Davis, Christian Eggeling, and Marco Fritzsche. Super-Resolved Traction Force Microscopy (STFM). *Nano Letters*, 16(4):2633–2638, apr 2016.

[10] Stig Falk, Carl Hellmuth Hertz, and Hemming I. Virgin. On the Relation between Turgor Pressure and Tissue Rigidity. I. Experiments on Resonance Frequency and Tissue Rigidity. *Physiologia Plantarum*, 11(4):802–817, oct 1958.

[11] Knittel-Glaeser. Knittel Glass Specification Sheet. *Web*, 2022.

[12] Pere Roca-Cusachs, Vito Conte, and Xavier Trepat. Quantifying forces in cell biology. *Nature Cell Biology*, 19(7):742–751, 2017.

[13] Lorna J. Gibson. The hierarchical structure and mechanics of plant materials. *Journal of The Royal Society Interface*, 9(76):2749–2766, nov 2012.

[14] R. J. Howard, M. A. Ferrari, D. H. Roach, and N. P. Money. Penetration of hard substrates by a fungus employing enormous turgor pressures. *Proceedings of the National Academy of Sciences*, 88(24):11281–11284, 1991.

[15] Yusuke Onoda, Feike Schieving, and Niels P.R. Anten. A novel method of measuring leaf epidermis and mesophyll stiffness shows the ubiquitous nature of the sandwich structure of leaf laminas in broad-leaved angiosperm species. *Journal of Experimental Botany*, 66(9):2487–2499, may 2015.

[16] Nils M. Kronenberg, Philipp Liehm, Anja Steude, Johanna A. Knipper, Jessica G. Borger, Giuliano Scarcelli, Kristian Franze, Simon J. Powis, and Malte C. Gather. Long-term imaging of cellular forces with high precision by elastic resonator interference stress microscopy. *Nature Cell Biology*, 19(7):864–872, jul 2017.

[17] Huw Colin-York and Marco Fritzsche. The future of traction force microscopy. *Current Opinion in Biomedical Engineering*, 5:1–5, mar 2018.

[18] Takami Saito, Kouichi Soga, Takayuki Hoson, and Ichiro Terashima. The Bulk Elastic Modulus and the Reversible Properties of Cell Walls in Developing Quercus Leaves. *Plant and Cell Physiology*, 47(6):715–725, jun 2006.

[19] Charles Puerner, Nino Kukhaleishvili, Darren Thomson, Sebastien Schaub, Xavier Noblin, Agnese Seminara, Martine Bassilana, and Robert A. Arkowitz. Mechanical force-induced morphology changes in a human fungal pathogen. *BMC Biology*, 18(1), sep 2020.

[20] J. N.M. Boots, R. Fokkink, J. Van der Gucht, and T. E. Kodger. Development of a multi-position indentation setup: Mapping soft and patternable heterogeneously crosslinked polymer networks. *Review of Scientific Instruments*, 90(1):015–108, jan 2019.

[21] K. L. Johnson. *Contact Mechanics*. Cambridge University Press, may 1989.

[22] K. H. Kim and M. K. Chaudhury. Shear-induced fracture at the interface of PDMS and a rigid slab modified with polyelectrolyte layers. *Journal of Adhesion*, 85(11):792–811, nov 2009.

[23] Douglas A. Davis, Andrew Hamilton, Jinglei Yang, Lee D. Cremar, Dara Van Gough, Stephanie L. Potisek, Mitchell T. Ong, Paul V. Braun, Todd J. Martínez, Scott R. White, Jeffrey S. Moore, and Nancy R. Sottos. Force-induced activation of covalent bonds in mechanoresponsive polymeric materials. *Nature*, 459(7243):68–72, may 2009.

[24] Gregory R. Gossweiler, Tatiana B. Kouznetsova, and Stephen L. Craig. Force-Rate Characterization of Two Spiropyran-Based Molecular Force Probes. *Journal of the American Chemical Society*, 137(19):6148–6151, may 2015.

[25] Robert W. Style, Callen Hyland, Rostislav Boltyanskiy, John S. Wettlaufer, and Eric R. Dufresne. Surface tension and contact with soft elastic solids. *Nature Communications*, 4, nov 2013.

[26] Peter J Gwynne and Maurice P Gallagher. Light as a broad-spectrum antimicrobial. *Frontiers in Microbiology*, 9(FEB), 2018.

[27] Lucile Michels, Vera Gorelova, Yosapol Harnvanichvech, Jan Willem Borst, Bauke Albada, Dolf Weijers, and Joris Sprakel. Complete microviscosity maps of living plant cells and tissues with a toolbox of targeting mechanoprobes. *Proceedings of the National Academy of Sciences of the United States of America*, 117(30):18110–18118, 2020.

A slicing mechanism facilitates host entry by plant-pathogenic *Phytophthora*

Phytophthora species, classified as oomycetes, are among the most destructive plant pathogens worldwide and pose a substantial threat to food security. Plant pathogens have developed various methods to breach the cuticle and walls of plant cells. For example, plant-pathogenic fungi use a 'brute-force' approach by producing a specialized and fortified invasion organ to generate invasive pressures. Unlike in fungi, the biomechanics of host invasion in oomycetes remains poorly understood. Here, using a combination of surface-deformation imaging, molecular-fracture sensors and modelling, we find that _Phytophthora infestans_, _Phytophthora palmivora_ and _Phytophthora capsici_ slice through the plant surface to gain entry into host tissues. To distinguish this mode of entry from the brute-force approach of fungi that use appressoria, we name this oomycete entry without appressorium formation 'naifu' invasion. Naifu invasion relies on polarized, non-concentric, force generation onto the surface at an oblique angle, which concentrates stresses at the site of invasion to enable surface breaching. Measurements of surface deformations during invasion of artificial substrates reveal a polarized mechanical geometry that we describe using a mathematical model. We confirm that the same mode of entry is used on real hosts. Naifu invasion uses actin-mediated polarity, surface adherence and turgor generation to enable _Phytophthora_ to invade hosts without requiring specialized organs or vast turgor generation.

Jochem Bronkhorst[1], *Michiel Kasteel*[2,3], *Stijn van Veen*[1], *Jess M. Clough*[1], *Kiki Kots*[2,3], *Jesse Buijs*[1], *Jasper van der Gucht*[1], *Tijs Ketelaar*[3], *Francine Govers*[2] *& Joris Sprakel*[1,*]

[1]*Physical Chemistry and Soft Matter, Wageningen University & Research, Stippeneng 4, 6708 WE Wageningen, The Netherlands*

[2]*Laboratory of Phytopathology, Wageningen University & Research, Droevendaalsesteeg 1, 6708 PB Wageningen, The Netherlands.*

[3]*Laboratory of Cell Biology, Wageningen University & Research, Droevendaalsesteeg 1, 6708 PB Wageningen, The Netherlands.*

Introduction

Plant pathogens cause huge losses in crop yields with negative impacts on global food security and economy[1,2]. One such pathogen is *P. infestans*, the causal agent of late blight, which is responsible for yield losses estimated at 15–20% globally[3]. Despite breeding efforts, late blight remains challenging to combat mainly due to the high genetic adaptability of the pathogen[4]. Unlike *P. infestans*, *P. palmivora* and *P. capsici* have a broad host range and and cause many destructive diseases—for example, in cacao and oil palm plantations, and in numerous vegetable crops[5,6].

Many pathogens must gain forcible entry into their host for successful infection[7–11]. Fungal and oomycete plant pathogens face a substantial challenge as the plant features a protective surface consisting of a cuticle and rigid epidermal cell layers[7,9,12]. The mechanics of host entry have been studied in detail for the fungus Magnaporthe oryzae[12–15], which employs a brute-force approach: first it undergoes a switch from polar to non-polar growth to establish an appressorium, a specialized and melanin-fortified invasion structure[9] capable of building high turgor pressure[14,15] of up to 8 MPa. After adhering to the host surface[16], a penetration peg is ejected in the centre of the adhesion ring to pierce the host surface[13]. Appressorium-mediated invasion in fungi requires both melanins and septins[17–19]. Despite the notion that convergent evolution has provided fungi and oomycetes with similar weaponry to attack and colonize plants[8,20,21], oomycetes lack septins and melanin, ruling out invasion by brute force. How host entry is achieved by oomycetes remains elusive. Here we unravel the mechanics of host entry of *Phytophthora* spp. and show how these pathogens exploit hyphal slicing to facilitate host invasion, avoiding the need to form a fortified appressorium.

Results

We begin by observing that invasion of *P. infestans* into host tissues, represented here by etiolated stems of potato plantlets, consistently occurs by hypha indenting and subsequently invading host tissues at a distinct oblique angle (Fig. 3.1a and Supplementary Video 1). We determine the average angle of invasion, defined relative to the surface normal (Fig. 3.1b), as $\theta = 36.2 \pm 13.0$ deg. This is in contrast to true fungi, in which a penetration peg emerges from the centre of an adhesion ring and enters the host tissue along the substrate normal[13,15].

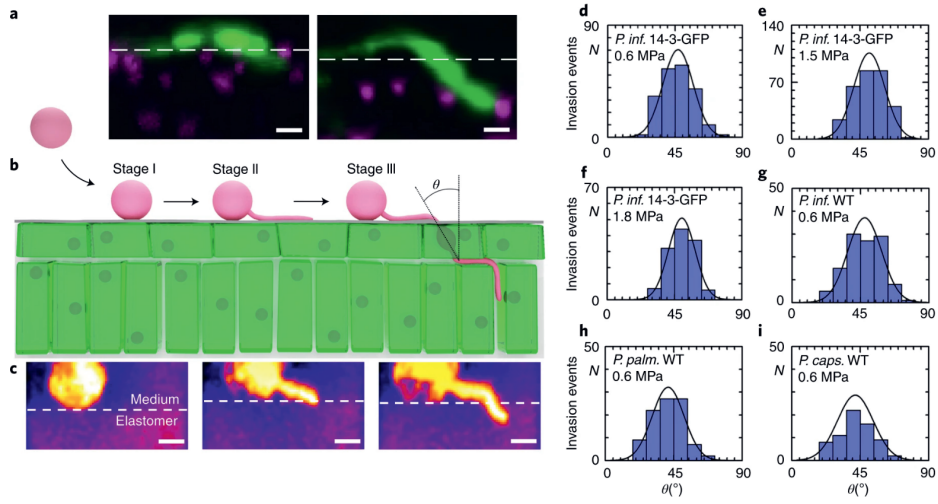

Figure 3.1. a, Two examples of the oblique angle of indentation and invasion of *P. infestans* 14-3-GFP on stems of potato plantlets (24 hpi) revealed by 3D confocal imaging (side view; GFP, green; host plastids, magenta; dotted line indicates the plant surface). b, Schematic illustration of host entry. Stage I: germination and non-invasive hyphal growth; stage II: substrate adherence and force application; stage III: surface fracture and invasion. c, Time series from confocal microscopy (side view) showing a single cyst (*P. infestans* 14-3-GFP) germinating and invading an elastomeric surface at an oblique angle (dotted line indicates elastomer–medium interface; Supplementary Video 1). d–i, Angle of invasion for *P. infestans* (*P. inf.*) 14-3-GFP (d–f), *P. infestans* WT (g), *P. palmivora* (*P. palm.*) (h) and *P. capsici* (*P. caps.*) (i) at the indicated substrate elasticity (in MPa). Substrate entry occurs at an angle of invasion (θ, x-axis) centred at 41–51$\deg$ (Supplementary Table 3) and is independent of the substrate elasticity. N (y-axis) is the number of invasion events monitored in several independent experiments. Scale bars, 5 μ m.

Artificial host mimics

To understand the significance of this observation, we continue our analysis on artificial hosts, where a full mechanical analysis is possible. We use polydimethylsiloxane (PDMS) substrates as a model surface, as it is transparent, hydrophobic (similar to the cuticle), and has elastic moduli in the range of reported leaf stiffnesses[22,23]. We observe that *P. infestans* invasion on these substrates occurs in a manner that is qualitatively similar to that on the natural hosts[24] (Fig. 3.1b); zoospores land on the substrate, encyst and develop a germ tube (stage I). The hypha then adheres to the substrate and applies an indentation pressure (stage II). This ultimately leads to surface fracture and host entry (stage III). Furthermore, invasion on these artificial substrates occurs at an oblique angle and without the

formation of a distinct appressorium (Fig. 3.1b and Supplementary Video 2). We determine that, for two *P. infestans* strains, 14-3-GFP[25] and wt[26], invasion into artificial substrates peaks at oblique invasion angles θ of approximately 49 ± 10deg and that this is independent of substrate stiffness (Fig. 3.1c–f). The same is observed for two other *Phytophthora* species, *P. palmivora* (wt)[27] ($\theta \approx 41 \pm 11$deg; Fig. 3.1g) and *P. capsici* (wt)[28] ($\theta \approx 42 \pm 12$deg; Fig. 3.1h).

Naifu invasion

From fracture mechanics it is known that oblique indentation, also known as slicing, can facilitate surface fracture[29] by localizing stresses at the surface and generating substantial tensile stresses. This effect is, for example, exploited in the single-bevel design of Japanese kitchen knives and guillotine blades to facilitate cutting. We hypothesize that *Phytophthora* spp. exploit hyphal slicing to invade their hosts without needing an appressorium. We call this the 'naifu' mechanism, after the Japanese word for knife. Our hypothesis leads to three testable predictions: (1) indentation leads to the propagation of a fracture along the direction of the applied force, which for oblique angles entails a crack that propagates ahead of the hypha; (2) to enable oblique application of force, unlike the radial symmetry observed in fungi, we should observe a polarized and non-concentric geometry of adhesion and indentation, lacking circular symmetry, that orients the force application vector; and (3) in turn, this is predicted to result in polarized surface deformations during pre-invasion (stage II) that are consistent with the angle of entry θ after invasion (stage III).

Molecular-fracture sensors

To visualize surface fracture, we incorporate the molecular mechanosensor spiropyran (Supplementary Figs. 3.3-7) into PDMS substrates. This sensor optically reveals mechanical damage by mechanochemical isomerization[30,31] (Fig. 3.2a). Invasion of *P. infestans* into these fracture-reporting surfaces reveals the predicted scenario; approximately 10–20 min after the start of pressure application, a fluorescent crack propagates ahead of the germ tube (Fig. 3.2b, Extended Data Fig. 3.9 and Supplementary Video 3), in agreement with our hypothesis of oblique angles, into which the pathogen enters.

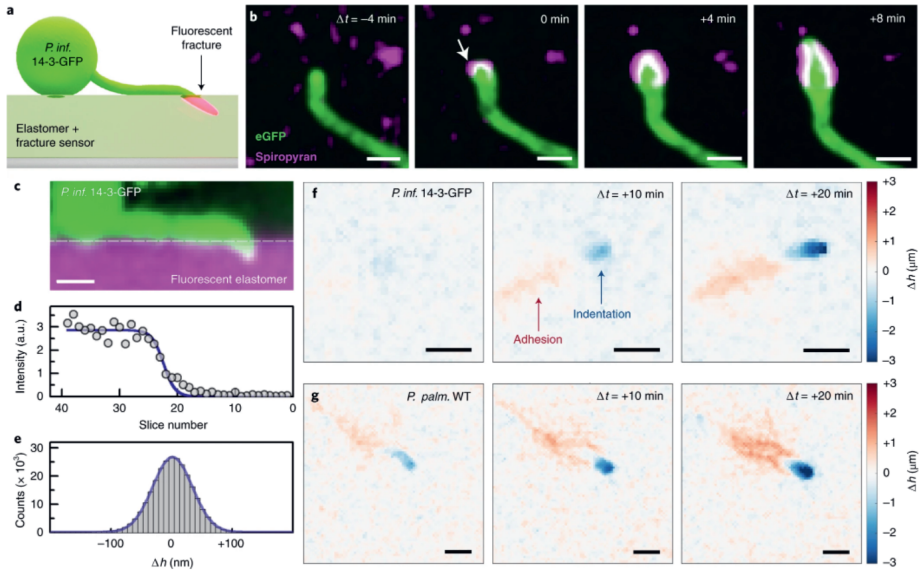

Figure 3.2. a, Illustration of crack visualization using the fluorogenic mechanosensor spiropyran, which reports mechanical damage. b, Time-lapse recording of invasion by *P. infestans* 14-3-GFP (green) shows how a surface crack (magenta), visualized by mechanoactivation of spiropyran, grows ahead of the growing germ tube consistent with oblique pressure application (Supplementary Video 2), with t = 0 defined as the moment of crack nucleation. The arrow indicates the nucleus of the surface crack. c, Confocal fluorescence image (side view) of a germ tube of *P. infestans* 14-3-GFP (green) indenting a fluorescent elastomer substrate. d, Example of an intensity profile (in arbitrary units, a.u.), measured in a single voxel, of substrate fluorescence in the h direction (symbols) fitted to a sigmoidal function (solid line) to the substrate height δh. e, The distribution of apparent height deviations of a flat elastomer substrate (grey bars) allows determination of the resolution in δh as the full-width at half-maximum of a Gaussian fit (solid line) at approximately 50 nm. f,g, Surface-deformation maps during invasion reveal the temporal increase in pressure application to induce fracture. Data reveal a polar mechanical geometry with separate adhesion and indentation sites, consistent with the naifu mechanism, for *P. infestans* 14-3-GFP (f) (Supplementary Video 3) and *P. palmivora* (wt) (g) (Supplementary Video 5). Scale bars, 5 μm.

Quantifying surface mechanics

To measure the surface deformations induced by the indentation pressure applied by the hypha, we fluorescently label the substrates. We use three-dimensional (3D) imaging (Fig. 3.2c) to measure the intensity profile across the substrate–medium interface in each pixel. By fitting these intensity profiles normal to the surface to a sigmoidal function, we extract the surface height δh (Fig. 3.2d) with an axial resolution of approximately 50 nm (Fig. 3.2e). The resulting surface-deformation maps reveal a highly polarized mechanical geometry as predicted (Fig. 3.2f,g) that breaks the concentric circular symmetry expected for invasion using an appressorium as utilized by fungi. We observe distinct and spatially separated zones of adherence (upward deformations) and indentation (downward deformations), the amplitude of which grow over time until the surface fractures and the pathogen gains entry. These phenomena are similar for both *P. infestans* strains (14-3-GFP: Fig. 3.2f, Extended Data Fig. 3.10 and Supplementary Video 4; and wt: Extended Data Fig. 3.12 and Supplementary Video 6), *P. palmivora* (wt) (Fig. 3.2g, Extended Data Fig. 3.11 and Supplementary Video 5) and *P. capsici* (wt) (Extended Data Fig. 3.13 and Supplementary Video 7). These results support our hypothesis and show that the naifu mechanism is conserved across *Phytophthora*. Cyst adhesion has no role in this process—we observe no adhesive (upward) deformations underneath the cysts (arrows in Extended Data Fig. 3.10). Moreover, invasion occurs only after substantial extension of hypha, which have an average length at invasion of 28 ± 8 μm and a minimum of 8 μm. This illustrates that the hypha itself is the invasion organ.

Mechanical equilibrium dictates that the indentation force Fi, and adhesive force Fa, are balanced. On this basis, we have developed a contact-mechanics model that describes naifu invasion (Fig. 3.3a). We model spatially separated, but mechanically coupled, adhesion and indentation sites onto which force is applied at an angle θ, equal to the angle of-invasion (Fig. 3.1c–h). We reduce our data (Fig. 3.2f) to a line profile of surface deformation δh(t) for each time point. We find quantitative agreement between data and model in the pre-fracture stages of invasion (Fig. 3.3b and Supplementary Video 8). This supports the notion that the polar invasion geometry emerges from the separation of an indentation site at the hyphal apex and a posterior site of adherence, separated by approximately 1-2 μm (parameter d in Supplementary Figs. 3.6 and 3.7). From these data, we compute the distribution of compressive and tensile stresses in the substrate (Fig. 3.3c), illustrating how oblique indentation localizes stresses towards the surface and gives rise to substantial tensile stresses (arrow in Fig. 3.3c) directed along the surface plane (Supplementary Fig. 3.8). We also note that the radius of curvature

at the indentation site, reflected by parameter a1 (Supplementary Figs. 3.6 and 3.7), is sharper than the average hyphal radius just posterior, hinting at morphological shaping of the apex to enhance stress localization. Combined, these effects lower the pressure required to induce a surface fracture[29].

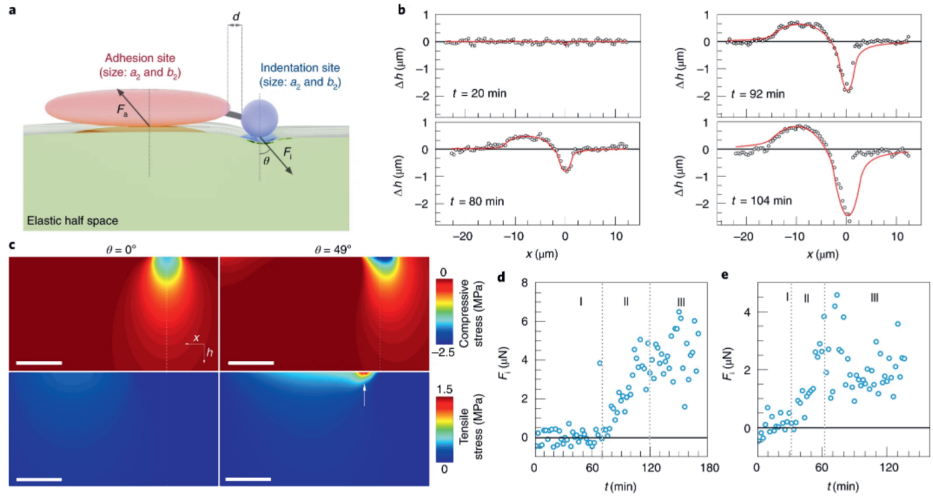

Figure 3.3. a, A linear-elastic contact-mechanics model for invasion by *Phytophthora* spp. b, Experimental surface-deformation profiles for *P. infestans* 14-3-GFP at various time points (t) during invasion (open circles) and corresponding fits to the mechanical model (solid lines) (see also Supplementary Video 7). c, Predicted stress distributions in the xh-plane in the substrate (surface located at top, indentor located at dotted line) on the basis of experimentally determined parameters, for indentation normal to the substrate (θ = 0deg) and under an oblique angle of θ = 49deg. Data show the maximal compressive and tensile stresses, taken as the maximum and minimum principal stress components. The arrow indicates a zone of tensile stress that emerges under oblique indentation. A full representation with all elements of the stress tensor is shown in Supplementary Information Fig. 3.8. d,e, Total indentation force F_i during invasion by *P. infestans* (d) and *P. palmivora* (e), obtained by fitting our model to experimental data, reveals three stages (see also Fig. 3.1a): a lag phase (I) followed by adherence and pressure application to induce fracture (II) and penetration into the substrate by crack growth (III). Scale bars, 5 μm.

The magnitude of the invasive force F_i follows from this analysis. Initially, non-invasive hyphal growth occurs without detectable forces on the substrate (phase I; Fig. 3.3d). A switch to invasive growth leads to an increase of F_i (phase II). After fracture, hyphae grow into the substrate at relatively constant pressure to advance the crack (phase III). Additional examples are shown in Extended Data Fig. 3.5. Forces are in the range of several μN, both for *P. infestans* (Fig. 3.3d) and for *P. palmivora* (Fig. 3.3e), and in agreement with forces reported for other pathogens[32–35]. We calculate the maximum pressure generated at the hypha–substrate contact at the moment of fracture to be approximately 0.3 MPa.

Disrupting naifu invasion

Naifu invasion involves several key steps: polarized hyphal growth, substrate adherence and polar force application. To ascertain the requirement for each of these steps, we perform a series of experiments in which each is individually inhibited. As a measure for invasiveness, we determine the percentage of hypha, counting only those with a length of at least 10 μm, that have successfully breached the substrate. As a reference, *P. infestans* wt, on untreated PDMS and in pure water, exhibits an invasion efficiency (IE) of 74 ± 11%, 2 h post-inoculation (hpi) (Fig. 3.4a,b,k).

First, we manipulate the cytoskeleton, as an orchestrator of cell polarity during tip growth of walled cells[36–38], using latrunculin B (LatB), which inhibits actin polymerization[39]. A low dose (0.1 μM) substantially reduces the IE to 34 ± 10% (Fig. 3.4k), whereas hyphal morphology is not affected (Fig. 3.4c,d); higher doses reduce IE further (Fig. 3.4k) and cause abnormal hyphal morphologies, as previously reported[39]. Treatment with LatB also slows down non-invasive hyphal growth (Fig. 3.4l); invasive growth is halted completely at 1 μM (Fig. 3.4k), while there is still finite non-invasive growth (Fig. 3.4l). This suggests an increased sensitivity to cytoskeletal disruption during invasion compared with non-invasive hyphal growth. In line with these observations, we observe that high doses of LatB also reduce infectivity on leaves (7 d post-inoculation (dpi); Extended Data Fig. 3.14). Clearly, actin is an essential coordinator of polarity both in non-invasive growth and in polar force generation during invasion, and thus crucial for naifu invasion.

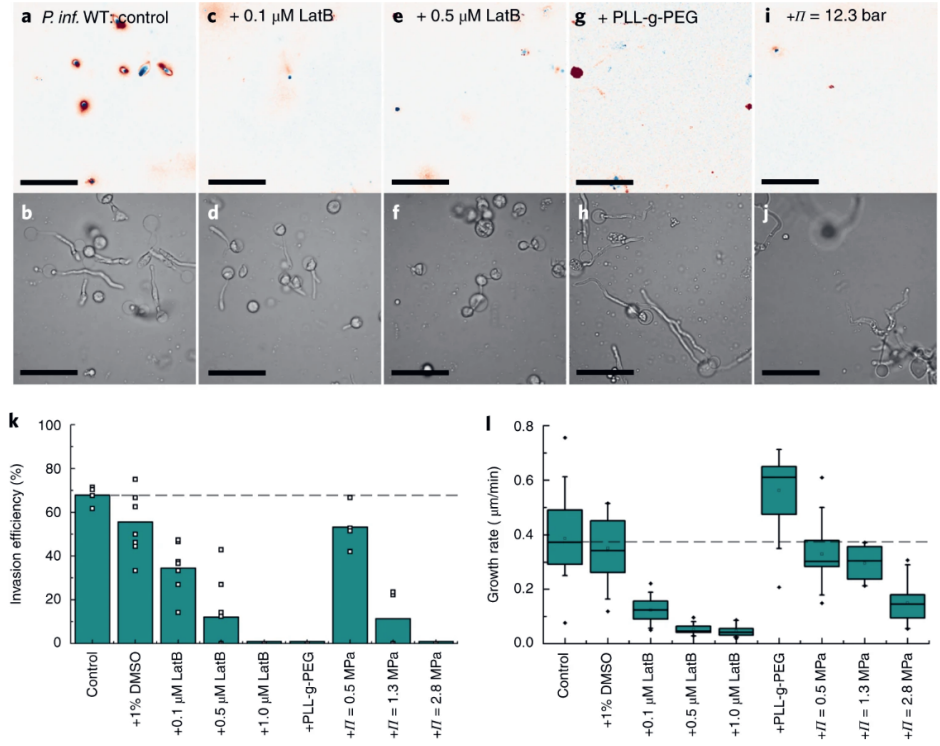

Figure 3.4. a–j, Surface-deformation profiles (a,c,e,g,i; colour code as in Fig. 3.2b,c) and corresponding bright-field images (b,d,f,h,j) of *P. infestans* WT invading PDMS surfaces, used to quantify invasion efficiency, subject to various treatments. Control (a,b), inhibition of actin polymerization with LatB (c–f), suppression of adhesion by coating PDMS with PLL-g-PEG copolymers (g,h) and inhibition of pressure generation by osmolyte treatment (i,j). Scale bars, 50 μm. k, The effect of these treatments on invasion efficiency, defined as the percentage of hypha >10 μm that breach the surface at 2 hpi. Dashed grey line indicates the mean value of the control. l, Effect of the same treatments on the rate of hyphal extension during non-invasive growth. In box plots, the centre line is the median, black diamonds show 1st and 99th percentiles, box bounds delineate 25th and 75th percentiles, whiskers span 5th and 95th percentiles and the dotted line indicates the median of the control as reference.

Second, we suppress adhesion of hypha to the substrate, which is mediated by protein secretions[40] and necessary to balance the indentation force. Adherence is a crucial element of pathogenicity in various plant pathogens[16,41,42]. We modify substrates with a poly(l-lysine)-graft-poly(ethylene glycol) (PLL-g-PEG) copolymer[43], which is known to suppress adhesion of a wide variety of biomolecules[44,45]. Adhesion suppression results in complete inhibition of invasion (Fig. 3.4k) without inhibiting hyphal growth (Fig. 3.4g,h,l). A similar non-adhesion treatment on

leaves also results in a substantial reduction in infection efficiency at 7 dpi (Extended Data Fig. 3.14). These data confirm the necessity for strong host adherence in naifu invasion on both model substrates and real hosts.

Finally, we modulate the invasive pressure that *Phytophthora* can generate by increasing the osmotic pressure Π of the medium[14]. Turgor generation is well-established to be a pre-requisite for pathogen invasion. We observe strong suppression of invasion efficiency at $\Pi > 1.3$ MPa at 2 hpi (Fig. 3.4k). We also note that these high pressures lead to reduced growth rates (Fig. 3.4l) and a strong reduction in the germination efficiency (Fig. 3.4i,j). Generation of turgor is thus essential for invasion, with an estimated maximum turgor of between 1.3 and 2.8 MPa. This also illustrates that not all turgor is converted into pressure at the invasion site; the maximum invasion pressure of 0.3 MPa is approximately 10–20% of the maximum turgor, in agreement with findings for the oomycete *Pythium graminicola*[46].

Discussion

Our data provide a picture of the mechanical strategy of host entry by *Phytophthora*. We find that these oomycetes invade hosts by a naifu mechanism, in which polar force application under an oblique angle facilitates surface failure and mediates host entry. We also show how cell polarization, substrate adherence and turgor generation are essential for naifu invasion. Despite the common use of the term appressorium when referring to a hyphal swelling at the point of host entry by *Phytophthora* spp., our observations of polar force application and the hypha itself as the invasion organ are incompatible with the definition of appressoriogenesis as involving a switch from polar to non-polar growth and the establishment of a new cell identity[9]. These findings warrant a critical reflection of the use of the term appressorium when describing oomycete invasion mechanisms. Moreover, the naifu mode of entry is in distinct contrast to the brute-force approach used by fungi[12–15,32,47]. As a consequence, fungicides that suppress force generation in fungi, for example, by targeting melanin-biosynthesis pathways, are not effective in controlling oomycetes. We have shown how *Phytophthora* invasion can be inhibited by cytoskeletal disruption or by blocking adhesion. These insights could lead to the identification of new targets in the search for effective control measures.

Methods

Biological material

Phytophthora strains used in this study are *P. infestans* (14-3-GFP and wt) (88069), *P. palmivora* (wt) (Pp6390) and *P. capsici* (wt) (BYA5). Details and growth conditions are described in the Supplementary Information and Supplementary Table 1. Potato (*Solanum tuberosum*) cultivar Bintje is propagated on tissue culture medium as described previously[48]. To obtain etiolated plantlets, in vitro grown plants are decapitated and placed in the dark for 2–4 weeks. *Nicotiana benthamiana* Cf-4 sobir1/sobir1-like (Nb-sobir1)[49] plants are grown in soil in the greenhouse for 6 weeks and the youngest leaves (>3 cm in diameter) are collected for detached-leaf assays.

In planta observations

Shoots from etiolated potato plantlets are cut in stem sections of 1 cm in length. These are stained in toluidine blue (0.05 mg ml-1 in 10 mM HEPES, pH 7.4) for 30 min, and subsequently rinsed 3 times in water. Each stem section is transferred to a well (Ibidi micro-Slide 8 well, uncoated) filled with 0.5 ml of a *P. infestans* 14-3-GFP zoospore suspension (10^5 zoospores per ml). Then, 1 mm glass beads are added to the well to maneuver the stem section in the correct focal plane for imaging.

Artificial substrates

Elastomers are prepared by spin coating pre-mixed Sylgard 184 base:crosslinker mixtures in ratios 30:1 (0.6 MPa), 10:1 (1.5 MPa) and 5:1 (1.8 MPa) onto cleaned no. 1 coverslips at 2,000 rpm, resulting in 33 μm layers. The Young's modulus, the elastic constant for uniaxial tensile deformations, of the substrates is determined on a home-built indentation setup, described in detail elsewhere[50] (Supplementary Fig. 1 and Supplementary Table 2). Cysts are loaded onto the surfaces in a 70 μl droplet (10^5 cells per ml) and placed inside bespoke 3D-printed sample chambers to minimize evaporation.

Confocal fluorescence microscopy

Three-dimensional confocal images are recorded on a Nikon C2 CSLM, equipped with a ×60, 1.40 NA immersion objective, at a resolution of 512 × 512 pixels (212 × 212 μm2) in the xy plane and a 0.5 μm step size in the axial (z) direction, at a stack acquisition rate of 0.5 min-1. In all imaging experiments, we minimize the illumination intensity (2% of 15 mW at 488 nm and 4% at 15 mW at 561 nm)

as high light doses were found to inhibit germination and invasive growth. All confocal fluorescence images shown are false-coloured from greyscale raw data. Microscopy images shown in Fig. 3.1c and Extended Data Fig. 3.8a,b are shown with a fire lookup table to improve visual contrast.

Image analysis

To detect the germ tube in image analysis, we threshold and binarize images recording either the cytosolic GFP channel (for *P. infestans* 14-3-GFP) or inverted images recorded on non-fluorescent WT species (*P. infestans*, *P. palmivora* and *P. capsici*) invading fluorescently tagged PDMS. In each xy slice, the centroid of the germ tube is detected using the regionprops function in MatLab, from which the centroid contour of the germ tube can be reconstructed; the centroid contour is then used to determine the angle of invasion with respect to the substrate normal.

Molecular-fracture sensor

A functionalized spiropyran is used as a switch-on fluorescent fracture sensor. The molecule is synthesized by adapting the procedure of Davis et al.[30] and features two vinyl groups placed on opposite sides of the scissile spiro bond. This results in incorporation into the elastomer as a crosslinker during curing and ensures force transmission from the elastomer onto the mechanosensitive probe. We have validated that detection of merocyanine fluorescence emission is only due to mechanical activation by a control experiment using a spiropyran of the same chemical design that is not mechanically coupled to the PDMS network. After synthesis and purification, the dye is added to the uncured PDMS mixture at 10 mg probe per g PDMS mixture. Preparation and characterization of the surfaces and imaging experiments are conducted as described above. Due to the low emission intensity of these fluorogenic probes, images shown in the main text are subjected to a Fourier-space bandpass treatment (lower threshold: 2 pixels, upper threshold 40 pixels, applied homogeneously to all images and between images) to suppress spurious single-pixel noise; examples of non-bandpass-filtered images are shown in Supplementary Fig. 3.9 for reference.

Surface-deformation profiling

Fluorescent PDMS elastomer substrates are prepared by adding 15 μl of a 2 mM solution of Pyrromethene 650 (Exciton) in toluene for every gram of PDMS mixture. Substrates are spincoated as described above and prepared fresh before each experiment to minimize dye degradation during storage. Three-dimensional

image stacks of the elastomer–water interface during pathogen invasion are recorded at a resolution of 0.41 × 0.41 × 0.5 μm3 and an acquisition rate of 0.5 min-1. Image stacks are analysed in a custom MatLab routine to extract the surface profile; for each xy pixel, the z-intensity profile of the Pyrromethene 650 channel is fitted to a sigmoidal function to obtain the local surface height with a determined sub-pixel resolution of 50 nm (Fig. 3.2e and Supplementary Information).

Mechanical model of invasion

We model the contact mechanics of invasion by a minimal linear-elastic model that describes the force balance between the indentation force applied by the pathogen and the force of adherence to the substrate. The forces generated by the pathogen are described as a Hertzian stress distribution[51] over two elliptical regions—with characteristic dimensions ai and bi (with subscript i = 1 for indentation site and 2 for adhesion site)—which are spatially separated by a distance d, and mechanically coupled. The substrate is treated as a linear-elastic half space. In the calculations, the Poisson ratio of the elastomer is taken to be 0.45, its modulus 0.58 MPa, as determined experimentally, and pressure is applied at an oblique angle of 49deg. The model was fitted to the experimental data using the geometrical parameters and total indentation force Fi as adjustable parameters, using a simulated-annealing algorithm, described in the Supplementary Information. The good agreement between model and experimental data breaks down once a surface-fracture nucleates, since fracture leads to non-linear deformations not captured by the linear-elastic model; however, by fitting the adhesive portion of the deformation profiles an estimate of the applied force can still be obtained during this final phase of the mechanical invasion.

Latrunculin B treatment

To perturb the organized actin cytoskeleton of pathogens during invasion, we follow the procedure established in chapter 3 for *P. infestans*, which revealed a dose-dependent inhibition of germ tube growth upon exposure to the drug LatB, which suppresses actin polymerization[39,52]. LatB solubilized in DMSO is added to the zoospore suspension just before inoculation of the PDMS substrates to final concentrations of 0.1, 0.5 and 1.0 mM LatB and 1 vol% DMSO, and, as a control, 1 vol% DMSO without LatB. We determine the invasion efficiency as the percentage of germinated cysts that have successfully fractured the artificial surface at 2 hpi. The hyphal growth rate is determined from the average germ tube length at 2 hpi for all germinated cysts, both invasive and non-invasive, in the field of view.

Adhesion suppression

To observe the effect of adhesion on pathogen invasivity on PDMS substrates, we pre-treat the elastomeric surfaces with a PLL-g-PEG graft copolymer following established procedures[43] known to suppress biomolecular adhesion and biofouling[44,45]. After spin coating and curing, PDMS surfaces are briefly exposed to an oxygen plasma followed by incubation in a 0.1 mg ml-1 solution of the PLL-g-PEG polymer (SuSoS Surface Technology, backbone PLL: Mw = 24.7 kg mol-1, polydispersity index = 1.18, PEG grafts: molecular mass = 2.2 kg mol-1, grafting ratio = 3.2). After rinsing with deionized water, substrates are used to determine invasion efficiencies and hyphal growth rates as described above.

Osmotic counter pressure

We manipulate the maximum differential pressure between cell interior and exterior by adding PEG2000 as a calibrated osmolyte[53], as was done previously for fungi[14]. Osmolyte is added to cysts from a stock solution to achieve osmotic pressures of Π = 0.5 MPa (85 mM PEG2000), 1.3 MPa (128 mM PEG2000) and 2.8 MPa (170 mM PEG2000). The cyst–osmolyte mixtures are applied to fluorescent PDMS substrates and invasion efficiencies and hyphal growth rates are determined 2 hpi as described above.

Infection assays

Detached leaves of Nb-sobir1 plants are used to test the effects of LatB and surface adhesion on infection efficiency of *P. infestans*. Detached-leaf assays are performed as described[54]. Leaves are inoculated by applying 10 μl droplets of a *P. infestans* WT zoospore suspension (105 zoospores per ml) onto the abaxial side. For LatB treatment, LatB dissolved in DMSO is added to the zoospore suspension. The final concentrations are 1 or 0.1 μM LatB with 1% DMSO, and 1% DMSO without LatB and pure water as controls. For testing surface adhesion, a non-adhesive coating is sprayed on the abaxial side of the leaves prior to drop inoculation. The polymer, poly(ethylene glycol) methacrylate (PEGMA), was previously shown to suppress fungal pathogen adhesion to leaves[55]. It is similar to the PLL-g-PEG polymer described above, but instead of a cationic backbone (used for activated PDMS binding), PEGMA has a hydrophobic backbone and therefore binds better to the cuticle. PEGMA is prepared as described[55]. After spraying with a 10 wt% PEGMA solution in 80/20 water/isopropanol, the leaves are dried for 5 min, rinsed with deionized water and inoculated. Infection efficiency is determined at 7 dpi as the percentage of inoculated spots that show distinct lesions.

Reporting Summary

Further information on research design is available in the Nature Research Reporting Summary linked to this article.

Data availability

Raw data associated with the figures in this manuscript have been archived at https://doi-org.ezproxy.library.wur.nl/10.4121/14115461 and are publicly available at https://data.4tu.nl/articles/dataset/Data_underlying_the_publication_Phytophthora_pathogens_exploit_slicing_action_for_host_invasion/14115461. Source data are provided with this paper.

Code availability

All data analysis algorithms used to perform the work presented in this manuscript were written by the authors using MatLab (v.2018b) and have been made publicly available at https://github.com/jorissprakel/Phytopthora_invasion.

References

[1] Matthew C. Fisher, Daniel A. Henk, Cheryl J. Briggs, John S. Brownstein, Lawrence C. Madoff, Sarah L. McCraw, and Sarah J. Gurr. Emerging fungal threats to animal, plant and ecosystem health. *Nature*, 484(7393):186–194, apr 2012.

[2] Serge Savary, Laetitia Willocquet, Sarah Jane Pethybridge, Paul Esker, Neil McRoberts, and Andy Nelson. The global burden of pathogens and pests on major food crops. *Nature Ecology and Evolution*, 3(3):430–439, mar 2019.

[3] A. J. Haverkort, P. C. Struik, R. G.F. Visser, and E. Jacobsen. Applied biotechnology to combat late blight in potato caused by *phytophthora infestans*. *Potato Research*, 52(3):249–264, 2009.

[4] Brian J. Haas, Sophien Kamoun, Michael C. Zody, Rays H.Y. Jiang, Robert E. Handsaker, Liliana M. Cano, Manfred Grabherr, Chinnappa D. Kodira, Sylvain Raffaele, Trudy Torto-Alalibo, Tolga O. Bozkurt, Audrey M.V. Ah-Fong, Lucia Alvarado, Vicky L. Anderson, Miles R. Armstrong, Anna Avrova, Laura Baxter, Jim Beynon, Petra C. Boevink, Stephanie R. Bollmann, Jorunn I.B. Bos, Vincent Bulone, Guohong Cai, Cahid Cakir, James C. Carrington, Megan Chawner, Lucio Conti, Stefano Costanzo, Richard Ewan, Noah Fahlgren, Michael A. Fischbach, Johanna Fugelstad, Eleanor M. Gilroy, Sante Gnerre, Pamela J. Green, Laura J. Grenville-Briggs, John Griffith, Niklaus J. Grünwald, Karolyn Horn, Neil R. Horner, Chia Hui Hu, Edgar Huitema, Dong Hoon Jeong, Alexandra M.E. Jones, Jonathan D.G. Jones, Richard W. Jones, Elinor K. Karlsson, Sridhara G. Kunjeti, Kurt Lamour, Zhenyu Liu, Lijun Ma, Daniel MacLean, Marcus C.

Chibucos, Hayes McDonald, Jessica McWalters, Harold J.G. Meijer, William Morgan, Paul F. Morris, Carol A. Munro, Keith O'Neill, Manuel Ospina-Giraldo, Andrés Pinzón, Leighton Pritchard, Bernard Ramsahoye, Qinghu Ren, Silvia Restrepo, Sourav Roy, Ari Sadanandom, Alon Savidor, Sebastian Schornack, David C. Schwartz, Ulrike D. Schumann, Ben Schwessinger, Lauren Seyer, Ted Sharpe, Cristina Silvar, Jing Song, David J. Studholme, Sean Sykes, Marco Thines, Peter J.I. Van De Vondervoort, Vipaporn Phuntumart, Stephan Wawra, Rob Weide, Joe Win, Carolyn Young, Shiguo Zhou, William Fry, Blake C. Meyers, Pieter Van West, Jean Ristaino, Francine Govers, Paul R.J. Birch, Stephen C. Whisson, Howard S. Judelson, and Chad Nusbaum. Genome sequence and analysis of the Irish potato famine pathogen *Phytophthora infestans*. *Nature*, 461(7262):393–398, sep 2009.

[5] Laurens P.N.M. Kroon, Henk Brouwer, Arthur W.A.M. De Cock, and Francine Govers. The genus *Phytophthora* anno 2012. *Phytopathology*, 102(4):348–364, 2012.

[6] Sophien Kamoun, Oliver Furzer, Jonathan D. G. Jones, Howard S. Judelson, Gul Shad Ali, Ronaldo J. D. Dalio, Sanjoy Guha Roy, Leonardo Schena, Antonios Zambounis, Franck Panabières, David Cahill, Michelina Ruocco, Andreia Figueiredo, Xiao-Ren Chen, Jon Hulvey, Remco Stam, Kurt Lamour, Mark Gijzen, Brett M. Tyler, Niklaus J. Grünwald, M. Shahid Mukhtar, Daniel F. A. Tomé, Mahmut Tör, Guido Van Den Ackerveken, John McDowell, Fouad Daayf, William E. Fry, Hannele Lindqvist-Kreuze, Harold J. G. Meijer, Benjamin Petre, Jean Ristaino, Kentaro Yoshida, Paul R. J. Birch, and Francine Govers. The Top 10 oomycete pathogens in molecular plant pathology. *Molecular Plant Pathology*, 16(4):413–434, may 2015.

[7] Martin Bastmeyer, Holger B. Deising, and Clemens Bechinger. Force Exertion in Fungal Infection. *Annual Review of Biophysics and Biomolecular Structure*, 31(1):321–341, jun 2002.

[8] Maita Latijnhouwers, Pierre J.G.M. de Wit, and Francine Govers. Oomycetes and fungi: similar weaponry to attack plants. *Trends in Microbiology*, 11(10):462–469, oct 2003.

[9] Nicholas J Talbot. Appressoria, *Current Biology*, 29(5):144-146 mar 2019.

[10] Amir Sanati Nezhad and Anja Geitmann. The cellular mechanics of an invasive lifestyle. *Journal of Experimental Botany*, 64(15):4709–4728, 2013.

[11] Andrew J Foster and Nicholas J Talbot. Getting a grip on blast. *Nature Microbiology*, 5(12):1457–1458, dec 2020.

[12] Richard J Howard and Barbara Valent. BREAKING AND ENTERING: Host Penetration by the Fungal Rice Blast Pathogen *Magnaporthe grisea*. *Annu. Rev. Microbiol*, 50:491–512, 1996.

[13] Lauren S Ryder, Yasin F Dagdas, Michael J Kershaw, Chandrasekhar Venkataraman, Anotida Madzvamuse, Xia Yan, Neftaly Cruz-Mireles, Darren M Soanes, Miriam Oses-Ruiz, Vanessa Styles, Jan Sklenar, Frank L H Menke, and Nicholas J Talbot. A sensor kinase controls turgor-driven plant infection by the rice blast fungus. *Nature*, 574(7778):423–427, oct 2019.

[14] R. J. Howard, M. A. Ferrari, D. H. Roach, and N. P. Money. Penetration of hard substrates by a fungus employing enormous turgor pressures. *Proceedings of the National Academy of Sciences*, 88(24):11281–11284, 1991.

[15] Richard A. Wilson and Nicholas J. Talbot. Under pressure: investigating the biology of plant infection by *Magnaporthe oryzae*. *Nature Reviews Microbiology 2009 7:3*, 7(3):185–195, 2009.

[16] Raquel O. Rocha, Christian Elowsky, Ngoc T.T. Pham, and Richard A. Wilson. Spermine-mediated tight sealing of the *Magnaporthe oryzae* appressorial pore–rice leaf surface interface. *Nature Microbiology*, 5(12):1472–1480, dec 2020.

[17] Forrest G. Chumley and Barbara Valent. Genetic analysis of melanin-deficient, non-pathogenic mutants of *Magnaporthe grisea*. *Mol. Plant-Microbe Interact*, 3(3):135– 143, 1990.

[18] Tan Wang, Dandan Ren, Han Guo, Xue Chen, Pinkuan Zhu, Haozhen Nie, and Ling Xu. CgSCD1 is essential for melanin biosynthesis and pathogenicity of colletotrichum gloeosporioides. *Pathogens*, 9(2):1–16, 2020.

[19] Michael H. Wheeler and Alois Bell , A. Melanins and Their Importance in Pathogenic Fungi. *JAMA: The Journal of the American Medical Association*, 255(7):959, feb 1986.

[20] Nicholas P. Money, Christopher M. Davis, and J. P. Ravishankar. Biomechanical evidence for convergent evolution of the invasive growth process among fungi and oomycete water molds. *Fungal Genetics and Biology*, 41(9):872–876, 2004.

[21] Shaowu Meng, Trudy Torto-Alalibo, Marcus C. Chibucos, Brett M. Tyler, and Ralph A. Dean. Common processes in pathogenesis by fungal and oomycete plant pathogens, described with Gene Ontology terms. *BMC Microbiology*, 9(SUPPL. 1):1–11, feb 2009.

[22] Yusuke Onoda, Feike Schieving, and Niels P.R. Anten. A novel method of measuring leaf epidermis and mesophyll stiffness shows the ubiquitous nature of the sandwich structure of leaf laminas in broad-leaved angiosperm species. *Journal of Experimental Botany*, 66(9):2487–2499, may 2015.

[23] Lorna J. Gibson. The hierarchical structure and mechanics of plant materials. *Journal of The Royal Society Interface*, 9(76):2749–2766, nov 2012.

[24] Stephen C. Whisson, Petra C. Boevink, Shumei Wang, and Paul RJ Birch. The cell biology of late blight disease. *Current Opinion in Microbiology*, 34:127–135, 2016.

[25] Elysa J.R. Overdijk, Jeroen De Keijzer, Deborah De Groot, Charikleia Schoina, Klaas Bouwmeester, Tijs Ketelaar, and Francine Govers. Interaction between the moss *Physcomitrella patens* and *Phytophthora*: a novel pathosystem for live-cell imaging of subcellular defence. *Journal of Microscopy*, 263(2):171–180, aug 2016.

[26] MJ Pieterse, Eddy P Risseeuw, and Leen C Davidse. An in planta induced gene of *Phytophthora infestans* codes for ubiquitin. *Plant Molecular Biology*, 17:799–811, 1991.

[27] B. M. Morris, B. Reid, and N. A. R. Gow. Electrotaxis of zoospores of *Phytophthora palmivora* at physiologically relevant field strengths. *Plant, Cell and Environment*, 15(6):645–653, aug 1992.

[28] Jianqiang Miao, Meng Cai, Xue Dong, Li Liu, Dong Lin, Can Zhang, Zhili Pang, and Xili Liu. Resistance Assessment for Oxathiapiprolin in *Phytophthora capsici* and the Detection of a Point Mutation (G769W) in PcORP1 that Confers Resistance. *Frontiers in Microbiology*, 7(APR):1–14, apr 2016.

[29] E Reyssat, T Tallinen, M. Le Merrer, and L Mahadevan. Slicing softly with shear. *Physical Review Letters*, 109(24), 2012.

[30] Douglas A. Davis, Andrew Hamilton, Jinglei Yang, Lee D. Cremar, Dara Van Gough, Stephanie L. Potisek, Mitchell T. Ong, Paul V. Braun, Todd J. Martínez, Scott R. White, Jeffrey S. Moore, and Nancy R. Sottos. Force-induced activation of covalent bonds in mechanoresponsive polymeric materials. *Nature*, 459(7243):68–72, may 2009.

[31] Asha Dee N. Celestine, Brett A. Beiermann, Preston A. May, Jeffrey S. Moore, Nancy R. Sottos, and Scott R. White. Fracture-induced activation in mechanophore-linked, rubber toughened PMMA. *Polymer*, 55(16):4164–4171, aug 2014.

[32] Clemens Bechinger, Karl Friedrich Giebel, Martin Schnell, Paul Leiderer, Holger B Deising, and Martin Bastmeyer. Optical measurements of invasive forces exerted by appressoria of a plant pathogenic fungus. *Science*, 285(5435):1896–1899, 1999.

[33] Yiling Sun, Ayelen Tayagui, Heather Shearer, Ashley Garrill, and Volker Nock. A microfluidic platform with integrated sensing pillars for protrusive force measurements on neurospora crassa. In *Proceedings of the IEEE International Conference on Micro Electro Mechanical Systems (MEMS)*, volume 2018-Janua, pages 1116–1119. IEEE, jan 2018.

[34] Richard J. Howard and Neil A. R. Gow. *Biology of the Fungal Cell*. Springer Berlin Heidelberg, Berlin, Heidelberg, 2007.

[35] Ayelen Tayagui, Yiling Sun, David A. Collings, Ashley Garrill, and Volker Nock. An elastomeric micropillar platform for the study of protrusive forces in hyphal invasion. *Lab on a Chip*, 17(21):3643–3653, 2017.

[36] I. Brent Heath and Gero Steinberg. Mechanisms of hyphal tip growth: Tube dwelling amebae revisited. *Fungal Genetics and Biology*, 28(2):79–93, 1999.

[37] Franklin M. Harold. Force and compliance: Rethinking morphogenesis in walled cells. *Fungal Genetics and Biology*, 37(3):271–282, 2002.

[38] Olivier Gossot and Anja Geitmann. Pollen tube growth: Coping with mechanical obstacles involves the cytoskeleton. *Planta*, 226(2):405–416, 2007.

[39] Tijs Ketelaar, Harold J.G. Meijer, Marjolein Spiekerman, Rob Weide, and Francine Govers. Effects of latrunculin B on the actin cytoskeleton and hyphal growth in *Phytophthora infestans*. *Fungal Genetics and Biology*, 49(12):1014–1022, dec 2012.

[40] Andrea V. Robold and Adrienne R. Hardham. During attachment *Phytophthora* spores secrete proteins containing thrombospondin type 1 repeats. *Current Genetics*, 47(5):307–315, may 2005.

[41] Andrew M. Smith. *Biological Adhesives*. Springer International Publishing, Cham, 2016.

[42] A. R. Hardham and W Shan. *Plant Relationships (ed. Deising, H. B.)*. Springer Berlin Heidelberg, Berlin, Heidelberg, 2009.

[43] Seunghwan Lee and Janos Vörös. An Aqueous-Based Surface Modification of Poly(dimethylsiloxane) with Poly(ethylene glycol) to Prevent Biofouling. *Langmuir*, 21(25):11957–11962, dec 2005.

[44] M. Heuberger, T. Drobek, and N.D. Spencer. Interaction Forces and Morphology of a Protein-Resistant Poly(ethylene glycol) Layer. *Biophysical Journal*, 88(1):495–504, jan 2005.

[45] Rodolphe Marie, Jason P Beech, Janos Vörös, Jonas O Tegenfeldt, and Fredrik Höök. Use of PLL- g -PEG in Micro-Fluidic Devices for Localizing Selective and Specific Protein Binding. *Langmuir*, 22(24):10103–10108, nov 2006.

[46] Erin MacDonald, Laurie Millward, J.P Ravishankar, and Nicholas P Money. Biomechanical interaction between hyphae of two *Pythium* species (Oomycota) and host tissues. *Fungal Genetics and Biology*, 37(3):245–249, dec 2002.

[47] Kurt Mendgen and Holger Deising. Infection structures of fungal plant pathogens – a cytological and physiological evaluation. Technical Report 2, 1993.

[48] Sanwen Huang, Vivianne G. A. A. Vleeshouwers, Richard G. F. Visser, and Evert Jacobsen. An Accurate In Vitro Assay for High-Throughput Disease Testing of *Phytophthora infestans* in Potato. *Plant Disease*, 89(12):1263–1267, dec 2005.

[49] Wen R.H. Huang, Christiaan Schol, Sergio L. Villanueva, Renze Heidstra, and Matthieu H.A.J. Joosten. Knocking out SOBIR1 in *Nicotiana benthamiana* abolishes functionality of transgenic receptor-like protein Cf-4. *Plant Physiology*, 185(2):290, mar 2021.

[50] J. N.M. Boots, R. Fokkink, J. Van der Gucht, and T. E. Kodger. Development of a multi-position indentation setup: Mapping soft and patternable heterogeneously crosslinked polymer networks. *Review of Scientific Instruments*, 90(1):015–108, jan 2019.

[51] K. L. Johnson. *Contact Mechanics*. Cambridge University Press, may 1989.

[52] Kiki Kots, Harold J.G. Meijer, Klaas Bouwmeester, Francine Govers, and Tijs Ketelaar. Filamentous actin accumulates during plant cell penetration and cell wall plug formation in *Phytophthora infestans*. *Cellular and Molecular Life Sciences*, 74(5):909–920, 2017.

[53] Nicholas P Money2. Osmotic Pressure of Aqueous Polyethylene Glycols' Relationship between Molecular Weight and Vapor Pressure Deficit. *Plant Physiol*, 91:766–769, 1989.

[54] Vivianne G A A Vleeshouwers, Willem Van Dooijeweert, L C Paul Keizer, Luc Sijpkes, Francine Govers, and Leontine T Colon. A laboratory assay for *Phytophthora infestans*

resistance in various *Solanum* species reflects the field situation. *European Journal of Plant Pathology*, 105:241–250, 1999.

[55] Cindy Vallieres, Andrew L Hook, Yinfeng He, Valentina Cuzzucoli Crucitti, Grazziela Figueredo, Catheryn R Davies, Laurence Burroughs, David A Winkler, Ricky D Wildman, Derek J Irvine, Morgan R Alexander, and Simon V Avery. Discovery of (meth)acrylate polymers that resist colonization by fungi associated with pathogenesis and biodeterioration. *Sci. Adv*, 6, 2020.

Supporting information

Supplementary Information for:

A slicing mechanism facilitates host entry by *Phytophthora* pathogens

Jochem Bronkhorst[1], *Michiel Kasteel*[2,3], *Stijn van Veen*[1], *Jess M. Clough*[1], *Kiki Kots*[2,3], *Jesse Buijs*[1], *Jasper van der Gucht*[1], *Tijs Ketelaar*[3], *Francine Govers*[2] *& Joris Sprakel*[1,*]

[1]*Physical Chemistry and Soft Matter, Wageningen University & Research, Stippeneng 4, 6708 WE Wageningen, The Netherlands*

[2]*Laboratory of Phytopathology, Wageningen University & Research, Droevendaalsesteeg 1, 6708 PB Wageningen, The Netherlands.*

[3]*Laboratory of Cell Biology, Wageningen University & Research, Droevendaalsesteeg 1, 6708 PB Wageningen, The Netherlands.*

[*]Correspondence to: joris.sprakel@wur.nl

List of Supplementary Videos

- *All movies available on the website of the original publication.*

- *SupplementaryVideo1.avi*
  Three-dimensional reconstruction of *P. infestans* invasion into a potato stem: several fluorescent pathogens (*P. infestans* – 14:3 GFP, in green) invade the stem of an etiolated potato cultivar (Bintje), with plant plastids shown in pink, at distinct oblique angles. Scale: the 3D volume has a size of 130 μm (length) x 60 μm (width) x 50 μm (height). Stem surface is located at approximately 35 μm from the base of the volume.

- *SupplementaryVideo2.avi*
  Side view of *P. infestans* invasion into an elastomer substrate: Time-series of maximum intensity projections in the XZ-plane showing the invasion of *P. infestans* – 14:3 GFP (green) into a fluorescent elastomer substrate (red).

- *SupplementaryVideo3.avi*
  Top view of *P. infestans* invasion into a fracture-reporting substrate: Time-series of maximum intensity projections of *P. infestans* – 14:3 GFP (green) invasion in a fracture-reporting elastomer surface, which is covalently modified to carry the molecular mechanosensor spiropyran (magenta). This movie reveals the initial stage of surface fracture nucleation.

- *SupplementaryVideo4.avi*
  Surface deformation maps for *P. infestans - 14:3 GFP* invasion: Right panel: Time-series of reconstructed surface deformation maps for *P. infestans* – 14:3 GFP invasion into a fluorescent elastomer substrate. Color bar indicates surface deformation height in micrometers. Left panel: corresponding GFP channel.

- *SupplementaryVideo5.avi*
  Surface deformation maps for *P. palmivora - wt* invasion: Right panel: Time-series of reconstructed surface deformation maps for *P. palmivora* – wt invasion into a fluorescent elastomer substrate. Color bar indicates surface deformation height in micrometers.

- *SupplementaryVideo6.avi*
  Surface deformation maps for *P. infestans - wt* invasion: Right panel: Time-series of reconstructed surface deformation maps for *P. infestans* – wt invasion into a fluorescent elastomer substrate. Color bar indicates surface deformation height in micrometers. Left panel: corresponding brightfield

channel (black box indicates corresponding area for surface deformation analysis).

- *SupplementaryVideo7.avi*
  Surface deformation maps for *P. capsici - wt* invasion: right panel: Time-series of reconstructed surface deformation maps for *P. capsici* – wt invasion into a fluorescent elastomer substrate. Color bar indicates surface deformation height in micrometers.

- *SupplementaryVideo8.avi*
  Fitting of surface deformation profiles with model: Time-series of surface deformation profiles (symbols) and fits to the mathematical model (lines) for *P. infestans* – 14:3 GFP invasion into a fluorescent elastomer substrate.

Oomycete strains and growth conditions

P. infestans transformant expressing cytosolic GFP (*P. infestans* 14:3 GFP)[1] was grown on a Rye, Sucrose (2%), Agar (1.5 % technical agar) culture media plate containing 20 μg/mL Vancomycin, 100 μg/mL Ampicillin, 10 μg/mL Amphotericin A and 5 μg/mL Geneticin (RSA-VAAG) in the dark and wrapped in plastic tape. Inoculated plates were incubated by transferring an $\approx$ 5x5 mm square piece of material from an older plate upside-down onto a fresh RSA-VAAG plate, leaving it for 10-14 days at 20°C to grow before inducing zoospore release. After 10-14 days, zoospore release was achieved by flooding with 10 mL of 4°C sterilized water and then left in a walk-in refrigerator at 4 °C for 3 hours. Samples were removed from the fridge, brought to room temperature and gyrated slowly to release the zoospores. All samples were encysted, and 5x/10x diluted with sterilised milli-Q or tap water for experimental use. *P. infestans-88069 (wt)* [2] was grown in the same way, but on RSA-VAA medium without Geneticin since this is the transformant selection marker.
P. palmivora-Pp6390 (wt) [3] was grown on a (20%) V8-VAA medium (10% V8 juice, 1 g/l $CaCO_3$, 1.5% technical agar) with 20 μg/mL Vancomycin, 100 μg/mL Ampicillin and 10 μg/mL Amphotericin A. *P. palmivora* was incubated at 25 °C and in continuous high light conditions. Surgical tape was used to close off the petridishes (with nocken), while an excess of evaporated water aggregated inside of the dishes onto the mycelium could pre-empt zoospore release. It was incubated under culture conditions 4-5 days before inducing zoospore release. *P. palmivora* was immersed with 10 ml of sterilised room temperature tap water and left for 30 minutes at room temperature. The plate was slowly gyrated after 30 minutes to resuspend zoospores, encysted and 5x diluted using sterilised tap water.
P. capsici - BYA5 (wt) [4] was grown on a (10%)V8 medium (10% V8 juice, 1 g/l CaCO3, 1.5% technical agar). It was incubated at 25 °C, with a 4 day dark, 4 day light regime to induce sporangium formation. Zoospore release was initiated by flooding the sample with 10 ml sterilised tap water, spending 30 minutes in cold temperatures (4°C) followed by 30 minutes at room temperature.
After releasing, zoospores were encysted using manual shaking for 1 minute (foam forms on top of the solution) directly sporulation. The resulting cyst concentration in the stock suspension was adjusted using 5x/10x dilution to approximately 10^5 cysts/ml.

Table 3.1. Summary of growth conditions of all used *Phytophthora* species and strains. $\mathbf{T}_{inc}$ is the incubation temperature, $\mathbf{t_{inc}}$ is the growth time in the incubator. * is incubator light conditions during growth with 4 days in dark, 4 days in light.

Species - strain	Medium	$\mathbf{T}_{inc}$ (°C)	$\mathbf{t_{inc}}$ (days)	Sporulation induction (hr)
P. infestans - 14:3 GFP	RSA-VAAG5	21	10	3
P. infestans - 88069 (wt)	RSA-VAA	21	10	3
P. palmivora - Pp6390 (wt)	(10%) V8-VAA	25	3-4	0.5
P. capsici - BYA5 (wt)	(10%) V8	25	8*	1 (.5h 4C, .5h RT)

Artificial Substrates

Preparation

Artificial substrate production was performed as described in Chapter 2. In brief, PDMS was spincoated after mixing (Base, Crosslinker and dye stock solution) in various ratios (to vary stiffnesses) on cleaned glass slides (18x18mm Knittel glass#1 slides, cleaned with IPA, MQ water and N_2/O_2 plasma), placed in a vacuum vessel, cured overnight at 70°C in a bespoke 3D printed holder.

Mechanical characterisation

Mechanical characterisation was performed as described in Chapter 2. In brief, an indentor setup was used to obtain force-distance curves for a predefined geomtry, which was fitted with the Hertz model to obtain the modulus of the PDMS slab.

Imaging procedure

Imaging procedures were followed as described in Chapter 2. In brief, conditions were chosen in such a way to minimise any phototoxic effects, samples were contained in high-humidy chambers and images taken on a 60x Nikon Eclipse Ti2 Confocal Laser Scanning Microscope (CLSM).

Invasion angle measurements

To quantify the invasion angle of many invading microbes, we have developed an automated image analysis routine; code is available per request to the corresponding author. The input data is either a single .tif file that contains three-dimensional image data (xyz), usually from a tiled measurement to increase the number of invasion events per data set. For cytosolic GFP transformants the data is read as is; for wt-species which are not autofluorescent, we stain the PDMS substrate using Pyrromethene 650 and invert the images prior to analysis.

First, we select RoIs that contain a single organism; for each z slice, the image is cropped using the coordinates of the RoI, then filtered using a gaussian filter with a 2-D smoothing kernel with a standard deviation of 0.1, and finally binarized using a threshold that is 30% of the maximum intensity found in the image. The resulting optical sections through the germ tube appear as ellipsoidal shapes. These are recognised using the 'regionprops' function in MatLab, which identifies their centroid coordinate in the xy-plane for each z-slice. For each z slice, the coordinates of the center are compared to the coordinates of the center in the z slice directly above it; the distances are computed using Pythagoras theorem. From these distances, we can also compute, using geometry, the angle between the tube and the flat substrate. To determine the angle of invasion, we average over the first 5 z-slices just below the surface; this entails an average over 2.5 micrometers in the axial direction.

Molecular fracture sensor

A molecular fracture sensor was developed as described in Chapter 2. In brief, a spiropyran based crosslinker was synthesized that enablse us to visualize mechanical fracture in PDMS elastomers.

Synthesis

Synthesis of a mechano-sensitive spiropyran was performed as described in Chapter 2.

Surface deformation profiling

Surface deformation profiling was followed as described in Chapter 2. In brief, every pixel intesity through a z-stack shows decay in fluorescence intensity from at the PDMS(fluorescent)/water(non-fluorescent) interface. This decay function was

fitted with a sigmoidal function, with the centre decay point used as the sample height. A linear correction was used on the border to compensate for sample tilt (very minor, few micron over 212 micron window), after which the height map was transformed to a displacement map (subtracting the median height from each pixel).

Mechanical model

Model & fitting

The pathogen applies a pressure to the substrate by generating pushing forces in a localized region with its tip. To indent and penetrate the substrate, this pushing force must be balanced by a force in the opposite direction brought about by an adhesion site. The total indentation force $\mathbf{F}_\mathrm{i}$ applied to the indentation site can be decomposed in a normal force $P_\mathrm{i} = F_\mathrm{i} \cos\theta$ and a tangential force $Q_\mathrm{i} = F_\mathrm{i} \sin\theta$, where θ is the angle of indentation. Mechanical equilibrium implies that these forces are balanced by forces in the adhesion site $P_\mathrm{a} = -P_\mathrm{i}$ and $Q_\mathrm{a} = -Q_\mathrm{i}$. We treat the elastic substrate as a linear elastic solid, characterized by a shear modulus G and a Poisson ratio ν, and assume that both the tip and the adhesion region of the pathogen can be described as indenters with an ellipsoidal shape. This allows us to model the forces generated by the pathogen as a Hertzian stress distribution applied over elliptical regions [6]:

$$\mathbf{p}_\mathrm{i}(x,y) = \frac{3\mathbf{F}_\mathrm{i}}{2\pi a_\mathrm{i} b_\mathrm{i}} \left[1 - \left(\frac{x - x_{c,\mathrm{i}}}{a_\mathrm{i}} \right)^2 - \left(\frac{y - y_{c,\mathrm{i}}}{b_\mathrm{i}} \right)^2 \right]^{1/2} \tag{3.1}$$

in the indentation site, i.e. within the region bounded by the ellipse

$$\left(\frac{x - x_{c,\mathrm{i}}}{a_\mathrm{i}} \right)^2 + \left(\frac{y - y_{c,\mathrm{i}}}{b_\mathrm{i}} \right)^2 \leq 1 \tag{3.2}$$

where $x_{c,\mathrm{i}}$ and $y_{c,\mathrm{i}}$ denote the coordinates of the center of the indentation site, and a_i and b_i the length and width of the indentation site, respectively. Similarly, for the adhesion site

$$\mathbf{p}_\mathrm{a}(x,y) = -\frac{3\mathbf{F}_\mathrm{i}}{2\pi a_\mathrm{a} b_\mathrm{a}} \left[1 - \left(\frac{x - x_{c,\mathrm{a}}}{a_\mathrm{a}} \right)^2 - \left(\frac{y - y_{c,\mathrm{a}}}{b_\mathrm{a}} \right)^2 \right]^{1/2} \tag{3.3}$$

for

$$\left(\frac{x - x_{c,\mathrm{a}}}{a_\mathrm{a}}\right)^2 + \left(\frac{y - y_{c,\mathrm{a}}}{b_\mathrm{a}}\right)^2 \leq 1 \tag{3.4}$$

Here, the x-axis is taken in the direction of the tangential force, corresponding to the axis through the centers of the indentation and adhesion sites, so that $y_{c,\mathrm{i}} = y_{c,\mathrm{a}} = 0$. The total stress distribution at the surface is $\mathbf{p}(x, y) = \mathbf{p}_\mathrm{i}(x, y) + \mathbf{p}_\mathrm{a}(x, y)$ and has normal and tangential components, as specified by the angle θ.

Within linear elasticity theory, the three-dimensional displacement $\mathbf{u}$ (with components u_x, u_y, and u_z) at any point in the elastic material due to this applied stress distribution can be found by integration:

$$\mathbf{u}(x, y, z) = \int\int \mathbf{G}(x - x', y - y', z)\mathbf{p}(x', y')\mathrm{d}x'\mathrm{d}y' \tag{3.5}$$

where $\mathbf{G}(x - x', y - y', z)$ is the Green's function that gives the response at position (x, y, z) due to a concentrated force at (x', y', z'). For the normal component of the force p_z, this is given by the Boussinesq relations [6]:

$$G_{xz}(x, y, z) = \frac{p_z}{4\pi G}\left[\frac{xz}{\rho^3} - (1 - 2\nu)\frac{x}{\rho(\rho + z)}\right] \tag{3.6}$$

$$G_{yz}(x, y, z) = \frac{p_z}{4\pi G}\left[\frac{yz}{\rho^3} - (1 - 2\nu)\frac{y}{\rho(\rho + z)}\right] \tag{3.7}$$

$$G_{xz}(x, y, z) = \frac{p_z}{4\pi G}\left[\frac{z^2}{\rho^3} + \frac{2(1 - \nu)}{\rho}\right] \tag{3.8}$$

with $\rho = \sqrt{x^2 + y^2 + z^2}$. For the tangential component q_x (in the x-direction) this is given by the Cerruti relations [6]:

$$G_{xx}(x, y, z) = \frac{q_x}{4\pi G}\left[\frac{1}{\rho} + \frac{x^2}{\rho^3} + (1 - 2\nu)\frac{1}{\rho + z} - \frac{x^2}{\rho(\rho + z)^2}\right] \tag{3.9}$$

$$G_{yx}(x, y, z) = \frac{q_x}{4\pi G}\left[\frac{yz}{\rho^3} - (1 - 2\nu)\frac{xy}{\rho(\rho + z)^2}\right] \tag{3.10}$$

$$G_{xx}(x, y, z) = \frac{q_x}{4\pi G}\left[\frac{xz}{\rho^3} + (1 - 2\nu)\frac{x}{\rho(\rho + z)}\right] \tag{3.11}$$

Using equations 1–9, we obtain the full displacement profile in the solid by numerical integration for given $\mathbf{F}_\mathrm{i}$, $x_{c,\mathrm{i}}$, $x_{c,\mathrm{a}}$, a_i, b_i, a_a and b_a. The displacement at the surface follows by setting $z = 0$ in equations 3.6-3.11.

The stress tensor at position (x, y, z) is obtained using Hooke's law:

$$\sigma_{ij} = \lambda \delta_{ij} u_{k,k} + \mu \left(u_{i,j} + u_{j,i} \right) \tag{3.12}$$

where $\lambda = 2G\nu/(1-2\nu)$ and $\mu = G$ are the Lamé coefficients, δ_{ij} is Kronecker's delta function and where the spatial derivatives $u_{i,j}$ are obtained from the displacement profile $u_i(x, y, z)$ by numerical differentiation. The principal stresses, finally, are obtained as the eigenvalues of the stress tensor. In our calculations, we have taken a Poisson ratio $\nu = 0.45$ and a Young's modulus $E = 0.58$ MPa, as measured (see section 'Substrates') corresponding to a shear modulus $G = E/2(1 + \nu) = 0.23$ MPa. The angle of invasion was fixed at the angle determined experimentally (see section 'Invasion angle measurements') at $\theta = 49°$.

The mechanical model was fitted to the experimental data using only the geometrical parameters and the total indentation force as the adjustable parameters. Since the set of equations is highly non-linear we adopted a simulated-annealing approach to fit model to experimental profiles. In the fitting procedure, a Monte Carlo algorithm creates a random mutation to the fit parameters and determines the Sum-of-Squares error between fit and data. If the SoS is reduced with respect to the previous iteration, the change is accepted. If the SoS increases, it is accepted with a 'Boltzmann' probability; this step is ensured to enable the escape from local fitting minima. For each curve, the routine is repeated for 10000 iterations to achieve an optimal fit result. Convergence of the model to the experimental data is usually observed within 1000-2000 steps.

Inhibiting polarized growth by LatB

To verify the role of the actin cytoskeleton in the mechanical invasion of *Phytophthora* spp. we perform experiments in the presence of the actin depolymerizing drug Latrunculin B (LatB). Previous work has indicated that LatB doses of >250 nM suppresses the formation of actin cables in *P. infestans*, while lower doses slow down polarised growth substantially [8,9]. Here we study the force generation capacity of *P. infestans - wt* in the presence of 100 nM, 500 nM and 1 μM Latrunculin B, in the presence of 1% DMSO to solubilize the drug. As controls, we also study the invasion of the same species in pure medium (sterilized tap water) and in medium with 1% DMSO without LatB. In all experiments, to 500 μL of diluted cyst suspension we add the desired amount of LatB from a stock solution in DMSO, ensuring a final DMSO concentration with respect to medium of 1%. The treated cyst suspension is used to inoculate fluorescent PDMS elastomer substrates ($E = 0.58$ MPa), which are left for 2h before commencing the imaging (2 hours post-inocculation, 2hpi), as described above.

Inhibiting substrate adhesion

Force balance dictates that the downward pressure applied by the pathogen onto its host to achieve entry must be balanced by an upward force of equal magnitude. Balance can only be accomplished by adhesion of the germ tube onto the substrate, also revealed by our surface deformation mapping. Suppression of adhesion logically should prevent the application of indentation pressure and thus stop mechanical host entry. To test this hypothesis, we have coated our PDMS surfaces with a pLL-g-PEG [10] polymer that results in a strongly hydrated and hydrophilic surface, which is known to effectively suppress adhesion of biomolecules and microbes. The coating follows established procedures for PDMS [10]; first we expose the PDMS substrates to oxygen/nitrogen plasma to activate the PDMS and generate anionic binding groups. Then, the activated slides are coated with the pLL-g-PEG polymers by spincoating 150 μL of a 0.1 mg/ml solution of pLL-g-PEG in HEPES buffer (pH=7.4) onto the substrate. This resulted in a obvious change in the contact angle of water droplets, turning the hydrophobic PDMS very hydrophillic. These substrates were inoculated as described above and imaging performed 2hpi.

Inhibiting turgor generation

The proposed main force generation method requires a high turgor pressure, in line with observations of filamentous plant pathogens [11,12]. A common method to assess internal turgor pressure of invasive phytopahtogens is the usage of PEG [11] to decrease the pressure differential between cell and surroundings. According tot the Van't Hoff law, osmotic pressure decreases when the concentration of osmolytes between inside and outside the cells becomes more equal. We used a 400 g/l PEG-2000 stock solution (0.2M) and MQ water to dilute cyst suspensions to assess the effect of high surrounding turgor on the invasion process. To clarify, we added the osmolytes only after sporulation and encystment steps to ensure that the difference between control and treated cells is only present at the invasion stage, not during sporulation itself. After addition of the high turgor pressures we deposited the cysts on the PDMS surfaces for 2 hours before commencing the imaging, as described above. All measurements were done under standard PDMS modulus (0.58 MPa).

Code availability

All codes used in this study are available on GitHub, when following this link. If the linking does not work: https://github.com/jorissprakel/Phytopthora_invasion.

Additional data

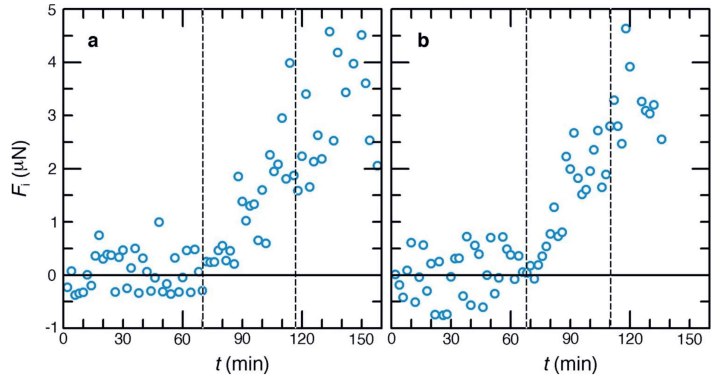

Figure 3.5. Two additional examples of total indentation force F_i as a function of time (t) for the mechanical invasion of *P. infestans - 14:3 eGFP* into 0.58 MPa elastomer substrates, exhibiting three temporal stages (see Fig. 1a): I) germ tube growth is observed but no detectable surface deformations occur, II) pressure application increases until a fracture nucleates, III) pathogen invades into the crack opening, during which the crack propagates at relatively constant force.

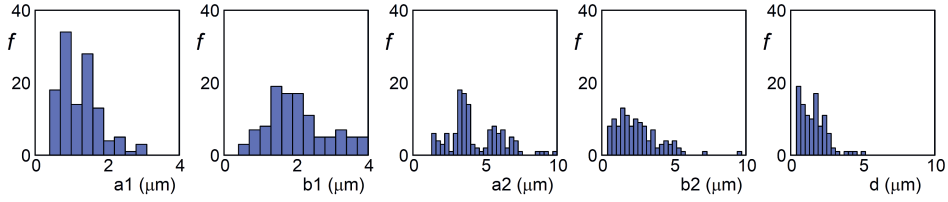

Figure 3.6. Aggregated data for the geometrical features of indentation (a_1 and b_1) and adhesion sites (a_2 and b_2) and connection distance d from fitting of time-series of surface deformation profiles for 3 *P. infestans - 14:3 GFP* invaders.

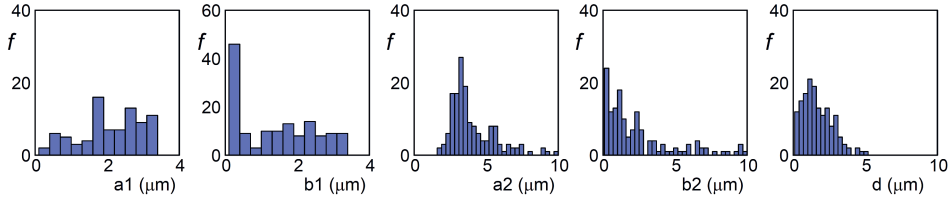

Figure 3.7. Aggregated data for the geometrical features of indentation (a_1 and b_1) and adhesion sites (a_2 and b_2) and connection distance d from fitting of time-series of surface deformation profiles for 3 *P. palmivora - wt* invaders.

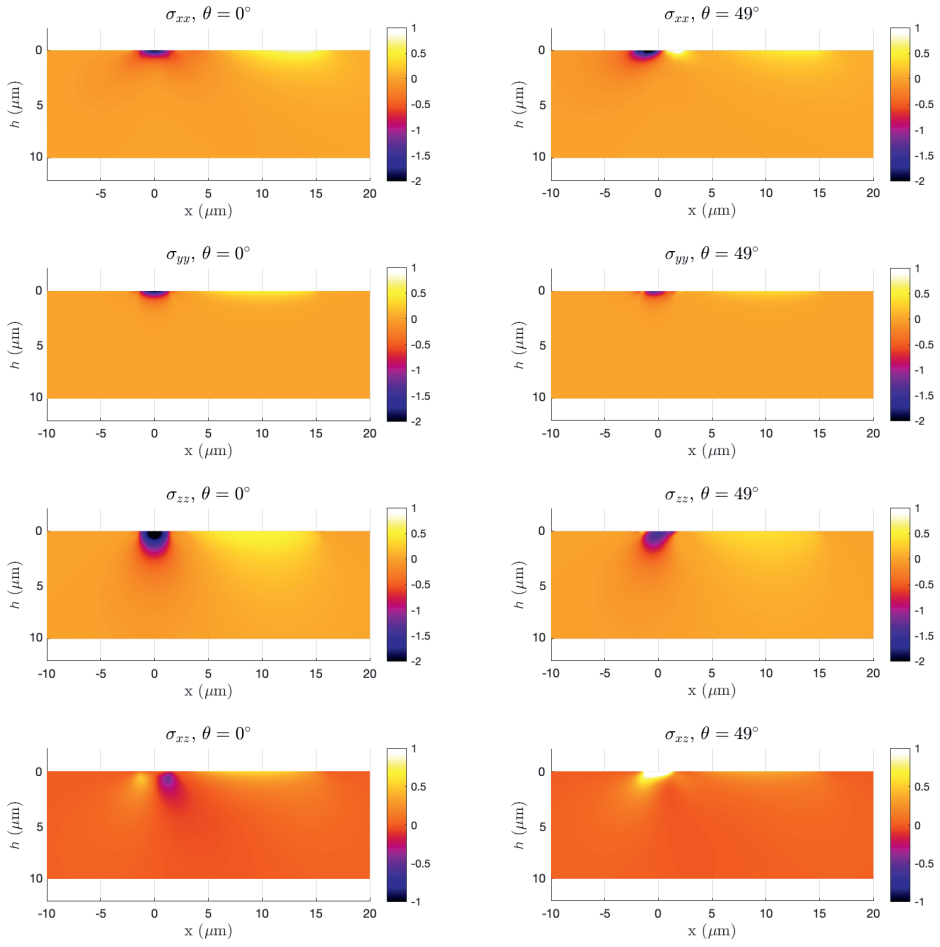

Figure 3.8. Calculated stress fields (unit MPa) inside the substrate upon naifu-indentation. These data are the result of first fitting our model to experimental surface deformation profiles to extract the geometrical parameters and the applied force, which together with the independently measured substrate modulus, is used to predict stress fields in all primary components of the stress tensor (sample: *P. infestans-wt* at the moment just prior to surface fracture).This data is an accompaniment to main text Figure 3c. Substrate interface is located at $z = 0$, indentation site at $(x = 0, z = 0)$.

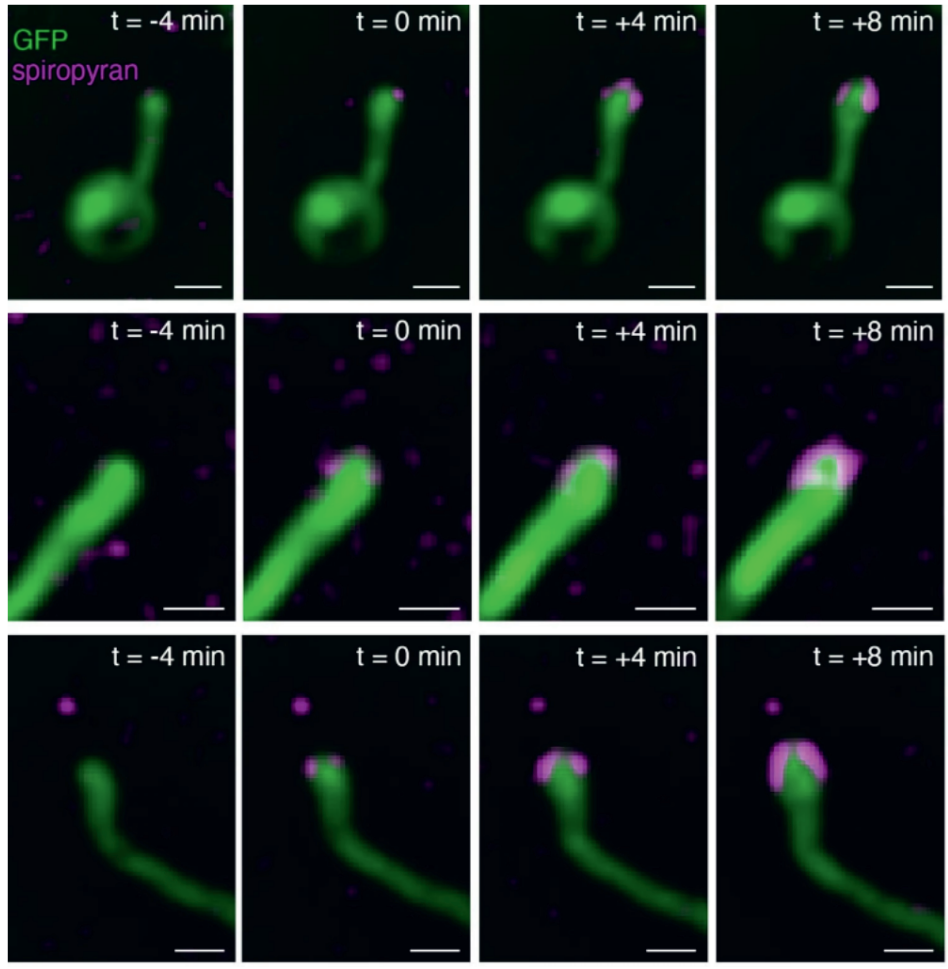

Figure 3.9. Additional examples of spiropyran fracture sensor activation by invasion of *P. infestans - 14:3 GFP* into a force-sensor elastomer substrate. GFP in green, spiropyran in magenta.

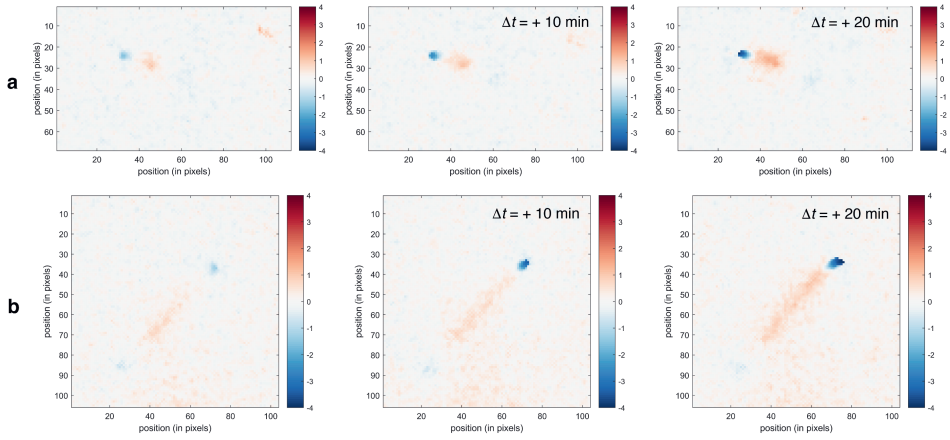

Figure 3.10. Two additional examples of time series of surface deformation patterns during invasion of *P. infestans - 14:3 GFP*; surface deformations in micrometers.

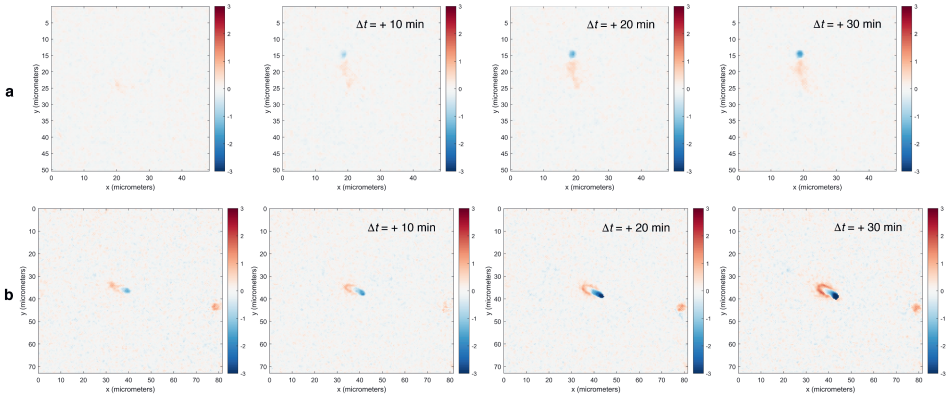

Figure 3.11. Two additional examples of time series of surface deformation patterns during invasion of *P. palmivora - wt*; surface deformations in micrometers.

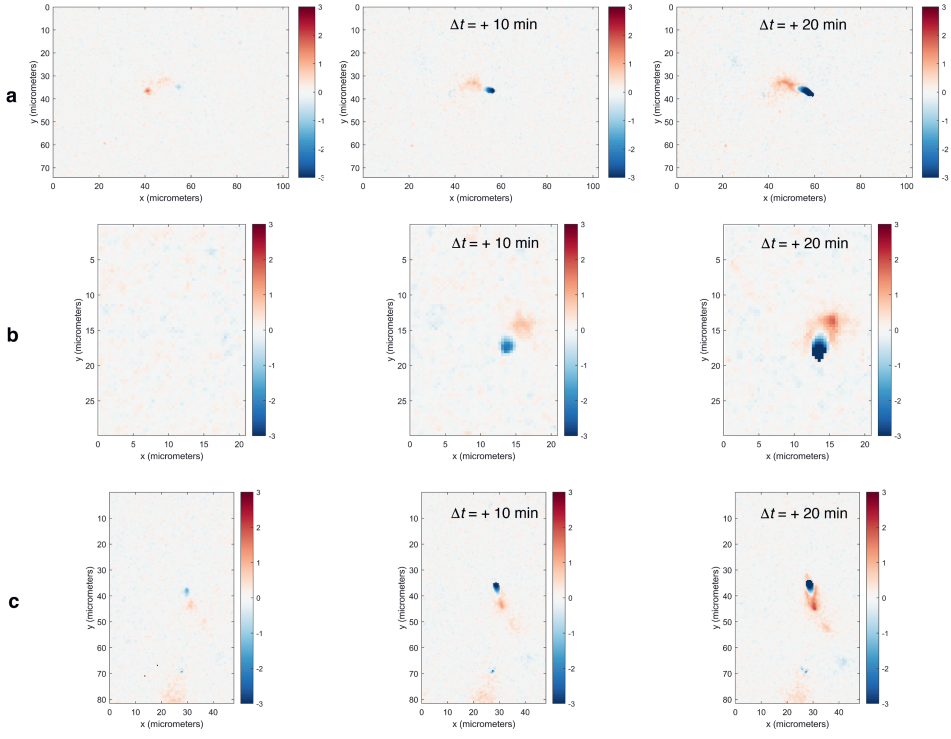

Figure 3.12. Three examples of time series of surface deformation patterns during invasion of *P. infestans - wt* which also exhibits a similar assymetric pattern of adherence and indentation; surface deformations in micrometers.

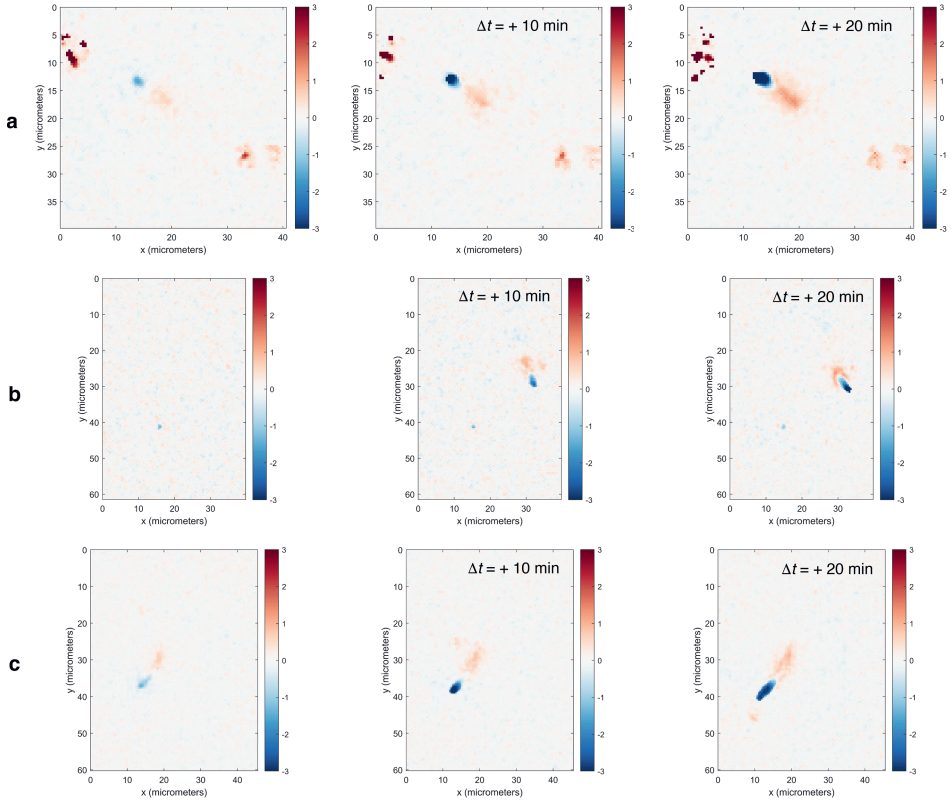

Figure 3.13. Three examples of time series of surface deformation patterns during invasion of *P. capsici* - *wt* which also exhibits a similar assymetric pattern of adherence and indentation; surface deformations in micrometers.

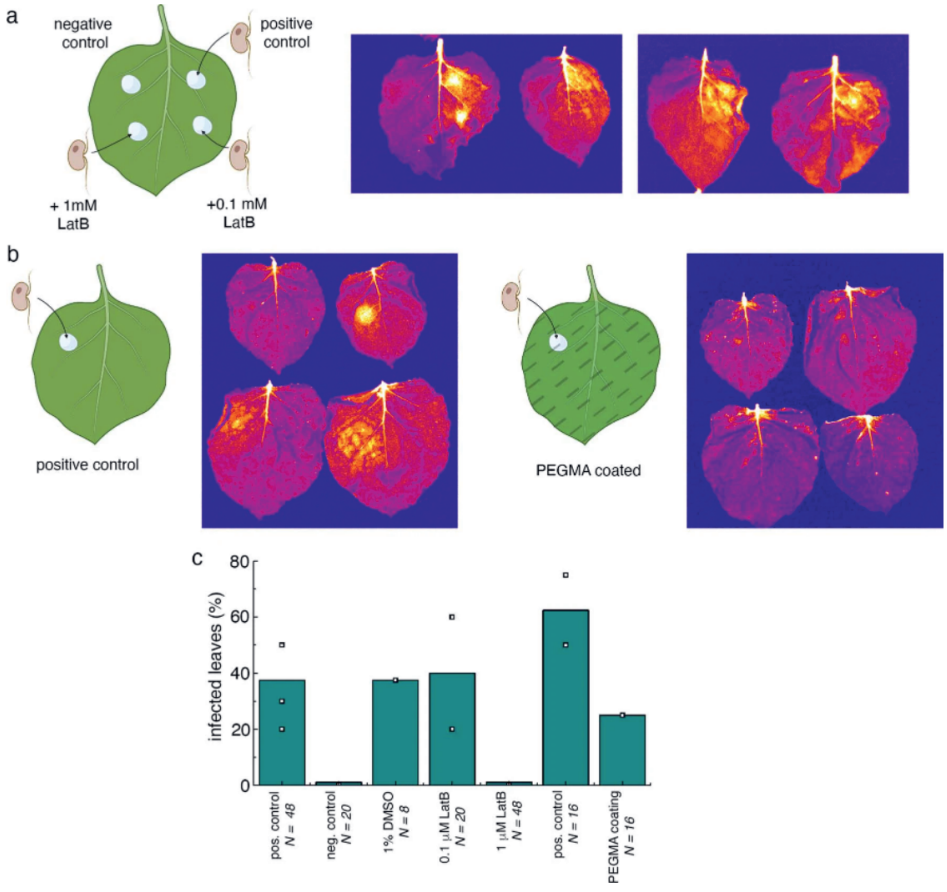

Figure 3.14. **a**, Detached leaf assay to test the effect of cytoskeletal disruption with LatB on *P.infestand-wt* infectivity on Nb-sobir1 leaves. **b**, Detached leaf assay to test the effect of a non-adhesion coating on *P. infestans-wt* infectivity on Nb-sobir1 leaves. Leaf images are deep-red images that reveal lesions as bright orange-white zones (**a**-**b**). Schematic illustrations created with BioRender.com. **c**, Infectivity, determined as the percentage of inoculated spots that show a clear lesion 7dpi, for various controls and treatments, showing clear reduction in pathogenicity for high LatB concentrations and the non-adhesion coating. Numbers N indicate the total number of leaves tested for each sample.

Table of experimental details

Experiment	Figure	Sample names and statistics
In-planta invasion angle	Fig. 3.1a	* (*P. infestans* - 14/3): N = 15 (5 independent expts)
Invasion angles	Fig. 3.1d-i	* 0.56 MPa (*P. infestans* - 14/3): N = 200 (8 independent expts) * 1.49 MPa (*P. infestans* - 14/3): N = 303 (3 independent expts) * 1.84 MPa (*P. infestans* - 14/3): N = 126 (2 independent expts) * 0.56 MPa (*P. infestans* - wt): N = 115 (2 independent expts) * 0.56 MPa (*P. palmivora* - wt): N = 94 (2 independent expts) * 0.56 MPa (*P. capsici* - wt): N = 68 (3 independent expts)
Fracture sensor	Fig. 3.2b and Extended Data Figure 3.9	* 0.10 MPa *P. infestans* - 14/3: N = 19 (3 independent expts)
Surface deformation maps	Fig. 3.2f and Extended Data Figure 3.10	* 0.56 MPa (*P. infestans* - 14/3 eGFP): N = 6 (3 independent expts)
	Fig. 3.2g and Extended Data Figure 3.11	* 0.56 MPa (*P. palmivora* - wt): N = 7 (3 independent expts)
	Extended Data Figure 3.12	* 0.56 MPa (*P. infestans* - wt): N = 6 (4 independent expts)
	Extended Data Figure 3.13	* 0.56 MPa (*P. capsici* - wt): N = 8 (4 independent expts)
Fitting to mechanical model	Fig. 3.3d and Extended Data Fig. 3.5	* 0.56 MPa (*P. infestans* - 14:3): N = 3 (3 independent expts)
	Fig. 3.3e	* 0.56 MPa (*P. palmivora* - wt): N = 2 (2 independent expts)
Actin depolymerization with LatB	Fig. 3.4	0.56 MPa *P. infestans* - wt: * control: N=111 (10 FoVs, 2 independent expt) * +1% DMSO: N=106 (8 FoVs, 2 independent expts) * +1% DMSO + 100 nM LatB: N=368 (8 FoVs, 2 independent expt) * +1% DMSO + 500 nM LatB: N=142 (9 FoVs, 2 independent expt) * +1% DMSO + 1 μM LatB: N=153 (8 FoVs, 2 independent expts)
Adhesion suppression with PEG-g-PLL	Fig. 3.4	0.56 MPa *P. infestans* - wt: * +PEG-g-PLL treated PDMS: N=74 (16 FOVs, 2 independent expts)
Osmotic treatment (2h post-inocc.)	Fig. 3.4	0.56 MPa *P. infestans* - wt: * +5.0 bar: N=105 (4 FOVs, 2 independent expts) * +13.2 bar: N=45 (4 FOVs, 2 independent expt) * +27.8 bar: N=20 (4 FOVs, 2 independent expt)
Leaf infection (7d post-inocc.)	Extended Data Figure 3.14	*P. infestans* - wt on *Nb-sobir1* leaves: * positive control LatB (zoospores + no treatment): N=48 leaves (4 independent expts) * negative control (no zoospores + no treatment): N=20 leaves (1 independent expt) * 1% DMSO: N=8 leaves (1 independent expt) * 0.1mM LatB + 1% DMSO: N=20 leaves (3 independent expts) * 1mM LatB + 1% DMSO: N=48 leaves (4 independent expts) * positive control PEGMA (zoospores + no coating): N=16 leaves (2 independent expts) * PEGMA treatment: N=16 leaves (2 independent expts)

References

1 Elysa J. R. Overdijk et al. Interaction between the moss *Physcomitrella patens* and *Phytophthora* : a novel pathosystem for live-cell imaging of subcellular defence. Journal Of Microscopy Volume 263, Issue 2 (2016)
2 C P Woloshuk, J S Meulenhoff, M Sela-Buurlage, P J van den Elzen & B J Cornelissen. Pathogen-induced proteins with inhibitory activity toward *Phytophthora infestans*. The Plant Cell Vol. 3, Issue 6, June (1991)
3 G. Mchau & M. Coffey. Isozyme diversity in *Phytophthora palmivora*: evidence for a southeast Asian centre of origin. Mycological Research, (1994), 1035-1043, 98(9)
4 J. Miao, M. Cai, X. Dong, L. Liu, D. Lin, C. Zhang, Z. Pang & X. Liu. Resistance Assessment for Oxathiapiprolin in *Phytophthora capsici* and the Detection of a Point Mutation (G769W) in PcORP1 that Confers Resistance. Front. Microbiol. 7:615 (2016)
5 J. N. M. Boots, R. Fokkink, J. van der Gucht & T. E. Kodger. Development of a multi-position indentation setup: Mapping soft and patternable heterogeneously crosslinked polymer networks. Review of Scientific Instruments 90, 015108 (2019)
6 Johnson, K. L. Contact Mechanics. (1985).
7 Davis, D.A. et al. Force-induced activation of covalent bonds in mechanoresponsive polymeric materials. Nature 459, 68-72 (2009).
8 Meijer HJG et al. Actin dynamics in *Phytophthora infestans*; rapidly reorganizing cables and immobile, long-lived plaques. Cell Microbiol 16(6):948–961 (2014)
9 Tijs Ketelaar et al. Effects of latrunculin B on the actin cytoskeleton and hyphal growth in *Phytophthora infestans* Fungal Genetics and Biology, (2012), 1014-1022, 49(12)
10 Lee S. and Vörös J. An Aqueous-Based Surface Modification of Poly(dimethylsiloxane) with Poly(ethylene glycol) to Prevent Biofouling. Langmuir, 21, 25, 11957–11962 (2005)
11 Howard, R. J. et al. Penetration of hard substrates by a fungus employing enormous turgor pressures. PNAS, 11281-11284, 88(24) (1991)
12 Johns, Scott et al. Pulses in turgor pressure and water potential: Resolving the mechanics of hyphal growth. Microbiological Research, 225-231, 154(3) (1999)

An actin mechanostat ensures hyphal tip sharpness in *Phytophthora infestans* to achieve host penetration

Filamentous plant pathogens apply mechanical forces to pierce their hosts surface and penetrate its tissues. Devastating *Phytophthora* pathogens harness a specialized form of invasive tip growth to slice through the plant surface, wielding their hypha as a microscopic knife. Slicing requires a sharp hyphal tip that is not blunted at the site of the mechanical interaction. How tip shape is controlled, however, is unknown. We uncover an actin-based mechanostat in *Phytophthora infestans* that controls tip sharpness during penetration. Mechanical stimulation of the hypha leads to the emergence of an aster-like actin configuration, which shows fast, local, and quantitative feedback to the local stress. We evidence that this functions as an adaptive mechanical scaffold that sharpens the invasive weapon and prevents it from blunting. The hyphal tip mechanostat enables the efficient conversion of turgor into localized invasive pressures that are required to achieve host penetration.

This chapter was submitted as:

Jochem Bronkhorst, Kiki Kots, Djanick de Jong, Michiel Kasteel, Thomas van Boxmeer, Tanweer Joemmanbaks, Francine Govers, Jasper van der Gucht, Tijs Ketelaar, Joris Sprakel *An actin mechanostat ensures hyphal tip sharpness in Phytophthora infestans to achieve host penetration* (2022)

4.1 Introduction

Host entry is the first step in the disease cycle of biotrophic filamentous plant pathogens[1–4]. To achieve penetration, pathogens adhere to the host surface[5,6] and apply substantial invasive forces[7–10] to induce a mechanical fracture in the plant cuticle and epidermis that serves as a port of entry. Although the two main phylogenetic groups that encompass filamentous plant pathogens, fungi and oomycetes, diverged between 1.2 and 1.7 billion years ago[11], it is commonly held that they developed similar strategies for host penetration[4,12,13]. Nonetheless, marked differences between fungi and oomycetes are apparent, although host penetration mechanics remain relatively poorly studied for pathogens in the group of oomycetes.

Plant pathogens harness a variety of mechanisms to gain first entry into host tissues from the exterior. Many fungi enter plants via natural openings, such as stomata or wounds, while others use direct penetration by invasive force generation to pierce through the plant cuticle and epidermis[14]. Direct penetration by fungi can, for example, occur from germ tubes or mycelium by outgrowths that penetrate epidermal cells and develop into haustoria or grow further intercellular or from germinating spores that form a specialized invasion structure known as an appressorium[15], which can build tremendous turgor pressures[7,9]. Appressorial penetration through the mechanical barrier of the plant surface involves converting the stored mechanical energy in the highly turgescent cell into penetrative forces by ejecting penetration peg that pierces the plant surface. Appressorium formation, following a recent definition[15], involves a change in cellular identity, a transition from polarized hyphal growth to nonpolar growth. Appressorial penetration is often mediated by septins[16,17], guanosine triphosphate (GTP)–binding cytoskeletal proteins that form filaments, and can involve the formation of a melanized shell around the cell that acts as a pressure-containment vessel, for example, in the well-studied rice blast fungus[18,19]. To mediate direct penetration, fungi also use biochemical weapons, e.g., by secreting cutinases and/or cell wall–degrading enzymes, which can weaken the mechanical barriers[14].

Oomycete host penetration strategies share similarities to those used by their fungal counterparts. Oomycete host entry also involves the conversion of turgor to penetrative forces, and lytic enzymes are secreted from their hypha, such as those that target pectins, to weaken the cohesion of plant cell walls[14,20]. However, marked differences are also evident. Oomycetes lack a melanin biosynthesis machinery and do not have septins; neither is invasion associated with a change in cellular identity nor a transition from polar to nonpolar growth. We recently uncovered the mechanical mechanism by which *Phytophthora* species, the most

notorious and damaging oomycete plant pathogens, create a break in the plant surface, which to our current understanding differs fundamentally from what is known for fungi[8]. Once germinated, single-celled cysts of *Phytophthora* spp. achieve host entry by using their hypha as the invasive weapon. The hyphal tip focuses turgor to the contact point to generate localized invasive stresses. A distinct oblique angle of force application gives rise to strong stress localization near the surface and the emergence of tensile stresses, the combination of which greatly reduces the pressures required to induce a surface fracture, thereby providing the pathogen a point of entry. The mechanics of this mode of entry are analogous to the way a single-bevel Japanese kitchen knife facilitates the formation of a clean cut; hence, we termed this host entry strategy naifu invasion[8], after the Japanese word for knife.

Host entry by *Phytophthora* spp. is sometimes accompanied by hyphal swelling at the point of entry; these inflated germ tube sections are often referred to as either appressoria or appressorium-like structures[21–24]. Because these structures lack several defining features of true appressoria[15], we argued in chapter 3 that this terminology in the context of oomycete pathogenicity may be misleading[8]. We hypothesize that these hyphal swellings, which are most often seen after surface penetration, are likely a collateral effect. Germ tube inflation under large turgor combined with the squeezing forces acting on the hypha at the site of entry may cause the tube to bulge, in the same way that inflating a balloon while squeezing a section of it will lead to a bulge near the constriction.

In essence, naifu invasion is a specialized form of invasive tip growth, a phenomenon studied extensively in plant pollen tube growth[25–27]. Tip growth, during which a walled cell extends by expansion of the cell wall at its tip, is driven by converting isotropic turgor pressure into polarized expansion by modulating the local stiffness and the yield stress of the wall[27–30]. Thus, tip growth involves a relative softening of the wall at its apex to achieve local viscoplastic flow[29] as the mechanism to direct polarized growth. Because application of indentation forces during host entry results from tip elongation[8], this same mechanism is most likely at the heart of invasive force application in oomycetes. In *Phytophthora*, this process is thought to be orchestrated by the actin cytoskeleton that has a polar architecture in the direction of growth and is believed to guide the transport of exocytotic vesicles to the site of wall expansion[31,32].

Without a scaffold to preserve tip shape, contact mechanics dictate that pressing a hypha into a surface of equal or larger stiffness under large indentation forces would invariably lead to tip flattening[33]. In the same way that one cannot create cuts with a bluntknife, naifu invasion also requires a sharp hyphal tip to localize stresses to the intended entry point and prevent the loss of mechanical energy

to the deformation of the pathogen itself. This creates a mechanical conflict in invasive growth via naifu invasion. Without additional mechanisms, such as the one we uncover here, a locally softened hyphal tip, as required for growth and force generation[27–30], would deform and flatten strongly upon mechanical contact with the cuticle that forms the outer protective layer of the host. In other words, these pathogens must simultaneously maintain tip softness to enable the conversion of isotropic turgor to directional growth and tip sharpness and stiffness to enable penetration. How this conflict is resolved remains elusive.

Here, we uncover an actin-based mechanostat in the potato late blight pathogen *Phytophthora infestans* that resolves this mechanical conflict. We find that mechanical stimulation of the hypha activates pronounced actin assembly and accumulation in vicinity of the site of mechanical contact. We combined live-cell cytoskeletal imaging with local force measurements to evidence fast, local, and quantitative feedback between the actin remodeling and the amplitude of the mechanical stress. We postulate, supported by mechanical modeling, that the force-gated actin remodeling results in an adaptive mechanical scaffold, whose stiffness is matched to the level of stress, that prevents tip deformations during host entry. Last, we show that mechanical stimuli lead to tip sharpening and the maintenance of tip sharpness even under large blunting stresses. This feedback mechanism constitutes a tip shape mechanostat that enables hyphal tips to remain malleable and sharp, thereby enabling invasive growth combined with efficient force localization to achieve host penetration.

Results

Actin cytoskeleton remodels during invasive growth

The actin cytoskeleton is well known to play a crucial role in the polarized tip growth of hypha in *P. infestans*[31,32]. We visualized the actin cytoskeleton by live-cell imaging of a transgenic *P. infestans* line, abbreviated Pi-LA-GFP[32], expressing the F-actin binding LifeAct–enhanced green fluorescent protein (eGFP) marker[34]. In line with previous reports[31,32], we observe several distinct cytoskeletal configurations. Germinated cysts show bright diffraction-limited spherical entities (Fig. 4.1, A to H, and fig. S1), known as plaques, whose precise function and internal structure remain elusive, but which are thought to play a role in actin organization and correlate to hyphal morphology[32,35–37]. Second, F-actin occurs as a network of interconnected cables of varying thickness that occupies the cytosol of the germ tube, but whose intensity is highest at the hyphal tip (Fig. 4.1, A to H, and fig. S1). This tip-focused actin network is thought to play an important role in regulating

tip growth by directing the transport of exocytotic vesicles filled with new cell wall material to the growing tip[31,32].

We asked the question whether the actin cytoskeleton, in addition to playing a role in the regulation of polarized growth, could play a mechanical role as well. Previous studies showed that contact with a glass substrate triggers a remodeling of the tip-localized network to an aster-like structure with thick actin cables emanating from the contact point with the surface and extending many micrometers into the germ tube posterior[31]. We visualized the actin cytoskeleton during interaction of the tip with two substrates whose stiffness differs by many orders of magnitude: glass, with a stiffness expressed by the Young's modulus of $E = 10^{11}$ Pa, and a soft silicone rubber [polydimethylsiloxane (PDMS)] with $E = 0.6 \times 10^6$ Pa[8]. Here, we define noninvasive growth as germ tube extension without mechanical interactions with the substrate, and invasive growth as the phase during which the germ tube growth is slowed substantially because of mechanical forces emerging between hypha and substrate. We find that both substrates facilitate a transition from noninvasive to invasive growth, which coincides with a remodeling of the actin cytoskeleton from a finely meshed network into a tip-localized structure consisting of F-actin cables in an aster-like geometry (Fig. 4.1). These effects are substantially more pronounced on the stiff substrate (Fig. 4.1, C, D, G, and H) than on the softer surface (Fig. 4.1, A, B, E, and F). These data provide a first hint to the force-gated remodeling of the cytoskeleton involved in invasive growth. We confirmed that the increased fluorescence and alterations in microstructure observed in the tip of the Pi-LA-GFP actin marker line are not simply due to an increased accumulation of cytoplasm in the apical region of the germ tube. Control experiments in a *P. infestans* line expressing an unbound cytosolic GFP [Pi-14-3-GFP[38]] show virtually no fluorescence increase in the tip before substrate penetration and the lack of any microstructure (see the Supplementary Materials and fig. S2).

We note that previous studies on actin in hyphal tips of *Phytophthora* spp. during invasive growth report inconsistent localizations. A study that stained the actin cytoskeleton with fluorescent conjugates of the actin-binding toxin phalloidin concluded that the hyphal tip is depleted of F-actin[39]. By contrast, a study using LifeAct-eGFP as the actin reporter showed the same actin aster-like structure as we observe here and concluded that F-actin accumulates in the tip[31]. To resolve this apparent contradiction, we compare hyphal tip images, growing invasively on PDMS substrates, stained by a phalloidin-rhodamine conjugate after fixation versus a live-cell imaging approach using LifeAct-eGFP (Fig. S3). Only the LifeAct-eGFP images reveal the actin aster in the tip, while images of the fixed and phalloidin-stained wt strain show a depleted zone (see the Supplementary Materials). This could suggest that the previously reported F-actin depletion in

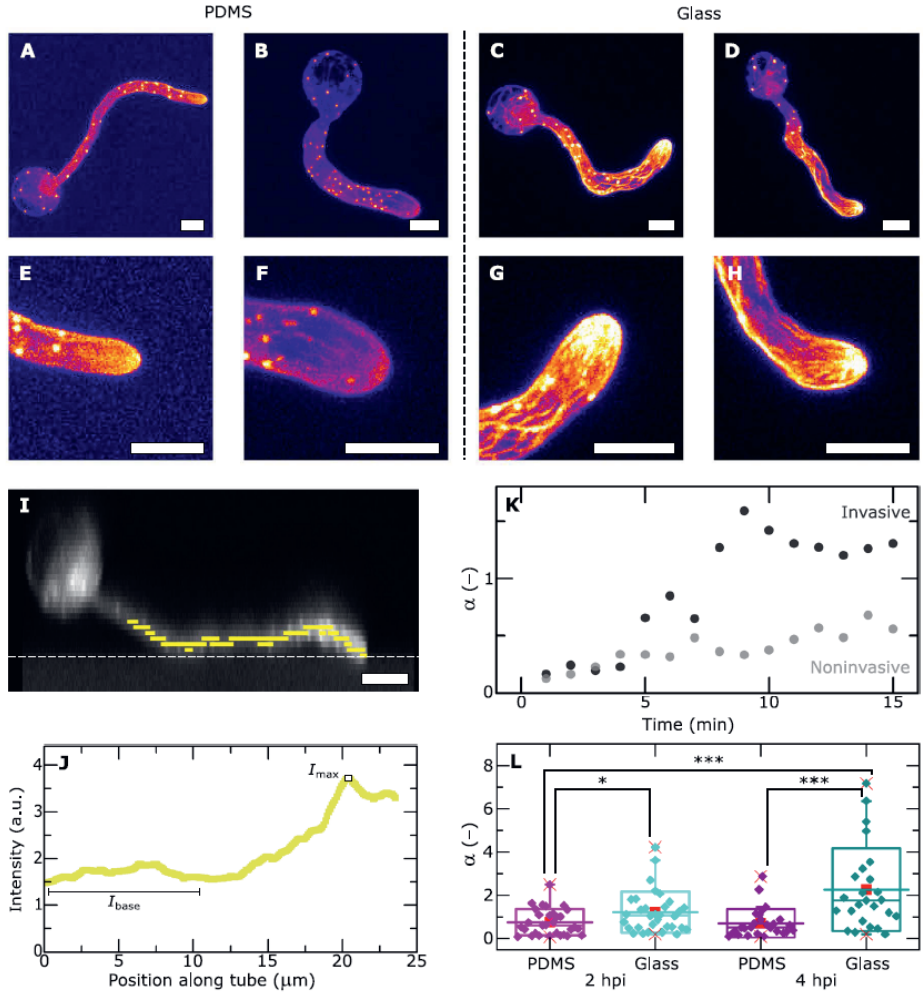

Figure 4.1. (A to D) Maximum intensity xy projections of hyphae of LifeAct-eGFP–expressing *P. infestans* (Pi-LA-GFP) on PDMS (**A** and **B**; N = 32 cells/3 independent experiments) and glass (**C** and **D**; N = 45 cells/3 independent experiments), with corresponding close-up images of the hyphal tips shown in (**E**) to (**H**). (**I**) xz projection of an invasively growing hypha on glass. Gray dotted line: substrate plane, yellow markers: germ tube centroid from image analysis, with the corresponding LifeAct-eGFP intensity as a function of position along the hypha in (**J**) (see fig. S4 for additional examples). a.u., arbitrary units. (**K**) Extent of actin accumulation in the hyphal tip expressed by parameter α (as defined in text) as a function of time for a single cell undergoing noninvasive growth (gray) versus a single cell that grows invasively into a PDMS substrate (black). N = 10 cells/6 independent experiments. (**L**) Box plot showing the distribution of α values for invasively growing hyphae on PDMS and glass substrates, 2 and 4 hours post-inoculation (hpi); a two-sided Wilcoxon rank sum test was used to compare α between glass and PDMS at 2 and 4 hpi, respectively (a < 0.05, *P > 0.02, ***P < 0.01). N = 31 cells/4 independent experiments (PDMS—2 hpi), N = 27 cells/2 independent experiments (PDMS—4 hpi), N = 32 cells/3 independent experiments (glass—2 hpi), and N = 27 cells/3 independent experiments (glass—4 hpi). Scale bars, 5 μm (A to I).

the tip[39] is an artifact, either due to a lack of phalloidin binding to this structure or due to the fixation that precedes staining.

We quantified the extent of actin accumulation near the hyphal tip by means of an image analysis routine that first identifies the centroid contour of the germ tube from two-dimensional projections in the xz plane of three-dimensional image stacks obtained with confocal microscopy (Fig. 4.1I and fig. S4). We verified (Fig. S5) that the orientation of the projection does not significantly influence the outcome of this analysis. Subsequently, we used the contour to measure the fluorescence intensity as a function of position in the germ tube (Fig. 4.1J). In virtually all germ tubes we analyzed, we observed a distinct increase in F-actin accumulation near the tip. We defined the excess of F-actin in the hyphal tip as $\alpha = \frac{I_{max}}{I_{base}} - 1$, where I_{max} is the peak intensity, located at or near the tip, and I_{base} is the mean baseline intensity, recorded in the posterior section of the germ tube (Fig. 4.1J). If the F-actin concentration is homogeneous along the germ tube, $\alpha = 0$, while strong tip accumulation gives $\alpha >> 0$.

We first observed that actin accumulation increases during germ tube initiation and growth also in noninvasive hyphae that do not experience measurable mechanical contact with the substrate (gray symbols in Fig. 4.1K), with α reaching a maximum value of 0.5. This reflects the polar actin structure involved in regulating tip growth in the absence of mechanical interactions. By contrast, in hyphae that push into a substrate and experience compressive mechanical stresses at their tip, the actin accumulation is more pronounced, with α increasing to well above 1 (black symbols, Fig. 4.1K). By aggregating data for multiple cells, we find that actin accumulation at the tip is significantly enhanced on stiffer substrates as compared to soft surfaces, especially during later stages of the growth process (Fig. 4.1L). Mechanical interactions with a substrate influence the extent to which the cytoskeleton remodels and accumulates near the hyphal tip.

A similar response of the actin cytoskeleton was observed in several unique observations made during attempts of *P. infestans* to enter plant cells. During the host entry attempt of Pi-LA-GFP on suspension-cultured cells of the tomato MsK8 cell line[40], we made a very low number of observations (N = 4) on hypha that attempted to penetrate a dead cell (Fig. 4.2, A and B). The penetration attempt caused the cell wall of the tomato cell to deform inward, but penetration was unsuccessful (Fig. 4.2B), potentially indicating that a host cell needs to be turgescent for successful penetration. Nonetheless, in our few observations, an actin aster was clearly visible at the site of mechanical contact (arrow in Fig. 4.2A). In addition, we serendipitously imaged a singular penetration event on in vitro grown potato plantlets (Fig. 4.2, C to E); we observe an actin aster (marked with an arrow in Fig. 4.2, C and E), the center of which localizes to the indentation

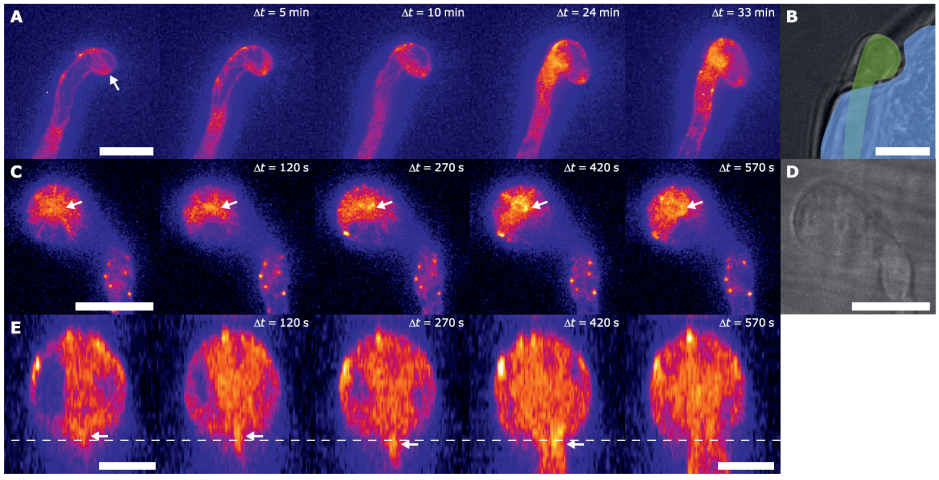

Figure 4.2. (**A**) Time sequence of confocal microscopy images of *P. infestans* Pi-LA-GFP during attempted penetration of a suspension-cultured tomato MsK8 cell, showing actin aster formation (indicated with arrow) at the site of contact (N = 4 cells/1 independent experiment). (**B**) Bright-field fluorescence overlay image shows the pathogen (green) indenting the dead tomato cell (blue) that has lost turgor pressure. Scale bars, 10 μm (**A** and **B**). (**C**) Singular unique observation of Pi-LA-GFP during penetration of an etiolated potato stem. Penetration occurs between 270 and 300 s. (**D**) Bright-field image of invasive hypha shown in (**C**). (**E**) xz projections showing an orthogonal view (90° rotation) of the images in (**C**). Scale bars, 10 μm (**A**to **D**) and 5 μm (**E**). Arrows in (**A**), (**C**), and (**E**) indicate aster, and the dashed line in (**E**) indicates the stem surface.

location. In this observation, we find penetration to occur at a time 270 to 300 s after starting the imaging (see also fig. S7A). We find that the actin fluorescence peaks approximately 1 min after penetration, after which the aster gradually disappears (Fig. 4.2C and fig. S7B). These few observations hint at the fact that the timing and localization of the actin aster correlate with the formation of mechanical interaction with a substrate or cell, and that the relaxation of the mechanical stress, by rupture of the surface, leads to disappearance of the actin aster. This suggests that the actin aster is only present when a mechanical force is active. These observations triggered us to study these processes more rigorously.

Cytoskeletal remodeling upon laser ablation

The mechanically induced actin restructuring described above appears to occur almost instantaneously when a mechanical stimulus emerges at the hyphal tip by contact with either an artificial surface or a plant cell. Because of the limited

time resolution in these experiments, it is difficult to quantify the kinetics of the remodeling. Since invasion occurs by indenting a substrate with the hyphal tip, we only observe the aster formation there; whether this is a specific feature of the cytoskeleton in the tip or an intrinsic feature of the entire cytoskeleton thus remains unanswered.

Laser ablation has been extensively used in other systems to induce a local disturbance in cytoskeletal networks by creating photothermal damage inside the cell as the result of strong local laser irradiance and to explore how the cytoskeletal networks respond to this acute upset of the mechanical balance of the biopolymer network[41,42]. Photothermal damage to the proteins in the ablation zone, here targeted to either actin cables or plaques, which are visible with the LifeAct-eGFP F-actin marker, causes a strong and acute disturbance in the mechanical balance of the cytoskeleton. We note that this approach to create a mechanical stimulus is not directly comparable to the mechanical stimulation of the hyphal tip at a substrate-tip contact zone; laser ablation results in an acute damage to the cytoskeleton, and other structures in the ablation zone, while the mechanics at the hyphal tip during penetration are more moderate and sustained. Nonetheless, it offers a way to create a local and acute disturbance of the cytoskeletal mechanical balance[41,42], to study how the network responds to such a stimulus.

We pointed an ablation laser to both the hyphal tip region and to a region distal from the tip and selected actin plaques or plaque-free regions as targets. Notably, independent of the position of ablation and the target, laser ablation leads to the rapid formation of cables organized in an aster-like geometry (Fig. 4.3, A and B, and fig. S6). In all cases, the center of the aster is located at the laser ablation spot. We also observe that for tens of seconds after application of the stimulus, the aster spontaneously disappears.

To quantify the kinetics of this process, we recorded the temporal changes in LifeAct eGFP intensity in the ablated zone, with 2-s resolution, and normalized this to the baseline intensity in that zone before ablation, defining t = 0 as the moment of stimulation. We aggregated data from multiple experiments for the same location or the same target (Fig. 4.3C). For all locations and ablation targets, we observe a rapid increase in LifeAct fluorescence, which signals the formation of the actin aster. The formation process is completed in 15 ± 1 s after ablation. Once the stimulus is removed, the cytoskeleton relaxes to its unperturbed configuration. This spontaneous disassembly process is completed in 29 ± 5 s. We note that these effects are absent in control experiments on a *P. infestans* line that expresses a cytosolic eGFP marker (PI-14-3-GFP; Fig. 4.3C), indicating that our observation relates to cytoskeletal reorganization and not to a disturbance of the entire cytosol.

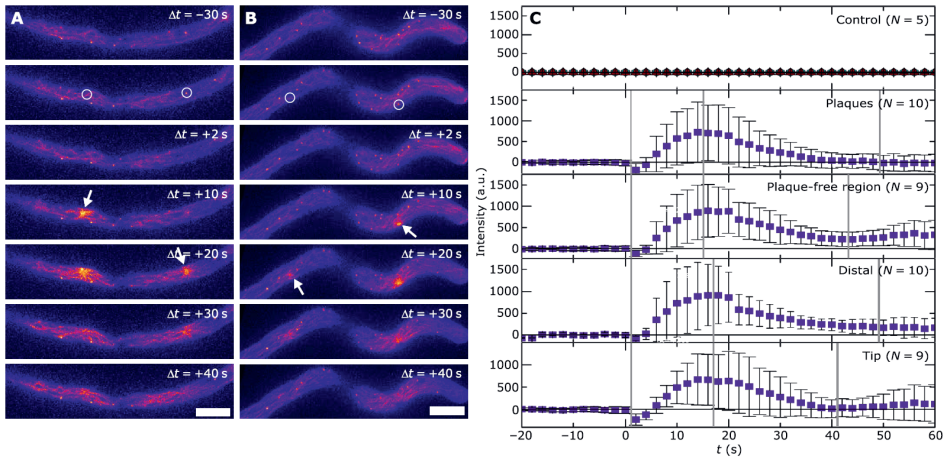

Figure 4.3. Live-cell imaging of *P. infestans* Pi-LA-GFP upon laser ablation at t = 0 in a distal area of the hypha (**A**) and in proximity of the hyphal tip (**B**) during a time frame of 40 s. In each hypha, the ablation laser was targeted to a plaque and to a plaque-free region of the cytoplasm (indicated with circles), respectively. Actin asters are indicated by arrows. Scale bars, 5 μm (**A** and **B**). (**C**) Fluorescence intensity in the ablation zone as a function of time, with t = 0 defining the time of the ablation pulse, for a cytosolic eGFP line (control, Pi-14-3-GFP) and the actin marker line (Pi-LA-GFP) for two different targets (plaques and plaque-free regions) and two different locations in the hypha. All curves are averaged over several repeated measurements (as indicated); symbols denote average normalized intensities, and error bars denote the SD across the repeated experiments (number of repeats as indicated). Error bars in the control experiment are smaller than the symbol size. Vertical gray lines indicate the start of the formation and dissolution phase, respectively.

These data provide several important clues about the mechanically induced changes in cytoskeletal structure. First, we observe that the formation of the actin aster is not specific to the hyphal tip but appears to be an intrinsic feature of the cytoskeleton throughout the hypha. Second, we find that the formation of the actin aster in response to photothermal damage is very local and rapid, occurring at the ablated site and requiring only 15 s to complete. Last, this structure appears to be under mechanical control: It only forms when a stimulus is applied and vanishes again within half a minute after the stimulus is removed.

Quantifying mechanical feedback

To quantify the extent to which mechanical forces elicit a structural remodeling of the actin cytoskeleton in the hyphal tip, we grow Pi-LA-GFP on surfaces that enable quantitative mapping of the surface forces involved in invasive growth. We use a previously developed approach that uses fluorescent elastomer surfaces and image analysis to measure the axial deformation of the substrate Δh induced by the pathogen[8]. Invasion on these surfaces begins with hyphal extension without mechanical contact, thereby leaving the substrate surface undeformed (Fig. 4.4, A and B). After a switch to invasive growth, the pathogen adheres to the surface and applies downward invasive force onto the surface to induce a fracture to gain entry (Fig. 4.4, C and D). This results in a distinct asymmetrical deformation pattern of an adhesion site (upward deformations, red in Fig. 4.4D) and an indentation zone (downward deformations, blue in Fig. 4.4D). The mechanics of these phases was discussed in more detail in chapter 3[8].

This approach allows us to simultaneously measure, in each pixel, the LifeAct-eGFP intensity, albeit at a lower resolution (Fig. 4.4, A and C) than for the experiments presented in Fig. 4.1, and the amplitude of surface deformations Δh (Fig. 4.4, B and D). We begin by asking our data whether the mechanically induced actin remodeling is a local phenomenon as suggested by our data presented above. We separate the data into pixels in adhesion sites ($\Delta h > +0.5\ \mu$m, blue), indentation sites ($\Delta h <$ min$0.5\ \mu$m, red), and noninteracting sites (min$0.5 < \Delta h < +0.5\ \mu$m, gray). When we plot, for a single cell at a single time point, the actin intensity in each pixel as a function of the absolute amplitude of the surface deformation $|\Delta h|$, we see how these three subpopulations occupy different spaces (Fig. 4.4E and fig. S8). Indentation sites, where stresses on the germ tube are compressive and which are localized to the tip (blue in Fig. 4.4F), correspond to high GFP fluorescence reflecting high local concentrations of F-actin, whereas adhesion sites, found posterior to the indentation site (red in Fig. 4.4F) and where stresses are tensile, show lower fluorescence pointing to lower actin concentrations. Zones, in which surface deformations are small or absent, on average correspond to low actin concentrations, except for the cyst body. The latter is responsible for the data points at low deformations and high intensities.

To quantify these observations further, we accumulated data for N = 6 cells and n = 5 time points per cell in a field of view surrounding the site of invasion, resulting in a total of 283,000 individual data points. Distributions of these data reveal a statistically significant increase in the F-actin concentration in pixels associated with indentation where the hypha experiences compressive stresses (red in Fig. 4.4G) as compared to noninteracting sites (gray in Fig. 4.4G). By contrast, in the

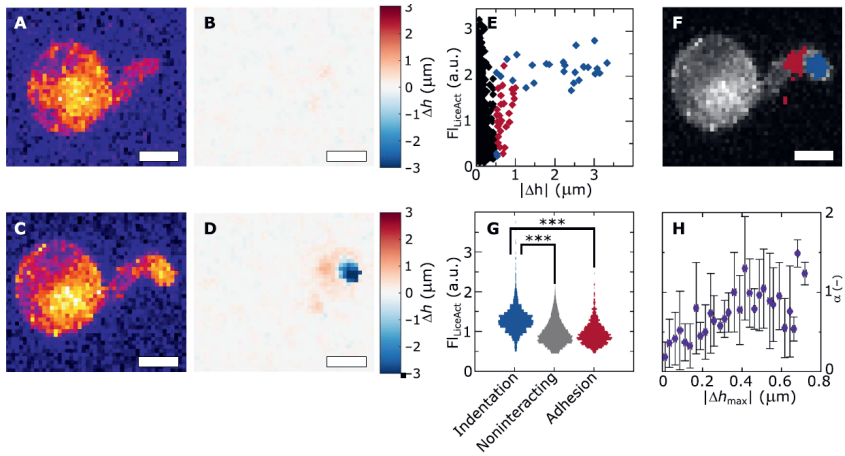

Figure 4.4. (**A** to **D**) LifeAct-eGFP imaging combined with local surface mechanics measurements, showing xy projections of *P. infestans* Pi-LA-GFP during invasive growth on a PDMS substrate (A and C) and corresponding surface deformation maps (**B** and **D**) in the phase just before (A and B) and during force generation (**C** and **D**). (**E**) Scatterplot, showing the local LifeAct eGFP intensity (y axis) and absolute surface deformation amplitude for each pixel at a single time point for a single cell (x axis); data are grouped into adhesive (red), indentation (blue), and noninteracting sites (black) on the basis of the sign and amplitude of the local surface deformation (as explained in text). (**F**) Overlay of identified adhesion (red) and indentation sites (blue) on the xy projection of the LifeAct eGFP signal for a single cell showing strong localization in two distinct zones; additional examples shown in fig. S8. Spatial correlation of LifeAct-eGFP and surface deformations was performed on N = 6 cells/5 independent experiments. (**G**) Violin plot showing the distribution of LifeAct eGFP intensities associated with the three distinct sites, collected from N = 6 cells and n = 5 time points per cell, resulting in a total number of data points of 26,000 (indentation), 232,000 (noninteracting), and 25,000 (adhesion). A two-sided unpaired Student's t test with Welch's correction was performed to compare relative fluorescence intensities in the indentation zone versus the noninteracting and adhesion regions (a < 0.05 and ***P < 0.01). (H) Quantitative correlation between the extent of actin accumulation in the tip, expressed by parameter α (y axis), and the maximum amplitude of surface deformations (x axis) as a proxy for the applied invasive force. Diamonds represent means, and scale bars represent SDs between aggregated time series for N = 6 cells/5 independent experiments. Scale bars, 5 μm (**A**to **D** and **F**).

adhesion sites, where the germ tube is also under mechanical stress of equal magnitude, due to force balance[8], but of opposing sign (predominantly tensile), we find no significant local increase in the F-actin concentration. The absence of a cytoskeletal response in the adhesion site suggests that the mechanical activation of the actin remodeling could be sensitive to the vectorial nature of the mechanical stimulus.

Using the same approach, we can also evaluate how the extent of actin accumulation in the tip, using the metric α, is sensitive to the amplitude of the mechanical stress. We measured the maximum indentation deformation $|\Delta h_{max}|$, which is proportional to the applied invasive force, as a function of time in 2-min intervals, aggregated for N = 6 cells during their invasive growth, and simultaneously determine α. We find a quantitative correlation between the amplitude of the surface deformation, as a measure for the applied indentation force, and the extent of actin accumulation at the hyphal tip, with α showing a near-linear growth with $|\Delta h_{max}|$ (Fig. 4.4H). An increase in the applied force results in the instantaneous, within the time resolution of our measurements, increase of the extent of actin accumulation. These results show that the mechanical feedback exhibited by the actin cytoskeleton is not only local and rapid but also quantitative.

Mechanostat hypothesis and model

Our results above demonstrate that the organization of the actin cytoskeleton in the hyphal tip of *P. infestans* is under mechanical control. It is likely that the observed mechanical feedback to the actin network plays a role in the mechanics of invasion. It is often presumed that actin plays no significant mechanical role in the invasive growth of walled cells, in part, because the cell wall rigidity and turgor are orders of magnitude larger than the stiffness of actin structure[43,44]. Actin polymerization cannot produce sufficient force to deform the cell wall or generate invasive forces[43], and invasive forces are caused solely by directing turgor to a localized area. However, this does not exclude that, in addition to being an orchestrator of polar transport, the actin network can play a role as a mechanical scaffold to shape the tip. The other known structural protein filaments in *Phytophthora*, microtubules, do not form scaffold structures in the hyphal tip of[45,46] and are nonobligatory for hyphal tip morphogenesis and polarized growth[47]. It thus seems likely that microtubules are not implicated in the responses we observe.

We hypothesize that the mechanically controlled actin structure in the hyphal tip serves as an adaptive mechanical scaffold, whose rigidity is matched by the quantitative feedback mechanism to the local and instantaneous level of mechanical

stress, which maintains tip sharpness during invasion. This proposed mechanism thus constitutes an actin mechanostat: The cytoskeletal stiffness is adaptively tuned to the level of stress acting on the tip to ensure a constant tip shape during invasion to accommodate the increase of the mechanical stresses during invasion. If true, this mechanostat would allow the cell wall to become locally weakened at the tip to accommodate tip growth without sacrificing penetration efficiency, thereby resolving the mechanical conflict involved in naifu invasion.

Typical elastic moduli for actin networks range from tens to hundreds of kilopascals, depending on their architecture, degree of bundling, density, and cross-linking state[48–52], whereas cell walls can be as stiff as hundreds of megapascals[53–55], but estimated to be substantially weaker, at tens of megapascals, in growing tips[26,56]. This large stiffness asymmetry raises the question whether the actin cytoskeleton is not too weak to play the suggested role of a tip shape scaffold. First, we realized that while stiff, the cell wall is a thin quasi–two-dimensional sheet, whereas the actin structure we studied above is not exclusively localized to the cell cortex; from our imaging, it appears to fill the three-dimensional space of the germ tube at its apex, thus having dimensions of several micrometers.

To evaluate whether a soft three-dimensional network can fortify a stiff quasi–two-dimensional shell, we constructed a mechanical finite-element model of this scenario (Fig. 4.5A, full details in Materials and Methods). Our model consists of a spherical indenter (radius = 5 μm), representing the hyphal tip, composed of a thin cell wall [thickness = 50 nm, E = 20 MPa[26]] that is filled with an elastic solid, representing the actin structure in the apex, with variable stiffness. The entire sphere is under 1 MPa turgor, as determined experimentally[8]. The outward turgor places the cell wall in a state of prestress, leading to lateral tensile stresses in the wall of approximately 50 MPa. The indenter is pushed into a soft substrate with E = 0.6 MPa, matching the stiffness of the PDMS surfaces used in our experiments.

In the absence of an actin network (Eactin = 0), indentation at a force of 1 μN, which corresponds to the typical forces applied by *P. infestans*[8], results in substantial flattening of the hyphal tip (line in Fig. 4.5B). Because a part of the mechanical energy is now used to deform the pathogen, the efficiency of stress transfer into the substrate is moderate (Fig. 4.5B). By contrast, introduction of an infinitely stiff actin network, as the other mechanical limit, completely counters the indenter deformation and thereby results in more efficient stress transfer into the substrate (Fig. 4.5C).

To analyze this in more detail and for realistic actin network stiffnesses[48–52], we study the deformation of the shell as a function of indentation force for indenters filled with actin networks of varying Young's modulus. We use the elastic strain energy in the cell wall as the result of the substrate contact as a measure for the

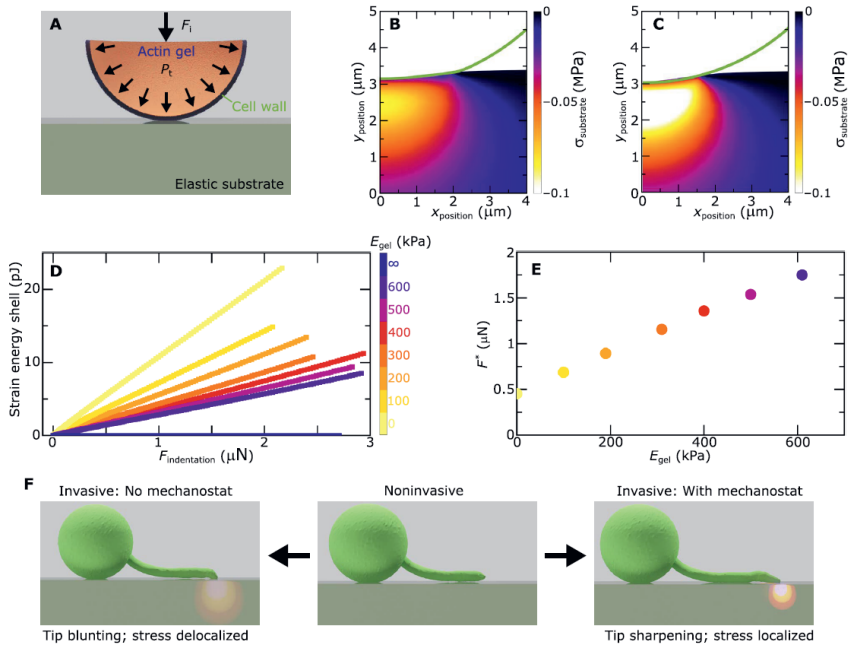

Figure 4.5. (**A**) Schematic illustration of the finite-element mechanical model. (**B** and **C**) Shape of the cell wall (green line) and stress distribution in the substrate for a tip without actin gel (**B**) and a tip with an infinitely stiff actin gel (**C**). The total indentation force is 1 μN in both cases. The color scale in the substrates indicates the principal compressive stress as the result of tip indentation. (**D**) Total strain energy in the cell wall (y axis), as a measure for the extent of tip deformation, as a function of the indentation force (x axis) for tips containing actin gels of different modulus; color scale expresses the actin gel modulus. (**E**) Indentation force F* (y axis) at which the strain energy in the shell reaches a threshold value of 5 pJ as a function of the modulus of the actin gel (x axis). (**F**) Schematic illustration of hyphal tip shape, and its effect on stress distributions in the substrate, upon switching from noninvasive to invasive growth, with and without a mechanostat to ensure tip sharpness.

extent to which the tip deforms during indentation. In all cases, the strain energy of the wall increases approximately linearly with the applied force (Fig. 4.5D). As the actin gel increases in stiffness, the strain energy of the shell for a given indentation force decreases, showing that also soft actin networks are effective in preventing excessive tip deformations. We analyze this further by considering the indentation force F* at which the strain energy in the shell reaches a certain threshold value, here taken as 5 pJ. As shown in Fig. 4.5E, this force increases with increasing stiffness of the actin gels, or vice versa, if the indentation force increases, a stiffer actin gel is required to maintain the tip shape. These in silico results show that despite a strong stiffness contrast, a soft actin gel is very effective in reducing cell wall deformations and that a stiffer actin gel is needed to maintain tip shape as the invasive process progresses and the forces on the tip grow. This demonstrates the mechanical feasibility of our hypothesized tip shape mechanostat.

These simulation results, together with the experimental data from the preceding sections, lead us to the following hypothesis: During noninvasive growth (middle panel, Fig. 4.5F), no invasive forces act on the hyphal tip or substrate and the actin cytoskeleton remains in its native configuration, resulting in a rounded hyphal tip prescribed by noninvasive tip growth mechanics[26,27,57]. Upon switching to invasive growth, turgor is converted to invasive indentation forces at the tip-substrate contact zone. Without a mechanostat, this would result in substantial tip blunting and a diffusive and inefficient generation of stresses in the substrate (left panel, Fig. 4.5F). By contrast, in the presence of a mechanostat, the onset of mechanical interactions activates the actin remodeling, which leads to hyphal tip sharpening and localized and efficient force transfer to the substrate (right panel, Fig. 4.5F).

Tip shape mechanostasis

To test our hypothesis of actin serving as an adaptive tip shape scaffold, we measured tip shapes and invasive forces during substrate penetration attempts. We again relied on the deformation reporting surfaces developed in chapter 3[8]. In Fig. 4.6(A to C), we show a time sequence of surface deformations during the invasive growth of a hypha emerging from a single *P. infestans* cyst, on a soft PDMS substrate. Also, here, we can recognize an initial noninvasive growth phase (Fig. 4.6A), followed by substrate adherence and invasive force application (Fig. 4.6B). The force grows over the course of tens of minutes (Fig. 4.6C) until the surface fractures and the pathogen grows into the elastomer through the crack void. From these two-dimensional surface deformation maps, we can extract a one-dimensional plot of the surface deformation amplitude as a function of

position, taken along the contour of the germ tube (Fig. 4.6, D to F). Using an elastic contact model derived in chapter 3[8], which treats the invasive hypha as two distinct zones for adhesion and indentation in the limit of linear mechanics, we can fit these deformation profiles with good accuracy up to the moment of penetration (solid lines in Fig. 4.6, D to F). From these fits, two independent parameters are extracted: (i) the indentation force Findent, applied by the pathogen at its contact point with the substrate, which governs the depth of the indentation minimum, and (ii) the radius of curvature of the hyphal tip R_{tip} at the same position, which determines the width of the indentation minimum as the elastic substrate conforms to the tip at the contact point. For a given cell at a given point in time, we thus obtain both the applied force and the tip shape. The indentation force, shown in Fig. 4.6G over the course of a host penetration cycle for a single cell, shows the three stages described above. The tip shape analysis is only tractable during the second phase, where the pathogen induces deformations of the surface but has not yet induced a fracture and the behavior obeys linear mechanics. During this phase, we surprisingly observe, for the same cell as shown in Fig. 4.6G, that the tip radius initially decreases, i.e., the tip sharpens, as the mechanical contact is established, and then reaches a time-independent plateau (Fig. 4.6H). This induced sharpening of the tip coincides with the formation of the actin aster analyzed in detail above.

Without an adaptive fortification mechanism, the indentation of a surface with a deformable object would invariably lead to tip flattening, i.e., an increase in tip radius, with increasing force[33]. Here, we observe the exact opposite. We aggregated data for multiple cells (N = 6) and plotted the tip radius as a function of the indentation force. This reveals evidence for our hypothesized mechanostat (Fig. 4.6I). Initially, when the force is zero, the tip has its original shape as dictated by the tip growth mechanism. As the force increases, the actin mechanostat is activated, which coincides with tip sharpening and the subsequent maintenance of a constant and sharp tip shape as the force is increased.

Our hypothesis involves a causal relationship between the force-induced formation of the actin structure and the ensuing sharpening of the hyphal tip. To evidence this causality, we performed experiments where we disrupted the actin cytoskeleton during invasive force generation by adding a pulse of the drug latrunculin B (LatB), which inhibits actin polymerization and disrupts the actin aster[31]. We inoculated fluorescent PDMS surfaces with Pi-LA-GFP in water. After 1 hour, when a fraction of the cells is involved in invasive force generation, but has not yet breached the surface, we gently add a drop of a concentrated LatB solution to a final concentration of 5 μM. During this chemical disruption, we simultaneously measured the change in actin distribution and associated alterations of surface deformation patterns. A distinct change in tip shape is visually apparent: The

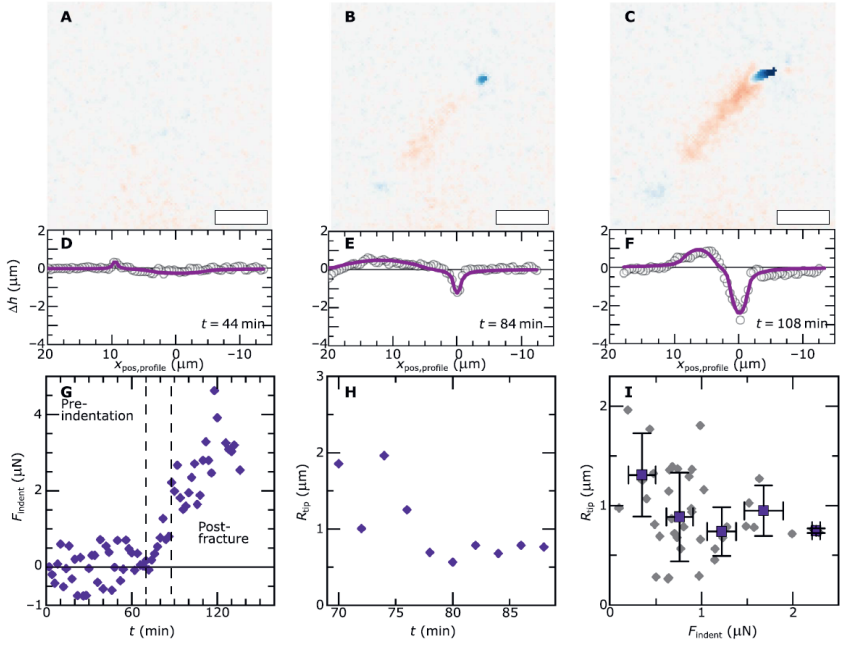

Figure 4.6. (**A** to **C**) Surface deformation maps during the invasive growth of *P. infestans* Pi-LA-GFP on elastomer surfaces (color code as in Fig. 3, **B** and **D**) during the initial noninvasive growth (**A**), invasive force generation (B), and after surface fracture and substrate penetration (**C**). (**D** to **F**) Associated surface height profiles (symbols) and fits to a mechanical model for invasive force generation (lines). (**G**) Invasive force applied onto the substrate (y axis) as a function of time (x axis) for a single cell, showing three regimes. (**H**) In the invasive force generation regime, the tip radius R_{tip} (y axis) can be extracted from the surface deformation fitting, for the same single cell as in (**G**). (**I**) Aggregated data for N = 5 cells/3 independent experiments, showing the correlation between the tip shape (y axis) and the applied invasive force Fi (x axis), revealing initial tip sharpening upon mechanical contact and tip shape stasis at higher forces. Gray diamonds: all data points; purple squares: binned and averaged data, with error bars representing the SD per bin along the force axis. Scale bars, 5 μm (**A** to **C**).

initially sharp tip rapidly blunts in response to the acute LatB treatment (Fig. 4.7A). This coincides with the dissolution of the actin aster and actin plaques (Fig. 4.7B) and the distinct broadening of the surface deformation under the hyphal tip (blue zones in Fig. 4.7C). As before, we fit these surface deformation patterns to our mechanical model to extract the tip shape and indentation force (Fig. 4.7D), which shows a distinct tip blunting, from the increase in its radius of curvature R_{tip}. Simultaneously, we observe that the invasive force remains

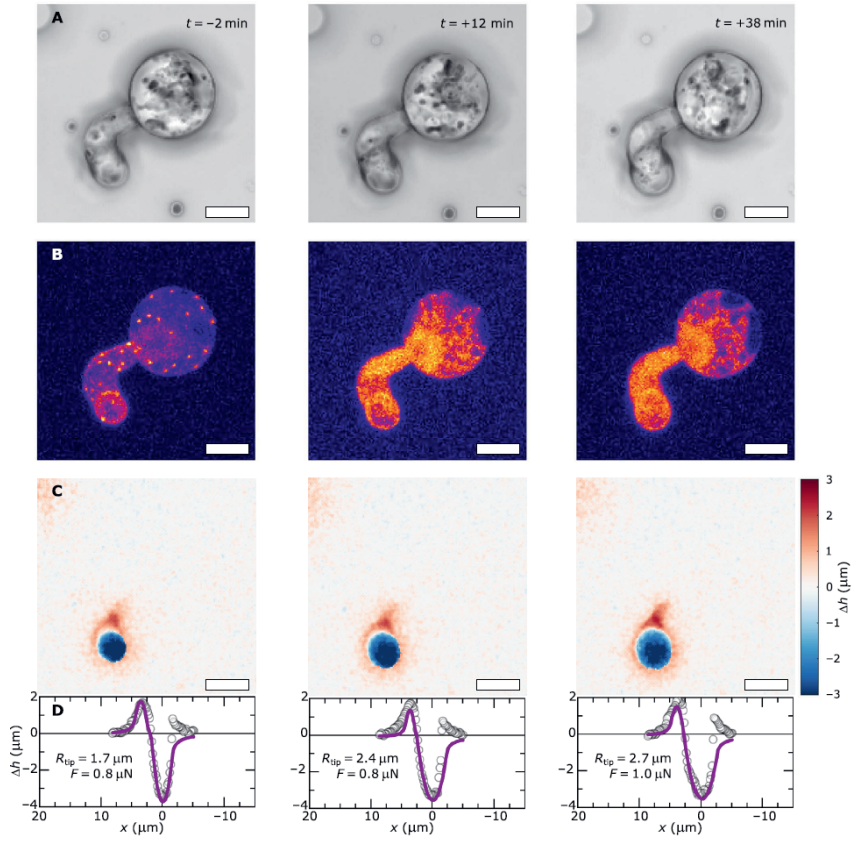

Figure 4.7. Effect of cytoskeletal mechanostat disruption, by acute treatment with 5 mM LatB at t = 0, on tip shape and surface mechanics of Pi-LA-GFP during invasive growth. (**A**) Bright-field images before (t = min2 min) and after (t = +12 and +38 min) LatB treatment. (**B**) Corresponding images from the LifeAct-eGFP channel showing disruption of the actin filaments by the lack of LifeAct-eGFP localization after treatment. (**C**) Corresponding surface deformation maps and (**D**) line profiles of surface deformations from experiments (symbols) and fitted to a mechanical model for invasive growth (solid lines) to extract tip curvature R_{tip} and indentation force F, as specified in the figure panels. Scale bars in (**A**) to (**C**) represent 5 μm; N = 6 cells from three independent experiments (see fig. S9 for additional examples).

constant, whereas this force was found to grow continuously during unperturbed invasion[8]. LatB disrupts the actin aster, which results in loss of the mechanostat and thus the blunting of the hyphal tip and the stalling of invasive force generation that prevents building up sufficient force to achieve surface fracture. Additional examples of these effects for N = 4 cells from two independent experiments are

shown in fig. S9 (A to F). We also recorded data at a lower spatial resolution and higher temporal resolution, shown in fig. S9 (G and H). The tip curvature and force before LatB treatment are indicated by the dashed line: Upon LatB injection at t = 0, we observe a rapid tip blunting, by an increase in tip radius (Fig. S9G), and an associated reduction in the invasive force (Fig. S9H). This experiment reveals that it takes approximately 30 to 40 min upon LatB addition for the tip blunting to reach completion.

We showed in chapter 3 that these high doses of LatB almost completely suppress the invasivity of *P. infestans*, both on artificial substrates and in potato leaves[8]. This suggests that the actin mechanostat is crucial for host penetration as it focuses forces to a small area, thereby increasing the invasive pressure at the intended site of entry, and its inhibition leads to not only tip blunting and redistribution of the invasive force over a large area but also the simultaneous stalling of force generation and inhibition of host entry.

Discussion

We have demonstrated that mechanical stimulation induces a remodeling of the actin cytoskeleton in the filamentous plant pathogen *P. infestans*. Mechanical force induces a transition from a finely meshed network to an aster-like structure composed of thick cables emanating from the locus of mechanical stimulation. This mechano-adaptive response was found to be local, rapid, and quantitative. This mechanically induced remodeling coincides with the sudden sharpening of the hyphal tip at the first stimulus and the maintenance of tip sharpness as the force on the organism grows during host entry. We posed that this constitutes an actin-based mechanostat that ensures hyphal tip sharpness by accommodating increasing mechanical forces on the tip during invasion by adapting the stiffness of the actin network as a mechanical scaffold. A mechanical model for this scenario illustrated the feasibility of this hypothesis, which was verified by our experimental studies of the tip shape evolution during invasive growth.

These findings raise the question how this mechanical feedback is organized. We find that the response is highly localized and occurs within 15 s of stimulation but rapidly vanishes when the stimulus is removed. The local and rapid response appears to rule out a key role for biochemical signals in activating the response; this requires chemical diffusion, which is most likely too slow at this length scale and would lead to diffusive spreading of the effect. Also, transcriptional responses are far slower than the kinetics observed here. Rather, it is more likely that this is an intrinsic response of the actin network mediated by mechano-receptive elements already present in or close to the cytoskeleton.

One possible mechanism for this mechanostat is that it is mediated by actin-associated proteins present in the cytoskeleton during the germination phase. A variety of actin-binding proteins and actin cross-linkers, studied mainly in mammalian cells or in vitro, are capable of rendering actin networks mechano-adaptive. These actin-binding proteins include catch bonding cross-linkers such as α-actinin[58] or vinculin[59] and the actin-branching protein complex ARP2/3[60,61]. The *P. infestans* genome contains several genes encoding actin-binding proteins that could be implicated in the mechano-adaptive response, including α-actinin[62], ARP2, and ARP3[37,63]. On the basis of their responses to mechanical stress in other organisms and in vitro studies, these proteins could be involved in orchestrating the mechanostat without requiring a biochemical signaling network. In reconstituted actin networks, studied in vitro, it was found that the mechano-sensitive ARP2/3 complex, which creates branch points in actin filaments, results in force-induced network densification and stiffening[61]. Also, catch bonding cross-linkers, such as α-actinin, whose bonding strength with actin filaments grows under the action of mechanical stress, can result in force-gated accumulation and filament bundling[64,65]. Cross-linking actin with these proteins does not result in aster formation, which implies that a more complex mechanism involving multiple regulators is at play in the mechanostat.

Last, we note that *Phytophthora* spp. secrete lytic enzymes during host entry[20,66], a strategy also used by fungi[14]. Especially, enzymes that target pectins in the host cell walls are of interest here: Pectin provides cell walls with elastic compliance, which is a key determinant in their mechanical resilience. It is unknown how the local degradation of plant cell walls influences the mechanics of host penetration by the naifu invasion mechanism and the mechanostat uncovered here. These enzymes do not sort any effect on our artificial substrates, which are held together purely by silicon-oxygen bonds; the observed effects on these model substrates are thus purely mechanical in origin. However, penetration of real hosts can undoubtedly be facilitated by enzymatic action: Local pectin degradation or demethoxylation can reduce the plant wall cohesion and mechanical resilience, which can, in turn, be speculated to lower the invasive pressure required to achieve penetration. Moreover, local secretion of wall-degrading enzymes can lead to a mechanical weak link in the plant epidermis. Such an induced mechanical heterogeneity could alter the distribution of stresses and enhance the concentration of invasive forces at the intended penetration site, in a very similar way as a mechanical defect concentrates stresses during material failure. Very recently, a new approach has been introduced to map local changes in cell wall porosity in in vivo imaging[67], which could make it tractable to probe these effects in situ

during host penetration on biological hosts; an in-depth exploration of these effects remains a topic for future study.

4.2 Materials and Methods

Cell culture

P. infestans 88069 wt, LifeAct-eGFP transformant Pi-LA-GFP[32], and a transformant expressing cytosolic GFP (Pi-14-3-GFP)[38] were maintained at 18°C in the dark on rye sucrose agar[68] supplemented with vancomycin (20 μg/ml), ampicillin (100 μg/ml), and amphotericin B (10 μg/ml), and, in addition, for the transformants with geneticin (5 μg/ml). Fresh zoospores were generated by immersing mature mycelium (9 to 11 days old) with 5 ml of sterilized tap water and incubation for 3 hours in the dark at 4°C during which zoospores are released in the water. The obtained zoospore-rich suspension was decanted from the mycelial plate into plastic tubes and used for experiments, as described in detail in[8] and below.

For inoculation of tomato cells, 2 ml of the zoospore suspension (5×10^6 zoospores per ml) was added to 2 ml of a 5-day-old tomato MsK8 cell suspension culture[40]. For imaging, 30 μl of this mixture was enclosed in a bio-foil slide and incubated overnight at room temperature in the dark. Inoculation of potato plantlets[69] was done by applying one droplet (10 μl) containing 5×10^4 zoospores to etiolated stems. After incubation overnight in the dark at room temperature, the plantlets were transferred to a glass bottom imaging dish (MatTek, Ashland, USA) and covered with an agar pad.

For invasion studies on artificial substrates, zoospores were encysted (manual shaking, 1 min) and diluted to a concentration of 10^5 spores per milliliter, and applied to an 18 mm × 18 mm glass slide, with or without a PDMS coating, in a 80-μl droplet. The slides were mounted in a bespoke three-dimensional printed sample chamber to retain high moisture levels. The digital design file for the three-dimensional printed sample chambers is available from the code repository for this paper. For the cytoskeletal disruption, we inoculated fluorescent PDMS surfaces with an 80-μl zoospore suspension, allowed the cells to incubate for 1 hour, and then added 20 μl of a 25 μM fresh stock solution of LatB to a final concentration of 5 μM.

For phalloidin staining of invasive cells, wt zoospores were encysted as described above and grown on PDMS for 3 hours during which the cysts germinate, and the hyphae invade the substrate. Cells were prefixed using 800 μM MBS and subsequently fixed by 30-min exposure to a freshly prepared 2% formaldehyde solution followed by transfer to a solution containing 4% formaldehyde, 0.5%

glutaraldehyde, 1 mM MgCl2, 1 mM CaCl2, and 75 mM KCl. Samples were washed in Pipes buffer (2×15 min), followed by staining with phalloidin-rhodamine at 1 μM for 1 hour, washing with buffer (2 × 15 min), and imaging.

Surfaces

Displacement sensors were produced and characterized as described in[8]. In brief, a 1:30 Sylgard 184 cross-linker:base mix with fluorophore (15 μl of Pyrromethane 650 at 400 μg/ml per gram of Sylgard) is prepared and degassed (10 min, 1000g centrifugation) followed by spin-coating 150 μl on a 18 mm × 18 mm #1 glass slide. Before spin-coating, slides are cleaned with isopropyl alcohol and MilliQ water and dried in an oven at 60°C and exposed to N2/O2 plasma for 1 min. The spin-coating is a two-stage process: 20 s at 500 rpm for surface wetting, followed by 120 s at 2000 rpm to reduce thickness to a layer of ≈33 μm. After coating with PDMS, the slides are placed in a vacuum chamber for 30 min to remove air bubbles followed by curing at 70°C overnight. The PDMS elastomer is highly optically transparent. Nonetheless, because of the mismatch in refractive with both the glass onto which it is deposited and the aqueous medium in which our experiments are performed, light refraction at the PDMS-water and PDMS-glass interfaces leads to a reduction in detected fluorescence emission of 16.5% as compared to uncoated glass coverslips (Fig. S10). To correct for this, all quantitative metrics used in this study are normalized with respect to the baseline intensity in a posterior section of the germ tube, away from the hyphal tip, and thus report on normalized relative variations within an image such that these results are insensitive to the absolute intensities.

Imaging

For experiments on plant cell invasion and laser ablation, we used a Roper Spinning Disk Confocal System (Evry, France) consisting of a CSU-X1 spinning disk head (Yokogawa, Japan) mounted on a Nikon Eclipse Ti microscope (Tokyo, Japan) equipped with Perfect Focus system and a 100× Plan-Apochromat 1.4 numerical aperture (NA) oil immersion objective was used for imaging. Fluorescence imaging was performed using a 491- or 543 nm laser line combined with band-pass or long-pass emission filtering (530/50 or 560 nm, Chroma Technology). Images were acquired with a Prime 95B Scientific CMOS camera (Photometrics), controlled by MetaMorph software (Molecular Devices, California). For experiments on PDMS surfaces, images were recorded on a Nikon C2 scanning head mounted to a Nikon Eclipse Ti microscope and equipped with a 60× oil immersion objective (NA = 1.4). For time series measurements, we imaged at the largest field-of-view size, using a

512 pixel × 512 pixel wide view of a region of interest 213 μm × 213 μm in size. Three-dimensional image stacks were acquired once per 2 min, taking 1 min per stack, followed by 1 min without illumination. Each three-dimensional image stack consisted of approximately 41 slices and a z-step size of 0.5 μm. Higher-resolution images were obtained 2 and 4 hours after applying cells to the surface with a field of view of 50 μm × 50 μm at 512 pixels × 512 pixels. All raw data were converted to Tag Image File Format (tiff) without compression before data analysis.

Laser ablation

For laser ablation, we made use of a high-power pulsed Teem Photonics SNG-03E 532 nm laser (Meylan, France) with a 1000-ns pulse length, which was fed into the Roper Spinning Disk microscope using an iLas 2 FRAP/PA illumination setup (Roper Scientific, Evry, France). Microscope slides containing germinating sporangia were prepared as described in[32].

Data analysis

For laser ablation experiments, images were postprocessed in FIJI (https://imagej.net/Fiji; background subtraction, rolling ball radius 50.0 pixels and linear contrast stretching). For all other experiments, images were analyzed using custom-built scripts in Matlab 2018b. In short, all images were imported after which a region of interest containing a single cell was selected. For surface deformation profiling, we refer to a detailed description in[8]. Actin accumulation in the hyphal tip, expressed by the scalar α, was determined from the XZ projections of three-dimensional image stacks, recorded by imaging LifeAct-eGFP, using a home-written algorithm. This procedure first traces the centerline of the hyphae from cyst to tip, locally averaging the LifeAct-eGFP intensity over a small window to segment the hyphae. Then, it computes the intensity profile along this tube contour to compute the actin accumulation. We have verified that the orientation of the projection has no qualitative effect on the results (see the Supplementary Materials).

Fitting surface deformations

We use a mechanical model to analyze the indenter geometry during the invasion process by fitting experimentally obtained surface deformation profiles. The mechanical model, described in detail in chapter 3[8], relies on balancing indentation and adhesion forces, applied by ellipsoidal elements that are spatially separated but mechanically coupled and that are both modeled as ellipsoidal Hertzian contact sites. We assume a Poisson ratio (μ) of 0.45 for the PDMS, and a modulus of

0.58 MPa as was previously measured[8]. The model assumes an invasion angle of 49°, also determined from experiments[8], and fits five geometrical parameters to a displacement profile of the surface in an iterative process. The geometrical parameters are the width/height of both indentation and adhesion sites and the distance between these sites. In this study, we use this procedure to extract the radius of curvature of the indentation site at the hyphal tip, defined as the smallest dimension of the indenter.

Finite-element simulations

To study the mechanical deformations in both the tip and the substrate during tip invasion, we develop a finite element model. We model the tip as a hemispherical shell of radius R = 5 μm that is supported by an elastic actin gel at the interior. The cell wall of the tip is treated as a thin elastic shell of thickness h = 50 nm, Young's modulus Ewall = 20 MPa, and Poisson ratio $\mu_{wall} = 0.3$[26,70,71]. While the mature cell wall has a modulus on the order of several gigapascals[70,71], the lower value used here reflects the cell wall softening that occurs to allow for tip growth[26]. The internal turgor pressure P in the tip results in a prestress in the cell wall, which can be estimated as $\sigma_{\theta\theta,0} = \sigma_{\phi\phi,0} = PR_0/(2h)$, where R_0 is the radius of the stress-free tip[72]. In our calculations, we assume P = 1 MPa, as determined previously for *Phytophthora*[8], leading to lateral stresses in the cell wall in the order of 50 MPa. The cell wall is supported by an actin gel, which we consider as an isotropic and linearly elastic material that fills the complete tip. The gel is characterized by a Young's modulus Egel, which we vary in our calculations, and a Poisson ratio $\mu_{gel} = 0.4$[73]. Last, the substrate is treated as a linearly elastic isotropic solid with Young's modulus Esub = 0.6 MPa and Poisson ratio $\mu_{sub} = 0.45$[8]. The indentation process is modeled by applying a prescribed displacement to the lower boundary of the elastic substrate while keeping the top of the tip fixed. The contact between the tip wall and the substrate is implemented using an augmented Lagrangian formalism, which effectively prevents overlap of the tip and the substrate. The equilibrium shape of the tip and substrate, the local stresses, and the resulting indentation force are found by minimizing the total elastic energy using the finite element method, as implemented in Comsol Multiphysics. We use quadratic elements on a quadrilateral mesh for the elastic substrate and a triangular mesh for the actin gel, which is refined in the contact region. We have checked the accuracy of the solutions by performing calculations for different mesh parameters. The contact problem leads to a highly nonlinear system of equations, which is solved iteratively using Newton's method. Small incremental steps in the prescribed displacement had to be used for the solution to converge. Convergence issues did

not allow us to obtain results for large indentation depths; therefore, we have only considered the initial stages of indentation when the forces and displacements are relatively small.

Supporting information

Computational analysis of image data

Image analysis was performed on home-developed scripts written in MatLab; all original code files and extended documentation are available publicly from: https://github.com/jorissprakel/phytophthora_mechanostat

Actin accumulation in hyphal tips

We used confocal microscopy to obtain three-dimensional image stacks of individual germ tubes during pressure application onto an artificial substrate. For analyzing the F-actin density, visualised by the LifeAct-eGFP reporter In *Phytophthora infestans* transformant Pi-LA-GFP, we first construct maximum intensity projections either as a top view (xy projection) or side view (xz projection). We have chosen this approach because we found that maximum projections enable comparison of the most fluorescent region independent of hyphal thickness, making comparisons more robust and independent of local cell morphology. From these projections, we first determined the hyphal centre line (indicated as a yellow line in main text Figure 1I) using an iterative skeletonization function. We note that the determined centre line never extends fully into the tip edge due to the reduction algorithm, which can lead to an underestimation of the accumulation factor α in extremely polarized cells, although rarely observed. We then record the fluorescence intensity along this centre line, averaged for each point on the centre line over the entire width of the germ tube. From the trace of fluorescence intensity versus position in the germ tube obtained in this way we compute the accumulation factor $\alpha = \frac{I_{max}}{I_{base}} - 1$, where I_{max} is the peak intensity, located at or near the tip, and Ibase the mean baseline intensity, recorded in the posterior section of the germ tube. If the F-actin concentration, judged from the LifeAct intensity, is homogeneous along the germ tube, $\alpha = 0$, while strong tip-accumulation gives $\alpha \gg 0$. Additional examples of this analysis are shown in Figure S4. We have confirmed that both, side (xz) and top (xy) projections give results that are qualitatively similar as shown in Figure S5.

Displacement analysis

Our approach to measure the pathogen induced surface deformations, expressed as the displacement Δh along the surface normal, was described in detail before[8]. In short: we record three-dimensional image stacks of a fluorescent PDMS in contact with a non-fluorescent aqueous medium. To extract, for each xy-pixel, the surface

location in z, denoted here as Δh, where Δh = 0 is the position of the substrate in area without deformation, we fit the intensity decay at the PDMS-medium interface to a sigmoidal function. We then perform a tilt correction, to resolve small tilt angles of the surface with respect to the imaging plane. This results in spatial (xy) maps of surface displacements (Δh), which are used in subsequent analysis.

Deformation-actin correlation analysis

We performed analyses to correlate, both spatially and temporally, the local surface displacement (Δh) with the local intensity of LifeAct-eGFP, as a F-actin marker. The code computes for each pixel the relative LifeAct-eGFP fluorescence and links this to the local displacement from the analysis described above. We then divided the data in 3 zones; adhesion zones, where Δh > +0.5μm (approximately 5x the surface displacement resolution), zones of no to weak mechanical interactions, where +0.5μm>Δh>-0.5μm, and indentation zones, where Δh < -0.5μm (approximately 5x the surface displacement resolution), and aggregated fluorescence intensity data for these different zones.

Additional data: cytoplasmic GFP reporter

To verify that the observed increase in actin accumulation during pressure application, and prior to substrate entry, is not the result of accumulation of cytoplasm containing unbound LifeAct reporter, we performed control experiments on a *P. infestans* transformant that expresses a cytoplasmic GFP (Pi-14-3-GFP). We performed three-dimensional confocal imaging both at higher frame rates and with lower resolution (Fig. S2A-B) and at lower frame rates with higher resolution (Fig. S2C-D). Upon contact and at the start of invasion a small increase in fluorescence is at times observed; this feature is substantially weaker as compared to the LifeAct actin reporter line Pi-LA-GFP, and does not show any microstructural features as expected. Only after host penetration, when cytoplasmic and nuclear repositioning are expected to occur to initiate the invasion process inside the host, we do observe a substantial accumulation of cytoplasm in the tip. This confirms that our reported results for the accumulation of actin in the hyphal tip prior to and during penetration are not the result of random cytoplasmic streaming but due to mechanical feedback to the cytoskeleton.

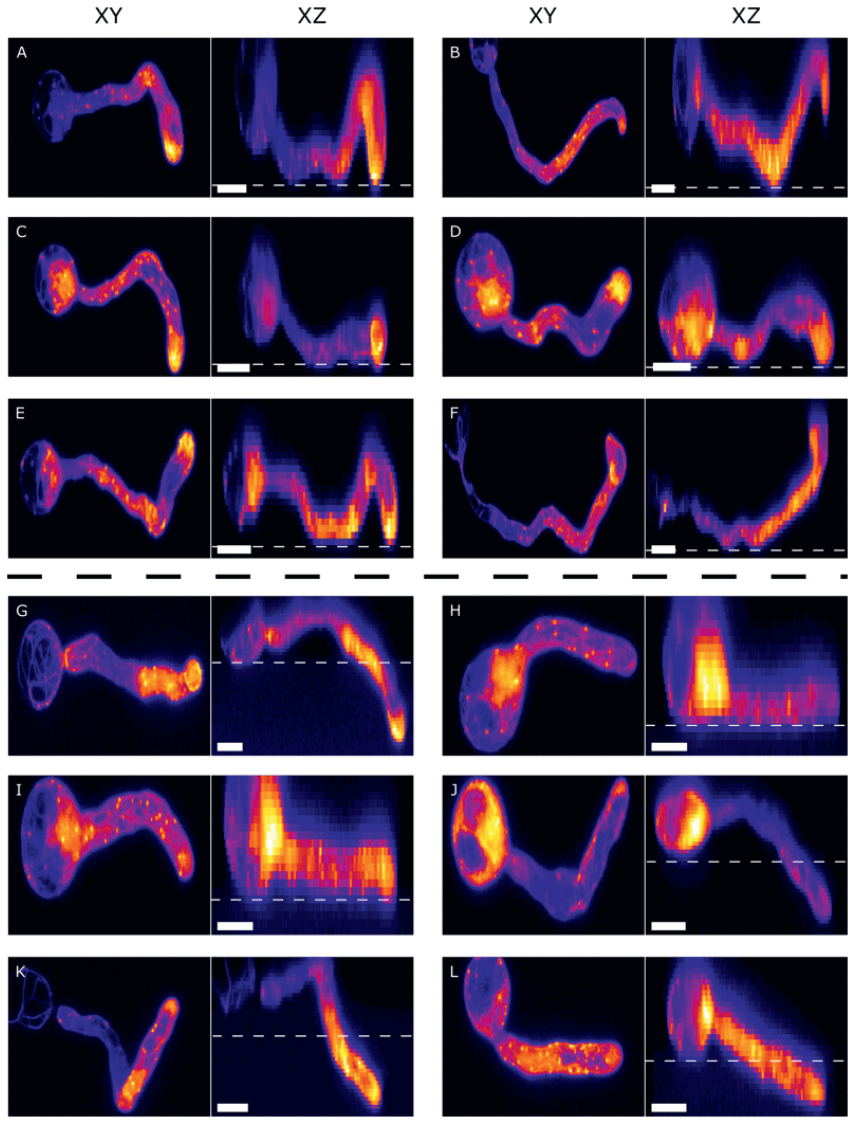

Figure 4.8. Additional examples of the actin cytoskeletal structure in Pi-LA-GFP during force application and penetration, all taken 4hpi on either glass (**A**-**F**) or PDMS (**G**-**L**), in a maximum intensity top view projection (xy, left) and side view projection (xz, right). Dashed lines indicate the substrate-medium interface. Scale bars represent 5 μm.

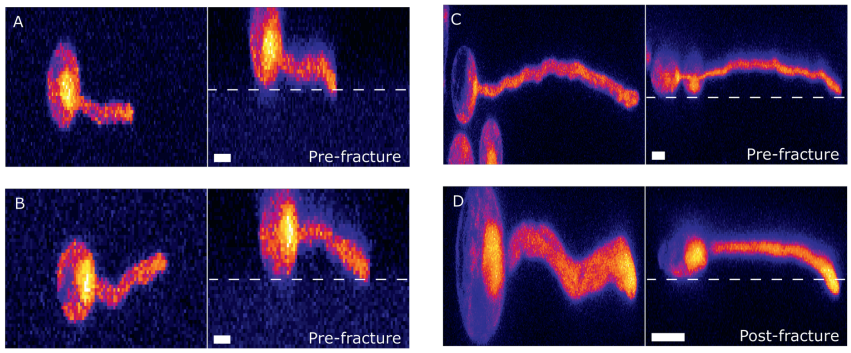

Figure 4.9. Confocal images of Pi-14-3-GFP on PDMS surfaces, showing a maximum intensity top (xy, left) and side (xz, right) projection. **A**-**B**: lower resolution from dynamic imaging, **C**-**D**: higher resolution images with a lower acquisition rate. Scale bar represents 5 μm.

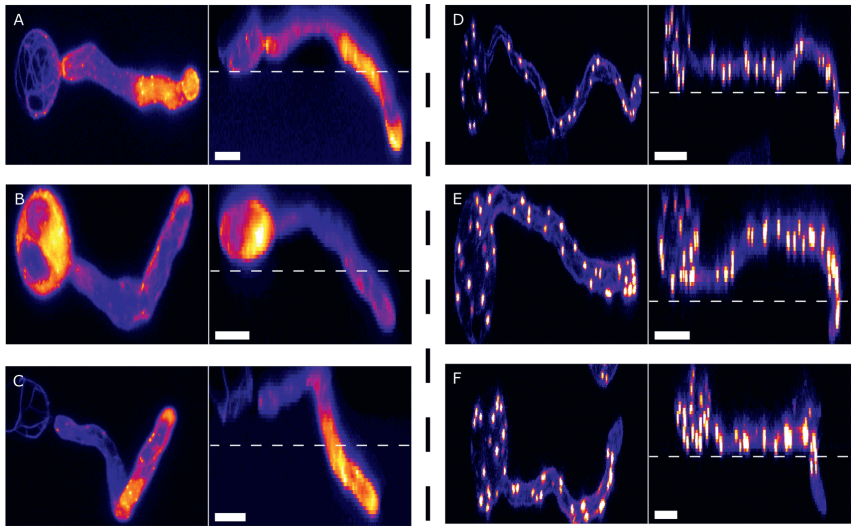

Figure 4.10. Comparison of actin cytoskeleton imaging with a genetically-expressed LifeAct-eGFP actin marker (Pi-LA-GFP) (**A**-**C**) and a phalloidin-rhodamine conjugate staining of fixed wt-Pi cells (**D**-**F**), all recorded during penetration of PDMS substrates. Each image shows maximum intensity top (xy, left) and side projections (xz, right). Scale bar represents 5 μm.

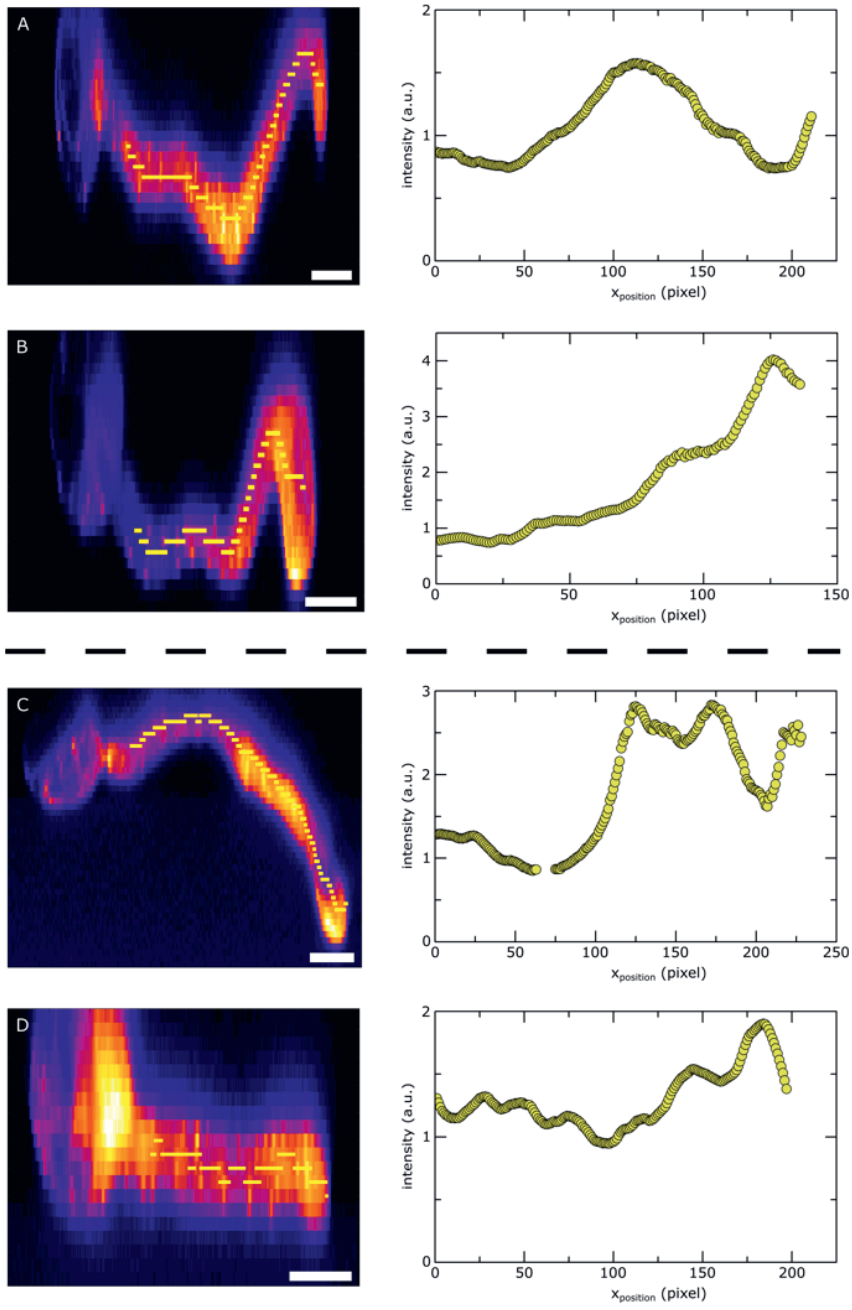

Figure 4.11. Additional examples of the centre line detection (left) and LifeAct-eGFP intensity profile (right) in maximum intensity xz projections for Pi-LA-GFP (2hpi) on glass (**A**-**B**) and PDMS (**C**-**D**). Scale bars represent 5 μm.

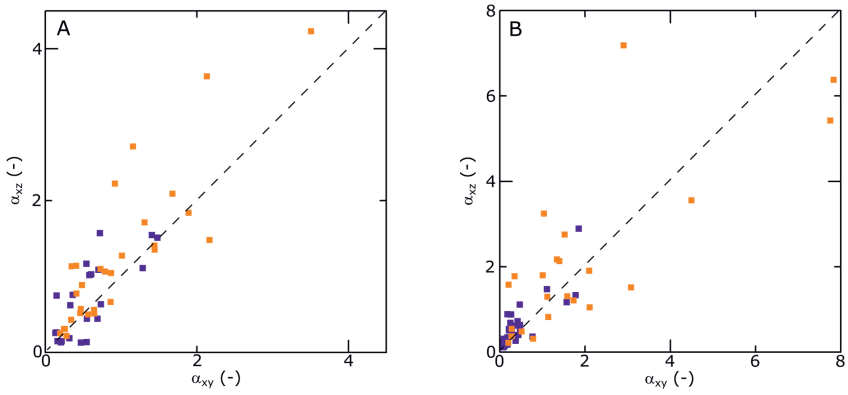

Figure 4.12. Comparison of the values of the accumulation parameter α from side view (xz) versus top view (xy) maximum intensity projections, at 2hpi (**A**) and 4 hpi (**B**). Purple squares represent data on PDMS substrates, orange squares on glass substrates. Dashed line is a guide to the eye that indicates perfect correlation.

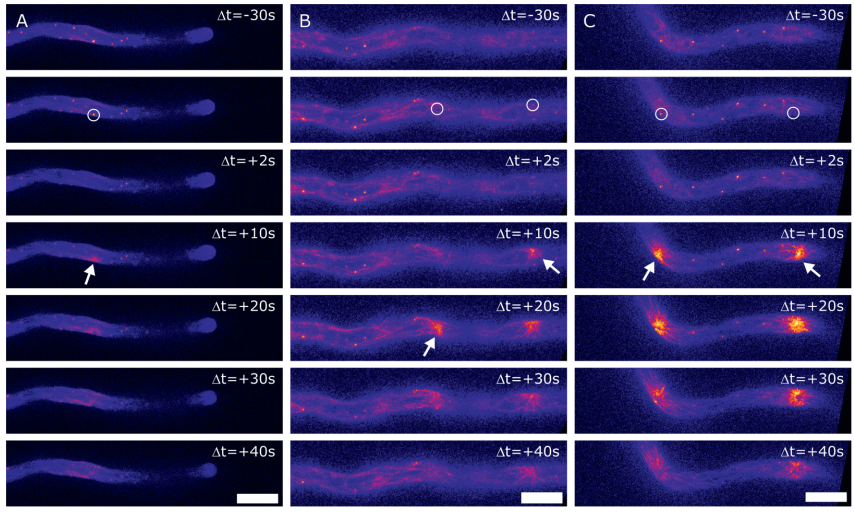

Figure 4.13. Additional data from laser ablation experiments on Pi-LA-GFP. Approximately 10-20 seconds post ablation a fluorescent response of the actin network is observed in the form of an aster-like configuration (arrow indicates first appearance). Scale bar represents 5 μm. The white circles indicate target locations of the ablation laser.

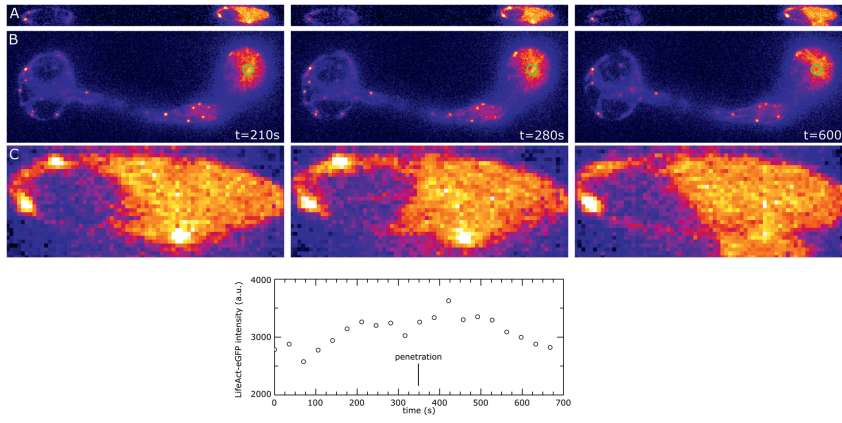

Figure 4.14. Additional analysis on a unique observation (N=1) of Pi-LA-GFP invasion of a potato plantlet, belonging to the data shown in main text Figure 2**C**&**E**. (**A** and **B**) Top and side view (xy and xz maximum intensity projection) to identify the time of penetration by the formation of a protrustion of the pathogen into the host tissue, occurring at the time point 270-300s in this time sequence. (**C** and scatterplot) Analysis of the local LifeAct-eGFP intensity (in the area indicated by the green circle) at the hyphal apex, showing a transient increase in LifeAct-eGFP intensity, signaling the formation of the actin aster, whose intensity peaks 1 minute after penetration, after which the signal gradually decreases over the course of several minutes.

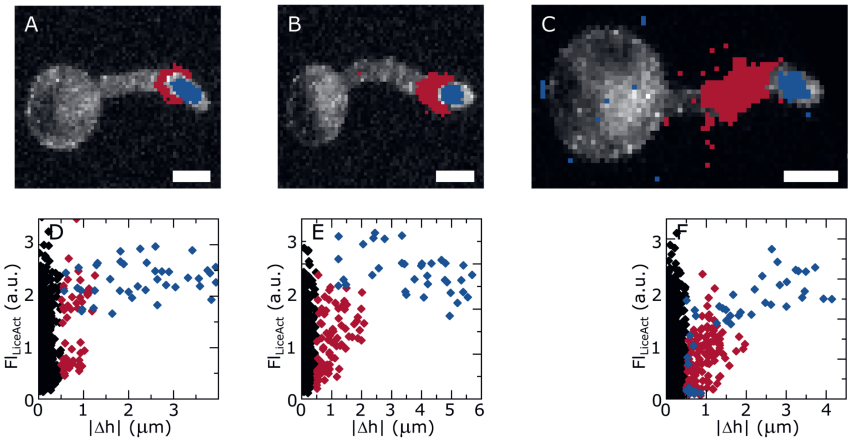

Figure 4.15. Additional examples of the data shown in main text Figures **4E**-**F**. Top row **A**-**C**: overlay of identified adhesion (red) and indentation sites (blue) on the xy-projection of the LifeAct eGFP signal for a single cell showing strong localization in two distinct zones. Bottom row **D**-**F**: corresponding scatterplots, showing the local LifeAct eGFP intensity (Y-axis) and absolute surface deformation amplitude for each pixel at a single time point for a single cell (X-axis); data is grouped into adhesive (red), indentation (blue) and non-interacting sites (black) on the basis of the sign and amplitude of the local surface deformation (as explained in main text).

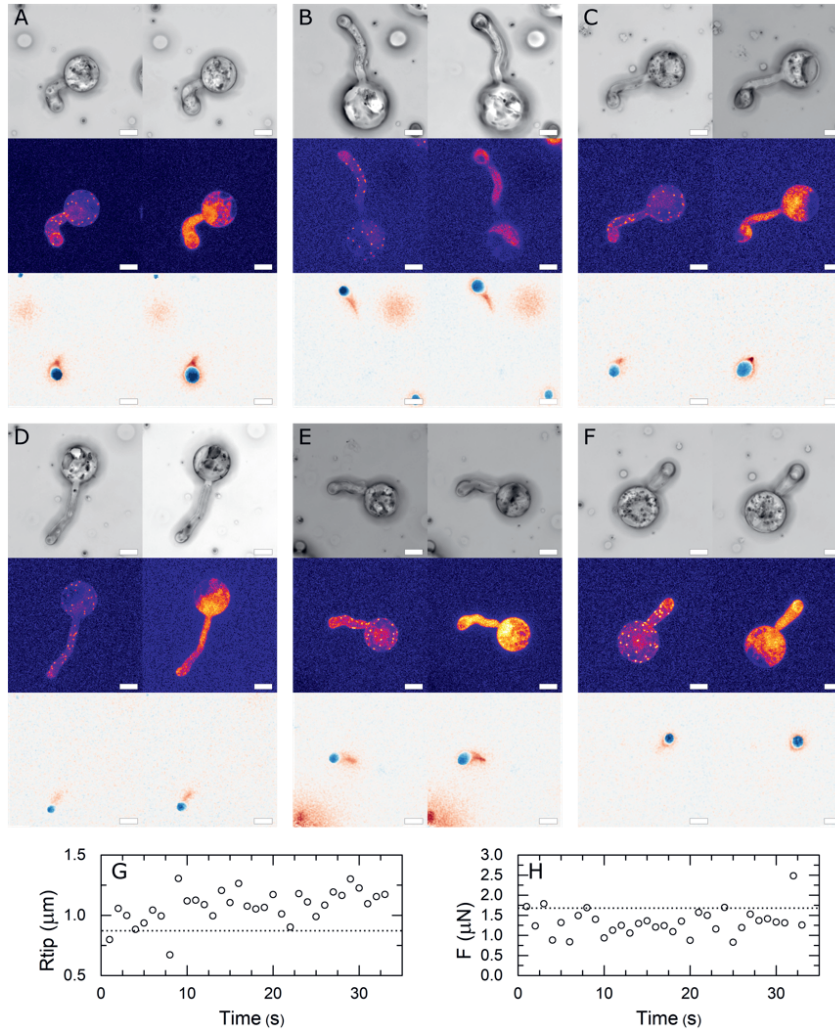

Figure 4.16. Additional examples (N=6 cells from 3 independent experiments) that visibly show tip widening upon LatB treatment. For each cell in **A**-**D** the same cell is shown immediately prior to LatB treatment (right, t=-2 min), and some time after LatB addition (left, **A**=38min, **B**=43min, **C**=38min, **D**=38min, **E**=76min, **F**=37min). Top rows show the brightfield channel, middle row the LifeAct-eGFP channel and bottom row the surface deformation map, in which the tip blunting is visible in the expansion of the indentation zone (blue). Scale bars represent 5 μm. **G**-**H**: kinetics of tip reshaping upon LatB treatment (at t=0) for a cell recorded at a lower spatial but higher temporal resolution showing the transient change in tip curvature (**G**) and indentation force (**H**).

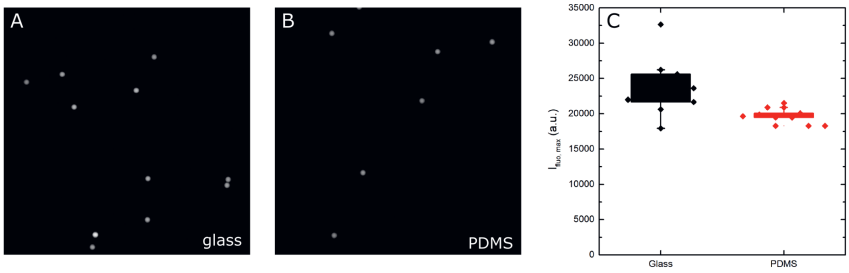

Figure 4.17. Quantification of the reduction in fluorescence emission detection in confocal microscopy experiments as the result of the PDMS elastomer layer on glass slides: **A**-**B**) confocal microscopy images of fluorescein-labelled melanin microparticles (nominal diameter = 5 mm), acquired using identical excitation/emission settings as during GFP-marker line imaging on both uncoated glass (**A**) and PDMS-coated glass (**B**). (**C**) Peak intensity comparison shows a modest 16.5% reduction in fluorescence transmission to the confocal detector. N=10 beads per substrate.

Experiment	Figure	Sample numbers
Actin structure	Figure 1 A-B, E-F	* 0.56 MPa PDMS Pi-LA-GFP: N = 32 (from 3 independent experiments)
	Figure 1 C-D, G-H	* 0.56 MPa Glass Pi-LA-GFP: N = 45 (from 3 independent experiments)
	Figure 1 K	* 0.56 MPa PDMS Pi-LA-GFP: N = 10 (from 6 independent experiments)
	Figure 1 L	* 0.56 MPa PDMS Pi-LA-GFP: 2hpi: N = 31 (from 4 independent experiments) * 0.56 MPa PDMS Pi-LA-GFP: 4hpi: N = 27 (from 2 independent experiments) * Glass Pi-LA-GFP: 2hpi: N = 32 (from 3 independent experiments) * Glass Pi-LA-GFP: 4hpi: N = 27 (from 3 independent experiments)
Cell / stem penetration	Figure 2 A-B (MsK8 tomato cells)	* Pi-LA-GFP: N = 4 (from 1 independent experiment)
	Figure 2 C-E (Etiolated potato stem section)	* Pi-LA-GFP: N = 1 (from 1 independent experiments)

Experiment	Figure	Sample numbers
Laser ablation	Figure 3	* Pi-14:3-GFP (Control): N = 5 (from 1 independent experiment) * Pi-LA-GFP: N = 10 (from 2 independent experiment) * Pi-LA-GFP: Plaques: N = 10 (from 1 independent experiment) * Pi-LA-GFP: Non-plaques: N = 9 (from 1 independent experiment) * Pi-LA-GFP: Distal: N = 10 (from 1 independent experiment) * Pi-LA-GFP: Tip: N = 9 (from 1 independent experiment)
Deformation & LifeAct-GFP correlation	Figure 4 A-F	* 0.56 MPa PDMS Pi-LA-GFP: N = 6 (from 5 independent experiments)
	Figure 4 H	* 0.56 MPa PDMS Pi-LA-GFP: N = 6 (from 5 independent experiments)
Force and tip curvature fitting	Figure 6	* 0.56 MPa PDMS Pi-LA-GFP: N = 5 (from 3 independent experiments)
LatB disruption	Figure 7	* 0.56 MPa PDMS Pi-LA-GFP + 5 μMLatB: N = 6 (from 3 independent experiments)

References

[1] Pascale V. Balhadère and Nicholas J. Talbot. Fungal pathogenicity—establishing infection. In *Molecular Plant Pathology*, pages 1–25. CRC Press, jan 2020.

[2] Stuart Fawke, Mehdi Doumane, and Sebastian Schornack. Oomycete Interactions with Plants: Infection Strategies and Resistance Principles. *Microbiology and Molecular Biology Reviews*, 79(3):263–280, 2015.

[3] Richard J Howard and Barbara Valent. BREAKING AND ENTERING: Host Penetration by the Fungal Rice Blast Pathogen *Magnaporthe grisea*. *Annu. Rev. Microbiol*, 50:491–512, 1996.

[4] Maita Latijnhouwers, Pierre J.G.M. de Wit, and Francine Govers. Oomycetes and fungi: similar weaponry to attack plants. *Trends in Microbiology*, 11(10):462–469, oct 2003.

[5] Raquel O. Rocha, Christian Elowsky, Ngoc T.T. Pham, and Richard A. Wilson. Spermine-mediated tight sealing of the *Magnaporthe oryzae* appressorial pore–rice leaf surface interface. *Nature Microbiology*, 5(12):1472–1480, dec 2020.

[6] Sara L. Tucker and Nicholas J. Talbot. Surface Attachment and Pre-Penetration Stage Development by Plant Pathogenic Fungi. *Annual Review of Phytopathology*, 39(1):385–417, sep 2001.

[7] Clemens Bechinger, Karl Friedrich Giebel, Martin Schnell, Paul Leiderer, Holger B Deising, and Martin Bastmeyer. Optical measurements of invasive forces exerted by appressoria of a plant pathogenic fungus. *Science*, 285(5435):1896–1899, 1999.

[8] Jochem Bronkhorst, Michiel Kasteel, Stijn van Veen, Jess M. Clough, Kiki Kots, Jesse Buijs, Jasper van der Gucht, Tijs Ketelaar, Francine Govers, and Joris Sprakel. A slicing mechanism facilitates host entry by plant-pathogenic *Phytophthora*. *Nature Microbiology*, 6(8):1000–1006, aug 2021.

[9] R. J. Howard, M. A. Ferrari, D. H. Roach, and N. P. Money. Penetration of hard substrates by a fungus employing enormous turgor pressures. *Proceedings of the National Academy of Sciences*, 88(24):11281–11284, 1991.

[10] Ayelen Tayagui, Yiling Sun, David A. Collings, Ashley Garrill, and Volker Nock. An elastomeric micropillar platform for the study of protrusive forces in hyphal invasion. *Lab on a Chip*, 17(21):3643–3653, 2017.

[11] Susannah M. Porter. The fossil record of early eukaryotic diversification. *The Paleontological Society Papers*, 10:35–50, nov 2004.

[12] Shaowu Meng, Trudy Torto-Alalibo, Marcus C. Chibucos, Brett M. Tyler, and Ralph A. Dean. Common processes in pathogenesis by fungal and oomycete plant pathogens, described with Gene Ontology terms. *BMC Microbiology*, 9(SUPPL. 1):1–11, feb 2009.

[13] Nicholas P. Money, Christopher M. Davis, and J. P. Ravishankar. Biomechanical evidence for convergent evolution of the invasive growth process among fungi and oomycete water molds. *Fungal Genetics and Biology*, 41(9):872–876, 2004.

[14] George Agrios. *Plant Pathology*, volume 6. Elsevier, 2005.

[15] Nicholas J Talbot. Appressoria, *Current Biology*, 29(5):144-146 mar 2019.

[16] Yasin F. Dagdas, Kae Yoshino, Gulay Dagdas, Lauren S. Ryder, Ewa Bielska, Gero Steinberg, and Nicholas J. Talbot. Septin-mediated plant cell invasion by the rice blast fungus, *Magnaporthe oryzae*. *Science*, 336(6088):1590–1595, jun 2012.

[17] Lin Li, Xue-Ming Zhu, Zhen-Zhu Su, Maurizio Del Poeta, Xiao-Hong Liu, and Fu-Cheng Lin. Insights of roles played by septins in pathogenic fungi. *Virulence*, 12(1):1550–1562, dec 2021.

[18] Forrest G. Chumley and Barbara Valent. Genetic analysis of melanin-deficient, non-pathogenic mutants of *Magnaporthe grisea*. *Mol. Plant-Microbe Interact*, 3(3):135– 143, 1990.

[19] Michael H. Wheeler and Alois Bell , A. Melanins and Their Importance in Pathogenic Fungi. *JAMA: The Journal of the American Medical Association*, 255(7):959, feb 1986.

[20] Leila M Blackman, Darren P Cullerne, and Adrienne R Hardham. Bioinformatic characterisation of genes encoding cell wall degrading enzymes in the *Phytophthora parasitica* genome. *BMC Genomics*, 15(1):785, 2014.

[21] L. J. Grenville-Briggs, V. L. Anderson, J. Fugelstad, A. O. Avrova, J. Bouzenzana, A. Williams, S. Wawra, S. C. Whisson, P. R.J. Birch, V. Bulone, and P. van West. Cellulose Synthesis in *Phytophthora infestans* Is Required for Normal Appressorium Formation and Successful Infection of Potato. *the Plant Cell Online*, 20(3):720–738, 2008.

[22] Adrienne R. Hardham. The cell biology behind *Phytophthora* pathogenicity. *Australasian Plant Pathology*, 30(2):91–98, 2001.

[23] V. A. Ludowici, Zhang WeiWei Zhang WeiWei, L. M. Blackman, and A. R. Hardham. Phytophthora nicotianae. In *Phytophthora: a global perspective*, chapter Phytophtho, pages 113–123. CABI, Wallingford, 2013 edition, 2013.

[24] Stephen C. Whisson, Petra C. Boevink, Shumei Wang, and Paul RJ Birch. The cell biology of late blight disease. *Current Opinion in Microbiology*, 34:127–135, 2016.

[25] Christine Cameron and Anja Geitmann. Cell mechanics of pollen tube growth, aug 2018.

[26] Pierre Fayant, Orlando Girlanda, Youssef Chebli, Carl Éric Aubin, Isabelle Villemure, and Anja Geitmann. Finite element model of polar growth in pollen tubes. *Plant Cell*, 22(8):2579–2593, aug 2010.

[27] Anja Geitmann and Jacques Dumais. Not-so-tip-growth. *Plant Signaling and Behavior*, 4(2):136–138, feb 2009.

[28] Jacques Dumais. Mechanics and hydraulics of pollen tube growth, nov 2021.

[29] Jacques Dumais, Sidney L. Shaw, Charles R. Steele, Sharon R. Long, and Peter M. Ray. An anisotropic-viscoplastic model of plant cell morphogenesis by tip growth. *The International Journal of Developmental Biology*, 50(2-3):209–222, 2006.

[30] Sidney L Shaw, Jacques Dumais, and Sharon R Long. Cell Surface Expansion in Polarly Growing Root Hairs of Medicago truncatula. *Plant Physiology*, 124(3):959–970, nov 2000.

[31] Kiki Kots, Harold J.G. Meijer, Klaas Bouwmeester, Francine Govers, and Tijs Ketelaar. Filamentous actin accumulates during plant cell penetration and cell wall plug formation in *Phytophthora infestans*. *Cellular and Molecular Life Sciences*, 74(5):909–920, 2017.

[32] Harold J G Meijer, Chenlei Hua, Kiki Kots, Tijs Ketelaar, and Francine Govers. Actin dynamics in *Phytophthora infestans*; rapidly reorganizing cables and immobile, long-lived plaques. *Cellular Microbiology*, 16(6):948–961, 2014.

[33] K. L. Johnson. *Contact Mechanics*. Cambridge University Press, may 1989.

[34] Julia Riedl, Alvaro H. Crevenna, Kai Kessenbrock, Jerry Haochen Yu, Dorothee Neukirchen, Michal Bista, Frank Bradke, Dieter Jenne, Tad A. Holak, Zena Werb, Michael Sixt, and Roland Wedlich-Soldner. Lifeact: a versatile marker to visualize F-actin. *Nature Methods*, 5(7):605–607, jul 2008.

[35] Chenlei Hua, Kiki Kots, Tijs Ketelaar, Francine Govers, and Harold J. G. Meijer. Effect of Flumorph on F-Actin Dynamics in the Potato Late Blight Pathogen *Phytophthora infestans*. *Phytopathology*, 105(4):419–423, apr 2015.

[36] Sandra L. Jackson and Adrienne R. Hardham. Dynamic Rearrangement of the Filamentous Actin Network Occurs during Zoosporogenesis and Encystment in the Oomycete *Phytophthora cinnamomi*. *Fungal Genetics and Biology*, 24(1-2):24–33, jun 1998.

[37] Tijs Ketelaar, Harold J.G. Meijer, Marjolein Spiekerman, Rob Weide, and Francine Govers. Effects of latrunculin B on the actin cytoskeleton and hyphal growth in *Phytophthora infestans*. *Fungal Genetics and Biology*, 49(12):1014–1022, dec 2012.

[38] Elysa J.R. Overdijk, Jeroen De Keijzer, Deborah De Groot, Charikleia Schoina, Klaas Bouwmeester, Tijs Ketelaar, and Francine Govers. Interaction between the moss P*hyscomitrella patens* and *Phytophthora*: a novel pathosystem for live-cell imaging of subcellular defence. *Journal of Microscopy*, 263(2):171–180, aug 2016.

[39] Sophie K. Walker, Kenny Chitcholtan, YuPing Yu, Gabrielle M. Christenhusz, and Ashley Garrill. Invasive hyphal growth: An F-actin depleted zone is associated with invasive hyphae of the oomycetes *Achlya bisexualis* and *Phytophthora cinnamomi*. *Fungal Genetics and Biology*, 43(5):357–365, may 2006.

[40] Charikleia Schoina, Klaas Bouwmeester, and Francine Govers. Infection of a tomato cell culture by *Phytophthora infestans*; a versatile tool to study *Phytophthora*-host interactions. *Plant Methods*, 13(1):88, dec 2017.

[41] Jun Wu, Richard B Dickinson, and Tanmay P Lele. Investigation of in vivo microtubule and stress fiber mechanics with laser ablation. *Integrative Biology*, 4(5):471–479, may 2012.

[42] Teresa Zulueta-Coarasa and Rodrigo Fernandez-Gonzalez. Laser ablation to investigate cell and tissue mechanics in vivo. In Yu Sun, Deok-Ho Kim, and Craig A. Simmons,

editors, *Integrative Mechanobiology: Micro- and Nano Techniques in Cell Mechanobiology*, pages 128–147. Cambridge University Press, Cambridge, nov 2015.

[43] Hannie S. van der Honing, Anne Mie C. Emons, and Tijs Ketelaar. Actin based processes that could determine the cytoplasmic architecture of plant cells. *Biochimica et Biophysica Acta (BBA) - Molecular Cell Research*, 1773(5):604–614, may 2007.

[44] Sophie K Walker and Ashley Garrill. Actin microfilaments in fungi. *Mycologist*, 20(1):26–31, feb 2006.

[45] I. BRENT HEATH and SUSAN G.W. KAMINSKYJ. The organization of tip-growth-related organelles and microtubules revealed by quantitative analysis of freeze-substituted oomycete hyphae. *Journal of Cell Science*, 93(1):41–52, may 1989.

[46] Eugen Temperli, Urs Peter Roos, and Hans R. Hohl. Germ tube growth and the microtubule cytoskeleton in *Phytophthora infestans*: Effects of antagonists of hyphal growth, microtubule inhibitors, and ionophores. *Mycological Research*, 95(5):611–617, may 1991.

[47] I.Brent Heath, Gagan Gupta, and Suk Bai. Plasma Membrane-Adjacent Actin Filaments, but Not Microtubules, Are Essential for both Polarization and Hyphal Tip Morphogenesis in *Saprolegnia ferax* and *Neurospora crassa*. *Fungal Genetics and Biology*, 30(1):45–62, jun 2000.

[48] M. L. Gardel, J. H. Shin, F. C. MacKintosh, L. Mahadevan, P. A. Matsudaira, and D. A. Weitz. Scaling of F-Actin Network Rheology to Probe Single Filament Elasticity and Dynamics. *Physical Review Letters*, 93(18):188102, oct 2004.

[49] J. H. Shin, M. L. Gardel, L. Mahadevan, P. Matsudaira, and D. A. Weitz. Relating microstructure to rheology of a bundled and cross-linked F-actin network in vitro. *Proceedings of the National Academy of Sciences*, 101(26):9636–9641, jun 2004.

[50] Jonathan Stricker, Tobias Falzone, and Margaret L Gardel. Mechanics of the F-actin cytoskeleton. *Journal of Biomechanics*, 43(1):9–14, 2010.

[51] Federica Burla, Yuval Mulla, Bart E. Vos, Anders Aufderhorst-Roberts, and Gijsje H. Koenderink. From mechanical resilience to active material properties in biopolymer networks. *Nature Reviews Physics*, 1(4):249–263, apr 2019.

[52] Jingyuan Xu, Andre Palmer, and Denis Wirtz. Rheology and microrheology of semiflexible polymer solutions: Actin filament networks. *Macromolecules*, 31(19):6486–6492, 1998.

[53] Amir Sanati Nezhad, Mahsa Naghavi, Muthukumaran Packirisamy, Rama Bhat, and Anja Geitmann. Quantification of the Young's modulus of the primary plant cell wall using Bending-Lab-On-Chip (BLOC). *Lab on a Chip*, 13(13):2599, 2013.

[54] C.-L. Huang, H. Lindstrom, R. Nakada, and J. Ralston. Cell wall structure and wood properties determined by acoustics?a selective review. *Holz als Roh- und Werkstoff*, 61(5):321–335, oct 2003.

[55] A E Smith, K E Moxhams, and A P J Middelberg -. On uniquely determining cell-wall material properties with the compression experiment. *Chemical Engineering Science*, 53(23):3913–3922, 1998.

[56] Elisabeth Chanliaud and Michael J. Gidley. In vitro synthesis and properties of pectin/Acetobacter xylinus cellulose composites. *The Plant Journal*, 20(1):25–35, oct 1999.

[57] Anja Geitmann. How to shape a cylinder: pollen tube as a model system for the generation of complex cellular geometry. *Sexual Plant Reproduction*, 23(1):63–71, mar 2010.

[58] Kamran Hosseini, Leon Sbosny, Ina Poser, and Elisabeth Fischer-Friedrich. Binding Dynamics of α-Actinin-4 in Dependence of Actin Cortex Tension. *Biophysical Journal*, 119(6):1091–1107, sep 2020.

[59] Derek L. Huang, Nicolas A. Bax, Craig D. Buckley, William I. Weis, and Alexander R. Dunn. Vinculin forms a directionally asymmetric catch bond with F-actin. *Science*, 357(6352):703–706, aug 2017.

[60] Vassilis Papalazarou and Laura M Machesky. The cell pushes back: The Arp2/3 complex is a key orchestrator of cellular responses to environmental forces. *Current Opinion in Cell Biology*, 2021:37–44, 2020.

[61] Peter Bieling, Tai-De Li, Julian Weichsel, Ryan McGorty, Pamela Jreij, Bo Huang, Daniel A. Fletcher, and R. Dyche Mullins. Force Feedback Controls Motor Activity and Mechanical Properties of Self-Assembling Branched Actin Networks. *Cell*, 164(1-2):115–127, jan 2016.

[62] Ana Virel and Lars Backman. A Comparative and Phylogenetic Analysis of the -Actinin Rod Domain. *Molecular Biology and Evolution*, 24(10):2254–2265, jul 2007.

[63] Michael F. Seidl, Adrian Schneider, Francine Govers, and Berend Snel. A predicted functional gene network for the plant pathogen *Phytophthora infestans* as a framework for genomic biology. *BMC Genomics*, 14(1), 2013.

[64] Eric S S. Schiffhauer, Tianzhi Luo, Krithika Mohan, Vasudha Srivastava, Xuyu Qian, Eric R R. Griffis, Pablo A A. Iglesias, and Douglas N N. Robinson. Mechanoaccumulative Elements of the Mammalian Actin Cytoskeleton. *Current Biology*, 26(11):1473–1479, jun 2016.

[65] Yuval Mulla, Mario J Avellaneda, Antoine Roland, Lucia Baldauf, Sander J Tans, and Gijsje H Koenderink. Weak catch bonds make strong networks, 2020.

[66] M. C. JARVIS, D. R. THRELFALL, and J. FRIEND. Potato Cell Wall Polysaccharides: Degradation with Enzymes from *Phytophthora infestans*. *Journal of Experimental Botany*, 32(6):1309–1319, 1981.

[67] Lucile Michels, Vera Gorelova, Yosapol Harnvanichvech, Jan Willem Borst, Bauke Albada, Dolf Weijers, and Joris Sprakel. Complete microviscosity maps of living plant cells and tissues with a toolbox of targeting mechanoprobes. *Proceedings of the National Academy of Sciences of the United States of America*, 117(30):18110–18118, 2020.

[68] C. E. Caten. Spontaneous variability of single isolates of *Phytophthora infestans*. *Canadian Journal of Botany*, 48(5):897–905, may 1970.

[69] Klaas Bouwmeester. *The interplay between a Phytophthora RXLR effector and an Arabidopsis lectin receptor kinase*. 2010.

[70] Amir J. Bidhendi and Anja Geitmann. Methods to quantify primary plant cell wall mechanics. *Journal of Experimental Botany*, 70(14):3615–3648, jul 2019.

[71] Jean-Françcois Bolduc, Laurent J. Lewis, Carl-Éric Aubin, and Anja Geitmann. Finite-Element Analysis of Geometrical Factors in Micro-Indentation of Pollen Tubes. *Biomechanics and Modeling in Mechanobiology*, 5(4):227–236, oct 2006.

[72] L. D. Landau, E. M. Lifshitz, J. B. Sykes, W. H. Reid, and Ellis H. Dill. *Theory of Elasticity: Vol. 7 of Course of Theoretical Physics*, volume 13. jul 1960.

[73] FrankG. Schmidt, Florian Ziemann, and Erich Sackmann. Shear field mapping in actin networks by using magnetic tweezers. *European Biophysics Journal*, 24(5):348–353, 1996.

Molecular sensors reveal the mechano-chemical response of *P. infestans* walls and membranes to mechanical and chemical stress

Phytophthora infestans, causal agent of late blight in potato and tomato, remains challenging to control. Unravelling its biomechanics of host invasion, and its response to mechanical and chemical stress, could provide new handles to combat this devastating pathogen. Here, we introduce two fluorescent molecular sensors that reveal the micromechanical response of the cell wall-plasma membrane continuum in *Phytophthora infestans* during invasive growth and upon chemical treatment. When visualized by live-cell imaging the two probes report changes in cell wall (CW) porosity, and in chemical polarity and lipid order in the plasma membrane (PM). During invasive growth, mechanical interactions between the pathogen and a surface reveal clear and localized changes in the structure of both CW and PM. Moreover, the probes can reveal the specificity of chemical treatment to either CW and/or PM, unravelling the mode-of-action of crop protection agents. This mechano-chemical imaging strategy resolves, non-invasively and with high spatiotemporal resolution, how the CW-PM continuum adapts and responds to abiotic stress, and provides information on the dynamics and locus of cellular stress responses for which, to date, no other methods are available.

This chapter was submitted as:

Lucile Michels, Jochem Bronkhorst, Michiel Kasteel, Djanick de Jong, Bauke Albada, Tijs Ketelaar, Francine Govers & Joris Sprakel *Molecular sensors reveal the mechano-chemical response of Phytophthora infestans walls and membranes to mechanical and chemical stress* (2021)

5.1 Introduction

Host infection by biotrophic filamentous plant pathogens invariably commences with host entry, a complex process in which the pathogen utilizes mechanical weaponry to breach the protective barrier posed by the plant surface, guided and aided by biochemical interactions between pathogen and host. Understanding the nature and mechanisms of host invasion is an important route to find new solutions to control plant pathogens and mitigate yield losses resulting from plant diseases. From this vantage point, obtaining a complete picture of the plant-microbe interactions during host entry requires study of the invasion process from the perspective of the host and that of the pathogen, and taking both mechanical and chemical interactions into account.

Among the most damaging plant pathogens, is the oomycete *Phytophthora infestans*, causal agent of late blight in potato and tomato, and responsible for large crop yield losses and economic damage[1,2]. Despite tremendous progress in unravelling the biochemical host-pathogen interactions and continued efforts to breed resistant crops, *P. infestans* remains challenging to control, in part due to its large and rapid genetic adaptability[3]. While studies into the invasion strategies of this pathogen from a genetic, biochemical and cell biological perspective are abundant, very little is known about the strategies it exploits to gain mechanical entry into plants.

Various molecular-genetic and biochemical approaches as well as omics analyses are widely used to identify, on the one hand, *Phytophthora* genes encoding effectors and other proteins required for pathogenicity[3–7] and, on the other hand, plant genes implicated in immunity and susceptibility to late blight[8–10]. Additionally, the molecular mechanisms underlying the manipulation of plant immunity by effectors are widely studied[11–13].

Studies on genetics, secreted effectors and cytoskeletal regulation are vital to elucidate essential components of the invasion machinery of *P. infestans*. Yet, connecting how these components work in synchrony during infection, and how they couple to the mechanical process necessary to breach the plant surface remains challenging.

In a recent study[14], we took a first step to unravel the mechanics of host entry by *Phytophthora* spp. By using a combination of surface deformation imaging, molecular fracture sensors and modelling, we uncovered a mechanism, coined as 'naifu'-mechanism, that *Phytophthora* spp. use to enter their hosts. The discovery of this mechanism gives rise to a plethora of new questions on how *Phytophthora*, perceives and processes mechanical signals at the pathogen-host interface into intracellular mechano-biological responses.

Resolving this challenge requires new tools that provide access to local mechano-chemical properties at the surface of and inside the pathogens during mechanical invasion, ideally in live-cell imaging and with high spatio-temporal resolution. In a previous study[15], we introduced a toolbox of molecular mechanoprobes that can resolve complex micromechanical patterns in plant cells during a range of cellular processes. Yet, these approaches remain to be utilized for the study of pathogens during invasive growth.

In addition to the understanding of their invasion mechanics, the identification of novel chemical control agents for *Phytophthora* pathogens is an important strategy to combat late blight diseases more effectively[16,17]. Suitable control agents typically act on specific parts of the pathogen anatomy. Usually, their effects are studied by monitoring alterations in colony propagation and cell morphology. However, this approach leaves the treatment's site- and mode-of-action unresolved. Moreover, screening the action of control agents quickly and at limited cost remains challenging and hinders deep screening of compounds. In that regard, mapping spatio-temporal variations in CW and PM properties using our molecular probes could reveal the outlines of the pathogen's mechano-chemical reaction to treatment relatively quickly and inexpensively, and provide a completely novel aspect to evaluate drug efficacy.

In this paper, we introduce a set of two synthetic molecular reporters that are capable of resolving the intracellular mechano-chemical response of the cell wall (CW) – plasma membrane (PM) continuum in *P. infestans* pathogens during hyphal and invasive growth. These reporters also reveal the CW and PM response to various chemical treatments known to inhibit invasion. The first molecular reporter is a cell-wall binding molecular rotor[15] that reports on spatial and temporal changes in CW porosity and composition. The second is a solvatochromic PM probe that reveals changes in membrane polarity and molecular order. Using a combination of both probes we show how invasive growth generates a localized sub-cellular response at the pathogen-host contact point as a gateway for mechanical signal internalization, and how chemical treatment elicits specific responses in the wall-PM continuum. These new tools can contribute to bridging the gap between the genetic, biochemical, cell biological and mechanical aspects of host entry by these devastating pathogens.

5.2 Materials and Methods

Synthesis of fluorescent molecular reporters

The CW probe CWP-BDP dye was synthesized as reported in Michels et al.[15], and the PM reporter, NR12S, was synthesized following the protocol reported by Kucherak et al.[18]. A comprehensive overview of all experimental details, including synthesis and chemical characterization of the probes are provided in the thesis of L. Michels. Absorbance and emission spectra of the probes are given in Figure 5.6.

P. infestans growth and spore generation

P. infestans wild-type strain 88069 (*P. infestans*-wt), was maintained on rye sucrose agar (RSA) medium[19] supplemented with Vancomycin (20 μg mL^{-1}), Ampicillin (100 μg mL^{-1}), and Amphotericin A (10 μg mL^{-1}). Cultures were grown for 10 days at 18°C in the dark, and maintained by regularly transferring a 5x5 mm mycelial plug to new plates. Zoosporogenesis was initiated by adding sterile tap water (4°C) (10 mL for 100-mm-diameter plates, 5 mL for 60-mm-diameter plates) to a 10 to 14-day-old culture, followed by incubation at 4°C for 3h. After cooling, the zoospore suspension was collected and zoospores were encysted through manual physical stimulation (i.e. shaking for 1 min). The cysts were diluted 5x with milli-Q water, to reach a concentration of c. 1 10^5 spores mL^{-1} for experimental use.

For imaging optimization experiments with NR12S, *P. infestans*-wt mycelium was exposed to a relatively low concentration of β-sitosterol. This was done by placing two mycelium plugs (about 2 mm diameter) from a 7 day old *P. infestans* culture grown on Plich medium[20] lacking sterols on opposite sites of a disk (1 cm diameter, 0.5 cm thickness) of synthetic agar medium supplemented with 0.2 μg mL^{-1} β-sitosterol (from a stock of 2 g L^{-1} β-sitosterol in DMSO) and allowing hyphae to grow into the disk.The final percentage DMSO in the medium was 0.1% (v/v). Disks were incubated at 18°C in the dark for three days before use in microscopy experiments.

Imaging procedures

Artificial substrate preparation
All reactive PDMS polymers were purchased from Gelest Inc. and used as received. For observation of invasive growth, artificial substrates that mimic the hydrophobicity and stiffness of plant leaves were used. Chapter 3 has shown that these substrates elicit a similar invasion response as real host surfaces[14]. Stiff PDMS elastomer surfaces were prepared from a commercial 2-component polydimethyl siloxane rubber (Sylgard 184, Dow Corning) in a 10:1 base: crosslinker ratio. The

two components were mixed by vortexing for 3 to 4 min. Bubbles and dust were removed from the viscous mixture by centrifugation at 1000g for 10 min. #1 18x18 mm glass coverslips were cleaned before spincoating with the elastomer precursor mixture; coverslips were rinsed sequentially with isopropyl-alcohol (IPA), Milli-Q deionized water, and IPA, and subsequently dried in a nitrogen stream, followed by heating to 60°C for 5 min. Coverslips were pre-treated using an O_2/N_2 plasma for 1 min and then spincoated with 130 μL of mixture, at 500 rpm for 30s, followed by 2000 rpm for 2 min, to reach a 33 μm layer thickness (as determined by confocal microscopy). The Young's modulus, representing the elastic constant for uniaxial tensile deformations, of these substrates was measured on a home-built indentation set-up, as described in chapter 2[21], and determined to be 1.5 MPa. The samples were placed inside a vacuum chamber for at least 30 min to remove air bubbles, beforecuring at 50°C overnight.

For observations in non-invasive hyphae, solvent-free PDMS elastomer surfaces were prepared following the procedure reported by Cai et al.[22]. For preparation of the precursor, the following components were used; Backbone: vinylmethylsiloxane–dimethylsiloxane copolymer, trimethylsiloxy terminated, c. 300 vinyl groups per molecule, Mw $\simeq$ 50 000 g mol^{-1} (VDT-5035). Side chain: monohydride-terminated poly(dimethylsiloxane), Mw $\simeq$ 4750 g mol^{-1} (MCR-H21). Crosslinking chain: hydride-terminated polydimethysiloxane, Mw $\simeq$ 17 200 g mol^{-1} (DMS-H25). The PDMS linear polymers were mixed at a VDT-5035: MCR-H21: DMS-H25 = 1:13.3:1.72 mass ratio to achieve a 1:140:5 backbone: side chains: crosslinks number ratio, and a final Young's modulus of 15 kPa. The three components were mixed by vortexing for 3 min. Bubbles were removed by sonicating the sample for 10s. The Karstedt's catalyst was added to the precursor mixture at a concentration of 5 μL g^{-1} from a 2% platinum solution in xylene. The solution was again thoroughly mixed and sonicated for 10s. Plasma cleaned #1 coverslips were then spincoated with 130 μL of mixture, at 500 rpm for 30s, followed by 2000 rpm for 2 min. The samples were eventually cured at 70°C for 48 h.

Cell incubation and fluorescence imaging

For imaging experiments, a 80 μL droplet of a spore suspension ($\simeq$105 cysts per mL) was deposited onto the elastomer surface, followed by placement inside bespoke 3D printed sample chambers (Fig. 5.7) to minimize water evaporation. For staining, a portion of the aqueous phase of the droplet, 50 μL, was replaced three times with a solution of either CWP-BDP or NR12S, dissolved at 10 μmol L^{-1} in water. The staining was performed for 15 min (CWP-BDP) or 7 min (NR12S), after which any unbound dye was removed by replacing 50 μL of the droplet three times with water.

To image PM polarity in *P. infestans* mycelium using NR12S, 80 μL of NR12S staining solution at 10 μmol L^{-1} in water were deposited onto the mycelium grown on a solid agar pad. Staining was performed for 7 min and the dye solution was subsequently removed. The agar pad was placed upside down on a coverslip for imaging.

Two-dimensional Fluorescence Lifetime Imaging (FLIM) experiments of samples stained with CWP-BDP were performed on a Leica TCS SP8 inverted confocal microscope coupled to a Becker&Hickl TCSPC lifetime module (SPC830). Samples were excited with a 514 nm pulsed laser source (pulse duration <1 ps) with a repetition rate of 40 MHz, and fluorescence emission was captured through a 63× water immersion objective (numerical aperture = 1.2). A line scanning speed of 400 Hz was used and the emission was collected, using a spectral window extending from 518 nm to 600 nm, onto a Leica HyD SMD hybrid photodetector. Acquisition time was fixed at 120 s for each 256 × 256 pixel image. FLIM images were processed using the SPCImage 7.1 software to fit the fluorescence decay curves in each pixel with a two-component exponential decay.

Three-dimensional FLIM imaging, using FastFlim, for CWP-BDP, as well as 2D- and 3D- ratiometric imaging with NR12S were performed on a Leica TCS SP8 Two-photon inverted confocal microscope. Samples were excited with a Chameleon Ti:Sapphire pulsed laser source (pulse duration = 140 fs), at either 810 nm (CWP-BDP) or 830 nm (NR12S), with a repetition rate of 80 MHz. Fluorescence was captured through a 40× water immersion objective (numerical aperture = 1.2). A line scanning speed of 400 Hz was used and the emission was collected in a Leica 4 Tune detection unit equipped with Leica HyD SMD hybrid photodetectors. The emission of CWP-BDP was collected in a single photodetector, using a spectral window extending from 500 nm to 600 nm. The emission of NR12S was collected in two separate channels, using spectral windows extending from 500 nm to 585 nm, and from 585 nm to 700 nm respectively. The acquisition time was fixed at 15 s for each 256 × 256 pixel image. For three-dimensional image stacks, the z-step was set to 0.5 μm.

FLIM images obtained with CWP-BDP imaging were processed using the SP8 Falcon software that determines lifetimes based on the average arrival time of photons. Ratiometric images obtained with NR12S were constructed from the recorded intensity images using a custom Matlab routine that divides the photon count in each pixel of the 500-585 nm (so-called 'blue') channel image, by the photon count in the corresponding pixel of the 585-700 nm (so-called 'red') channel image. Resulting images are reported in a false-color scale that represents the mean CWP-BDP fluorescence lifetime (in nanoseconds), or the NR12S intensity ratio for each pixel.

Control images for the evaluation of autofluorescence intensities and fluorescence lifetimes were recorded on unstained specimens with the same imaging conditions and the highest laser intensity used, i.e. less than 10 μW (single-photon microscope) or 5 mW (multiphoton microscope) at the sample level. The autofluorescence levels in the CW and PM were too low to perturb our results (Fig. 5.8).

Giant Unilamellar Vesicle (GUV) preparation

Stock solutions of sphingomyelin (SM) and 1,2-dioleoyl-sn-glycero-3-phosphocholine (DOPC) in chloroform were purchased from Avanti Polar Lipids and used as is. Cholesterol was purchased from VWR. Giant Unilamellar Vesicles (GUV) were formulated via agarose gel swelling using the method of Horger et al.[23]. Two types of vesicles were formulated, with the following lipid molar ratios; DOPC: SM = 1:1 and DOPC: SM: Chol = 1:1:0.7. To do so, two lipid solutions in chloroform were prepared; for the cholesterol-free solution, DOPC (1.2 mmol L^{-1}, 57 mg of 25 g L^{-1} stock solution in chloroform) and SM (1.2 mmol L^{-1}, 137 mg of 10 g L^{-1} stock solution in chloroform) were mixed in chloroform (370 μl). For the cholesterol-supplied solution, DOPC (1.0 mmol L^{-1}, 48 mg of 25 g L^{-1} stock solution in chloroform), SM (1.0 mmol L^{-1}, 117 mg of 10 g L^{-1} stock solution in chloroform), and cholesterol (0.7 mmol L^{-1}, 42 mg of 10 g L^{-1} stock solution in chloroform) were mixed in chloroform (361 μL).

In parallel, Type IX-A ultralow melting agarose (gel point, Tg $\leq$ 20 °C; melting point, Tm $\leq$ 62 °C; electroendosmosis, EEO $\leq$ 0.12) films were formed on glass slides. For that purpose, a 1% (w/w) solution of agarose in deionized water was prepared, of which 400 μL were spread on the glass surface equilibrated at 40°C on a heating plate. The agarose coated slide was then left to dry at 40°C for 2h, until formation of a dry agarose film.

To generate a lipid film on and inside the films of agarose, 30 μL of the lipid solution of interest were spread on the agarose using the procedure described in detail by Horger et al.[23]. The sample was dried for 20 min under vacuum to remove residual chloroform, and subsequently immersed in a 0.1 mol L^{-1} glucose aqueous solution to allow for agarose gel and simultaneous vesicle swelling. The dish remained undisturbed at room temperature for 3h to yield the giant vesicles suspension. The vesicles were then immobilized in a 0.5% (w/v) agarose gel for imaging, as reported previously[24].

Hypo-osmotic treatment

We subjected cysts to osmotic shock by adding poly(ethylene glycol) (PEG) 2000 g L^{-1} as a calibrated osmolyte[14,25,26]. The osmolyte was added to cysts at a 90 mmol L^{-1} concentration to achieve an osmotic pressure in the medium of 0.6 MPa. The cyst-osmolyte mixtures were applied to PDMS substrates, left to incubate for 3h upon which 50 μL of the droplet was exchanged three times with water. Staining with CWP-BDP or NR12S was performed right before applying the osmotic shock, as described above but using a 10 μmol L^{-1} dye solution in 90 mmol L^{-1} PEG2000. Analysis of the effect of the osmotic shock was performed by looking at the cyst exclusively.

Chemical treatments

Treatment with cell wall and plasma membrane-targeting control agents
To investigate the effect of chemical stress on the CW and PM properties, cells were treated with two different compounds reported to act on the structural properties of either the PM or the CW. Each treatment was started 1h after application of the encysted zoospores on the substrate, and performed during 1h before staining and imaging. During imaging, cells were kept in the same treatment conditions to avoid additional stress.

To perturb the CW composition and structure, valifenalate solubilized in a 0.25 mmol L^{-1} stock solution in DMSO was added to the germlings to a final concentration of 125 nmol L^{-1} valifenalate (DMSO content<0.05% (v/v)). To induce variations in PM composition and lipid order, fluopicolide solubilized in a 0.26 mmol L^{-1} stock solution in DMSO was added to the germlings to a final concentration of 25 nmol L^{-1} fluopicolide (DMSO content<0.05% (v/v)).

Treatment with cytoskeletal depolymerizing drugs
To perturb the organized actin cytoskeleton of the pathogens, LatB solubilized in a 0.1 mmol L^{-1} stock solution in DMSO was added to the germlings to a final concentration of 1 μmol L^{-1} LatB and 1% (v/v) DMSO. To disrupt the microtubule network, oryzalin solubilized in a 0.1 mmol L^{-1} stock solution in DMSO was added to the germlings to a final concentration of 0.1 μmol L^{-1} oryzalin and 1% (v/v) DMSO.

As a control, cells were also treated with 1% (v/v) DMSO only. Analysis of the effects of the chemical treatments was performed by looking at the hyphal tip exclusively.

Growth and invasivity assays

We verified the invasion efficiency under each treatment, following the procedure adopted chapter 3[14]. The invasion efficiency is defined as the percentage of germinated cysts, counting only those whose germ tube exceeds ca. 10 μm in length, that have successfully fractured the artificial surface 2h post application (hpa).

Statistical analysis

All the described imaging experiments, were repeated at least two times on different cell batches and different days (Table 5.1). For each repeat, at least ten cells were imaged. Fluorescence lifetime and intensity ratio distributions were extracted from the corresponding images, and summed over the different repeats. All distributions are built from at least 4000 data points. To ascertain the noise threshold for changes in lifetime or intensity ratio that can be detected with statistical significance, we perform measurements in homogeneous control media strictly deprived of spatial inhomogeneities (Fig. 5.9-5.10). We find a noise threshold, determined as the full-width at half-maximum (FWHM) of the observed distributions in homogeneous media to be 0.45 ns for the lifetime measurements on CWP-BDP and ratio = 0.02 for the ratiometric imaging of N12RS. We only consider an observed response significant if its change is either 1x larger than 1x the noise floor, for CWP-BDP, and or 3x larger than the noise floor for NR12S. The distribution widths we report in this paper on biological specimens are always well above those reported in homogeneous media; these thus do not represent measurement error but rather reflect real spatial inhomogeneities in the CW or PM properties of the organism.

5.3 Results

Molecular rotor CWP-BDP maps cell wall mesh sizes in *P. infestans*

While the method from Bronkhorst et al.[14] allowed visualization of stresses applied by the pathogen to the substrate, our method provides a way to visualize the response to these stresses in the CW and PM of the pathogen. In order to investigate CW and PM structural modifications during non-invasive and invasive hyphal growth of *P. infestans*, we implemented the wall-targeting fluorescent molecular rotor CWP-BDP, and the PM chemical polarity probe NR12S in encysted zoospores, 1.5 hpa.

CWP-BDP is a phenyl-substituted borondipyrromethene (Ph-BODIPY) molecular rotor, substituted on the phenyl ring by a peptide mimicking the pectin

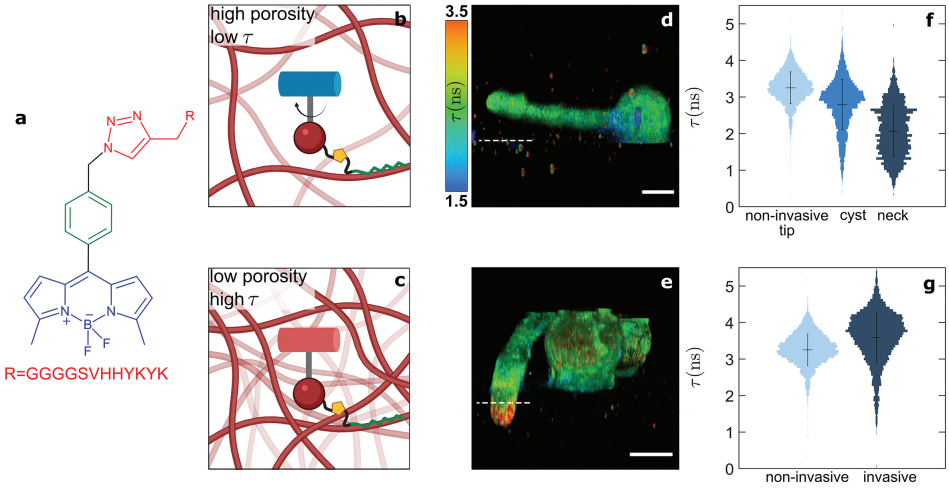

Figure 5.1. Mapping of spatial variations in the cell wall mesh size of *Phytophthora infestans* germlings using the molecular rotor CWP-BDP. (a) Chemical structure of CWP-BDP. (b,c) Schematic illustrations showing the molecular mechanism by which CWP-BDP reports mesh sizes. 3D fluorescence lifetime mesh size map of *Phytophthora infestans* germlings (d) upon growth at the PDMS substrate surface and (e) upon invasion. Scale bars = 5 μm. The colorscale translates the fluorescence lifetime values expressed in ns. The white dashed line is used to indicate substrate surface location (f) Fluorescence lifetime probability distributions obtained in different regions of the germlings (N = 30 cells). (g) Fluorescence lifetime probability distributions obtained in the tip of germ tubes before and after invasion (N = 30 cells).

binding domain of extensins, a family of glycoproteins that are highly abundant in plant CWs[27]. As such, it has been designed to target and bind specifically to the wall of plant cells. The molecular rotor, whose mode-of-action is described in detail elsewhere[15], offers a mechano-optical coupling that allows qualitative measurements of local CW mesh sizes, using a fluorescence lifetime read-out (Fig. 5.1a-c). Although the CWs of *Phytophthora* spp. have a different composition than plant CWs and contain mainly polymers of D-glucose[28,29], we observe that also in *P. infestans* CWP-BDP binds to the CW, presumably through electrostatic interactions with other anionic carbohydrates (Fig. 5.1d,e).

Solvatochromic probe NR12S reveals membrane chemical polarity and order *P. infestans*

NR12S is a solvatochromic Nile Red-based probe developed by Kucherak et al.[18] (Fig. 5.2a). In its design, the Nile Red unit is decorated with a long alkyl tail and

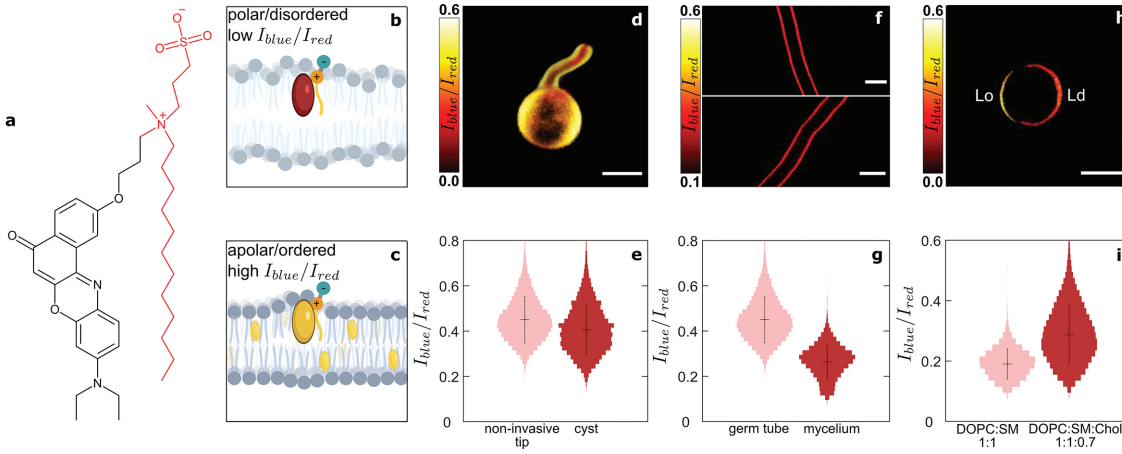

Figure 5.2. Mapping of spatial variations in the plasma membrane chemical polarity of *P. infestans* germlings using the solvatochromic probe NR12S. (a) Chemical structure of NR12S. (b,c) Schematic illustrations showing the mechanism by which NR12S reports changes in chemical polarity and lipid phase. (d) 3D intensity ratio chemical polarity map of *P. infestans* germlings upon growth at the PDMS substrate surface. Scale bar = 5 μm. The colorscale translates the intensity ratio values. (e) Intensity ratio probability distributions obtained in different regions of the germlings (N = 30 cells) (f) Intensity ratio chemical polarity map of *P. infestans* mycelium. Scale bars = 10 μm. (g) Fluorescence lifetime probability distributions obtained in the young germ tubes tip (N = 30 cells) versus mycelial cells grown on agar (3 mycelia, N = 30 images). (h) Intensity ratio chemical polarity map of DOPC:SM:Cholesterol = 1:1:0.7 (molar ratio) synthetic vesicles exhibiting phase separation between a cholesterol-rich ordered (Lo), and a cholesterol-poor disordered (Ld) phases. Scale bar = 5 μm. (i) Intensity ratio probability distributions obtained in DOPC:SM = 1:1 (molar ratio) (N = 20 vesicles) versus DOPC:SM:Cholesterol = 1:1:0.7 (molar ratio) (N = 20 vesicles) synthetic vesicles.

a zwitterionic group, which allows for specific staining of the PM and restricts flip-flopping of the dye from the outer to the inner leaflet, thereby reducing subsequent incorporation in intracellular membranes. This probe exhibits a shift in the wavelength of maximum emission in response to changes in the local chemical polarity of its surroundings. The read-out for this probe consists of ratiometric imaging, in which the total emission of the dye is split into two channels. Changes in membrane chemical composition and lipid phase both impact the chemical polarity of the probe microenvironment, triggering a change in the intensity ratio between the blue and red channels (Fig. 5.2b,c). Kucherak et al.[18] used these properties to image variations in PM lipid order and cholesterol content in mammalian cells. Here we extend the use of this probe to walled cells.

Mechano-chemical response of walls and membranes to mechanical stress

Using FLIM, we built three-dimensional reconstructions of the CW of *P. infestans* cells during non-invasive and invasive growth on an artificial host-mimicking substrate based on a PDMS elastomer[14] (Fig. 5.1d,e, Fig. 5.11-5.13). The FLIM mesh size images provide quantitative information, which we extract as lifetime probability distributions (Fig. 5.1f,g). For example, in non-invasive cells, variations in lifetime emerge when comparing the cyst to the germ tube neck and tip. The lifetime diminishes locally to 2.0 ± 1.9 ns in the neck, while increasing slightly in the tip of the germ tube to 3.2 ± 0.9 ns (Fig. 5.1d,f). These differences reflect a relative increase in wall mesh size in the neck, and concomitant reduction in mesh size in the germ tube tip. By contrast, upon invasion, the fluorescence lifetime recorded within the tip of the germ tube in contact with the substrate rises strongly and abruptly to 3.7 ± 1.2 ns (Fig. 5.1e,g). The lifetime distribution keeps a comparable width but exhibits a small shoulder centered on the non-invasive case value of 3.2 ns. To test whether this increase of lifetime is caused by compression of the CW between the PDMS substrate and the cytoplasm, we applied a hypo-osmotic shock to the cells; a similar increase in lifetime was observed in the wall of cysts (Fig. 5.3a-c, Fig. 5.14). These images reveal the compression of the CW upon substrate invasion, as the mechanical stress at the pathogen-substrate contact squeezes water from the carbohydrate network, increasing its density at the invasion site. This approach thus enables direct visualization of the locus of mechanical interactions between pathogen and substrate.

To unravel how growth and invasion affect the properties of the PM that lies underneath the CW, we compare the response of the probe NR12S between non-invasive versus invasive cysts. We measure the emission intensity in two channels in cells stained with the NR12S probe and represent the results as intensity ratio images from which we derive probability distributions (Fig. 5.2d,e). In cells growing non-invasively, the intensity ratio remains constant throughout the cell, around 0.4. This suggests that the PM composition and hydration level are relatively constant along the germ tube at early stages of growth. The invasive part of cells could not be imaged with NR12S due to the low dye penetration and emission intensity underneath the PDMS surface. Hypo-osmotic shock only results in small changes in the ratiometric measurements of the PM (Fig. 5.3d, f). This implies that the PM polarity and lipid order is only weakly sensitive to the compressive forces that push the PM against the cell wall. This observation implies that upon invasive growth, as the hyphal tip is mechanically stressed by the substrate, compressive forces would not substantially alter the properties of the membranes.

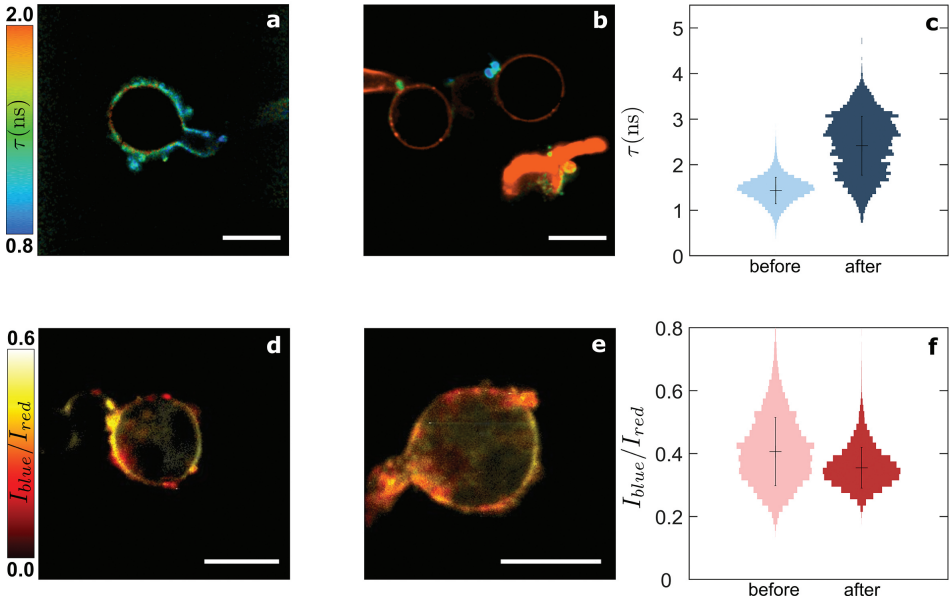

Figure 5.3. Effects of hypo-osmotic treatment on the cell wall and plasma membrane mechano-chemical properties of *P. infestans* germlings. Fluorescence lifetime cell wall mesh size map of germlings growing (a) in a 90 mmol L^{-1} PEG2000g mol^{-1} aqueous solution for 3h, (b) in a 90 mmol L^{-1} PEG2000g mol^{-1} aqueous solution for 3h followed by transfer to water. (c) Corresponding fluorescence lifetime probability distributions in (a-b) (N = 20 cells). Intensity ratio plasma membrane chemical polarity map of germlings growing (d) in a 90 mmol L^{-1} PEG2000g mol^{-1} aqueous solution for 3h, (e) in a 90 mmol L^{-1} PEG2000g mol^{-1} aqueous solution for 3h followed by transfer to water. (f) Corresponding intensity ratio probability distributions in (d-e) (N = 20 cells). Scale bars = 10 μm.

In mature *P. infestans* mycelium, the intensity ratio is decreased to 0.22 ± 0.15 (Fig. 5.2f,g), in comparison to the ratio of 0.42 ± 0.21 measured in the tip of young germ tubes. This observation suggests a significant change in PM composition and lipid order as the cells grow and maturate, and confirms the probe responsiveness to changes in membrane chemical polarity. We validated this hypothesis by implementing NR12S in synthetic giant-unilamelar vesicles made of DOPC, SM, and cholesterol (1:1:0.7 molar ratio). This lipid composition can lead to phase separation between an ordered (Lo) phase rich in SM and cholesterol, and a liquid-like (Ld) phase, enriched in DOPC (Fig. 5.2h). GUVs made of only DOPC and SM show a single phase, and a narrow intensity ratio distribution centered around 0.17 ± 0.11. In the cholesterol-supplemented GUVs, phase separation and the global increase in lipid order is reflected by an upward shift of the ratio distribution mean value and width to 0.26 ± 0.22 (Fig. 5.2i). These results confirm the responsiveness of NR12S to changes in lipid phase. The difference in PM properties in the mycelium as compared to the cyst life stage thus hints at a reduced lipid order and packing density in mycelial membranes. We speculate that these differences are due to changes in PM composition, e.g. lipid composition and/or protein content, as both life stages utilize distinct metabolic pathways in which lipids, and hence the PM, play different roles[30–33].

Revealing the mode-of-action of chemical control agents

Using the CWP-BDP CW and the NR12S PM probes, we investigated the effects of different chemical stresses on *P. infestans* germinated cysts during substrate contamination and invasion process. In particular, we looked at the effect of adding active ingredients from fungicides (i.e. valifenalate, fluopicolide) (Fig. 5.4).

We selected the PM targeting compound fluopicolide and the cellulose synthase inhibitor valifenalate[34] to verify their specifity of action to either membranes or walls. Fluopicolide dislocates spectrin-like proteins in *Phytophthora* from the membrane to the cytoplasm[35,36]. Upon treatment with 25 nmol L^{-1} fluopicolide, NR12S reports a significant drop in the NR12S intensity ratio within the PM, going from 0.42 ± 0.21 to 0.23 ± 0.09 (Fig. 5.4e,f,h, Fig. 5.15). This change could reflect either a loss in PM tensegrity by spectrin-like protein expulsion and potential cytoskeletal de-adhesion from the membrane, or result from the intercalation of the rather polar fluopicolide molecule into the PM. To discriminate between these two hypotheses, we perform experiments in synthetic vesicles which lack spectrins and other PM proteins, by submitting GUVs to the same concentration of fluopicolide (Fig. 5.4i-k, Fig. 5.16). No change in intensity ratio was reported in synthetic vesicles, which confirms that the increase in polarity within the PM is due to an alteration of the membrane structure and not by fluopicolide entry

into the PM. By contrast, the same fluopicolide treatment results in only minor changes in the CW, as confirmed by CWP-BDP fluorescence lifetime imaging (Fig. 5.4a,b,d, Fig. 5.15), likely due to the presence of DMSO (Fig. 5.4d, Fig. 5.17). This suggests that there is no direct link between the correct localization of spectrin-like proteins in the PM and wall mechanics and biosynthesis. We note that while NR12S displays a significant shift in intensity ratio upon treatment with this low fluopicolide concentration, this dose does not lead to a significant inhibition of pathogen invasion. In the absence of fluopicolide the invasivity is 71.3% (N=138 cells), versus 63% (N=84 cells) with fluopicolide. Even though the treatment has a limited effect on the invasivity of cells that remain viable, we do note that this dose leads to a substantial fraction of non viable cells, i.e. cells that do not germinate and become highly autofluorescent upon laser exposure. At higher fluopicolide doses, we observe a decrease in the amount of germination, but no substantial reduction in invasivity of the remaining germinated cells. This indicates that NR12S is sensitive enough to report changes in the physico-chemical properties of the viable cells well before invasivity is hampered.

Valifenalate is used to target and weaken the CW of oomycetes[37,38]. We observe that valifenalate distinctly changes the pathogen wall properties; imaging with CWP-BDP reveals an increase in fluorescence lifetime from 3.2 ± 0.9 ns in non-treated germlings to 3.6 ± 0.8 ns in germlings treated with 125 nmol L^{-1} valifenalate, and the emergence of distinct spatial variations along the germ tube, marking the transition between the wall portions synthesized before and during treatment (Fig. 5.4a,c,d, Fig. 5.18). Staining of an unknown structure inside the cells led to an intracellular fluorescent signal that was excluded from the analysis. This structure could result from the accumulation of CW precursors in the cytoplasm. After treatment, cellulose synthase inhibition results in a denser CW, which not only changes the probe lifetime but also weakly reduces the staining efficiency due to a lower permeability. We previously reported a similar trend in the evolution of the wall mesh size during polarized growth of Arabidopsis root hairs[15]. During root hair growth and maturation, the CW starts from a dense network of flexible carbohydrates, malleable enough to yield under turgor to enable tip growth. At later stages, the wall is reinforced by a network of stiff cellulose fibers which exhibit a much larger mesh size. In other words, a loss of the cellulose network results in a decrease in porosity and an increase in fluorescence lifetime of the probe. Even though the chemical composition of the CW in oomycetes is less known than the Arabidopsis root hair CW, our observations are consistent with this picture where valifenalate treatment inhibits cellulose synthesis, resulting in less porous and more malleable CWs. By comparison, the intensity ratio of NR12S is not affected, showing no influence of valifenalate on PM properties (Fig. 5.4e,g,h, Fig. 5.18).

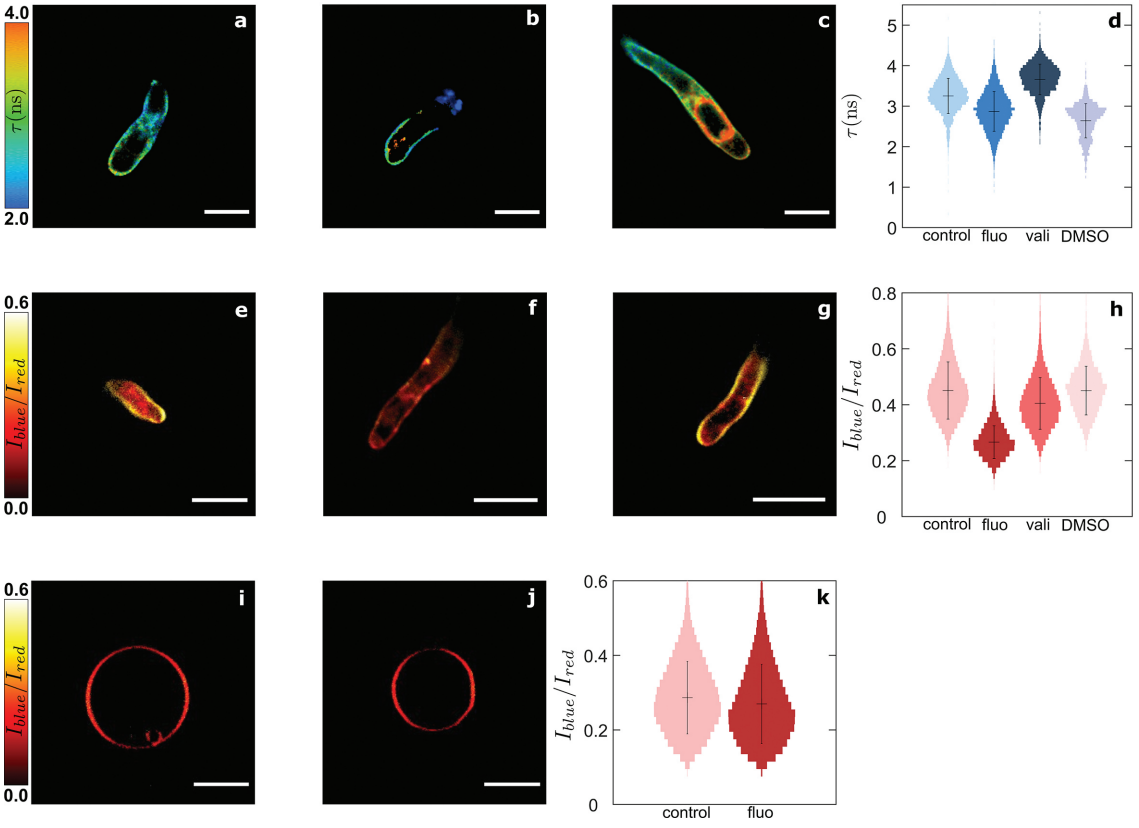

Figure 5.4. Effects of treatments with control agents on the cell wall and plasma membrane mechano-chemical properties of *P. infestans* germlings. Fluorescence lifetime cell wall mesh size map of germlings growing in (a) water for 1h, (b) in water for 1h followed by treatment with 25 nmol L^{-1} fluopicolide (fluo) for 1h and (c) in water for 1h followed by treatment with 125 nmol L^{-1} valifenalate (vali) for 1h. (d) Fluorescence lifetime probability distributions in (a-c) (N = 30 cells). Intensity ratio plasma membrane chemical polarity map of germlings growing (e) in water for 1h (f) in water for 1h followed by treatment with 25 nmol L^{-1} fluopicolide (fluo) for 1h and (g) in water for 1h followed by treatment with 125 nmol L^{-1} valifenalate (vali) for 1h. (h) Intensity ratio probability distributions in (e-g) (N = 30 cells). Intensity ratio chemical polarity map of DOPC:SM:Cholesterol = 1:1:0.7 (molar ratio) synthetic vesicles in (i) absence and (j) presence of 25 nmol L^{-1} fluopicolide (fluo). (k) Fluorescence lifetime probability distributions in (i-j) (N = 30 cells). Scale bars = 10 μm.

Also for this compound, the effects on CW and PM are decoupled and the chemical acts specifically on a singular target in the CW-PM continuum. When investigating invasion efficiency under treatment with 125 nmol L^{-1} valifenalate, we only notice a slight reduction in the invasivity from 71.3% (N=138 cells) to 59.2% (N=103 cells), while leading to a large amount of non-viable autofluorescent cells. This confirms the sensitivity of CWP-BDP to changes in CW properties even before large effects on invasivity can be detected.

Changes in wall and membranes in response to cytoskeletal disruption

The cell cytoskeleton is known to play a leading role in establishing and maintaining the polarity required for hyphal growth and thereby in the invasion fitness of *Phytophthora* pathogens[14,39–44]. To examine how the CW-PM continuum of *P. infestans* responds to perturbations in cytoskeletal organization, we studied the consequences of treatment with the actin depolymerising drug LatB[44] and treatment with the microtubule inhibitor oryzalin[41,45,46]. Treatment with LatB at 1 μmol L^{-1} affects the morphology of the cells, which exhibit the tip swelling behavior characteristic for the loss of polarization. However, very minor fluorescence lifetime changes are visible within the CW (Fig. 5.5a,b,g, Fig. 5.19). A shift in intensity ratio from 0.42 ± 0.21 to 0.36 ± 0.17 is visible within the PM (Fig. 5.5d,e,i, Fig. 5.19). Large doses of LatB strongly disrupt the actin cytoskeleton involved in the transport of CW precursors to the growing tip[44,47,48]. Even though one could have expected that 1 μmol L^{-1} of LatB would affect CW synthesis, our images reveal an intact CW for all cells studied under this treatment. Hence we conclude that LatB treatment does not substantially affect the CW. The same treatment results in an increase in the PM polarity, possibly reflecting a reduction of membrane stability due to the lack of tension applied by the disrupted cytoskeleton. This LatB dose applied being highly cytotoxic, we observe that the majority of cells treated for the invasivity assay - right before application on the substrate - show lysis, and the few remaining viable cells are incapable of substrate penetration. Treatment with the microtubule inhibitor oryzalin at 0.1 μmol L^{-1}, leads to a reduction of fluorescence lifetime of CWP-BDP to 2.5 ± 0.9 ns in the hyphal tip (Fig. 5.5a,c,h, Fig. 5.20), while the intensity ratio of NR12S decreases to 0.34 ± 0.18 (Fig. 5.5d,f,j, Fig. 5.20). While the exact function of microtubules in the lifestage of germinated cysts, both during invasive and non-invasive growth, is yet unresolved, our results show that disruption of the microtubule network leads to changes in both the CW porosity and PM tensegrity. This could point towards a role for microtubules in regulating the structure and tension in both organs. At this low dose of oryzalin, the invasivity of the cells remains at 68.1% (N=201 cells). Also here, the combination of our molecular probes enables connecting action on other cellular components to their

effects on the cell exterior formed by the CW and PM, even when invasivity is not affected.

5.4 Discussion

The CW and PM of cells form a continuum that plays a major role in the mechano-chemical response of cells. The CW being the stiffest part of the cell, and the direct connection between the cell and its immediate surroundings, it is where the perception and transduction of mechanical cues begins. While the molecular mediators of mechano-perception in *Phytophthora* are still unknown, other walled microorganisms – yet, not showing invasive growth - such as yeasts exhibit various CW-localized mechano-receptors[49–51]. In the case of species that grow invasively, such as *Phytophthora*, mechano-perception becomes central to the understanding of cell function. Physical perturbations of the CW are internalized into the cells through the PM. In response to mechanical force, the PM can deform and change composition, for example through recruitment of proteins, or opening of mechanosensitive ion channels by increased lateral tension[52,53]. Structural modifications of these two entities reflect part of the mechano-chemical response of cells to external stress.

The oomycete CW and PM undergo structural and chemical modifications during development. After zoospore encystment, a CW is formed around the cyst and the cell is able to generate turgor pressure. During germination of the cyst, the CW progressively extends and thickens[54]. Subsequent germ tube growth requires local modification of the CW to reduce its yield limit at the tip, such that turgor action leads to polarized tip growth[42,55]. Meanwhile, very little is known about modulations of the PM properties, to allow for e.g. recruitment of stretch-activated ion channels involved in tip growth[56,57], or active vesicle secretion of effector proteins[58]. This dynamic adaptation of the cells can be triggered by external stimuli, such as mechanical and chemical interactions with the host plant. To date, the development of treatments to inhibit *P. infestans* growth and combat the late blight has relied partly on chemicals able to prevent its structural adaptation, or that induce structural modifications as a side effect[43,59].

Resolving these modifications with spatio-temporal resolution could help understanding the mechanics of growth and invasion, as well as the mode of action of chemical control agents. In agriculture, chemical control is still crucial to combat oomycete plant pathogens. In this study, we implemented the CW targeting molecular rotor CWP-BDP and the PM ratiometric probe NR12S in *P. infestans*, but this method is readily applicable to other oomycetes. In parallel, we also tried to implement other fluorescent molecular rotors reported previously[15],

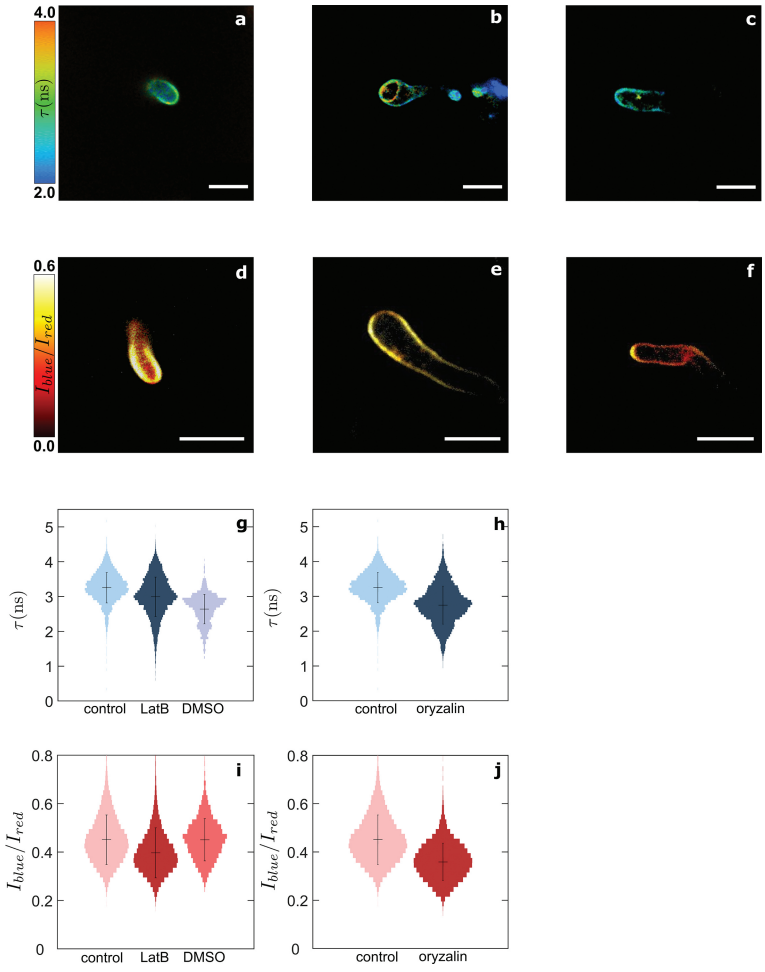

Figure 5.5. Effects of treatments with cytoskeletal depolymerizing drugs on the cell wall and plasma membrane mechano-chemical properties of *P. infestans* germlings. Fluorescence lifetime cell wall mesh size map of germlings growing (a) in water for 1h, (b) in water for 1h followed by treatment with 1 μmol L^{-1} latrunculin B for 1h, (c) in water for 1h followed by treatment with 0.1 μmol L^{-1} oryzalin for 1h. Intensity ratio plasma membrane chemical polarity map of germlings growing (d) in water for 1h, (e) in water for 1h followed by treatment with 1 μmol L^{-1} latrunculin B for 1h, (f) in water for 1h followed by treatment with 0.1 μmol L^{-1} oryzalin for 1h. (g, h) Fluorescence lifetime probability distributions in (a-c) (N = 30 cells). (i, j) Intensity ratio chemical polarity probability distributions in (d-f) (N = 30 cells). Scale bars = 10 μm.

analog to CWP-BDP but used to target the PM, the cytoplasm and the vacuole respectively; the PM probe could stain the plasma membrane successfully but its dynamic response range to changes in membrane tension was not suitable to clearly highlight variations in membrane structural properties. Meanwhile, the cytoplasm and vacuole dyes did not penetrate the cells at all, highlighting the lower permeability of oomycete cells in comparison to plant root cells.

With our combination of fluorescent reporters, we are able to map variations in CW mesh size and PM chemical polarity, respectively, during growth and invasion. Upon treatment with active compounds found in oomycide mixtures, or with cytoskeletal depolymerizing drugs, clear changes in CW and PM structural properties are visible and give a real-time indication on the effect of the chemical stress. To achieve a quantitative measurement, systematic calibrations of the two probes are needed. These are not trivial steps as they need to be conducted in a medium that is simultaneously representative of the chemical composition for the compartment of interest, regarding both polarity and length scales, and quantitatively tuneable. For example, to have a reference in terms of CW mesh size, we could imagine implementing CWP-BDP in a synthetic polysaccharide network with controlled mesh sizes and polymer charge densities. In parallel, to determine the PM chemical polarity and lipid phase, we envision systematic studies of the NR12S response in vesicles reconstituted from cell extracts and systematically introducing sterols in the preparation protocol as a way to tune the lipid order. These calibrations can be challenging, as the CW and PM compositions are highly complex and vary from species to species, cell to cell and location to location. Yet, even without calibration to enable quantitative data, the probes already provide valuable qualitative insights into mechano-chemical heterogeneities, reflecting relative changes in probe confinement and local chemical polarity, respectively, as well as providing information on the dynamics of cellular processes at a high resolution that cannot currently be achieved by other means. These probes could be valuable in combination with genetic modification techniques, such as CRISPR-CAS and silencing, as it could help to decipher the role of different biochemical pathways and proteins in determining CW and PM structural properties.

Unravelling the complex mechano-chemical interactions between pathogens and host would ultimately require implementation of this method on real plant hosts rather than on artificial surfaces, to take into account the complex mechano-biological responses of both parties. Chemical engineering of the probes to provide even more precise, and organism specific, targeting, and using designs with two complementary emission wavelengths would allow simultaneous mapping of both pathogen and plant properties, and help understand their mechanical interactions. To do so, several promising strategies to achieve selective binding arise; for

instance, the use of metabollic labelling, previously employed to incorporate alkyne or azide groups in the pectin network of Arabidopsis seedling roots CW, allowing for a subsequent click-reaction to fluorescent dyes[60–62], or the use of genetic labelling by means of SNAP-tags, previously implemented in animal cells to label e.g. PM proteins[63,64]. Such approaches could prove valuable for a more systemic perspective on the complex mechanobiology and mechanochemistry of host invasion.

5.5 Supporting Information

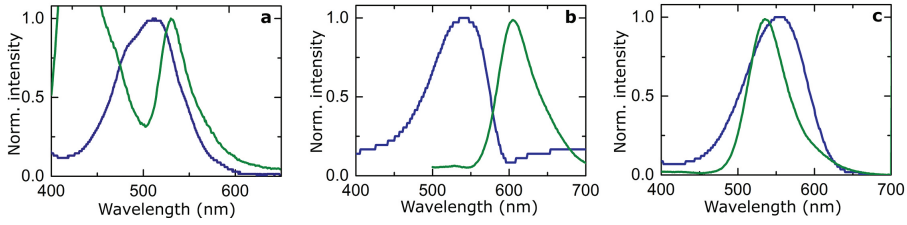

Figure 5.6. Spectroscopic characterization of CWP-BDP and NR12S. Absorbance (blue) and fluorescence emission (green) spectra of (a) CWP-BDP in chloroform, (b) NR12S in chloroform, (c) NR12S in methanol.

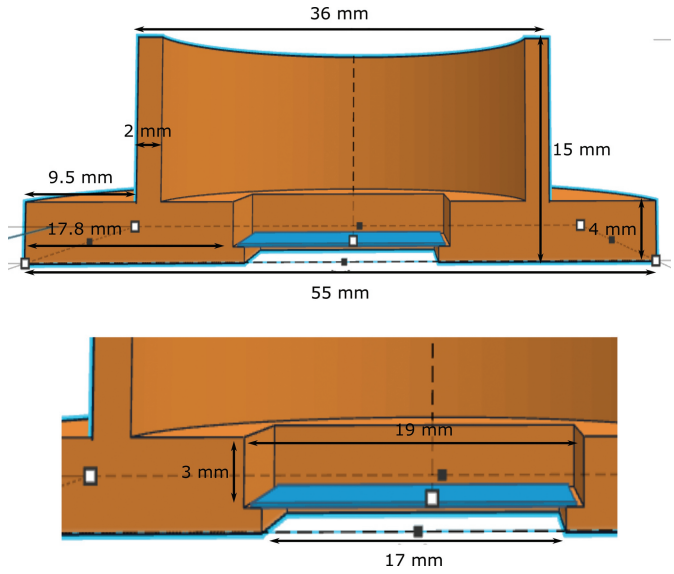

Figure 5.7. Schematic of the 3D-printed observation chambers used for all cell imaging experiments.

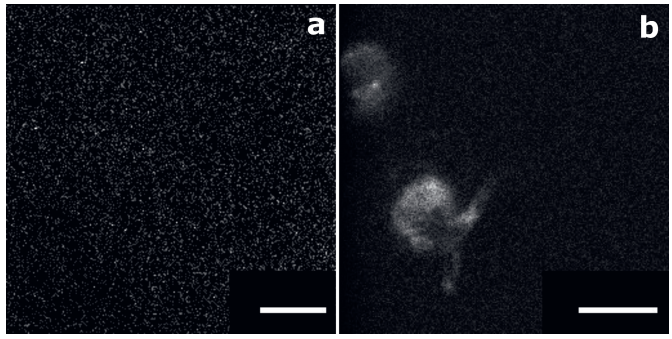

Figure 5.8. Autofluorescence signal of the *P. infestans* germlings. (a) Autofluorescence obtained by single-photon excition on the TCS SP8, with a laser intensity ten times higher than the maximum laser intensity used for CWP-BDP excitation. Only noise was imaged. Scale bar = 50 µm. (b) Autofluorescence obtained by two-photon excitation on the TCS SP8 multiphoton, with the maximum laser intensity used for CWP-BDP and NR12S excitation. The autofluorescence signal is low and only visible inside the cell, not within the cell wall and plasma membrane. Scale bar = 10 μm.

Table 5.1. Number of samples and observations

Experiments	Figures	Sample numbers
Growth of germinated cysts	Figure 5.1d,e Figure 5.2d Figure 5.4a,e Figure 5.5a,d Figure 5.11-5.13	Non-invasive: N=30 cells from 3 cell batches for each probe; invasive: N=30 cells from 3 cell batches for CWP-BDP
DMSO	Figure 5.17	N=30 cells from 2 cell batches for each probe
Giant synthetic vesicles	Figure 5.2h Figure 5.4i,j Figure 5.16	DOPC:SM=1:1 (molar ratio): N=20 vesicles from 3 vesicle batches for NR12S; DOPC:SM:cholesterol=1:1:0.7 (molar ratio): N=20 vesicles from 3 vesicle batches for NR12S; vesicles supplemented with fluopicolide: N=20 vesicles from 2 vesicle batches for each vesicle type (cholesterol-free and cholesterol-rich), for NR12S
Mycelium	Figure 5.2f	Supplemented with 0.2 μg ml^{-1} β-sitosterol: N=3 mycelia for NR12S
Hypo-osmotic shock	Figure 5.3a,b,d,e Figure 5.14	N=20 cells from 2 cell batches for each probe
Fluopicolide	Figure 5.4b,f Figure 5.15	N=30 cells from 3 cell batches
Valifenalate	Figure 5.4c,g Figure 5.18	N=30 cells from 3 cell batches for each probe
Latrunculin B	Figure 5.5b,e Figure 5.19	N=30 cells from 2 cell batches for each probe
Oryzalin	Figure 5.5c,f Figure 5.20	N=30 cells from 2 cell batches for each probe
Autofluorescence control	Figure 5.8	2 cell batches for both single-photon and two-photon excitation set-ups

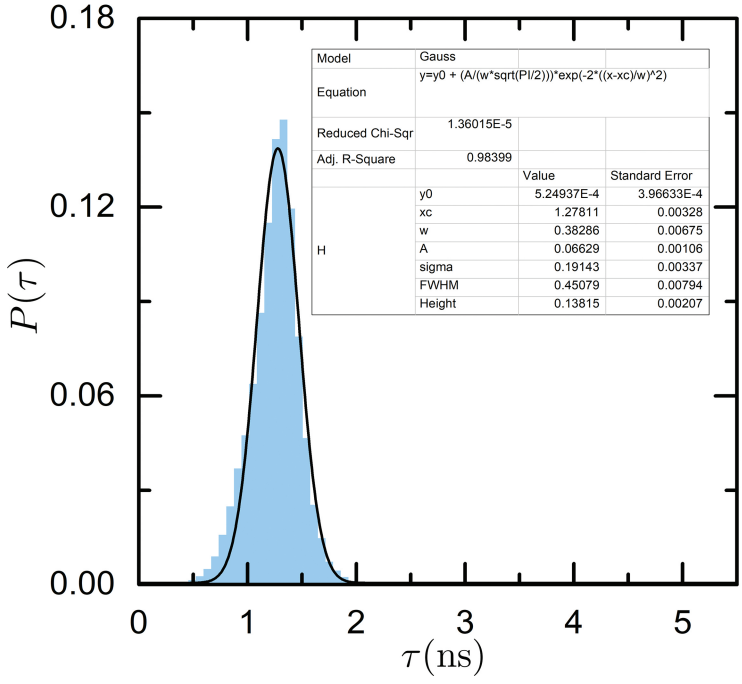

Figure 5.9. Fluorescence lifetime distribution of CWP-BDP in water. The fluorescence lifetime distribution obtained in a homogeneous aqueous solution is fitted with a Gaussian to determine the noise threshold of the probe.

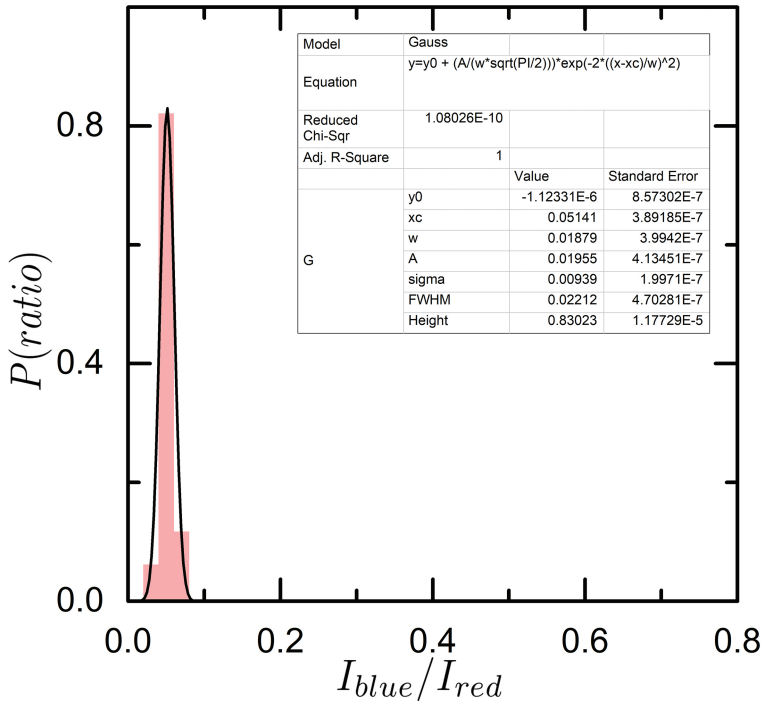

Figure 5.10. Intensity ratio distribution of NR12S in chloroform. The intensity ratio distribution obtained in a homogeneous solution in chloroform is fitted with a Gaussian to determine the noise threshold of the probe. The same experiment performed in methanol or dimethylsulfoxide does not allow to plot a ratio distribution given the very low photon count obtained in the blue channel.

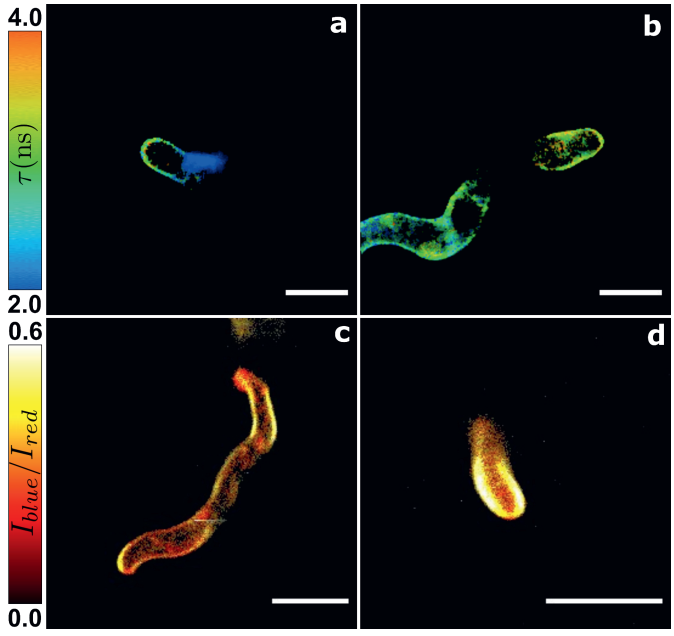

Figure 5.11. Mapping of spatial variations in the cell wall mesh size and plasma membrane chemical polarity of *P. infestans* germlings. (a, b) Fluorescence lifetime mesh size map of control germlings growing in water 1h post application. (c, d) Intensity ratio chemical polarity map of control germlings growing in water 1h post application. Scale bars = 10 μm.

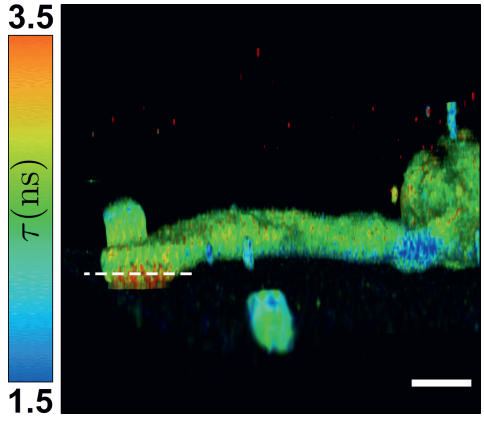

Figure 5.12. 3D-mapping of spatial variations in the cell wall mesh size of *P. infestans* germlings. 3D fluorescence lifetime mesh size map of *P. infestans* germlings upon interaction with the host surface. Scale bar = 5 μm.

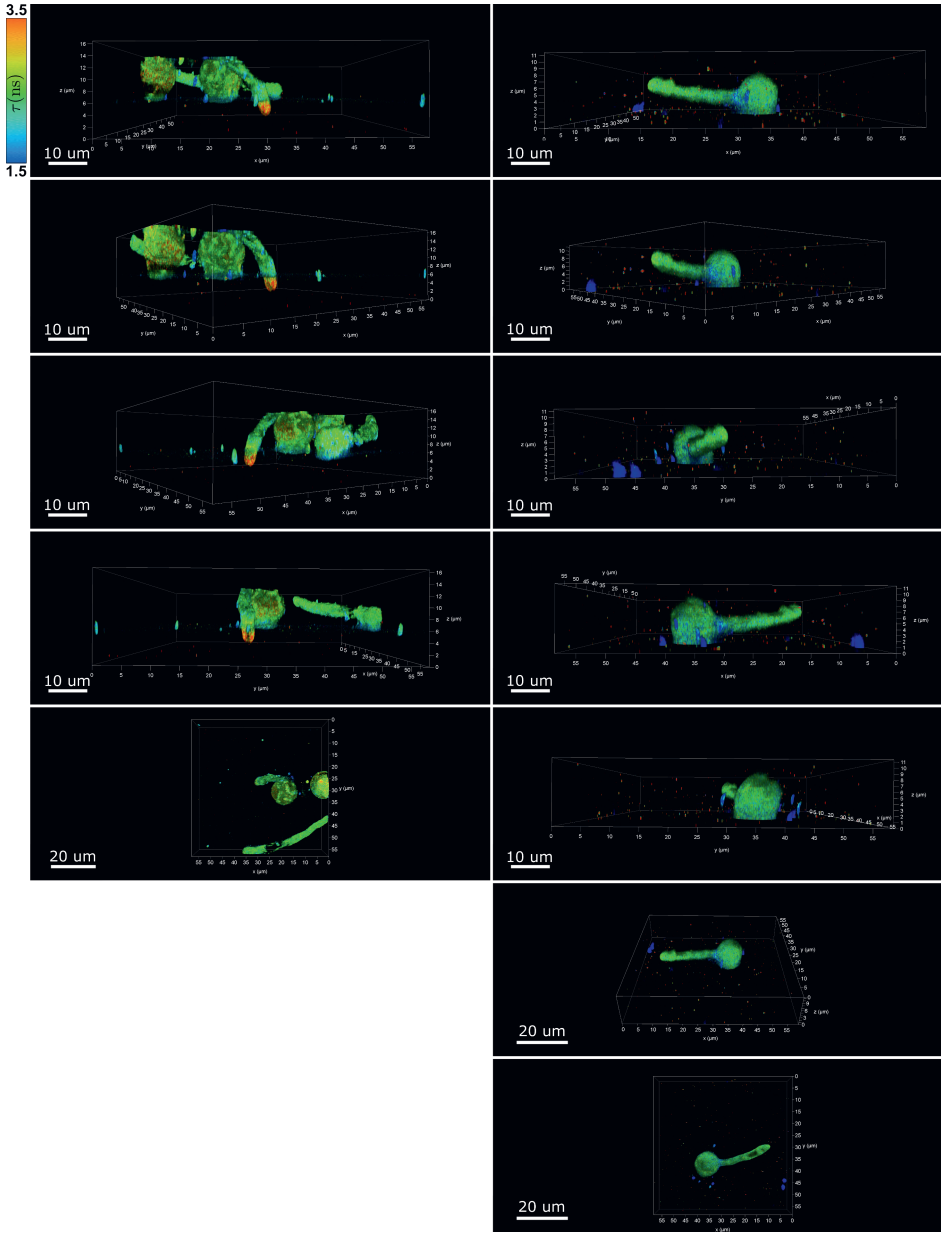

Figure 5.13. 3D-mapping of spatial variations in the cell wall mesh size of *P. infestans* germlings. Rotation views of the 3D fluorescence lifetime mesh size maps of *P. infestans* germlings represented in Fig. 5.1.

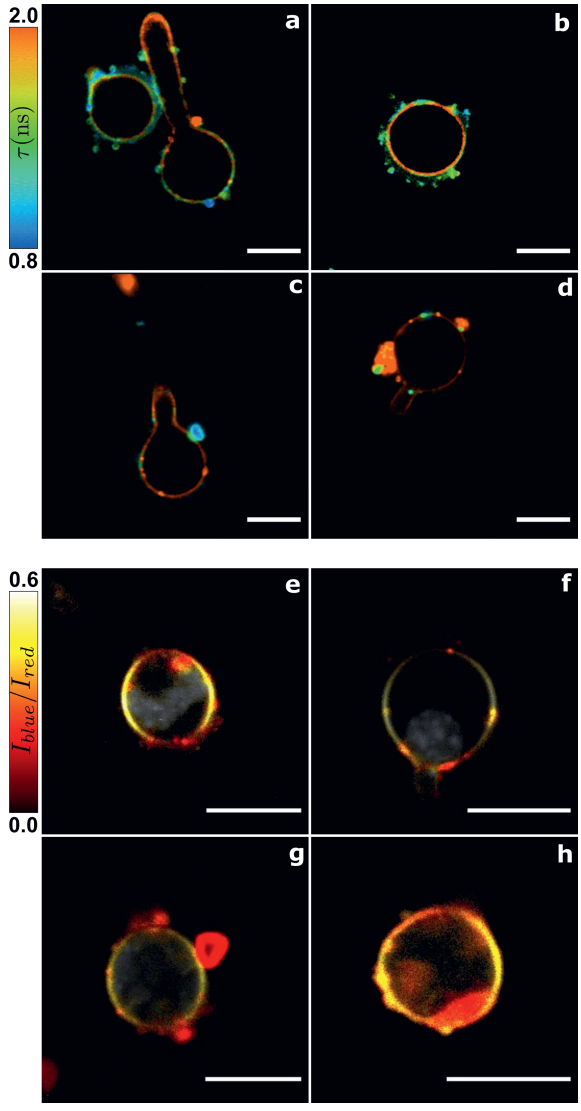

Figure 5.14. Hypo-osmotic treatment on *P. infestans* germlings, and effect on their cell wall and plasma membrane mechano-chemical properties. (a, b) Fluorescence lifetime mesh size map of germlings growing in a 90 mmol L^{-1} PEG2000g mol^{-1} aqueous solution. (c, d) Fluorescence lifetime mesh size map of germlings after transfer from the 90 mmol L^{-1} PEG2000g mol^{-1} aqueous solution to water. (e, f) Intensity ratio chemical polarity map of germlings growing in a 90 mmol L^{-1} PEG2000g mol^{-1} aqueous solution. (g, h) Intensity ratio chemical polarity map of germlings after transfer from the 90 mmol L^{-1} PEG2000g mol^{-1} aqueous solution to water. Scale bars = 10 μm.

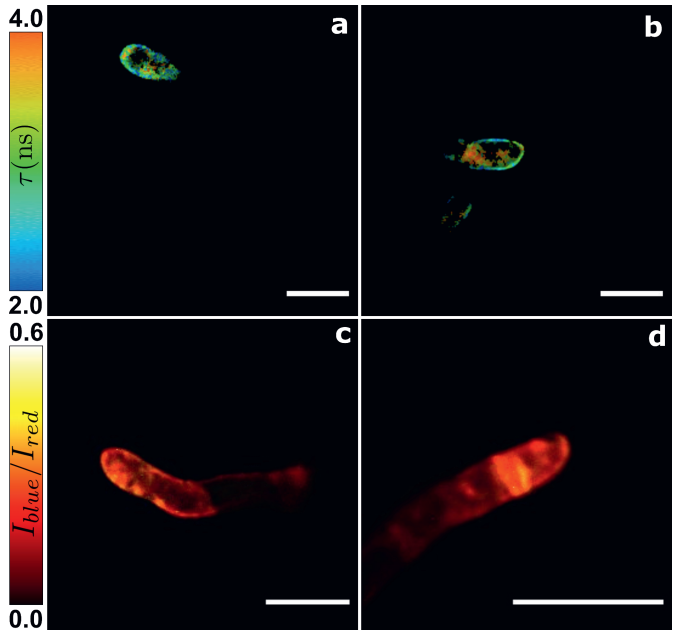

Figure 5.15. Mapping of spatial variations induced by treatment with 25 nmol L^{-1} fluopicolide in the cell wall mesh size and plasma membrane chemical polarity of *P. infestans* germlings. (a, b) Fluorescence lifetime mesh size map of germlings growing in water 1h post application, and treated with 25 nmol L^{-1} fluopicolide for 1h. (c, d) Intensity ratio chemical polarity map of germlings growing in water 1h post application, and treated with 25 nmol L^{-1} fluopicolide for 1h. Scale bars = 10 μm.

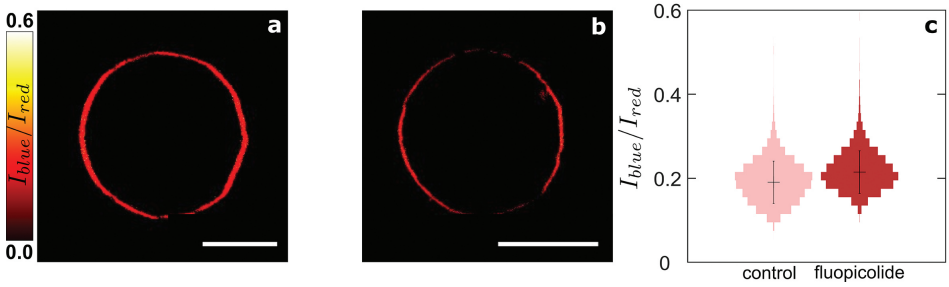

Figure 5.16. Mapping of spatial variations in plasma membrane chemical polarity in DOPC:SM synthetic vesicles. (a) Intensity ratio chemical polarity map of 1,2-dioleoyl-sn-glycero-3-phosphocholine (DOPC):sphingomyelin (SM) = 1:1 (molar ratio) synthetic vesicles. (b) Intensity ratio chemical polarity map of the same vesicles incubated with 25 nmol L^{-1} fluopicolide. (c) Corresponding intensity ratio probability distributions. Scale bars = 10 μm.

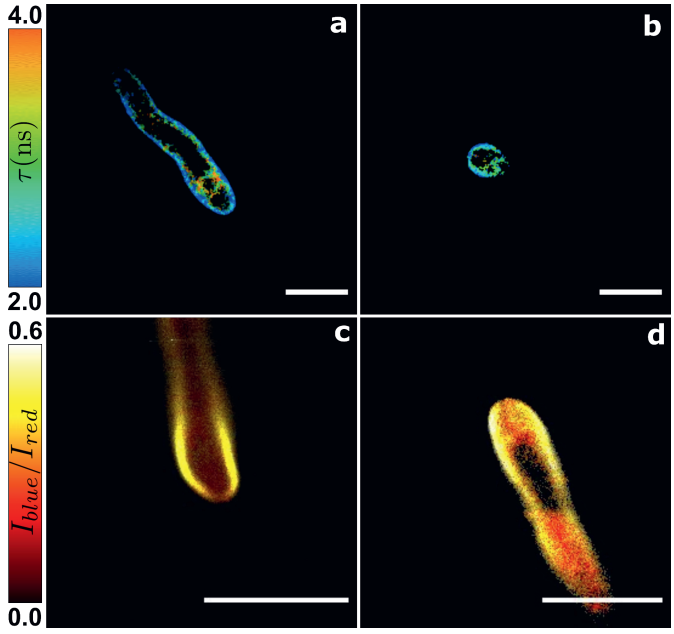

Figure 5.17. Mapping of spatial variations induced by treatment with 1% (v/v) DMSO in the cell wall mesh size and plasma membrane chemical polarity of *P. infestans* germlings. (a, b) Fluorescence lifetime mesh size map of germlings growing in water 1h post application, and treated with 1% (v/v) DMSO for 1h. (c, d) Intensity ratio chemical polarity map of germlings growing in water 1h post application, and treated with 1% (v/v) DMSO for 1h. Scale bars = 10 μm.

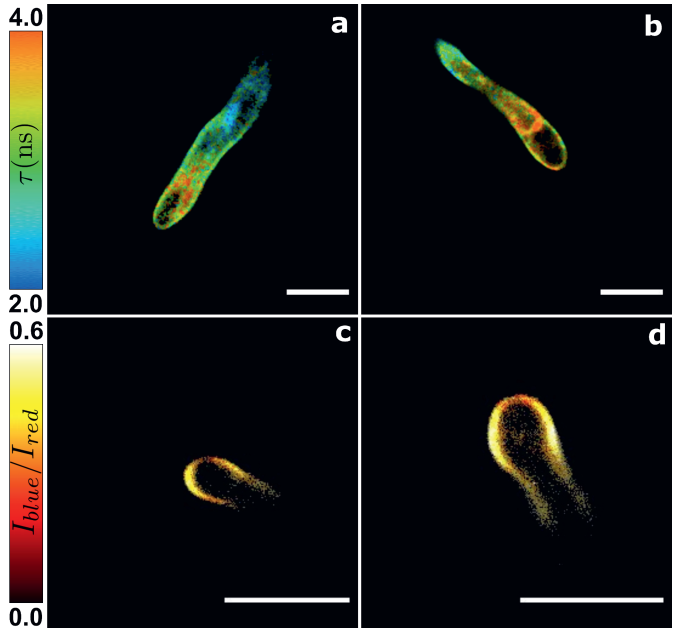

Figure 5.18. Mapping of spatial variations induced by treatment with 125 nmol L^{-1} valifenalate in the cell wall mesh size and plasma membrane chemical polarity of *P. infestans* germlings. (a, b) Fluorescence lifetime mesh size map of germlings growing in water 1h post application, and treated with 125 nmol L^{-1} valifenalate for 1h. (c, d) Intensity ratio chemical polarity map of germlings growing in water 1h post application, and treated with 125 nmol L^{-1} valifenalate for 1h. Scale bars = 10 μm.

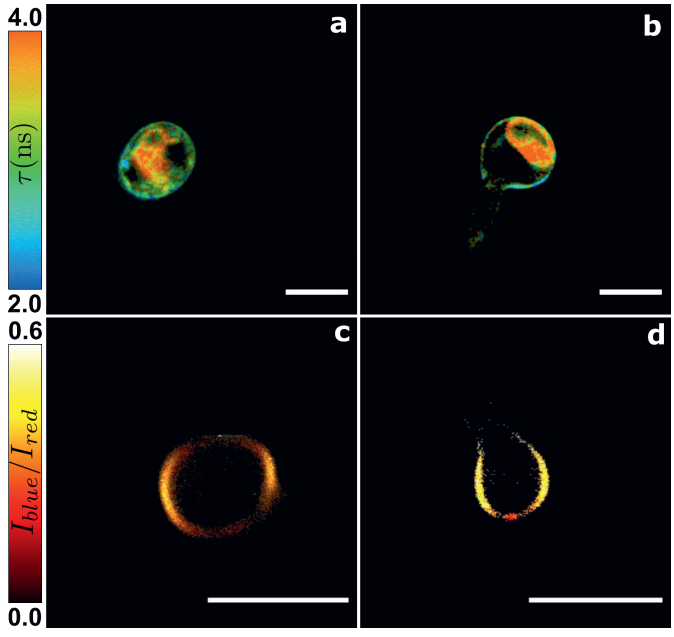

Figure 5.19. Mapping of spatial variations induced by treatment with 1 μmol L^{-1} latrunculin B in the cell wall mesh size and plasma membrane chemical polarity of *P. infestans* germlings. (a, b) Fluorescence lifetime mesh size map of germlings growing in water 1h post application, and treated with 1 μmol L^{-1} latrunculin B for 1h. (c, d) Intensity ratio chemical polarity map of germlings growing in water 1h post application, and treated with 1 μmol L^{-1} latrunculin B for 1h. Scale bars = 10 μm.

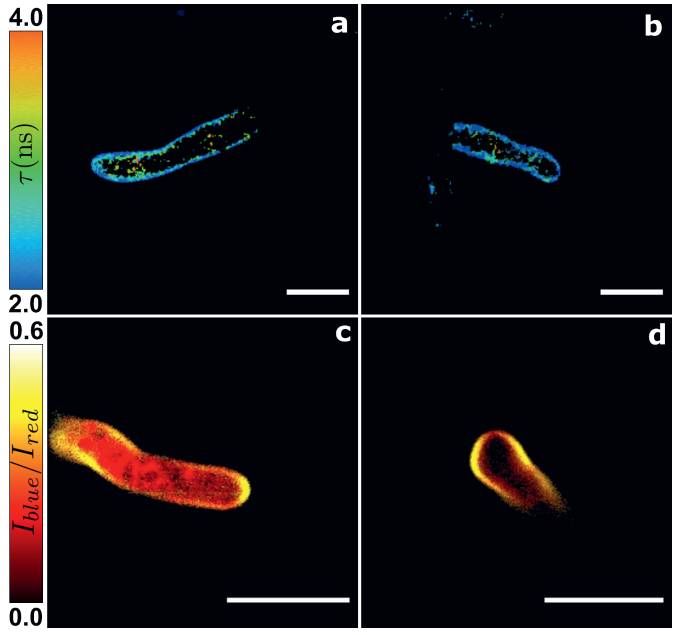

Figure 5.20. Mapping of spatial variations induced by treatment with 0.1 μmol L^{-1} oryzalin in the cell wall mesh size and plasma membrane chemical polarity of *P. infestans* germlings. (a, b) Fluorescence lifetime mesh size map of germlings growing in water 1h post application, and treated with 0.1 μmol L^{-1} oryzalin for 1h. (c, d) Intensity ratio chemical polarity map of germlings growing in water 1h post application, and treated with 0.1 μmol L^{-1} oryzalin for 1h. Scale bars = 10 μm.

References

[1] A. J. Haverkort, P. C. Struik, R. G.F. Visser, and E. Jacobsen. Applied biotechnology to combat late blight in potato caused by *phytophthora infestans*. *Potato Research*, 52(3):249–264, 2009.

[2] Sophien Kamoun, Oliver Furzer, Jonathan D. G. Jones, Howard S. Judelson, Gul Shad Ali, Ronaldo J. D. Dalio, Sanjoy Guha Roy, Leonardo Schena, Antonios Zambounis, Franck Panabières, David Cahill, Michelina Ruocco, Andreia Figueiredo, Xiao-Ren Chen, Jon Hulvey, Remco Stam, Kurt Lamour, Mark Gijzen, Brett M. Tyler, Niklaus J. Grünwald, M. Shahid Mukhtar, Daniel F. A. Tomé, Mahmut Tör, Guido Van Den Ackerveken, John McDowell, Fouad Daayf, William E. Fry, Hannele Lindqvist-Kreuze, Harold J. G. Meijer, Benjamin Petre, Jean Ristaino, Kentaro Yoshida, Paul R. J. Birch, and Francine Govers. The Top 10 oomycete pathogens in molecular plant pathology. *Molecular Plant Pathology*, 16(4):413–434, may 2015.

[3] Brian J. Haas, Sophien Kamoun, Michael C. Zody, Rays H.Y. Jiang, Robert E. Handsaker, Liliana M. Cano, Manfred Grabherr, Chinnappa D. Kodira, Sylvain Raffaele, Trudy Torto-Alalibo, Tolga O. Bozkurt, Audrey M.V. Ah-Fong, Lucia Alvarado, Vicky L. Anderson, Miles R. Armstrong, Anna Avrova, Laura Baxter, Jim Beynon, Petra C. Boevink, Stephanie R. Bollmann, Jorunn I.B. Bos, Vincent Bulone, Guohong Cai, Cahid Cakir, James C. Carrington, Megan Chawner, Lucio Conti, Stefano Costanzo, Richard Ewan, Noah Fahlgren, Michael A. Fischbach, Johanna Fugelstad, Eleanor M. Gilroy, Sante Gnerre, Pamela J. Green, Laura J. Grenville-Briggs, John Griffith, Niklaus J. Grünwald, Karolyn Horn, Neil R. Horner, Chia Hui Hu, Edgar Huitema, Dong Hoon Jeong, Alexandra M.E. Jones, Jonathan D.G. Jones, Richard W. Jones, Elinor K. Karlsson, Sridhara G. Kunjeti, Kurt Lamour, Zhenyu Liu, Lijun Ma, Daniel MacLean, Marcus C. Chibucos, Hayes McDonald, Jessica McWalters, Harold J.G. Meijer, William Morgan, Paul F. Morris, Carol A. Munro, Keith O'Neill, Manuel Ospina-Giraldo, Andrés Pinzón, Leighton Pritchard, Bernard Ramsahoye, Qinghu Ren, Silvia Restrepo, Sourav Roy, Ari Sadanandom, Alon Savidor, Sebastian Schornack, David C. Schwartz, Ulrike D. Schumann, Ben Schwessinger, Lauren Seyer, Ted Sharpe, Cristina Silvar, Jing Song, David J. Studholme, Sean Sykes, Marco Thines, Peter J.I. Van De Vondervoort, Vipaporn Phuntumart, Stephan Wawra, Rob Weide, Joe Win, Carolyn Young, Shiguo Zhou, William Fry, Blake C. Meyers, Pieter Van West, Jean Ristaino, Francine Govers, Paul R.J. Birch, Stephen C. Whisson, Howard S. Judelson, and Chad Nusbaum. Genome sequence and analysis of the Irish potato famine pathogen *Phytophthora infestans*. *Nature*, 461(7262):393–398, sep 2009.

[4] Howard S. Judelson, Audrey M. V. Ah-Fong, George Aux, Anna O. Avrova, Catherine Bruce, Cahid Cakir, Luis da Cunha, Laura Grenville-Briggs, Maita Latijnhouwers, Wilco Ligterink, Harold J. G. Meijer, Samuel Roberts, Carrie S. Thurber, Stephen C. Whisson, Paul R. J. Birch, Francine Govers, Sophien Kamoun, Pieter van West, and John Windass. Gene Expression Profiling During Asexual Development of the Late Blight

Pathogen *Phytophthora infestans* Reveals a Highly Dynamic Transcriptome. *Molecular Plant-Microbe Interactions*, 21(4):433–447, apr 2008.

[5] Svante Resjö, Maja Brus, Ashfaq Ali, Harold J.G. Meijer, Marianne Sandin, Francine Govers, Fredrik Levander, Laura Grenville-Briggs, and Erik Andreasson. Proteomic analysis of *phytophthora infestans* reveals the importance of cell wall proteins in pathogenicity. *Molecular and Cellular Proteomics*, 16(11):1958–1971, 2017.

[6] Yan Wang and Yuanchao Wang. *Phytophthora sojae* effectors orchestrate warfare with host immunity. *Current Opinion in Microbiology*, 46:7–13, dec 2018.

[7] Jamie McGowan and David A. Fitzpatrick. Recent advances in oomycete genomics. *Advances in Genetics*, 105:175–228, jan 2020.

[8] Vivianne G.A.A. Vleeshouwers, Sylvain Raffaele, Jack H. Vossen, Nicolas Champouret, Ricardo Oliva, Maria E. Segretin, Hendrik Rietman, Liliana M. Cano, Anoma Lokossou, Geert Kessel, Mathieu A. Pel, and Sophien Kamoun. Understanding and Exploiting Late Blight Resistance in the Age of Effectors. *http://dx.doi.org.ezproxy.library.wur.nl/10.1146/annurev-phyto-072910-095326*, 49:507–531, aug 2011.

[9] Kaile Sun, Anne Marie A. Wolters, Jack H. Vossen, Maarten E. Rouwet, Annelies E.H.M. Loonen, Evert Jacobsen, Richard G.F. Visser, and Yuling Bai. Silencing of six susceptibility genes results in potato late blight resistance. *Transgenic Research*, 25(5):731–742, oct 2016.

[10] Kamil Witek, Florian Jupe, Agnieszka I. Witek, David Baker, Matthew D. Clark, and Jonathan D.G. Jones. Accelerated cloning of a potato late blight–resistance gene using RenSeq and SMRT sequencing. *Nature Biotechnology 2016 34:6*, 34(6):656–660, apr 2016.

[11] Yu Du, Mohamed H. Mpina, Paul R. J. Birch, Klaas Bouwmeester, and Francine Govers. *Phytophthora infestans* RXLR effector AVR1 interacts with exocyst component Sec5 to manipulate plant immunity. *Plant Physiology*, 169(3):pp.01169.2015, sep 2015.

[12] Petra C. Boevink, Paul R. J. Birch, Dionne Turnbull, and Stephen C. Whisson. Devastating intimacy: the cell biology of plant– *Phytophthora* interactions. *New Phytologist*, 228(2):445–458, oct 2020.

[13] Benjamin Petre, Mauricio P. Contreras, Tolga O. Bozkurt, Martin H. Schattat, Jan Sklenar, Sebastian Schornack, Ahmed Abd-El-Haliem, Roger Castells-Graells, Rosa Lozano-Durán, Yasin F. Dagdas, Frank L H Menke, Alexandra M E Jones, Jack H. Vossen, Silke Robatzek, Sophien Kamoun, and Joe Win. Host-interactor screens of Phytophthora infestans RXLR proteins reveal vesicle trafficking as a major effector-targeted process. *The Plant Cell*, 33(5):1447–1471, jul 2021.

[14] Jochem Bronkhorst, Michiel Kasteel, Stijn van Veen, Jess M. Clough, Kiki Kots, Jesse Buijs, Jasper van der Gucht, Tijs Ketelaar, Francine Govers, and Joris Sprakel. A slicing mechanism facilitates host entry by plant-pathogenic *Phytophthora*. *Nature Microbiology*, 6(8):1000–1006, aug 2021.

[15] Lucile Michels, Vera Gorelova, Yosapol Harnvanichvech, Jan Willem Borst, Bauke Albada, Dolf Weijers, and Joris Sprakel. Complete microviscosity maps of living plant cells and tissues with a toolbox of targeting mechanoprobes. *Proceedings of the National Academy of Sciences of the United States of America*, 117(30):18110–18118, 2020.

[16] Niklaus J. Grünwald, Anne K. Sturbaum, Gaspar Romero Montes, Edith Garay Serrano, Hector Lozoya-Saldaña, and William E. Fry. Selection for Fungicide Resistance Within a Growing Season in Field Populations of *Phytophthora infestans* at the Center of Origin. *Phytopathology*, 96(12):1397–1403, dec 2006.

[17] Wen-qiao Wang, Peng Zhang, Run-jie Meng, Jian-jiang Zhao, Qi-liang Huang, Xiu-ying Han, Zhi-qiang Ma, and Xiao-feng Zhang. Fungitoxicity and synergism of mixtures of fluopicolide and pyraclostrobin against *Phytophthora infestans*. *Crop Protection*, 57:48–56, mar 2014.

[18] Oleksandr A. Kucherak, Sule Oncul, Zeinab Darwich, Dmytro A. Yushchenko, Youri Arntz, Pascal Didier, Yves Mély, and Andrey S. Klymchenko. Switchable Nile Red-Based Probe for Cholesterol and Lipid Order at the Outer Leaflet of Biomembranes. *Journal of the American Chemical Society*, 132(13):4907–4916, apr 2010.

[19] C. E. Caten. Spontaneous variability of single isolates of *Phytophthora infestans*. *Canadian Journal of Botany*, 48(5):897–905, may 1970.

[20] Theo Van der Lee, Ijfke De Witte, André Drenth, Carlos Alfonso, and Francine Govers. AFLP Linkage Map of the Oomycete *Phytophthora infestans*. *Fungal Genetics and Biology*, 21(3):278–291, jun 1997.

[21] J. N.M. Boots, R. Fokkink, J. Van der Gucht, and T. E. Kodger. Development of a multi-position indentation setup: Mapping soft and patternable heterogeneously crosslinked polymer networks. *Review of Scientific Instruments*, 90(1):015–108, jan 2019.

[22] Li-Heng Cai, Thomas E. Kodger, Rodrigo E. Guerra, Adrian F. Pegoraro, Michael Rubinstein, and David A. Weitz. Soft Poly(dimethylsiloxane) Elastomers from Architecture-Driven Entanglement Free Design. *Advanced Materials*, 27(35):5132–5140, sep 2015.

[23] Kim S. Horger, Daniel J. Estes, Ricardo Capone, and Michael Mayer. Films of Agarose Enable Rapid Formation of Giant Liposomes in Solutions of Physiologic Ionic Strength. *Journal of the American Chemical Society*, 131(5):1810–1819, feb 2009.

[24] Rafael B Lira, Jan Steinkühler, Roland L Knorr, Rumiana Dimova, and Karin A Riske. Posing for a picture: Vesicle immobilization in agarose gel. *Scientific Reports*, 6(1):25254, jul 2016.

[25] Nicholas P Money2. Osmotic Pressure of Aqueous Polyethylene Glycols' Relationship between Molecular Weight and Vapor Pressure Deficit. *Plant Physiol*, 91:766–769, 1989.

[26] R. J. Howard, M. A. Ferrari, D. H. Roach, and N. P. Money. Penetration of hard substrates by a fungus employing enormous turgor pressures. *Proceedings of the National Academy of Sciences*, 88(24):11281–11284, 1991.

[27] Alistair J. MacDougall, Gary M. Brett, Victor J. Morris, Neil M. Rigby, Michael J. Ridout, and Stephen G. Ring. The effect of peptide–pectin interactions on the gelation behaviour of a plant cell wall pectin. *Carbohydrate Research*, 335(2):115–126, sep 2001.

[28] Harold J. G. Meijer, Peter J. I. van de Vondervoort, Qing Yuan Yin, Chris G. de Koster, Frans M. Klis, Francine Govers, and Piet W. J. de Groot. Identification of Cell Wall-Associated Proteins from *Phytophthora ramorum*. *Molecular Plant-Microbe Interactions®*, 19(12):1348–1358, dec 2006.

[29] Jennifer Mach. Cellulose Synthesis in *Phytophthora infestans* Pathogenesis. *The Plant Cell*, 20(3):500–500, mar 2008.

[30] B. R. Grant, W. Greenaway, and F. R. Whatley. Metabolic Changes during Development of *Phytophthora palmivora* Examined by Gas Chromatography/Mass Spectrometry. *Microbiology*, 134(7):1901–1911, jul 1988.

[31] Alon Savidor, Ryan S. Donahoo, Oscar Hurtado-Gonzales, Miriam L. Land, Manesh B. Shah, Kurt H. Lamour, and W. Hayes McDonald. Cross-species Global Proteomics Reveals Conserved and Unique Processes in *Phytophthora sojae* and *Phytophthora ramorum*. *Molecular & Cellular Proteomics*, 7(8):1501–1516, aug 2008.

[32] Zhili Pang, Vaibhav Srivastava, Xili Liu, and Vincent Bulone. Quantitative proteomics links metabolic pathways to specific developmental stages of the plant-pathogenic oomycete *Phytophthora capsici*. *Molecular Plant Pathology*, 18(3):378–390, apr 2017.

[33] Sander Y.A. Rodenburg, Michael F. Seidl, Dick de Ridder, and Francine Govers. Genome-wide characterization of *Phytophthora infestans* metabolism: a systems biology approach. *Molecular Plant Pathology*, 19(6):1403–1413, jun 2018.

[34] Fungicide Resistance Action Committee (FRAC). FRAC classification of fungicides. *FRAC Poster ® 2019*, (March):2019, 2020.

[35] Wolfgang Kramer and Ulrich. Schirmer. *Modern crop protection compounds*. Wiley-VCH, 2007.

[36] Valérie Toquin, François Barja, Catherine Sirven, Stéphanie Gamet, Lucile Mauprivez, Philippe Peret, Marie-pascale Latorse, and Jean-luc Zundel. *Recent Developments in Management of Plant Diseases*. Springer Netherlands, Dordrecht, 2009.

[37] E. Marsilii, S. O. Cacciola, A. Salamone, G. Scarito, F. Raudino, A. Pane, and G. M. di San Lio. Efficacy of valifenalate against *Phytophthora* spp. of ornamental plants. *Protezione delle Colture*, 2:108–109, 2009.

[38] A. Salamone, F. Raudino, S. O. Cacciola, and G. D. San Lio. Efficacy of the fungicide valifenalate against crown rot of rose caused by *Phytophthora citrophthora*. *Proceedings of the 17th International Reinhardsbrunn Symposium*, pages 55–60, 2013.

[39] I. Brent Heath and Susan G.W. Kaminskyj. The organization of tip-growth-related organelles and microtubules revealed by quantitative analysis of freeze-substituted oomycete hyphae. *Journal of Cell Science*, 93(1):41–52, may 1989.

[40] Eugen Temperli, Urs Peter Roos, and Hans R. Hohl. Germ tube growth and the microtubule cytoskeleton in *Phytophthora infestans*: Effects of antagonists of hyphal growth, microtubule inhibitors, and ionophores. *Mycological Research*, 95(5):611–617, may 1991.

[41] G J Hyde and A R Hardham. Microtubules regulate the generation of polarity in zoospores of *Phytophthora cinnamomi*. *Eur J Cell Biol*, 62(1):75–85, 1993.

[42] Anja Geitmann and A. M.C. Emons. The cytoskeleton in plant and fungal cell tip growth. Technical Report 3, 2000.

[43] Mathias Blum, Martine Boehler, Eva Randall, Vanessa Young, Michael Csukai, Sabrina Kraus, Florence Moulin, Gabriel Scalliet, Anna O. Avrova, Stephen C. Whisson, and Raymonde Fonne-Pfister. Mandipropamid targets the cellulose synthase-like PiCesA3 to inhibit cell wall biosynthesis in the oomycete plant pathogen, *Phytophthora infestans*. *Molecular Plant Pathology*, 11(2):227–243, mar 2010.

[44] Tijs Ketelaar, Harold J.G. Meijer, Marjolein Spiekerman, Rob Weide, and Francine Govers. Effects of latrunculin B on the actin cytoskeleton and hyphal growth in *Phytophthora infestans*. *Fungal Genetics and Biology*, 49(12):1014–1022, dec 2012.

[45] L. C. Morejohn, T. E. Bureau, J. Mol-Bajer, A. S. Bajer, and D. E. Fosket. Oryzalin, a dinitroaniline herbicide, binds to plant tubulin and inhibits microtubule polymerization in vitro. *Planta*, 172(2):252–264, oct 1987.

[46] V. Dostál and L. Libusová. Microtubule drugs: action, selectivity, and resistance across the kingdoms of life. *Protoplasma*, 251(5):991–1005, sep 2014.

[47] Harold J G Meijer, Chenlei Hua, Kiki Kots, Tijs Ketelaar, and Francine Govers. Actin dynamics in *Phytophthora infestans*; rapidly reorganizing cables and immobile, long-lived plaques. *Cellular Microbiology*, 16(6):948–961, 2014.

[48] Kiki Kots, Harold J.G. Meijer, Klaas Bouwmeester, Francine Govers, and Tijs Ketelaar. Filamentous actin accumulates during plant cell penetration and cell wall plug formation in *Phytophthora infestans*. *Cellular and Molecular Life Sciences*, 74(5):909–920, 2017.

[49] Christian Kock, Yves F. Dufrêne, and Jürgen J. Heinisch. Up against the Wall: Is Yeast Cell Wall Integrity Ensured by Mechanosensing in Plasma Membrane Microdomains? *Applied and Environmental Microbiology*, 81(3):806–811, feb 2015.

[50] Tarek Elhasi and Anders Blomberg. Integrins in disguise – mechanosensors in *Saccharomyces cerevisiae* as functional integrin analogues. *Microbial Cell*, 6(8):335–355, aug 2019.

[51] Ramakanth Neeli-Venkata, Celia Municio Diaz, Ruben Celador, Yolanda Sanchez, and Nicolas Minc. Detection of surface forces by the cell-wall mechanosensor Wsc1 in yeast. *Developmental Cell*, 56(20):2856–2870.e7, oct 2021.

[52] Naomi Nakayama, Richard S. Smith, Therese Mandel, Sarah Robinson, Seisuke Kimura, Arezki Boudaoud, and Cris Kuhlemeier. Mechanical regulation of auxin-mediated growth. *Current Biology*, 22(16):1468–1476, aug 2012.

[53] Olivier Hamant and Elizabeth S. Haswell. Life behind the wall: Sensing mechanical cues in plants, dec 2017.

[54] L. J. Grenville-Briggs, V. L. Anderson, J. Fugelstad, A. O. Avrova, J. Bouzenzana, A. Williams, S. Wawra, S. C. Whisson, P. R.J. Birch, V. Bulone, and P. van West. Cellulose Synthesis in *Phytophthora infestans* Is Required for Normal Appressorium Formation and Successful Infection of Potato. *the Plant Cell Online*, 20(3):720–738, 2008.

[55] Rabah Zerzour, Jens Kroeger, and Anja Geitmann. Polar growth in pollen tubes is associated with spatially confined dynamic changes in cell mechanical properties. *Developmental Biology*, 334(2):437–446, oct 2009.

[56] Ashley Garrill, Roger R Lew, and I Brent Heath. Stretch-activated Ca 2+ and Ca 2+-activated K channels in the hyphal tip plasma membrane of the oomycete *Saprolegnia ferax*. *Journal of Cell Science*, 101:721–730, 1992.

[57] A. Garrill, S. L. Jackson, R. R. Lew, and I. B. Heath. Ion channel activity and tip growth: tip-localized stretch-activated channels generate an essential Ca2+ gradient in the oomycete *Saprolegnia ferax*. *European Journal of Cell Biology*, 60(2):358–365, apr 1993.

[58] Stephan Wawra, Rodrigo Belmonte, Lars Löbach, Marcia Saraiva, Ariane Willems, and Pieter van West. Secretion, delivery and function of oomycete effector proteins. *Current Opinion in Microbiology*, 15(6):685–691, 2012.

[59] Ulrich Gisi and Helge Sierotzki. Oomycete Fungicides: Phenylamides, Quinone Outside Inhibitors, and Carboxylic Acid Amides. In *Fungicide Resistance in Plant Pathogens*, pages 145–174. Springer Japan, Tokyo, 2015.

[60] Charles T Anderson, Ian S Wallace, and Chris R Somerville. Metabolic click-labeling with a fucose analog reveals pectin delivery, architecture, and dynamics in Arabidopsis cell walls. *PLANT BIOLOGY*, 109(4):1329–1334, 2012.

[61] Marie Dumont, Arnaud Lehner, Boris Vauzeilles, Julien Malassis, Alan Marchant, Kevin Smyth, Bruno Linclau, Aurélie Baron, Jordi Mas Pons, Charles T Anderson, Damien Schapman, Ludovic Galas, Jean-Claude Mollet, and Patrice Lerouge. Plant cell wall imaging by metabolic click-mediated labelling of rhamnogalacturonan II using azido 3-deoxy- <scp>d</scp> - manno -oct-2-ulosonic acid. *The Plant Journal*, 85(3):437–447, feb 2016.

[62] Yuntao Zhu, Jie Wu, and Xing Chen. Metabolic Labeling and Imaging of N-Linked Glycans in *Arabidopsis Thaliana*. *Angewandte Chemie International Edition*, 55(32):9301–9305, aug 2016.

[63] Xiaoli Sun, Aihua Zhang, Brenda Baker, Luo Sun, Angela Howard, John Buswell, Damien Maurel, Anastasiya Masharina, Kai Johnsson, Christopher J Noren, Ming-Qun Xu, and Ivan R. Corrêa. Development of SNAP-Tag Fluorogenic Probes for Wash-Free Fluorescence Imaging. *ChemBioChem*, 12(14):2217–2226, sep 2011.

[64] Peter J. Bosch, Ivan R. Corrêa, Michael H. Sonntag, Jenny Ibach, Luc Brunsveld, Johannes S. Kanger, and Vinod Subramaniam. Evaluation of fluorophores to label

SNAP-Tag fused proteins for multicolor single-molecule tracking microscopy in live cells. *Biophysical Journal*, 107(4):803–814, aug 2014.

General Discussion

Introduction

In this thesis, we have presented a focused effort to elucidate the mechanobiology of host invasion by *Phytophthora* species, a group of notorious plant pathogens that cause huge yield losses in agriculture and substantial damage in natural ecosystems. In the course of the project, we have elucidated the mechanical mechanism of host penetration employed by these pathogens (Chapter 3), unraveled how mechanical stresses link to their cytoskeleton (Chapter 4) and studied how mechanical, or chemical, stress alters the properties of their cell wall and plasma membranes (Chapter 5). Since mechanobiology is a relatively novel and emerging field, in particular for studying pathogens and pathogenesis, many of the tools required to measure mechanical patterns in living cells during host penetration needed to be conceived, designed and developed from scratch first (Chapter 2). Now that we have established, benchmarked and tested these tools, they offer a plethora of possibilities for either by extending and further optimizing them to answer unresolved questions, or to apply them to pathogenesis phenomena in other microorganisms. Some of the ideas developed in those directions did not find completion within the time frame of this project. Nevertheless, they provide promising clues for future research in this novel field of 'Physical Phytopathology'. In this chapter, I illustrate how some of the open questions may be addressed, providing some preliminary results and discussion on future challenges and conclude with an outlook.

Fluorometric pectinesterase assay

The first material a filamentous plant pathogen encounters is cutin, a rigid, waxy and crosslinked polyester that coats the exterior of leaves, stems and roots. This cuticle functions as a water barrier[1] and protects against pathogens[2]. It is also the first mechanical barrier the pathogen must conquer to invade. In addition to using mechanical tactics, many pathogens also secrete enzymes as biochemical weapons to weaken plant structures and facilitate invasion[3]. A variety of fungi and also oomycetes, including *Phytophthora* species[4], secrete cutinase, which is a serine esterase that cleaves the cutin polyester linkages. Moreover, many plant pathogens also secrete cell wall degrading enzymes to weaken wall mechanics and make penetration easier; in particular those that target pectins are important, as pectins are crucial components in the mechanical resilience of plant cell walls[5]. Several *Phytophthora* species secrete pectinesterases[6], that alter cell wall mechanics by desterification of pectin into pectate and methanol. The interplay between enzymatic activity and mechanical force generation to accomplish host invasion is currently unknown. It is not possible to directly visualize the enzymatic action of these esterase enzymes, fundamental to understanding their activity and functionality, a major challenge in the field. To address this challenge, in contrast to focusing on the genetic modification of *P. infestans*, we developed a surface sensor for esterase activity.

We embedded a fluorophore-quencher pair in the synthetic polyester Poly(Lactic Acid) (PLA), which we can coat onto a surface from a stock solution. Inside the PLA film, the quencher inhibits fluorescence emission. Upon esterase activity, the PLA matrix becomes loosened, and the dye (coumarin) and quencher are released into solution, where dilution effects cause the emergence of fluorescence as a signal of esterase activity. We have coated the inside of cuvettes with this material and first exposed it to a solution containing trypsin. Trypsin is known to cleave PLA[7] and can be used as a positive control. Both a high and low concentration of trypsin result in fluorescence-turn on (Fig 6.1A, orange+red). By contrast, exposure to pure water, the negative control, lead to a neglectable incease in fluorescence (Fig 6.1A, green). Next, we exposed the esterase surface sensor to a suspension of *P. infestans* cysts that were followed for several hundred minutes, more than enough time to start germination and hyphal growth. This resulted in clear fluorescence activation and hence this provides evidence for the presence of esterases in the suspensions, presumably secreted by the germinated cysts.

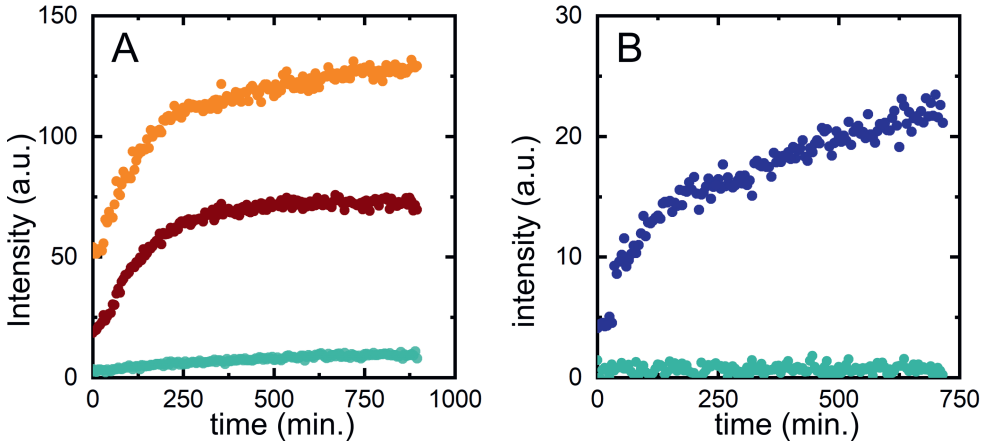

Figure 6.1. (A) Fluorimetric measurement of coumarin release in a PLA coated cuvette over time upon adding a trypsin solution at 5x (upper orange line), 1x (middle red line) concentrations and no trypsin (lower green line). (B) Fluorimetric measurement of coumarin release of a PLA coated cuvette over time upon adding *P. infestans* cysts (upper blue line) and PBS (lower green line).

We attempted to combine these enzyme-responsive coatings with our PDMS elastomer surfaces for in-situ imaging of enzymatic activity of *P. infestans* during invasion. The main problem encountered when spincoating esterase sensitive molecule incorporated PLA on PDMS was surface inhomogeneity, resulting in a "bumpy" layer. We hypothesized this to be caused by the uneven evaporation of a polymer film on an elastomer surface with an affinity for the solvent. Potentially, using a diluted sample and lower spin speeds could avoid surface homogeneity. Future efforts should focus at obtaining homogenous enzyme-responsive coatings preferably for a diverse array of enzymes that are implicated in invasion. This would not only provide a means to evaluate the time and site of enzymatic action during host entry, but also allow bringing the PDMS elastomer substrates one step closer to the mechanical geometry of plant exteriors: a solid and rigid polyester layer on top of a more compliant structure, formed by the epidermal cells.

Immunostaining

A common tool used to study sub-cellular organization in electron and fluorescence microscopy is immunostaining[8], an approach exploiting the specificity of antibodies; proteins with highly specific binding to an epitope in the cell. Our study on mechanical feedback in the cytoskeleton (Chapter 4), lead us to hypothesize which proteins are at play to orchestrate these responses. We have attempted to use immunofluorescence labeling to find evidence for the involvement of cytoskeletal proteins in the tip shape mechanostat. We have tried visualizing specific actin-associated proteins through the use of antibodies, in particular antibodies against α-actinin[9] and ARP2/3[10,11], which are both known to be mechano-sensitive[12,13] of which encoding genes are present in the *Phytophthora*[14,15] genome. Immunostaining in *P. infestans* and several other *Phytophthora* spp. has been reported previously[8,16]. Usage of antibodies requires fixation of the biological material followed by antibody entry into the cell. This requires passage of both the cell wall (which we have partially degraded using enzymes) and the plasma membrane to bind to the actin cytoskeleton. We use a complementary fluorescent actin marker, AlexaFluor647-phalloidin, as a control of actin cytoskeletal integrity.

The results of antibody and phalloidin staining are shown in Fig 6.2. The phalloidin staining, which easily enters the cell to stain the actin cytoskeleton, shows that our fixation and staining method is suitable and the actin cytoskeleton is (partially) conserved[17,18], but we consistently find antibodies to aggregate at the cell boundary as seen in (Fig 6.2C/F). We hypothesize this to be due their size; phalloidin is $\approx$ 1 nm in size vs $\approx$ 5-10 nm for antibodies[19], requiring a much more permeable cell wall. To increase the viablility of antibody staining, we have employed cell wall degrading enzymes to increase cell wall porosity. While the phalloidin staining appears to work well, we discovered (Chapter 4) that it does not exactly reproduce the same actin configurations as our live-cell genetic actin marker LifeAct-eGFP, suggesting that not all actin-binding probes will provide the same information, and that care must be taken to interpret these types of data. More detailed studies of cytoskeletal responses during invasive growth will require resolving these issues, either by optimizing the antibody labelling procedure, or by the development of fluorescent markers lines for actin-binding proteins of interest.

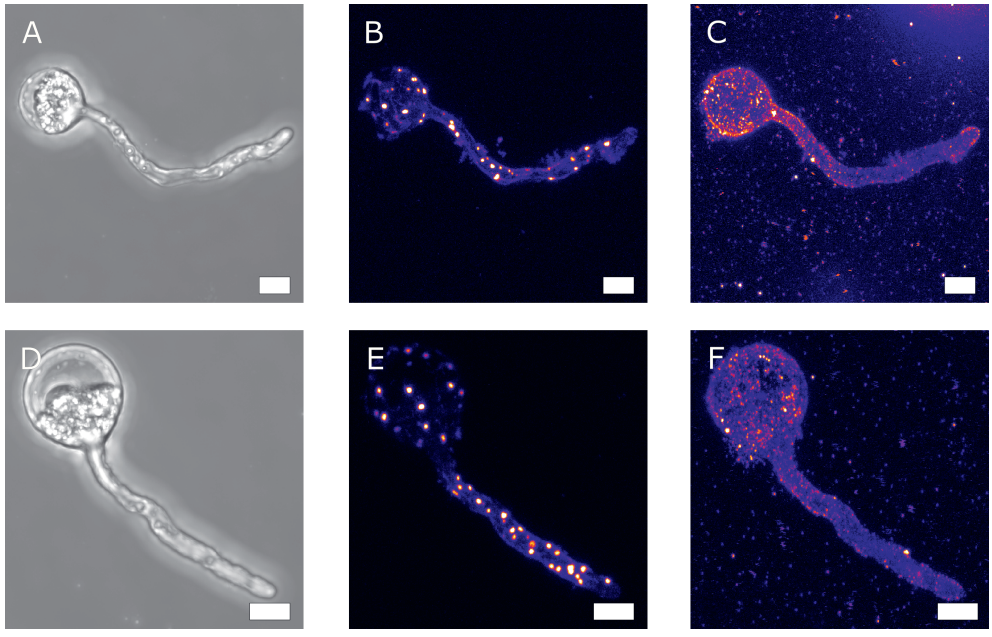

Figure 6.2. Confocal microscopy images of *P infestans* (88069, wt) cells that were fixed on glass slides and simultaneously (A/D) stained with alexa647-phalloidin (B/E) and incubated with actin antibodies (C/F). Cell wall degrading enzymes used to digest cell walls were Cellulase (1 mg/ml) and Driselase (10 mg/ml), followed by staining with both alexa647-phalloidin and anti-actin antibodies (produced in rabbit, unconjugated, polyclonal, primary) and anti-rabbit antibodies (produced in goat, conjugated to CF488A, polyclonal, secondary) (2 microgram/ml). Fish gelatin was used as a blocking agent (15 mg/ml). All reagents were purchasde from Sigma-Aldrich. Images are minimum (A/D) and maximum (B/C/E/F) xz projections, scale bars are 5 micron.

Mechanobiology of host invasion by *Magenaporthe oryzae*

Magnaporthe oryzae is a potent fungal plant pathogen[20], causal agent of the rice blast disease. Since approximately 25 % of caloric intake in South-East Asia comes from rice, and the rice blast disease can decrease rice yields by up to 30%, *M.oryzae* forms a severe threat to food security[21]. Its major impact is the reason why *M. oryzae* is one of the fungal pathogens whose pathogenicity is the most well studied[22]. Yet, many aspects of the mechanical mechanism facilitating host invasion remain unclear. *M. oryzae* invades above-ground plant parts from asexual spores, which germinate and form appressoria to enter their host. The appressorium is a specific cellular structure, able to build enormous pressures[23] by forming a tough layer of melanin on its exterior that acts as a pressure-containment jacket. Upon reaching a critical pressure[24], a pressure-sensitive kinase[25] is activated initiating a signal transduction cascade, and a penetration peg is ejected downwards, breaching the surface and penetrating the epidermis from where host invasion proceeds to the next cell layer. Generating these large forces in the downwards direction requires high adhesive strength to balance invasion forces. How the mechanical balance is maintained is still unknown[26]. After germination of a *M. oryzae* conidium, the appressorium that appears at the germ tube tip (Fig 6.3A/B) builds up turgor pressure over time, resulting in the increased application of indentation and adhesive forces.

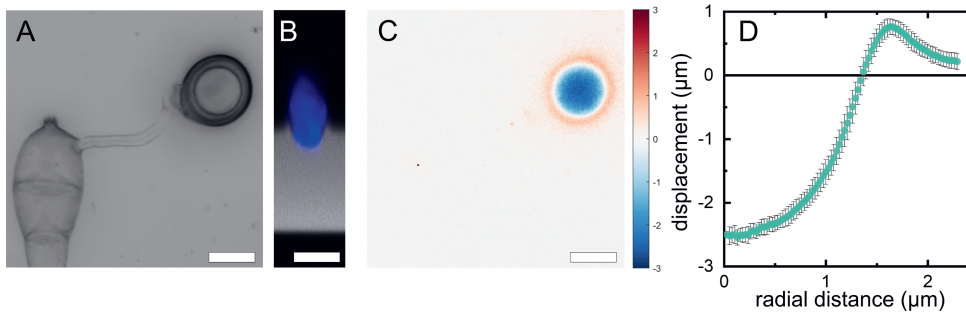

Figure 6.3. Displacement of *Magnaporthe oryzae* appressorium on PDMS. (A) Confocal microscopic image of conidium, germ tube and mature appressorium. (B) xz projection of appressorium (blue) on PDMS layer (white). (C) Displacement map of mature appressorium. (D) radially averaged displacement profile of appressorium displacement in C. Scale bars are 5 micron (A/C) and 2.5 micron (B). Data recorded by Dr. Lauren Ryder, TSL Norwich, UK.

We started applying the surface displacement sensors developed in this thesis (Chapter 2 and 3) to monitor the invasion mechanics of this fungal pathogen in a collaboration with dr. Lauren Ryder and prof. Nicolas Talbot (the Sainsbury

Laboratory, Norwich (UK)). High resolution surface displacement maps reveal the mechanical pattern created by the appressorium (Fig 6.3C). First, we note that the pattern is radially symmetric, a reflection of the apolar nature of the appressorium, versus the strongly asymmetric pattern for the polar growth typical for *Phytophthora* (Chapter 3 and 4). We observe an adhesive ring encircling a circular indentation site. This displacement pattern looks similar to the one observed for the indentation of an elastomer surface with an adhesive sphere[26], the so-called Johnson-Kendal-Roberts (JKR) scenario. To date, we have not been able to elicit penetration peg ejection by *M. oryzae* on PDMS substrates. Whether this is due to a lack of a mechanical trigger (e.g. the surface isn't sufficiently rigid) or lack of chemical signals, is currently under investigation.

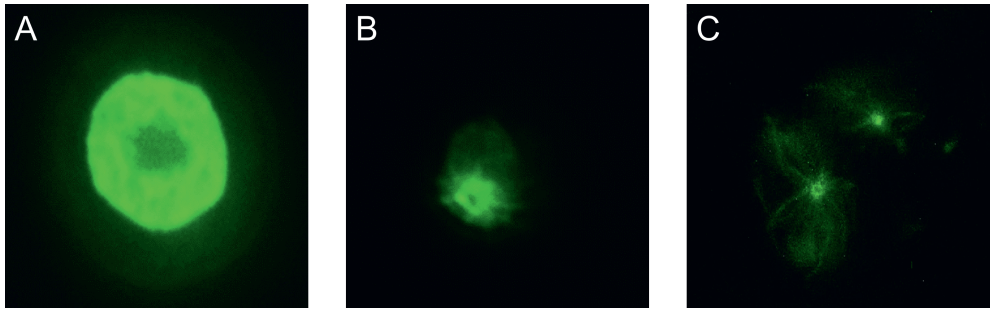

Figure 6.4. Confocal microscopic images of a appressoria of a *Magnaporthe oryzae* transformant expressing GFP-tagged Septin5 (Sep5-GFP) on three substrates: (A) glass, (B) PDMS and (C) rice leaf. Data recorded by Dr. Lauren Ryder, TSL Norwich, UK.

Septins are critical regulators of appressorium formation and pathogenesis in fungi[27]. To investigate the role of septins in surface displacement, we studied a transformant of *M. oryzae* where the Septin5 is fused to GFP (Sep5-GFP) (Fig 6.4). Interestingly, we find that Sep5 organisation is strongly influenced by local mechanics (Fig 6.4A-C). A very clear and large septin ring is observed on a very rigid substrate, i.e. glass (Fig 6.4A), shrinking in size and forming more web-like structures on the more compliant PDMS surface (Fig 6.4B), while reducing in size even further on rice leaves (Fig 6.4C). This suggests that Sep5 localization appears to be dependent upon local mechanical cues (glass vs PDMS) and on other either topographical or biochemical cues on the rice leaf surface.

This case study shows how applying mechanical tools presented in this thesis to studying a variety of other plant pathogens is a promising avenue for broadening our physical perspective on pathogen-host interactions. Studying the mechanical feedback between pathogen and host in conjunction with genetically modified lines expressing fluorescently marker proteins or with targeted muta-

tions/transformants, would also allow elucidating how mechanical cues can rewire biological programs, an essential step in mechanical perception and responses to accomplish successful host penetration. We see a plethora of opportunities for a new look at host penetration by filamentous plant pathogens using the approaches described in this thesis.

Durotropism

The work reported in this thesis shows that *Phytophthora* spp. can actively and quantitatively respond to the mechanical forces of host penetration, utilizing its actin cytoskeleton as a mechanosensor (Chapter 4). In many other walled organisms, a wide array of mechanosensors is used to sense their mechanical surroundings, ranging from mechanical contact sensors in yeasts[28], mechanosensitive ion channels in plants[29] to mechanosensitive kinases in fungi[25]. Whether *Phytophthora* spp. feature such mechanosensors at their cell boundaries is currently unknown. It is known that oomycetes can direct their motion and growth towards chemical cues. Zoospores, the motile propagules of *Phytophthora* spp, swim towards the edge of water droplets on leaves for optimized dispersal in aqueous environment[30], whilst guided by chemical[31] and/or electrical cues[32] to find hosts. Once the host is found, zoospores encyst[33] and start germinating. The germ tube grows along the substrate, without making strong mechanical contact, as shown in this thesis (Chapter 3), for a certain amount of time, until it "decides" to invade the substrate it is on. How the decision for the invasive site is made is unclear; in particular it is unknown if the pathogen can sense physical cues from the substrate to identify the optimal location. For example, leaves are highly heterogeneous in their mechanics[34]; can germ tubes 'feel' weak spots in the plant surface to facilitate their entry? Moreover, plant surfaces feature intricate topographical patterns; what role topography detection plays in host recognition and invasion site selection is not known.

In a team effort, spearheaded by dr. Lucile Michels, we have set out a new project to answer the question: do *Phytophthora* pathogens integrate physical cues from the surfaces they invade? If so, the ability of growing tubes to sense stiffness gradients by mechanosensory mechanisms and changing growth direction/behaviour as a function of substrate stiffness (called durotropism) could be tested[35]. To answer this question, we developed surfaces with a patterned stiffness. This is accomplished by first patterning a texture of 30 micrometer heigh of a very stiff polymeric material SU8, with a modulus of 2 GPa[36], onto a glass slide (Fig 6.5A). Then a thin layer of a soft PDMS elastomer layer is placed on top. The mechanical coupling between the thin soft layer on top of the SU8 structures[37] results in an high effective stiffness on top of the rows, and a much softer material between the rows. Since germtubes are generally 30+ micron in length before switching to invasive growth, this design allows hyphae to sense both pillar supported (stiff) elastomer and free elastomer spaces (soft) before invading the substrate. We now have these patterned PDMS surfaces ready, as shown in Fig 6.5B/C, where the elastomer layer (B) and pillar layer (C) are clearly distinguishable. These new surfaces will allow

us in the near future to dive deeper into the ways *Phytophthora* spp. perceive their physical surroundings, e.g., by monitoring if there is an invasion bias towards the weaker sites. If durotropism can indeed be observed, we can change the thickness of the PDMS layer to vary the stiffness contrast. Tunable stiffness contrast would allow identifying the sensitivity of the durotropic machinery. Uncovering how such speculated durotropic responses are mediated at the molecular scale would provide new strategies for controlling pathogens and protecting crops from diseases. Disruption of this machinery would disable the pathogen's ability to select weakened sites of the plant, lowering their infectivity.

A logical next step would be to also include surface topography in our mechanobiological toolbox. Approaches to microfabricate surface structures are widely available[38,39], and it is even possible to replicate the exact topographical structure of host versus non-host leaves using negative replica templating[40,41] to further explore the role of topography in host recognition.

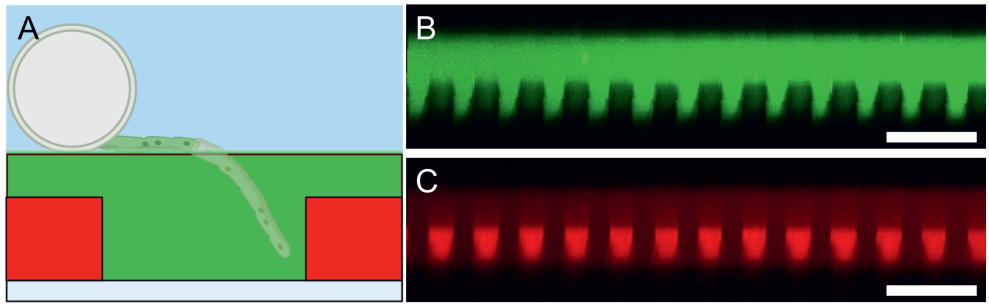

Figure 6.5. (A) Schematic illustration of spatially inhomogenous stiffness PDMS slab, with a ghost outline of an invasive hyphae. Cell size not to scale, created with BioRender.com. Preliminary confocal microscopic data of sensor design, xz projections of (B) a dyed PDMS layer and (C) SU-8 pillars. Data of Dr. Lucile Michels, WUR. Scale bar is 100 μm.

Outlook

A mechanobiological viewpoint on pathogen-host interactions is fertile ground for both fundamental and translational research. Despite the progress made in this thesis, many open questions beg to be answered.

The use of Lab-On-Chip techniques to generate complex "challenge" mazes show that hyphae are able to respond dynamically to their environment, bending around and displacing obstacles to accommodate growth[42]. Understanding how mechanical information is transduced from outside to inside the cell, mediated through the cell wall, plasma membrane and cytoskeleton, will shine light on fundamental biological processes essential for pathogen survival. We anticipate that this will become more and more feasible, in particular due to recent advances in tailoring molecular mechanoprobes, e.g. those based on DNA[43], proteins[44] or synthetic fluorophores[45], that bring quantitative mechanical imaging at the subcellular level in all the relevant structures involved in mechanical signal transduction, within reach.

One of our guiding principles has been to design tools that are reasonably simple, both in their set-up and use, and make data analysis as straightforward as possible, to allow for widespread adoption of these methodologies. The preparation of the PDMS sensor surfaces requires commercially procured elastomer and fluorophores and a simple spin coater. Measuring entrance angles into the PDMS does not require coding or complex analysis tools per-se but can be performed using free image processing software, or our openly shared code database resulting from this project. The algorithms used for high resolution displacement analysis are simple in use, although do require some basic knowledge of MatLab coding. In principle this could be simplified, e.g. by using a linear fitting approach to the fluorescence decay, which would speed up the analysis considerably, at the expense of accuracy, and allow for real-time displacement analysis. The case study shown above for the fungus *Magnaporthe oryzae*, demonstrates that this toolbox can be readily expanded to a larger array of species. We hope that our tools are instrumental to further develop mechanobiology to a quantitative discipline, and as such, complimenting other approaches to build our understanding of how mechanics control biological processes.

A final outlook worth mentioning is of more translational nature. We and others showed how adhesion of plant pathogens to the host surface plays a major role in penetration[26,46,47]. We then prepared adhesion-blocking polymers, which, when coated between *P. infestans* and PDMS surfaces or potato leaves, led to reduced adhesive interactions, evidenced from the increased hyphal growth rate, which in turn reduced invasiveness to almost zero. Reducing adhesion by e.g. coating

the leaves[48] with non-adhesive substances, modifying the leaf surface by targeted breeding or via genetic modification, or blocking the secretion of adhesins from exocytotic vesicles[16], are potentially interesting avenues to pursue when designing novel strategies for disease control.

References

[1] Lukas Schreiber. Transport barriers made of cutin, suberin and associated waxes. *Trends in Plant Science*, 15(10):546–553, oct 2010.

[2] M. B. Dickman, G. K. Podila, and P. E. Kolattukudy. Insertion of cutinase gene into a wound pathogen enables it to infect intact host. *Nature*, 342(6248):446–448, 1989.

[3] George Agrios. *Plant Pathology*, volume 6. Elsevier, 2005.

[4] Pruthvi B. Kalyandurg, Poorva Sundararajan, Mukesh Dubey, Farideh Ghadamgahi, Muhammad Awais Zahid, Stephen C. Whisson, and Ramesh R. Vetukuri. Spray-Induced Gene Silencing as a Potential Tool to Control Potato Late Blight Disease. *Phytopathology*, 111(12):2166–2175, dec 2021.

[5] Gabriel Levesque-Tremblay, Jerome Pelloux, Siobhan A. Braybrook, and Kerstin Müller. Tuning of pectin methylesterification: consequences for cell wall biomechanics and development. *Planta*, 242(4):791–811, oct 2015.

[6] Henk Brouwer, Pedro M. Coutinho, Bernard Henrissat, and Ronald P. de Vries. Carbohydrate-related enzymes of important *Phytophthora* plant pathogens. *Fungal Genetics and Biology*, 72:192–200, nov 2014.

[7] D. F. Williams. Enzymic Hydrolysis of Polylactic Acid. *Engineering in Medicine*, 10(1):5–7, jan 1981.

[8] Helga Förster and Kurt Mendgen. Immunocytochemical localization of pectinesterases in hyphae of *Phytophthora infestans*. *Canadian Journal of Botany*, 65(12):2607–2613, dec 1987.

[9] Allen J. Ehrlicher, Ramaswamy Krishnan, Ming Guo, Cécile M. Bidan, David A. Weitz, and Martin R. Pollak. Alpha-actinin binding kinetics modulate cellular dynamics and force generation. *Proceedings of the National Academy of Sciences of the United States of America*, 112(21):6619–6624, may 2015.

[10] Siyang Guo, Olga S. Sokolova, Johnson Chung, Shae Padrick, Jeff Gelles, and Bruce L. Goode. Abp1 promotes Arp2/3 complex-dependent actin nucleation and stabilizes branch junctions by antagonizing GMF. *Nature Communications*, 9(1), dec 2018.

[11] Michael F. Seidl, Adrian Schneider, Francine Govers, and Berend Snel. A predicted functional gene network for the plant pathogen *Phytophthora infestans* as a framework for genomic biology. *BMC Genomics*, 14(1), 2013.

[12] Peter Bieling, Tai-De Li, Julian Weichsel, Ryan McGorty, Pamela Jreij, Bo Huang, Daniel A. Fletcher, and R. Dyche Mullins. Force Feedback Controls Motor Activity and Mechanical Properties of Self-Assembling Branched Actin Networks. *Cell*, 164(1-2):115–127, jan 2016.

[13] Antoine Jégou and Guillaume Romet-Lemonne. Mechanically tuning actin filaments to modulate the action of actin-binding proteins. *Current Opinion in Cell Biology*, 68:72–80, feb 2021.

[14] Marie-Claude Gagnon, Lawrence Kawchuk, D. Mathieu Tremblay, Odile Carisse, Giovanna Danies, William E. Fry, C. André Lévesque, and Guillaume J. Bilodeau. Identification of the Dominant Genotypes of *Phytophthora infestans* in Canada Using Real-Time PCR with ASO-PCR Assays. *Plant Disease*, 100(7):1482–1491, jul 2016.

[15] Karina Persson and Lars Backman. Structural and functional characterization of a plant alpha-actinin. *FEBS Open Bio*, 11(8):2198–2210, aug 2021.

[16] Frank Gubler and Adrienne R. Hardham. Secretion of adhesive material during encystment of *Phytophthora cinnamomi* zoospores, characterized by immunogold labelling with monoclonal antibodies to components of peripheral vesicles. *Journal of Cell Science*, 90(2):225–235, 1988.

[17] Sophie K. Walker, Kenny Chitcholtan, YuPing Yu, Gabrielle M. Christenhusz, and Ashley Garrill. Invasive hyphal growth: An F-actin depleted zone is associated with invasive hyphae of the oomycetes *Achlya bisexualis* and *Phytophthora cinnamomi*. *Fungal Genetics and Biology*, 43(5):357–365, may 2006.

[18] Tijs Ketelaar, Harold J.G. Meijer, Marjolein Spiekerman, Rob Weide, and Francine Govers. Effects of latrunculin B on the actin cytoskeleton and hyphal growth in *Phytophthora infestans*. *Fungal Genetics and Biology*, 49(12):1014–1022, dec 2012.

[19] Michael Reth. Matching cellular dimensions with molecular sizes. *Nature Immunology*, 14(8):765–767, 2013.

[20] Richard A. Wilson and Nicholas J. Talbot. Under pressure: investigating the biology of plant infection by *Magnaporthe oryzae*. *Nature Reviews Microbiology 2009 7:3*, 7(3):185–195, 2009.

[21] Magdalena Martin-Urdiroz, Miriam Oses-Ruiz, Lauren S Ryder, and Nicholas J Talbot. Investigating the biology of plant infection by the rice blast fungus *Magnaporthe oryzae*. *Fungal Genetics and Biology*, 90:61–68, 2016.

[22] Ralph Dean, Jan A.L. Van Kan, Zacharias A. Pretorius, Kim E. Hammond-Kosack, Antonio Di Pietro, Pietro D. Spanu, Jason J. Rudd, Marty Dickman, Regine Kahmann, Jeff Ellis, and Gary D. Foster. The Top 10 fungal pathogens in molecular plant pathology. *Molecular Plant Pathology*, 13(4):414–430, may 2012.

[23] R. J. Howard, M. A. Ferrari, D. H. Roach, and N. P. Money. Penetration of hard substrates by a fungus employing enormous turgor pressures. *Proceedings of the National Academy of Sciences*, 88(24):11281–11284, 1991.

[24] Tengsheng Zhou, Yasin F. Dagdas, Xiaohan Zhu, Shiqin Zheng, Liqiong Chen, Zachary Cartwright, Nicholas J. Talbot, and Zonghua Wang. The glycogen synthase kinase MoGsk1, regulated by Mps1 MAP kinase, is required for fungal development and pathogenicity in *Magnaporthe oryzae*. *Scientific Reports*, 7(1):945, dec 2017.

[25] Lauren S Ryder, Yasin F Dagdas, Michael J Kershaw, Chandrasekhar Venkataraman, Anotida Madzvamuse, Xia Yan, Neftaly Cruz-Mireles, Darren M Soanes, Miriam Oses-Ruiz, Vanessa Styles, Jan Sklenar, Frank L H Menke, and Nicholas J Talbot. A

sensor kinase controls turgor-driven plant infection by the rice blast fungus. *Nature*, 574(7778):423–427, oct 2019.

[26] Raquel O. Rocha, Christian Elowsky, Ngoc T.T. Pham, and Richard A. Wilson. Spermine-mediated tight sealing of the *Magnaporthe oryzae* appressorial pore–rice leaf surface interface. *Nature Microbiology*, 5(12):1472–1480, dec 2020.

[27] Wasin Sakulkoo, Miriam Osés-Ruiz, Ely Oliveira Garcia, Darren M. Soanes, George R. Littlejohn, Christian Hacker, Ana Correia, Barbara Valent, and Nicholas J. Talbot. A single fungal MAP kinase controls plant cell-to-cell invasion by the rice blast fungus. *Science*, 359(6382):1399–1403, mar 2018.

[28] Ramakanth Neeli-Venkata, Celia Municio Diaz, Ruben Celador, Yolanda Sanchez, and Nicolas Minc. Detection of surface forces by the cell-wall mechanosensor Wsc1 in yeast. *Developmental Cell*, 56(20):2856–2870.e7, oct 2021.

[29] Debarati Basu and Elizabeth S. Haswell. Plant mechanosensitive ion channels: an ocean of possibilities. *Current Opinion in Plant Biology*, 40:43–48, dec 2017.

[30] Andrew I.M. Savory, Laura J. Grenville-Briggs, Stephan Wawra, Pieter Van West, and Fordyce A. Davidson. Auto-aggregation in zoospores of *Phytophthora infestans*: The cooperative roles of bioconvection and chemotaxis. *Journal of the Royal Society Interface*, 11(94):20140017, may 2014.

[31] Maita Latijnhouwers, Wilco Ligterink, Vivianne G.A.A. Vleeshouwers, Pieter Van West, and Francine Govers. A Gα subunit controls zoospore motility and virulence in the potato late blight pathogen *Phytophthora infestans*. *Molecular Microbiology*, 51(4):925–936, feb 2004.

[32] P Van West, B M Morris, B Reid, A A Appiah, M C Osborne, T A Campbell, S J Shepherd, and N A R Gow. Oomycete Plant Pathogens Use Electric Fields to Target Roots. *Molecular Plant-Microbe Interactions MPMI*, 15(8):790–798, 2002.

[33] Andrea V. Robold and Adrienne R. Hardham. During attachment *Phytophthora* spores secrete proteins containing thrombospondin type 1 repeats. *Current Genetics*, 47(5):307–315, may 2005.

[34] Yusuke Onoda, Feike Schieving, and Niels P.R. Anten. A novel method of measuring leaf epidermis and mesophyll stiffness shows the ubiquitous nature of the sandwich structure of leaf laminas in broad-leaved angiosperm species. *Journal of Experimental Botany*, 66(9):2487–2499, may 2015.

[35] Ronny Reimann, Delf Kah, Christoph Mark, Jan Dettmer, Theresa M Reimann, Richard C Gerum, Anja Geitmann, Ben Fabry, Petra Dietrich, and Benedikt Kost. Durotropic growth of pollen tubes. *Plant Physiology*, 183(2):558–569, jun 2020.

[36] Jiali Gao, Le Guan, and Jinkui Chu. Determining the Young's modulus of SU-8 negative photoresist through tensile testing for MEMS applications. In *The International Society for Optical Engineering*, volume 7544, page 754464. SPIE, aug 2010.

[37] Edwin P. Chan, Yuhang Hu, Peter M. Johnson, Zhigang Suo, and Christopher M. Stafford. Spherical indentation testing of poroelastic relaxations in thin hydrogel layers. *Soft Matter*, 8(5):1492–1498, feb 2012.

[38] Jinwen Zhou, Dmitriy A. Khodakov, Amanda V. Ellis, and Nicolas H. Voelcker. Surface modification for PDMS-based microfluidic devices. *ELECTROPHORESIS*, 33(1):89–104, jan 2012.

[39] Zhiwei He, Senbo Xiao, Huajian Gao, Jianying He, and Zhiliang Zhang. Multiscale crack initiator promoted super-low ice adhesion surfaces. *Soft Matter*, 13(37):6562–6568, 2017.

[40] Charchit Kumar, Alejandro Palacios, Venkata A. Surapaneni, Georg Bold, Marc Thielen, Erik Licht, Timothy E. Higham, Thomas Speck, and Vincent Le Houérou. Replicating the complexity of natural surfaces: technique validation and applications for biomimetics, ecology and evolution. *Philosophical Transactions of the Royal Society A: Mathematical, Physical and Engineering Sciences*, 377(2138):20180265, feb 2019.

[41] Wenming Wu, Rosanne M. Guijt, Yuliya E. Silina, Marcus Koch, and Andreas Manz. Plant leaves as templates for soft lithography. *RSC Advances*, 6(27):22469–22475, feb 2016.

[42] Sayumi Fukuda, Riho Yamamoto, Naoki Yanagisawa, Naoki Takaya, Yoshikatsu Sato, Meritxell Riquelme, and Norio Takeshita. Trade-off between Plasticity and Velocity in Mycelial Growth. *mBio*, 12(2):1–32, apr 2021.

[43] Yun Zhang, Chenghao Ge, Cheng Zhu, and Khalid Salaita. DNA-based digital tension probes reveal integrin forces during early cell adhesion. *Nature Communications 2014 5:1*, 5(1):1–10, oct 2014.

[44] Yang Liu, Kornelia Galior, Victor Pui-Yan Ma, and Khalid Salaita. Molecular Tension Probes for Imaging Forces at the Cell Surface. *Accounts of Chemical Research*, 50(12):2915–2924, dec 2017.

[45] Lucile Michels, Vera Gorelova, Yosapol Harnvanichvech, Jan Willem Borst, Bauke Albada, Dolf Weijers, and Joris Sprakel. Complete microviscosity maps of living plant cells and tissues with a toolbox of targeting mechanoprobes. *Proceedings of the National Academy of Sciences of the United States of America*, 117(30):18110–18118, 2020.

[46] Jochem Bronkhorst, Michiel Kasteel, Stijn van Veen, Jess M. Clough, Kiki Kots, Jesse Buijs, Jasper van der Gucht, Tijs Ketelaar, Francine Govers, and Joris Sprakel. A slicing mechanism facilitates host entry by plant-pathogenic *Phytophthora*. *Nature Microbiology*, 6(8):1000–1006, aug 2021.

[47] Andrea V. Robold and Adrienne R. Hardham. During attachment *Phytophthora* spores secrete proteins containing thrombospondin type 1 repeats. *Current Genetics*, 47(5):307–315, may 2005.

[48] Cindy Vallieres, Andrew L Hook, Yinfeng He, Valentina Cuzzucoli Crucitti, Grazziela Figueredo, Catheryn R Davies, Laurence Burroughs, David A Winkler, Ricky D Wildman, Derek J Irvine, Morgan R Alexander, and Simon V Avery. Discovery of

(meth)acrylate polymers that resist colonization by fungi associated with pathogenesis and biodeterioration. *Sci. Adv*, 6, 2020.

Summary

Host entry by filamentous plant pathogens like *Phytophthora infestans* is a a vital step in their life cycle, but is hard to build understanding of as explained in the introduction (**chapter 1**). Invasion is mediated through invasive hyphae just a few microns accross, into highly autofluorescent plant materials in a 10-minute time frame. High-resolution microscopy to study host entry is therefore very challenging, making artificial plant-like substrates an important tool to study invasive behavior. Although highly interesting, most systems currently are limited in their scope, being too stiff to facilitate invasive behavior or not including adhesion to discern surface forces. Understanding the interplay between forces and genetics is vital in the maturing field of mechanobiology, making the study of mechanoperception and its genetic regulation possible. Mechanoperception plays a vital role in both pathogen penetration into plants, and in their plant hosts defense, making the interplay of forces and genetic regulation vital for successful host entry.

In this thesis we have developed transparent, microscopy compatible rubber materials with stiffness and surface properties similar to leaves to study host entry of *Phtyophthora* spp. Moreover, we are able to modify our substrates to enable displacement and fracture reporting whilst invasive forces are being applied. We have verified that our substrates are non-phototoxic and minimise disruption of invasive behavior in (**chapter 2**). In this chapter we show which designs were trialed and reasons why we settled on the final displacement sensor design.

We have used the developed techniques (**chapter 3**) to first study the invasion mechanism of *Phytophthora* spp. into displacement sensors. It was clear that multiple species applied forces to enable entry at an approximate 45 degree angle into the host material. Such "slicing" action is known to be a highly effective method to maximize tensile fracture forces from soft matter mechanics. Efficient fracture forces break open the material, in which hyphae grow and propagate to invade this model substrate, which we coined the **Naifu**-mechanism. From modeling we have deduced both the invasive force buildup in the pre-fracture regime, and the force concentration at the tip of the hyphae. Using fracture sensors, we were further able to confirm that our models were a good fit to experimental observations, further strengthening the Naifu mechanism. Expanding, we performed experiments to target disruption of vital elements of the Naifu-mechanism and saw major reduction in invasion efficiency and changes of cellular morphology as expected. When released on their native hosts we again were able to confirm the Naifu mechanism of entry from both literature and experiments, further broadening the scope of research.

Although knowledge of the forces at play during invasion of hyphal tips is very valuable, a central mechanical contradiction in invasive tip growth is present in *P. infestans* invasion. Force application is best performed by a stiff tip; but growth is mediated by turgor pressure from the inside and tip softening. We have studied to actin cytoskeleton to bridge this gap (**chapter 4**), which is much less stiff than the cell wall surrounding the tip. However, the actin network shows clear regulatory changes upon mechanical challenges; be it substrate stiffness or the invasive behavior. The transient increase in tip-focussed actin at the moment of invasion when stresses are maximized show that the network is a mechanosensor, and we hypothesize that the tip actin network also has a mechanical role in supporting the tip to maintain tip-shape. This is called tip-shape mechanostasis, an hypothesis underpinned by the observed decrease in tip radius with increasing invasive force application, the exact opposite of what should happen in normal elastic materials. Increases in tip radius were observed when the actin network was depolymerised during invasive behavior, as well as an arrest in force buildup and loss of tip polarization. Such efforts are vital for successful invasion; the hyphal tip mechanostat enables the efficient conversion of turgor into localized invasive pressures that are required to achieve host penetration.

Complimenting the intercellular observation, we have used chemical micro-mechanical sensors to study both the cell wall and plasma membrane behavior under various stressors (**chapter 5**). Such sensors provide the ability to study cell wall porosity and plasma membrane chemical polarity at a high temporal and spatial resolution. We see shifts of the cell wall porosity upon invasive force behavior, whilst observing only very minor shifts in plasma membrane properties during this process, as expected. During live-cell imaging, we are able to discern if either the plasma membrane or cell wall is being influenced by different plant protection compounds and confirm their proposed mode of action. The application of such chemical micro-mechanical sensors could be highly useful for crop protection compounds screening/discovery processes, enabling researchers to quickly determine if their compounds have a major influence on a specific sub-cellular compartment. Understanding the effect of cellular stresses on the cell wall-plasma membrane continuum is a unique tool to build up both fundamental and industrially relevant knowledge, of which there are few alternatives.

This thesis concludes with a general discussion (**chapter 6**), that includes preliminary data of different aspects/behavior of *Phytophthora* spp. that were studied but were not incorporated in the experimental chapters. We have also aimed to broaden the species scope in and have included some interesting data on the blast fungus *Magnaporthe oryzae* obtained in collaboration with TSL. It shows that the developed displacement sensor and other techniques could enable high resolution

study of invasive mechanics among a range of plant pathogenic species. We also note some of the possible further improvements/enhancements of our techniques in this final chapter, and hope that others will use the developed knowledge contained within this thesis to build further understanding of (pathogenic) life.

List of publications

This thesis

- Jochem Bronkhorst, Michiel Kasteel, Stijn van Veen, Jess M. Clough, Kiki Kots, Jesse Buijs, Jasper van der Gucht, Tijs Ketelaar, Francine Govers & Joris Sprakel. A slicing mechanism facilitates host entry by plant-pathogenic *Phytophthora*. *Nature microbiology* **2021** *6*(8), 1000-1006. (Chapter 3)

- Jochem Bronkhorst[+], Kiki Kots[+], Djanick de Jong, Michiel Kasteel, Thomas van Boxmeer, Tanweer Joemmanbaks, Francine Govers, Jasper van der Gucht, Tijs Ketelaar, Joris Sprakel. An actin mechanostat ensures hyphal tip sharpness in *Phytophthora infestans* to achieve host penetration. *Science advances* **2022** *Release under embargo until 10 June.* (Chapter 4)

- Lucile Michels[+], Jochem Bronkhorst[+], Michiel Kasteel, Djanick de Jong, Bauke Albada, Tijs Ketelaar, Francine Govers, Joris Sprakel. Molecular sensors reveal the mechano-chemical response of *Phytophthora infestans* walls and membranes to mechanical and chemical stress. *The Cell Surface* **2022** *8* , 100071. (Chapter 5)

[+] = shared first authors.

Other work

- Jan Maarten van Doorn, Jochem Bronkhorst, Ruben Higler, Ties van de Laar, and Joris Sprakel. Linking Particle Dynamics to Local Connectivity in Colloidal Gels. *Physical Review Letters* **2017** *118*(18), 188001.

Acknowledgements

The past five years have been a rollercoaster journey of personal and scientific exploration, and I would like to thank all who have joined along. I will probably forget people in this acknowledgment but would like to thank all who have supported me during my PhD period, and hope to have given back as much as possible to others! Thank you for everyone at PCC who have helped with both the personal and scientific sides of doing research. And many thanks to the groups of Cell Biology and Phytopathology for opening their doors to me and teaching biology to a physical chemist.

Joris, your name is the golden thread in both the scientific and personal development contained within this thesis, and I cannot thank you enough for all you have done. Your emotional honesty at the low points, and generosity to give second chances as well as incredible drive and passion for science are an incredible inspiration. I will never forget the support you showed at my lowest point, and will support others when they are down. Even whilst balancing so many things, you find the time to support, help and guide us PhD's to collaborate and quickly develop, and I have been proud for being part of your scientific family. There are too few words to thank you.

Mara and Anita, I cannot thank you enough for supporting me during my mental episode at the start of the PhD. Your support meant I could really take a step back and build up energy reserves to build mental strength, which has been invaluable to happiness. It is awesome to see that both of you have pursued post-PCC paths that have brought you much happiness and flourishing! Leonie, our conversations were always incredibly stress relieving and interesting while your taste in group activities and food is stellar. Mara, Leonie and Marioes, thank you for making space for all the calendar requests and order forms send over and all you do for us PhDs. Tom, Remco, Diane and Raoul, our conversations during lunch and over technical things were always interesting and exciting, and your support has been incredibly helpful in getting this project off the ground.

Jasper, thank you for your interest and quick response when I could not figure out analytical matters. Your modelling has been very insightful, helping with experimental efforts and puts the work in perspective. Francine and Tijs, thank you both for your support during the PhD project and taking the plunge to try to build understanding of host entry. Your tutoring on how to grow, multiply and image biological cells has been very helpful, and the ideas brought to the table in our progress meetings were always very useful. The open access to the laboratories and even space to supervise students was always appreciated.

Talking about students; Tim, Stijn, Martijn, Djanick, Thomas, Tanweer, Pieter and Elvira, I cannot thank you enough for the great collaborations we have had! Am grateful for the energy you all have brought to the table in your research. Although experimental success was not equally distributed, I have learned as much about *Phytophthora* as about collaborative efforts in supervising you, which has been an absolute pleasure. Many of you have been included in our publications or your work can be found in this thesis, whilst even more interesting observations might form the basis of future research! Wish you all the best in the future and hope you look back positively on your thesis/internship.

There is much to life next to science, and although the blending of professional and personal relationships always takes place with coworkers, there are too many people to thank. Jesse, Pieter, Aurelie, Inge and Justin, thank you for asking me to be your paranymph; it has been an absolute pleasure to (try to) support you during the thesis defence next to the great relationships we have! Jesse, next to working, discussing and seeying each other in the lab, our drives from Arnhem to the lab were always lots of fun and I really treasure the relationship we have build up. Justin and Raoul, we have spend much of our study and research lives together and I have always found working and relaxing with you an absolute highlight and I'm sure we will see each other more in the future. Janmaarten, Ties, Ruben and Pieter, your supervision and help in the lab has been incredibly valuable during my periods at PCC, next to being great friends who you can call upon. Ellard, Ralph and Cheng, thank you for the awesome environment in the 6055 office.

Lucile, your help, good conversation and scientific collaboration has been awesome and I hope we can laugh about silly things as much as we did in the future! Jessica and Martijn, we always had fun in the lab and good discussion, and the visit to Montreal was very special, especially considering the global pandemic that started just a little later. Annemarie, Hanne, Prathap, Inge, Riccardo, Maarten, Kasper, Ramakanth, Cecilia, Yosapol and Sophie, it was great to form part of the Sprakel family with you, having nice lunches and building a great team together. Your support and good questions during meetings tickle the mind. The large scope of research within the group has been an enlightening experience.

Lauren and Nick, your help from TSL to trial *Magnaporthe* on the force sensing surfaces, and your patience on the iterative process across the channel, including the uncertain brexit period, was very special, and I loved our discussions. It is unfortunate that the pandemic has meant no visit to the UK was feasible in the project time-frame; I am convinced that many interesting and nice observations can be found in our collaboration and your further work. Lauren, thank you for the personal messages as well, and it is awesome to hear the stroopwafels were well appreciated!

Kiki and Michiel, your help during the research period has been invaluable, and it was a great feeling to be rowing the *Phytophthora* boat together and push research ahead. Next to working together, blowing off steam whilst focussing on *Phytophthora* was always great to relieve stress and brighten the day. Your inclusion on our collaborative papers has been invaluable and hope you have enjoyed working together as much as I did.

Thanks to the NWO for funding this fundamental research, provinding the space to collaborate and enable scientific research at a high level.

Prof. Dr J. L. van Leeuwen, Prof. Dr G. Koenderink, Prof. Dr G. van den Ackerveken and Dr E. Evangilisti, distinguished opponents, thank you for critically reading the PhD thesis in detail and make time for the defence and preparation of questions. Without your gracefulness of time and effort, a PhD defence could not take place.

Lieve vrienden en familie, van de VvdO, HKW tot 7 nm, dankjewel voor jullie steun in de promotieperiode. Jullie hulp met het afblazen van stoom als het nodig was, samen lekker muziek maken en gezellig samen gamen maakt het leven leuk. Sorry als ik soms enorm doorratelde over het onderzoek, hopelijk zal dit na de verdediging mee vallen! Annemarie (en Gerrie en Gerard), hoewel 2018 een zwaar jaar was, ben ik je heel erg dankbaar voor alle liefde en tijd die we samen hebben gedeeld en alle steun die je mij hebt gegeven.

Ewald, Tecla, Hilde, Lucienne en Mathijs, jullie vorming, hulp en steun heeft me voorbereid en door deze PhD geholpen. Dankzij jullie stimulering om zaken te ondernemen en voor mezelf op te komen heb ik dit project af kunnen ronden. Ewald, dat we elkaar wekelijks zien en samen muziek maken, en erna met een biertje samen stoom afblazen is echt enorm fijn en altijd een highlight in de week. Tecla, samen wandelen en eten doen we gelukkig erg vaak, het is super om je te zien en goede gesprekken te hebben! Hilde, naast een goede tandarts zijn, is het echt top om te zien dat je je steeds beter in je vel voelt, en weet zeker dat ook jouw PhD helemaal goed komt. Mathijs (en Marinke), het is mooi om jullie liefde samen en die voor Jasper te zien, en wens jullie alle goeds. Lucienne, mijn bonus-moeder, dankjewel voor alle warmte en openheid, ook in de afgelopen tumulteuze tijd.

Saskia, Anton-Eelco, Emi (Peter), Ilse en de rest van de familie, dankjewel voor jullie acceptatie van mij in jullie gezinnetje en alle mooie momenten in de afgelopen jaren. Als laatste, maar ook belangrijkste: Anne, dankjewel voor alle liefde, steun en plezier, en het samen delen van het leven. Het is heerlijk emotioneel om als twee labradors samen door het leven te kunnen gaan, en samen van de grote en kleine dingen te genieten. Ik kijk enorm uit om samen ons leven verder uit te bouwen en vele jaren met je samen te zijn.

Jochem – Arnhem, 2022

About the author

Jochem Bronkhorst was born on 31 July 1993 in Nijmegen, the Netherlands. He lived there only shortly, and moved to Elst, where he enjoyed his childhood.

After primary education at "Het Startblok" in Elst, he attained a bilingual english/dutch high-school diploma from the Overbetuwe College in Bemmel. Jochem went to Wageningen University in 2011 to study Molecular Life Sciences, including a board year for the study association Alchimica. After obtaining a Bachelor degree, a Master degree with specialization physical chemistry was achieved. During this master phase, a confocal based study of single particle dynamics in colloidal gels was understaken under supervision of Dr. Jan-Maarten van Doorn, Prof. Jasper van der Gucht and Prof. Joris Sprakel. A research internship was then performed in the Schools of Physics and Astronomy in St. Anderws on whispering gallery mode resonated lasers under supervision of Prof. Malte Gather and Dr. Marcel Schubert.

After returning to Wageningen, Jochem started his PhD at the Laboratory of Physical Chemistry and Soft Matter under supervision of Prof. Joris Sprakel, focussing on organic ligt-emitter synthesis in July 2017. After 6 months of unsuccesful effort and developing mental problems, a break was performed to improve mental health. After the break a new research line on developing plant mimicing materials to study host entry of filamentous plant pathogens, was started up and has led to this thesis, in close collaboration with Prof. Francine Govers (laboratory of Phytopathology) and Dr. Tijs Ketelaar (Laboratory of Cell Biology). As from June 2022, Jochem has embarked on a renewed scientific effort in the laboratory of Biochemistry at Wageningen University as a post-doc.

Overview of completed training activities

Discipline-specific activities

- Dutch Polymer days, PTN, Lunteren, 2017.
- Masterclass by Nick Talbot, WUR, Wageningen, 2019.
- Han-sur-Lesse Winter School, WUR/UU/UvA/UL, Han-sur-Lesse, 2019.
- Dutch Soft Matter Days, WUR/UU/UvA/UL, Leiden, 2018.
- Joint Workshop on Nano-Characterisation, 4TU, Utrecht, 2019.
- MechanoChemBio (poster), MPI, Montreal, 2019.
- CHAINS 2019 (poster), NWO, Veldhoven, 2019.
- Dutch BioPhysics (oral presentation), NWO, online, 2020.
- CHAINS 2020, NWO, online, 2020.
- Physics@FOM (poster), NWO, online, 2021.
- CEMB Mechanobiology Symposium (oral presentation), University of Pennsylvania, online, 2021.
- NWO life symposium (oral presentation), NWO, online, 2021.
- Leibniz plant symposium, IPBT, online, 2021.

General courses

- VLAG PhD week, VLAG, Baarlo, 2018.
- PhD Lecture series, VLAG, online, 2020.
- Journal Club, PCC, Wageningen, 2018-2021.
- Infographics and Iconography, WUR library, Wageningen, 2019.
- Introduction to R, WUR, online, 2021.
- Scientific integrity session, AFSG-PCC, online, 2021.
- Netherlands Code of Conduct for Research Integrity course, VLAG, Wageningen 2021.
- The Choice: Un-box your PhD process & take charge of your performance, Wageningen Graduate School, Wageningen, 2021.

Optionals

- Preparation of research proposal, PCC, Wageningen, 2017.
- Weekly group meeting, PCC, Wageningen, 2017-2021.
- Phytophthora meeting/PhytoSeminarSeries, Phytopathology/Cell Biology laboratories, Wageningen, 2018-2021.
- Sprakel group meeting, PCC, Wageningen 2019-2021.

Cover design by Selma van Tartwijk || http://selmavantartwijkartworks.webflow.io/

Printed by ProefschriftMaken || www.proefschriftmaken.nl

This work was financed by an NWO ECHO grant, project #712.016.001. Financial support from Wageningen University for printing this thesis is gratefully acknowledged.